Optimisation of Hall cross devices towards magnetic particle counting

Holly Martha Herbert

Supervisor: Prof. R. P. Cowburn

Department of Physics

University of Cambridge

This dissertation is submitted for the degree of

Doctor of Philosophy

Darwin College

December 2022

Declaration

This thesis is the result of my own work and includes nothing which is the outcome of work done in collaboration except as declared in the preface and specified in the text. It is not substantially the same as any work that has already been submitted before for any degree or other qualification except as declared in the preface and specified in the text. It does not exceed the prescribed word limit of 60,000 words, excluding table of contents, photographs, diagrams, figure captions, list of figures/diagrams, list of abbreviations/acronyms, bibliography, and acknowledgements, for the Physics and Chemistry Degree Committee.

Holly Martha Herbert

December 2022

Abstract

The magnetic detection of magnetically labelled disease biomarkers from a sample of bodily fluid presents an interesting architecture for a disease diagnostic device. Many advantages are offered over conventional optical labelling and detection techniques, including reduced background signals and sample pre-processing requirements due to the lack of magnetically responsive material in biological samples, as well as enhanced control over various steps of the assay protocol as magnetic labels may be actuated remotely via the application of magnetic fields.

In this thesis, Hall cross sensors are explored for the detection and enumeration of large numbers of magnetic particles for applications in magnetic immunoassays. The response of a Hall cross to a magnetic particle is directly proportional to the stray field of that particle averaged over the active area of the cross. As the active area size increases relative to the particle size, due to the solenoidal nature of the particle's stray field, this average tends towards zero. As a result, large area Hall sensors suffer from low single particle signals, limiting device resolution. In addition, the Hall response is found to be highly inhomogeneous as a function of particle position, limiting the certainty with which particles may be counted. Hall cross sensors for which the active area size match the particle size produce a much larger response and can be used detect the binary presence or absence of a particle, thus resolving issues with both signal strength and homogeneity. However, dense arrays of individually contactable sensors must be fabricated to detect meaningful numbers of particles, limiting their usefulness.

This work focuses on the optimisation of large area Hall cross sensors towards the goal of counting large numbers of magnetic particles simultaneously with improved resolution and measurement uncertainty. It is hypothesised that the inclusion of perforations within the active area of such devices could make the Hall cross insensitive at locations where the stray field components of a landing magnetic particle reduce the overall Hall signal, thus enhancing the response. This concept is explored using COMSOL simulations and it is found that when an array of perforations is added to the active area of a Hall cross and particles land at certain subsets of positions relative to these perforations, both the magnitude of the Hall response and the homogeneity of the response with position are vastly improved. Experimental prototype devices are fabricated from GaAs/AlGaAs at which a 2DEG has formed and the response of perforated devices to arrays of magnetic disks is measured at room temperature, with the aim of demonstrating the same improvement. Good agreement between computational and experimental results is found for the perforated devices, while for the equivalent continuous devices, the measured response suggests that the fabrication of magnetic particles directly on top of the GaAs/AlGaAs resulted in the local, partial depletion of the underlying 2DEG. As such, these devices behave in a manner consistent with having partially formed perforations.

Acknowledgements

I would firstly like to extend my thanks to Prof. Russell Cowburn for accepting me into his wonderful research group and offering his exciting ideas and insightful feedback over the years. For showing me what it means to be a great scientist, I would like to especially thank Dr. Dorothee Petit. I will be forever grateful for her guidance, support, and mentorship. I would also like to thank Dr. Pierre Roy and Dr. Georgios Stefanou with whom it was a pleasure to collaborate. Finally, I would like to thank all the members of the Cowburn group who I had the opportunity to work with over the years; Tarun Vemulkar, Jereon Verheyen, Emma Welbourne, Jake Zipfel, Mike Stanton and Spencer Brennan.

Beyond the realm of academia, I would like to thank my family for their endless love and support. They inspired me, taught me the value of independence, raised me to be curious and instilled in me the confidence to tackle something as challenging as a PhD. For the remnants of my sanity, I must thank the communities of Harding Way and DarBar, who lit the way to the end of this PhD. Finally, for single-handedly keeping me alive and showing me that good things can still grow in dark places, I would like to thank Josh Grantham. The submission of this thesis would not have been possible without his patience, kindness, and creative tactics for keeping me calm.

Contents

List of figures

List of tables

Nomenclature

Acronyms/Abbreviations

H_C	Coercive field
H_N	Nucleation field
H_J	Coupling field
H_{SW}	Switching field
M_S	Saturation magnetisation
M_r	Remanent magnetisation
FM	Ferromagnet
SAF	Synthetic Antiferromagnet
PMA	Perpendicular magnetic anisotropy
MOKE	Magneto Optical Kerr Effect
VSM	Vibrating Sample Magnetometer
AFM	Atomic Force Microscope
SEM	Scanning Electron Microscope
RKKY	Ruderman-Kittel-Kasuya-Yosida
SRT	Spin Reorientation Transition
V_{Hall} or V_H	Hall Voltage
CV	Coefficient of variation
FEA	Finite Element Analysis
FEM	Finite Element Method
2DEG	Two-dimensional electron gas
PDE	Partial differential equation
GaAs	Gallium Arsenide
AlGaAs	Aluminium Gallium Arsenide
MRAM	Magneto resistive memory
GMR	Giant Magnetoresistance
MR	Magnetoresistive or magnetoresistance

TMR	Tunnel Magnetoresistance
AMR	Anisotropic Magnetoresistance
GMI	Giant Magneto-impedance
SQUID	Superconducting quantum interference device
CMOS	Complementary metal oxide semiconductor
NP	Nanoparticle
SPM	Superparamagnetic
NM	Non-magnetic
EM	Electromagnet

1. Introduction

Molecular diagnostics has emerged as a promising approach to the identification of illness through detecting or quantifying the presence of specific biomolecules, indicative of human disease. It is hypothesised that a platform capable of the rapid, sensitive and specific detection of a panel of biomarkers from a sample of bodily fluid will revolutionise healthcare, enabling quick and accurate diagnostics, disease staging, appropriate treatment prescription and the analysis of patient response to care. In recent years, vast progress towards such a platform has been made, with large emphasis placed on the development of portable and cost-effective technology, facilitating the need for point of care testing both at home and in the developing world.

There are currently many well-established approaches to detecting or quantifying the presence of disease biomarkers. Western blotting[1], ELISA (enzyme-linked immunosorbent assay)[2] and protein microarrays [3] are widely accepted as the gold standards of protein detection, while Southern Blotting [4] and DNA microarrays [5] present themselves as the equivalent champions in DNA detection. Multiplexed bead array assays such as Luminex xMAP[6] technology have more recently emerged, presenting a rapid and sensitive technique, capable of the simultaneous detection of multiple biological species. In addition, flow cytometry[7] enables the detection and characterisation of different cell types, facilitating screening for rare and diseased cells.

Each approach involves the use of specific recognition molecules which bind to the biomarker of interest, followed by the labelling of the biomarker with a signal transducer, generally a fluorophore. Detection or quantification is achieved via the subsequent analysis of a fluorescent or colorimetric signal. The sensitivity of such techniques is limited by several factors, including the photobleaching of fluorescent labels and substantial background signals stemming from autofluorescence of the biological matrix. While DNA detection is aided by amplification techniques such as Polymerase Chain Reaction (PCR) [8], the detection threshold of proteins via these methods is limited to concentrations in the pM regime[9][10] (~0.1 pg/ml) and above. It is expected that many biomarkers are present in fM (~0.1 fg/ml) concentrations and below, thus leaving numerous proteins indicative of disease undetectable[11]. In addition, extensive sample pre-processing is generally required and often the need for bulky, complex and expensive optical components prevents the application of the technology in a point of care setting.

Advances in nanotechnology have facilitated the development of many alternative signal transducers and innovative detection schemes, including the use of DNA origami in combination with nanopores [12], micro-cantilevers [13], nanowires [14], carbon nanotubes [15], gold nanoparticles [16] and quantum dots [17]. However, these systems also suffer from several limitations, including unreliability in conditions of varying pH or ionic strength. Samples may thus require even more extensive processing, which is not a realistic requirement for point of care testing. In addition, of the novel approaches mentioned, those which are optical in nature (use of gold nanoparticles and quantum dots) continue to suffer from optical background signals and the requirement of expensive optical apparatus.

The magnetic detection of magnetically tagged biomarkers, well suited to overcome many of these shortcomings, presents itself as an ideal candidate for development. Firstly, magnetic nanoparticles (MNPs) have been studied widely as diagnostic and therapeutic tools; they have been used as MRI contrast agents [18], for targeted drug delivery [19] and in hyperthermia treatment of tumours [20]. They have also been used extensively to manipulate biochemical species, in particular in biological separations [21]. Due to their vast demand in these medical applications, their toxicity and biocompatibility have been extensively investigated and many different forms are commercially available. Secondly, there is no measurable magnetic signal present in the biological matrix, dramatically reducing background signals and so enabling quantification of lower biomarker concentrations. Finally, and perhaps most importantly, the ability to manipulate magnetic tags remotely via the application of magnetic fields provides an additional degree of freedom, enabling enhanced control of various assay steps.

While advances were being made in the production of magnetic particles for biological applications, the semiconductor industry was making substantial progress in the development of microfabrication technology, specifically in the fabrication of cheap, highly sensitive, CMOS integrable magnetic sensors designed for use in magnetic memory devices (MRAM). The combination of these sensors with commercially available magnetic tags and emerging microfluidic technology constituted a promising architecture for a novel disease diagnostic device, and in the last 20 years, vast developmental effort has been dedicated to the investigation and commercialisation of magnetic biosensing technology.

The concept of adapting MRAM sensor technology for use in biosensing in combination with magnetic tags was pioneered by Basalt et al in 1998 [22]. In collaboration with Non Volatile Electronics (NVE), the research group combined commercially available superparamagnetic beads, specifically 2.8 μm diameter Dynabeads, with an array of giant magnetoresistive (GMR) sensors to produce the Bead Array Counter (BARC). In their simplest form, GMR sensors are tri-layer structures composed of two magnetic layers separated by a non-magnetic conductive layer, in which the resistance of the structure depends on the relative orientation of the magnetisation of the two magnetic layers. This relative orientation can be altered by an applied magnetic field, and the resistance of the structure varies with the square of this field. The group initially applied the technology to the detection of biological warfare agents [23], [24], rapidly producing a table-top prototype device. Several improvements were made to the GMR sensors over the years, with the third iteration of the chip, BARC III [25], integrated with microfluidic technology to produce cBASS [26]. Focusing on the microfluidic technology, the group developed a technique known as Fluidic Force Discrimination which enabled the discrimination between tags which were bound specifically or non-specifically with the sensor surface via fluidic forces, eventually leading to a platform which reached aM protein sensitivities [27], fM DNA hybridisation sensitivities [28], all encompassed in a shoebox-sized apparatus [29].

Inspired by this revolutionary approach, many research groups from around the world joined the field, working towards the development of magnetic immunoassays and DNA chips. The Freitas group at IST in Portugal are one of the most noteworthy contributors and were the first group to employ Spin Valve (SV) sensors[30], [31] which are GMR structures engineered to have a linear response to applied fields, thus constituting a much more ideal magnetic sensor. The group took full advantage of the magnetic nature of the tags, manipulating them in novel ways in order to control various assay steps. For example, tapered current lines[32], [33] were used to guide magnetic tags to the sensors and

U-shaped current lines were developed to focus magnetic tags at the sensor active area, which was shown to increase the speed of DNA hybridisation[34], [35]. The group developed a portable detection platform based on these advancements [36], [37], [38] and demonstrated its use for the viability assessment of Salmonella cells[39] and the detection of BCG bacteria for the diagnosis of tuberculosis[40]. The group excelled when they moved to the realm of dynamic detection, in which microfluidics were employed and cells, covered in magnetic tags, were detected in flow as opposed to statically on the surface of the sensors. Based on this approach, a platform was developed and verified for bacteria detection in milk [41], [42]. The technology was licensed to the company Magnomics [43], which is attempting to commercialise a DNA chip, primarily employed in the detection of bovine mastitis-causing pathogens in milk.

Of equal importance is the research produced by the Wang group at Stanford, California. The Wang group aimed for single-molecule detection from the outset and focused on using custom-made, nanometer scale magnetic tags in combination with SV sensors [44]. They were the first group to produce a dense array (>1000 sensors per chip) of CMOS integrated sensors [45], and went on to build a platform consisting of 64 sensing zones, each zone composed of 64 sub-micron SV sensors, striking the right balance between good magnetic sensitivity (small sensors) and good biological sensitivity (large sensors enabling the detection of high numbers of biomarkers) [46]. The group was the first to really excel in the biological arena, moving rapidly from proof of principle experiments to working with complex biological samples, achieving sensitivities 1000 times better than ELISA [47], [48]. They demonstrated the quantification of many clinically relevant biomarkers, for example those for radiation exposure [49], allergen response [50], mycotoxins [51] and HPV [46], all in the pM to fM range. They continued to improve their device, incorporating a novel assay procedure, referred to as autoassembly [52], with an ultrathin (30 nm) passivation layer and the concept of magnetic nanotag amplification [53]. Essentially, only magnetic nanotags which are bound directly to the surface produce a measurable signal, removing the need for washing steps. The rate at which the tags assemble on the surface is monitored in real time, and if necessary, secondary magnetic tags can be added and attached to the primary tags, amplifying the magnetic signal. The high sensitivity of this device and the obviation of the need for washing steps made it highly suitable for point of care testing, and in 2016, the first version of the Eigen Diagnosis Platform was revealed [54] with a second iteration produced in 2019 [55]. The platform comes equipped with a smartphone interface and is carried out with a $4 disposable test stick and one step user intervention. The platform has been validated for use in the diagnosis of lung cancer nodules having undergone clinical trials [56]. The platform has been commercialised by MagArray [57] and constitutes the first clinical application of magnetic immunoassay technology.

While these groups are considered some of the most successful in the field, they are far from the only research groups who contributed innovative magnetic biosensing strategies over the years. Also employing magnetoresistive (MR) sensors for bio-detection are groups at Phillips [58], the University of Bielefeld [59] and the University of Minnesota [60], to mention but a few. In addition, several different magnetic sensors also emerged in the biosensing arena over the years, including SQUID [61], Flux gates [62], GMI sensors [63] and AMR rings [64].

While most of the developmental effort has been invested in magnetoresistive (MR) sensors, they are not inherently well suited to the detection of superparamagnetic particles. The response of MR sensors tends to saturate at low applied fields, thus limiting the extent to which superparamagnetic particles may be magnetised for detection. Hall

cross sensors [65] exhibit a linear response across a much larger range of applied field and as such, present an advantageous alternative. These sensors rely on the classical Hall effect, whereby current propagating through a device is deflected in the presence of an orthogonal magnetic field. The deflected charge carriers accumulate on one side of the device and the resultant transverse voltage is referred to as the Hall voltage. The linearity of the Hall response with applied field enables the application of much stronger magnetising fields, increasing the moment and so the emanating stray field of the superparamagnetic beads, resulting in a larger signal per particle for detection. An additional benefit of high field operation is the possibility to measure the hysteresis loops of magnetic particles. This may allow particles with recognisable and tuneable switching behaviour to be detected using their characteristic hysteresis loop as a signature. Hall cross sensors have also benefitted from advances in semiconductor technology, specifically the compatibility of silicon Hall crosses with CMOS technology, enabling the cheap production of dense arrays of Hall crosses. In addition, the development of high mobility 2DEG materials has enabled the production of Hall devices with enhanced Hall sensitivities [66].

The development of Hall cross sensors towards the detection of superparamagnetic beads for biomedical applications began with Besse et al. [67], who first demonstrated the detection of a single 2.8 µm Dynabead using a silicon Hall cross sensor. In this work, the group developed a phase sensitive detection approach, whereby a DC magnetic field applied perpendicular to the sensor plane magnetised the bead, while an AC field caused the bead's moment to oscillate, producing an AC Hall voltage response which was measured via lock-in detection. The DC field was stepped, and a corresponding change in the magnitude of the AC Hall voltage was taken as evidence for the presence of the bead. This technique, among others as well as adaptations, was utilised by the research community over the following years to demonstrate the detection [68], [69], [70], [71], [72], [73] and characterisation [74] of a single superparamagnetic bead positioned on the surface of a Hall cross sensor.

It is widely accepted that to maximise the Hall voltage response to a magnetic particle, the sensor size and particle size should be matched. This is because the generated Hall voltage is directly proportional to the stray field of the particle averaged into the active area of the cross. As the active area increases in size relative to the particle, the average field of the particle, and so the Hall voltage response, tends towards zero. As the active area decreases, the positively directed stray field below the particle is captured by the sensor, while the surrounding negatively directed stray field falls beyond the sensor boundaries. As a result, the averaged stray field, and so the Hall voltage response, increase. Naturally, for use in magnetic immunoassays, the simultaneous detection and enumeration of many magnetic particles is needed. To this end, much research focused upon the integration of dense arrays of Hall cross sensors, with each Hall element capable of the detection of a single magnetic particle bound specifically to its surface. The most notable contribution in this area was the work of Gambini et al., who developed an integrated 64x160 Hall element platform [75]. Using 1 to 4.5 µm Dynabeads detected via a magnetic relaxation approach earlier developed by the group [76], the functionality of the sensor was verified in an assay context. The sensor array was coated with a known concentration of Human Serum Albumin (HSA), and magnetic beads, functionalised to specifically bind to HSA, were incubated with the array surface and enumerated. Arrays of Hall cross sensors integrated with microfluidics have also been successfully used in biological applications, for the in-flow detection of bacteria [77] and rare cells [78] specifically labelled with magnetic particles.

The use of a single, large area Hall cross sensor for magnetic bead counting has also been investigated [79], however these sensors suffer from low single particle Hall voltage signal due to the dilution of the average stray field into the large active areas, as well as signal inhomogeneity as a function of position. In particular, the response of the cross is much more sensitive at the corners than the centre, and changes polarity when a particle lands close to, but not upon, the cross [80], [81]. The inhomogeneity of the response with position limits the accuracy with which particles can be counted, as the total signal can vary greatly for a given number of particles, depending upon the configuration in which they land.

In this work, we investigate the optimisation of large area Hall cross sensors for the detection and enumeration of large particle numbers via optimisation of the Hall cross sensor geometry. Optimising the response of a Hall cross sensor to the presence of a local inhomogeneous magnetic field via geometric alterations is not a novel concept. Several publications have investigated the effects of narrowing the voltage probe arm(s) and found increased sensitivity in the vicinity of the narrowed arm(s) [82], [83]. Effects of the Hall cross corner geometry have also been investigated, showing that corner rounding reduces the Hall voltage response [84], while the presence of sharp angle slits increases the Hall voltage response[85]. In the context of large area Hall cross sensors for magnetic bead counting, optimisations to improve Hall signal homogeneity with position have been identified [80]. Increasing the bead-sensor distance as well as the sensor active area (such that the cross corners may be further from the array of beads to be counted) have been shown to improve the homogeneity of the signal as a function of position, however the improvements in signal homogeneity come at the expense of single particle signal magnitude.

Here, we aim to adapt large area Hall cross sensors and improve them towards the counting of many particles with a single electrical readout signal, ideally with single particle resolution. To achieve this, we propose the addition of arrays of perforations to large area Hall cross sensors, equal in diameter to the magnetic particles to be counted. We find that when particles land at certain subsets of positions with respect to these perforations, large improvements in device operation emerge. Ultimately, the Hall cross becomes insensitive at locations where the stray field components of the magnetic particle reduce the overall Hall signal (due to the presence of the perforations), and more sensitive at locations where the stray field components are to be taken into account (due to locally enhanced current density). Depending on the magnetic particle type (both beads and disks are considered in this work) and landing configuration, enhancements in signal particle signals of over an order of magnitude are seen, as well as significant enhancements in signal homogeneity as a function of position. The number of particles measurable with an uncertainty of ±1 particle is taken as the main metric for homogeneity in this work and increases of at least 50% are shown. Our work relies on the concept that the positions at which particles land upon the sensor may be precisely controlled. Proof of this aspect was considered beyond the scope of this project, however the control of magnetic particles in fluids is well documented in the literature [86],[87],[88], [89] and thus we have reason to believe it is possible with some engineering and will not be a road-block in this work.

In this thesis, chapter 2 will introduce the main concepts necessary to understand this work. We will discuss the use of magnetic particles as labels in magnetic immunoassays and provide the theory to understand the magnetic behaviour of both the commonly used superparamagnetic beads and the less well-known thin film magnetic disks. A mathematical description of the stray field profile for each particle type is presented. We outline the theory of the Hall

effect in both uniform and spatially inhomogeneous magnetic fields and present the mathematical model which we use in our computational work to simulate the Hall voltage response of 2DEG Hall cross sensors in the (room temperature) diffusive regime to the presence of magnetic beads and disks. We discuss Finite Element Analysis and the implementation of our model in COMSOL Multiphysics. Finally, we discuss the experimental techniques used in this work to fabricate, characterise and measure prototype Hall cross devices, aimed at demonstrating the operation and benefits of our optimised Hall cross geometry. The Hall voltage measurement setup, built to enable Hall voltage measurements to be conducted on these devices, is discussed and the different measurement approaches used in the project are presented.

In chapter 3, the results of our computational simulations conducted using COMSOL Multiphysics are presented. The results of our model are firstly extensively verified against results presented in the literature. The various tests that needed to be carried out to ensure that our results can be trusted (have reached a stable state with respect to various computational parameters) are discussed and the results presented. With trust in our model established, we present the model Hall cross system which our computational work primarily focuses on. This model system is a 100 µm x 100 µm active area Hall cross with experimentally realistic material parameters and is investigated for the enumeration of 6 µm diameter magnetic beads and disks, firstly in its continuous form and later with a 7x7 array of 6 µm diameter perforations. We explore how the continuous Hall cross responds to the presence of experimentally realistic magnetic beads and disks, both when situated at the sensor centre and as a function of position and establish the number of particles which can be measured to within an uncertainty of ±1 particle, which we use as our metric to quantify homogeneity. We investigate the same for the perforated sensor and show improvements in signal strength of over an order of magnitude and improvements in homogeneity with position of 50%, when particles land either aligned with the perforations or at the central, diagonal position between four perforations. Results naturally differ depending on the particle type and landing configuration, with the most promising results shown when magnetic particles land aligned with the perforations and sit embedded within them, with their equator at the level of the 2DEG (~30-fold increase in signal for magnetic disks, and ~15-fold increase for magnetic beads, relative to the equivalent continuous device). We investigate the central mechanisms at play in the signal improvement. Primarily, we find this to be a result of the enhanced average field of a particle into the sensor's effective active area with the addition of perforations. Having demonstrated the improvements towards magnetic particle counting gained from the addition of perforations, we further explore the perforated device geometry, aiming to optimise the design.

In chapter 4, the fabrication and characterisation of prototype devices are presented. The Hall voltage signal from arrays of magnetic disks of diameter 6, 4 and 3 µm fabricated both within the perforations of perforated devices and upon the surface of continuous devices is measured and the results and analysis are shown. Upon comparison of the experimental results with computational predictions, it is found that the results of measurements performed on the perforated devices agree well when several factors are accounted for, primarily the separation between the perforation and particle edges due to the non-ideal fabrication process. Best agreement is demonstrated for the 6 µm disks (within 32%) and agreement worsens as the particle diameter decreases, to 60% for the 3 µm magnetic disks. However, we also show that the impact of the disk-perforation spacing will be largest for the smallest diameter particles. We find that the Hall voltage measurements taken on equivalent continuous crosses do not agree well with

computational predictions, most obviously in terms of the polarity of the signal. Possible explanations are explored and based on experimental measurements and computational results; we propose that partial perforations were created on the continuous devices via the partial, local depletion of charge carriers from the 2DEG in the regions below the magnetic particles. We propose that the depletion is due to the GaAs/AlGaAs – gold interface and the formation of a Schottky barrier, which has been shown in the literature to cause depletion of the 2DEG below deposited gold[90]. When these local depletion zones are included in our computational model, both the magnitude and polarity of the experimental results are well reproduced. Finally, we propose improvements to the device fabrication process, which we expect will improve agreement between experimental and computational results in future iterations of devices.

2. Theory

In this chapter we present the relevant theory for this project subdivided into three central sections. Firstly, we discuss the basic theory of magnetic particles for use in biological applications, focusing on commercially available superparamagnetic beads and thin film magnetic disks. In addition, the basic theory of the Hall effect in the diffusive regime in response to both global uniform magnetic fields and local inhomogeneous field profiles is discussed, and the mathematical model is presented. Secondly, we present the basic theory behind the Finite Element Method employed by COMSOL and illustrate how our model is built using this software. Finally, we discuss the experimental techniques used in the course of this work to build and characterise prototype Hall cross devices in both the continuous and perforated forms. We present details of the experimental measurement setup which was built to allow the Hall voltage response of our devices to arrays of magnetic disks to be measured. Several measurement approaches were developed and employed for this purpose and these approaches and the contexts in which they are used are also discussed.

2.1 Magnetic particles as labels in immunoassays

Magnetic particles on the micro to nano scale can be produced with a variety of interesting magnetic properties. Some such properties are a natural and direct consequence of the small magnetic particle volume, while others can be engineered and tuned using thin film magnetism techniques. Particles of both types have proven useful in a plethora of biological settings, with their use in magnetic immunoassays of principal interest in this project.

In a magnetic immunoassay, magnetic particles are used as labels with which bind to specific biomolecules of interest contained within a sample of bodily fluid. These biomolecules, when indicative of a disease, are commonly referred to as biomarkers. A magnetic immunoassay can be performed by functionalising the surface of a magnetic sensor with biomolecular probes to which the biomarker of interest selectively binds. Upon introduction of the test sample, the biomarkers, if present, are captured by the probes and become immobilised upon the sensor surface. Magnetic particles are then added, functionalised to bind specifically to the biomarkers. The sensor surface is then washed to remove all magnetic particles which are not specifically bound. It is also possible to first add the magnetic particles to the test sample and then to incubate this mixture with the functionalised sensor surface. In either case, magnetic detection and enumeration of the magnetic labels attached to the sensor surface allows the quantity of biomarkers in the sample to be measured and a disease diagnosis to be inferred.

To use magnetic particles as labels in immunoassays there are two pivotal criteria that must be met. Firstly, the particles must be non-remanent. This means that in the absence of an applied magnetic field, such particles produce no stray field and thus do not interact magnetically, avoiding self-agglomeration in solution. This is important, as the particles are required to efficiently search the test sample volume and to be individually detectable, neither of which can occur should the particles clump together. In addition, the labels must produce a stray field when an external field is applied, making them magnetically detectable when desired. Secondly, the particles must have a surface which can be easily functionalised for the recognition and capture of the target biomolecules.

Magnetic particles satisfying these criterial are fit for use and offer many advantages compared to non-magnetic equivalents. Firstly, samples of bodily fluid contain no magnetic background. As a result, the samples require minimal processing, a significant advantage in comparison to optical detection techniques, in particular for the analysis of optically opaque blood samples. Additionally, the motion of magnetic particles can be controlled within a fluid via the application of magnetic field gradients. This offers many interesting advantages, including the potential to speed up assay times by accelerating the rate at which particles reach the sensor surface and once there, by actuating them to increase binding rates [91]. Magnetic washing has also been demonstrated [92] to remove unbound and even non-specifically bound magnetic particles from the sensor surface.

2.1.1 Superparamagnetic beads

Superparamagnetic particles satisfy these criteria. Superparamagnetism is exhibited by single domain ferromagnetic particles with radii of roughly 10 nm. Magnetic uniaxial anisotropy imposes an easy axis along which the magnetic moment lies, and two stable orientations exist, separated by an energy barrier Δ. At finite temperature, there is a discrete probability that this barrier will be surmounted, and the moment will flip orientation. The relaxation time for a spin flip is the product of the attempt frequency and the Boltzmann probability that the particle has the thermal energy to make the flip, $e^{\Delta/KT}$. In the absence of applied field, if a measurement is made for a time greater than the relaxation time, the moment of the particle appears to average to zero and the particle is said to be in the superparamagnetic state.

Superparamagnetic (SPM) particles may be magnetised by an applied field, behaving like paramagnetic particles with much higher susceptibility. Due to the small particle volumes required for the emergence of superparamagnetism, the magnetisation of a single superparamagnetic particle is small and thus difficult to detect. To improve upon this, beads consisting of many superparamagnetic iron oxide nanoparticles dispersed in a solid biocompatible polymer matrix have been developed. These beads are commercially available with a range of sizes, filling factors and biological coatings. The most well-known is the Dynabead, produced by Thermofisher. These beads are used in an abundance of biological applications and are relied upon heavily within the magnetic immunoassay community.

When an external magnetic field is applied to a SPM bead containing an assembly of SPM nanoparticles, the magnetic moments of the nanoparticles tend to align along the applied field direction, giving rise to a net magnetisation. Figure 1 shows the magnetisation (expressed as moment/mass) versus applied field curve, measured for M280 Dynabeads [93], demonstrating the typical sigmoidal shape characteristic of superparamagnetic behaviour. The magnetisation of the SPM bead in the absence of external field is zero and increases rapidly at low applied fields. At high applied fields, the magnetisation saturates, as all the nanoparticle moments align with the applied field direction.

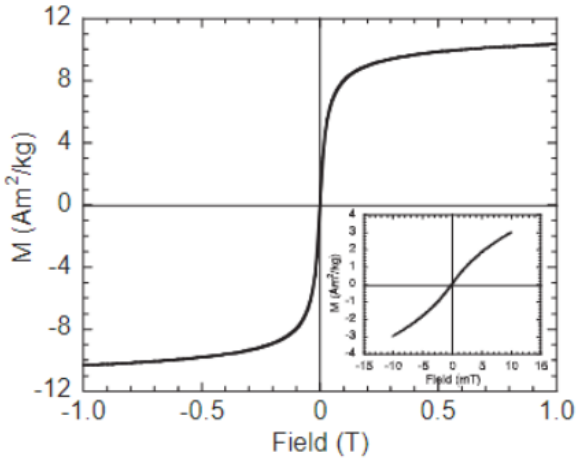

Figure 1: Magnetisation versus applied field for M280 Dynabead, demonstrating characteristic superparamagnetic behaviour. Reprinted from reference [93], Characterisation of Dynabeads® by magnetization measurements and Mössbauer spectroscopy, Vol 293, Geir Fonnum,Christer Johansson,Astrid Molteberg,Steen Mørup,Elin Aksnes, pg 41-47, Journal of Magnetism and Magnetic Materials, 2005, with permission from Elsevier. doi: https://doi.org/10.1016/j.jmmm.2005.01.041

The magnetisation M of a SPM bead in an applied field H is given by:

$$\vec{M}(H) = \chi\vec{H} \quad (1)$$

where χ is the (dimensionless) magnetic susceptibility. The magnetisation is often expressed via the Langevin function, $\mathcal{L}(x)$, where:

$$\mathcal{L}(x) = cothx - 1/x \quad (2)$$

$$x = \frac{\mu_o \mu_{NP} H}{k_B T} \quad (3)$$

$$M(H) = n\mu_{NP}\mathcal{L}(x) \quad (4)$$

Here, μ_{NP} is the moment of a single SPM nanoparticle and n is the number density (number/volume) of SPM nanoparticles in the bead. The net moment, m, of such a bead, with total volume V, in an applied field H, is given by:

$$\vec{m}(H) = \vec{M}(H)V \quad (5)$$

To model the stray field of such a bead the dipole approximation is used. It has been shown that the stray field of a uniformly magnetised spherical object outside of the volume of the sphere is equal to that of a point dipole [94]. The stray field of such a dipole is given by:

$$\vec{B}(r) = \frac{\mu_0}{4\pi}\left[3\frac{(\vec{m}\cdot\vec{r})\vec{r}}{r^5} - \frac{\vec{m}}{r^3}\right] \quad (6)$$

Where $\vec{r}$ is the position vector of the evaluation point relative to the dipole moment, taken to be the centre point of the spherical volume. When considering a magnetic bead magnetised in the z direction sitting above a sensor defined in the XY plane, this expression can be re-written for the z component of the field as:

$$B_Z(x,y) = \frac{\mu_0 m}{4\pi}\left[\frac{3h^2 - \left(\sqrt{x^2+y^2+h^2}\right)^2}{\left(\sqrt{x^2+y^2+h^2}\right)^5}\right] \quad (7)$$

Where h is the distance from the point dipole to the plane of the sensor in the z direction. When modelling a magnetic bead of a given radius R, h is set to be the sum of R and the distance to the plane of the sensor.

2.1.2 Thin film magnetic disks

While superparamagnetic beads satisfy the most basic criteria for use as labels, they are far from optimum. Ideally, a magnetic label should also have low susceptibility in low field to avoid being magnetised by small fields in the environment, which would lead to agglomeration. This also ensures that even if the particles were to agglomerate under externally applied field, they would readily re-disperse in the fluid when the magnetising field is removed. A sharp switch to full magnetisation at a desired applied field, H_{SW}, allows full access to the saturation moment in a controllable manner. The hysteresis loop of such an optimised particle is shown Figure 2. Using thin film fabrication techniques adapted from the MRAM industry, particles with a strikingly similar hysteresis loop can be fabricated and released into solution. These particles have the additional advantages of tuneable magnetic properties, tuneable particle sizes and large planar surfaces ideal for functionalisation.

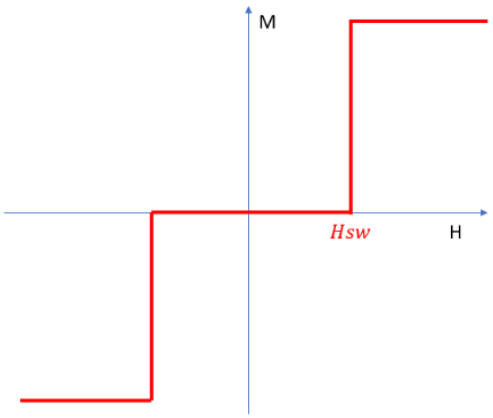

Figure 2: Ideal M-H curve of a magnetic particle for use in biological applications.

The magnetic particles developed in the Cowburn lab with these ideal properties are synthetic antiferromagnetic (SAF) disks with perpendicular magnetic anisotropy (PMA) [95]. A synthetic antiferromagnetic film is composed of two ferromagnetic (FM) layers separated by a non-magnetic (NM) spacer layer inducing RKKY interactions between the two FM layers. When the spacer layer is engineered so that the RKKY interaction it generates is antiferromagnetic, the magnetisation of the FM layers wants to align antiparallel. Due to shape anisotropy, the magnetisation of the FM layers usually lies in the plane of the film. However, in thin film structures designed to exhibit PMA, the magnetisation of the layers is oriented perpendicular to the film plane.

Disks with these magnetic properties are fabricated by producing magnetic thin films engineered to have the desired properties on top of a sacrificial underlayer. The magnetic thin films can then be patterned into disks and the disks released into solution via the dissolution of the underlayer to yield magnetic disks which retain the magnetic properties of the film. In the Cowburn group, the fabrication of micron sized disks via optical lithography [95] and nanoscale disks (as small as 100 nm in diameter) via nanosphere lithography in combination with ion milling [96] have been demonstrated. The magnetic properties of the films are successfully transferred to the disks in both approaches.

2.1.2.1 RKKY interaction

In magnetic metals, the spins of the conduction electrons, s, and localised core spins, S, are coupled via the s-d interaction. The interaction is proportional to the dot product s·S and as a result, the conduction band of the metal tends to be spin polarised parallel or antiparallel with respect to the core spins. It was shown by Ruderman, Kittel, Kasuya and Yosida (RKKY) [97] that a single magnetic impurity creates an oscillating spin polarisation in the conduction band which decays away from the impurity as $1/r^3$. The combination of this effect and the s-d interaction gives rise to long range oscillatory coupling between magnetic impurities and also between localised core spins.

In FM multilayers in which two FM layers are separated by a NM spacer layer, an analogous oscillatory interaction is found, where each FM layer acts as a magnetic impurity, with the oscillating spin polarisation from each layer extending over the NM spacer layer, giving rise to the same effect. By tuning the thickness of the spacer layer, usually Ruthenium, the layers can be coupled ferromagnetically or antiferromagnetically, as illustrated in Figure 3. The strength of the RKKY coupling may be further tuned by adding a layer of Platinum on both sides of the Ruthenium and varying the thickness of the Platinum layers [98].

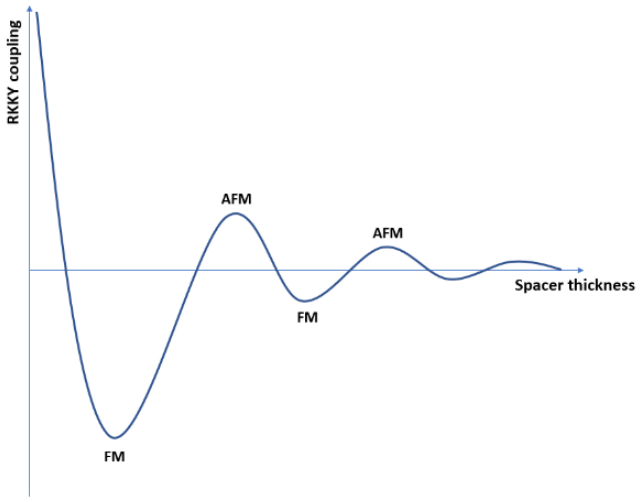

Figure 3: RKKY interaction, oscillating between FM and AFM as spacer thickness increases.

2.1.2.2 Magnetic anisotropy

In magnetic materials with uniaxial anisotropy, the magnetisation wants to lie along a single easy axis (EA). This tendency is represented by the energy density term:

$$E_a = K\sin^2\theta \quad (8)$$

where θ is the angle between the EA and the magnetisation, and K is the anisotropy constant. The main sources of magnetic anisotropy are shape anisotropy, magneto-crystalline anisotropy and surface anisotropy.

2.1.2.2.1 Shape anisotropy

In ellipsoidal FM materials, the demagnetising field, H_d, is given by:

$$\overrightarrow{H_d} = -N\vec{M} \quad (9)$$

where N is the shape-dependent demagnetising tensor and M is the sample magnetisation. The energy of a magnetic sample in its own demagnetising field is referred to as its self-energy, E_d, and is given by:

$$E_d = -\frac{1}{2}\int \mu_0 \overrightarrow{H_d} \cdot \vec{M}\, dV \quad (10)$$

To minimise energy, the material will attempt to minimise the demagnetising field by aligning its magnetisation parallel with the direction in which the demagnetising field is smallest. In the case of a thin film, $N_X = N_Y = 0$ and $N_Z = 1$. Thus, M tends to lie in the plane of the film, such that H_d and E_d are zero. As N is defined by the shape of the sample, this contribution to the anisotropy is referred to as shape anisotropy.

2.1.2.2.2 Magneto-crystalline anisotropy

The tendency of M to lie along specific crystallographic directions is known as magneto-crystalline anisotropy. This contribution to the anisotropy of a sample stems from a combination of the crystal field interaction and the spin-orbit interaction (SOI).

The crystal field interaction is the interaction of the electronic charge distribution of an atom with the electrostatic potential created at that lattice site by all the surrounding charges in the crystal. Due to this interaction, and depending on the specific crystal structure, certain electronic orbitals of the outermost atomic electrons are lowered in energy and so stabilised. The outermost electrons thus tend to occupy these stabilised orbitals. The SOI then couples the spin and orbital angular momentum of these electrons, resulting in their spins tending to align along specific crystallographic directions.

2.1.2.2.3 Perpendicular magnetic anisotropy

As magnetic samples become ultrathin, another contribution to the magnetic anisotropy begins to become important: the surface anisotropy. The anisotropy K_{eff} of the sample can be separated into a volume, K_v, and a surface, K_s, contribution, which has been empirically shown to follow the relation [99]:

$$K_{eff} = K_v + \frac{2K_s}{t} \quad (11)$$

The relation represents a weighted average of the anisotropy of interface atoms and the bulk inner atoms in sample of thickness t. With specific interfaces, for example Co/Pt, it is found that at extremely low thicknesses, the surface anisotropy can dominate over the volume shape anisotropy and pull the magnetisation of the sample out of plane. Such a sample is referred to as having Perpendicular Magnetic Anisotropy (PMA). It is thought that this effect occurs due to an enhancement in SOI at the interface between magnetic material and high Z (atomic number) material,

enhancing coupling of electron spin to certain crystallographic directions. In the case of the Co/Pt interface, strong PMA is found when Pt is grown with (111) texture.

2.1.2.3 Tuning the magnetic properties

Magnetic thin films tend to be composed of multiple layers of nm thickness, with each layer contributing to the overall magnetic behaviour of the film. In the case of SAF films, the basis of the magnetic stack is formed by the layer structure illustrated in Figure 4a and b. Here, we show both the basic motif (a) and a magnetic stack (b) in which this motif is repeated to produce a film with ideally equivalent magnetic switching behaviour (c), but with a larger total moment, due to the increased volume of magnetic material.

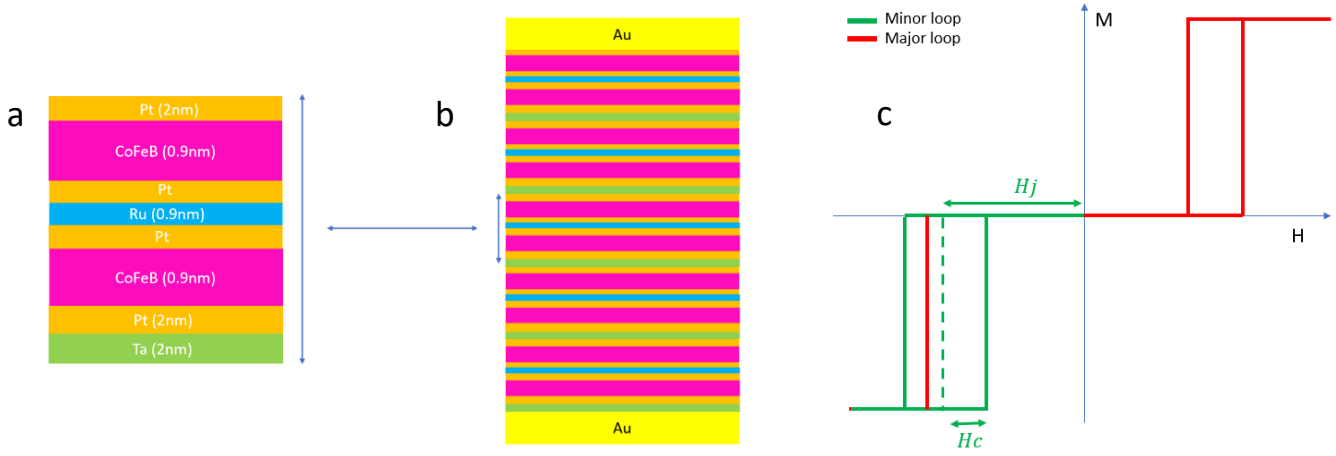

Figure 4: Tuning the magnetic properties of thin film disks. (a) basic motif, (b) repeating magnetic stack (c) typical hysteresis loop.

In the basic motif, starting from the bottom, the base layer is Tantalum (Ta), which acts as a buffer layer that seeds the growth of 111 textured Pt. The following Pt layer induces a strong PMA in the adjacent magnetic CoFeB layer. The second Pt layer, in contact with both the CoFeB and the Ru layer, stabilises the PMA of the CoFeB layer and allows tuning of the strength of the RKKY interaction provided by the Ru layer. The thickness of the Ru layer is chosen to correspond to the first (strongest) AFM peak. The basic motif layer structure is symmetric about the Ru layer. When repeating this motif to build higher-total-moment structures, the Ta and Pt layers are included as they de-couple sequential motifs, such that the entire structure behaves as a single block with enhanced moment. The number of repeats however is limited, with 12 taken as possible but challenging [95]. The entire structure is coated with a capping layer of gold on both the top and bottom to enable surface functionalisation.

By tuning the thicknesses of the different layers, the magnetic properties of the films may be tuned. The RKKY interaction is coarsely altered by varying the thickness of the Ru spacer layer; the chosen thickness of 0.9 nm corresponds to the first AFM peak [100]. The strength of the RKKY coupling may then be finely tuned by varying the thickness of the Pt layers on either side of the Ru [98], [101]. For Pt thicknesses below 2.2 nm, the RKKY interaction is FM and can thus be used to attenuate the AFM interaction between CoFeB layers [98]. It has been shown that the strength of the RKKY interaction falls exponentially with Pt thickness up to 2.2nm [98]. Tuning the RKKY interaction tunes the coupling field H_j, as shown in Figure 4c and so the switching field, H_{SW}, with stronger coupling resulting in a larger switching field.

Tuning the CoFeB thickness tunes the strength of the PMA. For strong PMA, thicknesses between 0.6 nm and 1 nm are needed [98]. The CoFeB magnetisation transitions to the in-plane orientation for thicknesses beyond 1 nm (spin reorientation transition - SRT), and films below 0.6 nm do not form full, continuous layers. Within this thickness range, sharp switching and full remanence are seen.

While the SAF is the most obvious choice for use in a magnetic immunoassay due to its non-remanent state, other structures can also be used. Ferrimagnetic particles are produced via the same approach as a SAF, however here, the CoFeB layer thicknesses are intentionally disbalanced [102]. Depending on the extent of the disbalance, this can produce particles with small magnetic moments at zero applied field. An advantage of this structure is the ability to apply small external fields (below the switching field of either layer) to guide the motion of the particles in a fluid without agglomeration. This would allow, for example, guided self-assembly of the particles on the sensor surface using field gradients.

Ferromagnetic particles with PMA are not applicable for use in an immunoassay as they are remanent and so very likely to agglomerate in solution. They have however found use in this project in proof of principle experiments to demonstrate device operation. A ferromagnetic particle with PMA is produced using a much simpler stack structure, simply repeated layers of CoFeB/Pt.

2.1.2.4 Mathematical description of the stray field of a magnetic disk

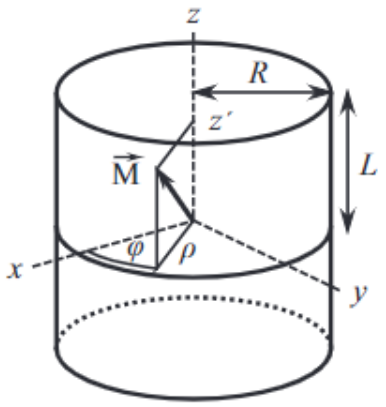

Figure 5: Schematic explaining the coordinate system and geometry of the cylinder, used in the derivation of the stray field of a uniformly magnetised cylinder. Reprinted from reference [103], Exact expression for the magnetic field of a finite cylinder with arbitrary uniform magnetization, Vol 456, Alessio Caciagli,Roel J. Baars,Albert P. Philipse,Bonny W.M. Kuipers, Journal of Magnetism and Magnetic Materials, pg 423 – 432, 2018, with permission from Elsevier. doi: https://doi.org/10.1016/j.jmmm.2018.02.003

An idealized solenoid (one with strictly azimuthal current in a thin sheet wrapped around a right circular cylinder) serves as a good model for a permanent cylindrical magnet, provided that its magnetization is uniform [104]. Reference [104] presents a derivation and exact solution for the magnetic field of an ideal solenoid, which we use to describe the stray field of cylindrical magnetic disks.

We consider a cylinder of length 2L and radius R, as shown in Figure 5. The cylinder is wrapped by an azimuthal sheet of current, I_{total}, equivalent to a tightly wound solenoid, with n turns per unit length, carrying a current I, such that:

$$I_{total} = In2L \quad (12)$$

The magnetic moment, m, associated with the solenoid is given by:

$$m = I_{total}A = In2L\pi R^2$$

(13)

and the magnetisation, M, is given by:

$$M = \frac{m}{V} = nI$$

(14)

where V is the volume of the cylinder. Cylindrical coordinates are used, with an origin at the centre of the magnetic solenoid. To calculate the stray field due to the solenoid, the surface is divided into strips, each of width dz. The current in each strip is nIdz. The Biot-Savart law is used to calculate the magnetic field associated with a single strip of current, at evaluation point P:

$$\vec{B}(r) = \frac{\mu_0}{4\pi}\int \frac{nIdz\,\overrightarrow{dl} \times \vec{r}}{|r|^3}$$

(15)

Where $\overrightarrow{dl}$ is an infinitesimal vector along the tangent to the circumference of the considered current loop and $\vec{r}$ is the vector from the current element $I\,\overrightarrow{dl}$ to the point of evaluation P. To extend this expression to cover all current strips composing the solenoid, integration over the length of the cylinder in z is needed:

$$\vec{B}(r) = \int_{-L}^{L} \frac{\mu_0}{4\pi}\int \frac{nIdz\,\overrightarrow{dl} \times \vec{r}}{(|r|)^3}$$

(16)

From here, the authors of this paper reach an expression for the stray field, which they express using a generalised complete elliptic integral. Their expression is re-expressed in reference [103], in a more digestible form, which is used in our simulations. As for the superparamagnetic bead, only the z component of the stray field is considered, as this component only generates a Hall voltage response in an underlying Hall cross device. The expression for B_Z is as follows:

$$B_z = \frac{\mu_o MR}{\pi(\rho + R)}.\left(\beta_+ P_2(k_+) - \beta_- P_2(k_-)\right)$$

(17)

$$P_2(k_\pm) = -\frac{\gamma}{1-\gamma^2}.(P - \mathrm{K}) - \frac{\gamma}{1-\gamma^2}.(\gamma^2 P - \mathrm{K})$$

(18)

$$\zeta_\pm = z \pm L$$

(19)

$$\alpha_{\pm} = \frac{1}{\sqrt{\zeta_{\pm}{}^2 + (\rho + R)^2}}$$

(20)

$$\beta_{\pm} = \zeta_{\pm} + \alpha_{\pm}$$

(21)

$$\gamma = \frac{\rho - R}{\rho + R}$$

(22)

$$k_{\pm} = \frac{\zeta_{\pm} + (\rho - R)^2}{\zeta_{\pm} + (\rho + R)^2}$$

(23)

$$\rho = \sqrt{x^2 + y^2}$$

(24)

The symbols K and P are used to indicate the evaluation of complete elliptic integrals of the first and third kind, according to:

$$K = K\left(\sqrt{1 - k_{\pm}{}^2}\right) = \int_0^{\frac{\pi}{2}} \frac{d\theta}{\sqrt{1 - \left(1 - k_{\pm}{}^2\right) sin^2\theta}}$$

(25)

$$P = \Pi\left(1 - \gamma^2, \sqrt{1 - k_{\pm}{}^2}\right) = \int_0^{\frac{\pi}{2}} \frac{d\theta}{(1 - (1 - \gamma^2) sin^2\theta)\sqrt{1 - \left(1 - k_{\pm}{}^2\right) sin^2\theta}}$$

(26)

These integrals can be solved both in python and COMSOL Multiphysics to evaluate the z-component of the stray field of a magnetic disk uniformly magnetised in the z direction.

2.2 The Hall Effect

The Hall effect, discovered in 1879 by Edwin Hall [105], describes the behaviour of electric charges under the influence of both an electric and a magnetic field. The force on a charge q, under the influence of an electric field E, is given by:

$$\overrightarrow{F_E} = q\vec{E}$$

(27)

Where q can be positive or negative. In a conductor of cross-sectional area A, given by the product of the conductor width w and thickness t, the electric force will produce a current, I, and corresponding current density, J, given by:

$$I = n|qv_d|A$$

(28)

$$\vec{J} = nq\overrightarrow{v_d}$$

(29)

where v_d is the drift velocity and n the carrier concentration. A magnetic field applied perpendicular to the current direction exerts a Lorentz force on the carriers constituting the current, given by:

$$\overrightarrow{F_L} = q(\overrightarrow{v_d} \times \vec{B})$$

(30)

The Lorentz force deflects the carriers in the direction perpendicular to both the current and the applied field. Thus, the total force on a charge is given by the sum of electric and magnetic forces:

$$\overrightarrow{F_{tot}} = q\vec{E} + q(\overrightarrow{v_d} \times \vec{B})$$

(31)

The deflected charges accumulate along the edge of the conductor, as shown in Figure 6 as a long rectangular plate. This figure also illustrates, for a given applied bias voltage, the direction in which electrons are deflected by the Lorentz force in correspondence with the right-hand rule.

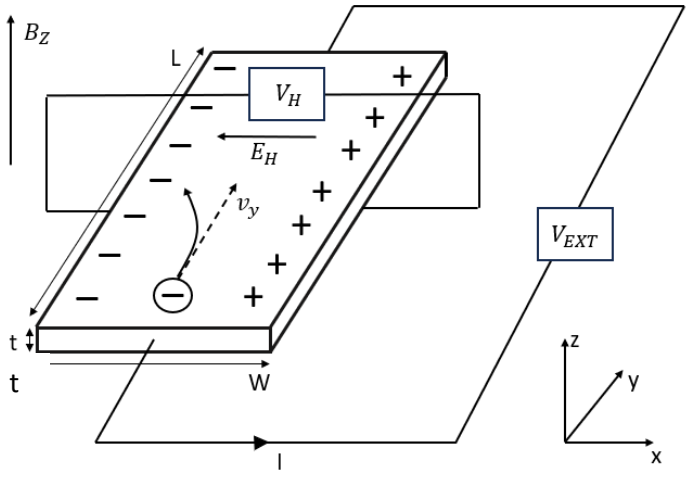

Figure 6: Illustration of the Hall effect mechanism in a rectangular conductor. A magnetic field applied in the z direction causes electrons to be deflected and build up on the left side of the device. The resulting Hall field is indicated by E_H and the measured Hall voltage by V_H.

The accumulation of these carriers causes a transverse voltage to develop across the device with an associated electric field, the Hall field, E_H. The force on a charge due to the Hall field is opposite in direction to that of the Lorentz force. The magnitude of the Hall field increases as carriers continue to accumulate until these forces balance and carriers are no longer deflected:

$$q\overrightarrow{E_H} = q(\overrightarrow{v_d} \times \vec{B})$$

(32)

At this point, the current proceeds as normal through the device. For a device in the XY plane and magnetic field applied in the Z direction, as illustrated in Figure 6, the transverse Hall field can be measured via the voltage difference between opposite sides of the device, separated by distance w, and is known as the Hall voltage, V_{Hall}:

$$\frac{V_{Hall}}{w} = v_d B_z \quad (33)$$

$$V_{Hall} = \frac{B_z I}{nqt} \quad (34)$$

where often, the factor 1/nq is replaced by the Hall constant, R_H. The resultant electric field in the device now makes an angle with respect to the applied electric field E, responsible for the current. This angle, θ_H, is referred to as the Hall angle and is given by:

$$\tan(\theta_H) = \frac{E}{E_H} = \mu B_z \quad (35)$$

where μ is the electron mobility, which characterises how quickly an electron can move through a material under the influence of an applied electric field. Equation (34) fully describes the Hall voltage response of an infinitely long rectangular plate, however for more general device geometries, an additional factor is required – the geometric factor G_H (always between 0 and 1) which describes the effect of the device geometry on the build-up of the Hall voltage:

$$V_{Hall} = \frac{B_z I \, G_H}{nqt} \quad (36)$$

The Hall effect forms the basis of many commercially available magnetic sensors. The sensitivity S of such a device is commonly defined as the ratio of the Hall voltage to the applied magnetic field:

$$S = \frac{V_{Hall}}{B_z} \quad (37)$$

Depending on whether the Hall sensor is operated in current (constant current maintained through the device) or voltage (constant voltage applied across the device) mode, two relative sensitivities can also be considered, the current (S_I) and voltage (S_V) sensitivities. These are defined as the absolute sensitivity divided by the relevant bias quantity, and it can be shown [106] that they have the following relations:

$$S_I = \frac{1}{I}\frac{V_{Hall}}{B_z} \propto \frac{1}{nt} \quad (38)$$

$$S_V = \frac{1}{V}\frac{V_{Hall}}{B_z} \propto \mu$$

(39)

These expressions highlight the importance of the material from which the device is made. For optimum sensitivity, materials with a low concentration of high mobility carriers are required. Common materials for use in Hall cross sensors include metals such as Gold and Bismuth, semiconductors such as Silicon, and semiconductor heterostructures in which a conductive 2DEG is formed, such as GaAs/AlGaAs. In the literature, studies have been conducted to compare room temperature operation of Hall cross devices made from different materials [66], [107], with 2DEG heterostructures generally offering the highest sensitivities. These material systems tend to have the highest carrier mobilities and very low thicknesses for the conductive layer, with the possibility to tune the carrier concentration, explaining their superior performance.

A semiconductor heterostructure is formed from layers of different semiconductors, often produced using Molecular Beam Epitaxy (MBE). The GaAs/AlGaAs heterostructure is an extensively studied material system [108] at which a 2DEG may be formed and is used in this project as the material from which all Hall cross devices are fabricated. Here, the band gap of GaAs is smaller than that of AlGaAs, such that when in intimate contact, free electrons from the AlGaAs move across the heterostructure interface into the GaAs. The AlGaAs layer is usually n-doped, often by Silicon, to provide these free electrons. Upon moving into the GaAs, the electrons lose energy (ΔE_C – the difference in energy between the conduction bands of the two materials) and thus are unable to return to the AlGaAs, despite being attracted to the positively charged donor ions. This charge separation across the interface results in an electrostatic potential which traps the electrons at the interface in a roughly triangular-shaped potential well, as shown in Figure 7. The well is usually 10-20 nm thick, and while the energy levels for motion in the z direction are quantised, the electrons are free to move in x and y. These electrons, confined to motion in 2D, are referred to as a 2DEG.

Figure redacted for copyright reasons

Figure 7: (a) Conduction bands of GaAs and n-AlGaAs, highlighting the difference in energy between the levels ΔEc and the subsequent motion of electrons from AlGaAs to GaAs, when materials are placed in intimate contact. (b) Band structure at the interface, showing the formation of a 2DEG, reproduced based on reference [108].

The process of doping one region of the structure with the intention of the liberated charges subsequently moving into another region is referred to as modulation doping. The central advantage is that the scattering of free charges via Coulomb interactions with the ionised donors is drastically reduced, leading to enhanced carrier mobilities relative to doped semiconductors which do not employ this technique. Further optimisations of the heterostructure are often also employed, including the addition of an undoped AlGaAs spacer layer between the GaAs and n-AlGaAs, which acts to enlarge the physical separation of electrons and positive donors, further enhancing the mobility. A thin capping

layer of GaAs can be used to prevent the oxidation of AlGaAs and the addition of metallic gate contacts is also common, whereby with the application of a bias voltage, the carrier concentration below the gate can be controlled.

2.2.1 Mathematical model

We assume for the purposes of our model that electron transport will be diffusive (room temperature) and that the mobility of one carrier type (electrons) is vastly greater than the other (holes) such that the conductivity of the sample, σ, can be reasonably approximated by:

$$\sigma = q(n_e\mu_e + n_h\mu_h) \rightarrow qn_e\mu_e$$

(40)

where n_e and μ_e represent the carrier concentration and mobility of electrons in the sample respectively, with n_h and μ_h representing the equivalent quantities for holes. In the absence of magnetic field, conduction under the influence of an applied electric field, E, in a uniform conductor is assumed to be isotropic such that the conductivity tensor can be written as:

$$\overline{\overline{\sigma_o}} = \begin{bmatrix} \sigma_o & 0 & 0 \\ 0 & \sigma_o & 0 \\ 0 & 0 & \sigma_o \end{bmatrix}$$

(41)

And the current density, J, following Ohm's law, can be written as:

$$\vec{J} = \overline{\overline{\sigma_o}}\vec{E}$$

(42)

In the presence of a magnetic field perpendicular to the direction of current flow, the conductivity tensor becomes anisotropic due to the Lorentz force. To derive this tensor, we consider the forces acting on a charge q (which may be positive or negative) under the influence of an electric field E and a magnetic field B:

$$\vec{F} = q\vec{E} + q(\overrightarrow{v_d} \times \vec{B})$$

(43)

We can represent the magnetic force, $q(\overrightarrow{v_d} \times \vec{B})$ as an equivalent electric field, E_{mag}, responsible for the same deflection:

$$\overrightarrow{E_{mag}} = \frac{\overrightarrow{F_{mag}}}{q} = (\overrightarrow{v_d} \times \vec{B})$$

(44)

We may think about the current density that results from the sum of the standard electric field E and E_{mag}, as:

$$\vec{J} = \overline{\overline{\sigma_o}}(\vec{E} + \overrightarrow{v_d} \times \vec{B})$$

(45)

Which can be re-written, using the relation $\vec{J} = nq\overrightarrow{v_d}$, as:

$$\vec{J} = \overline{\overline{\sigma_o}} \left(\vec{E} + \frac{\vec{J} \times \vec{B}}{nq} \right)$$

(46)

It is desirable to re-write equation (46) in the form:

$$\vec{J} = \overline{\overline{\sigma(B)}} \vec{E}$$

(47)

where $\sigma(B)$ is the anisotropic, field-dependent conductivity tensor. For our purposes, we consider current flow through a Hall cross device which we define in the XY plane. We assume that no current flows in the Z direction such that any X or Y component of an applied magnetic field will not contribute to charge deflection. Modelling the conduction in 2D only is a common approach used extensively in the literature [80], [85], [109]–[111].

To re-write equation (46) in the form of equation (47) considering conduction in 2D and a magnetic field applied in the Z direction, we evaluate the cross product of J and B, bringing us to:

$$\begin{bmatrix} J_x \\ J_y \end{bmatrix} = \begin{bmatrix} \sigma_o & 0 \\ 0 & \sigma_o \end{bmatrix} \begin{bmatrix} E_x \\ E_y \end{bmatrix} + \frac{\sigma_o}{nq} \begin{bmatrix} J_y B_z \\ -J_x B_z \end{bmatrix}$$

(48)

Re-writing these equations for E_X and E_Y gives:

$$\begin{bmatrix} E_x \\ E_y \end{bmatrix} = \frac{1}{\sigma_o} \begin{bmatrix} 1 & -\frac{\sigma_o B_z}{nq} \\ \frac{\sigma_o B_z}{nq} & 1 \end{bmatrix} \begin{bmatrix} J_x \\ J_y \end{bmatrix}$$

(49)

where we now have extracted an expression for the anisotropic resistivity tensor:

$$\overline{\overline{\rho(B)}} = \frac{1}{\sigma_o} \begin{bmatrix} 1 & -\frac{\sigma_o B_z}{nq} \\ \frac{\sigma_o B_z}{nq} & 1 \end{bmatrix}$$

(50)

By inverting the matrix $\rho(B)$, we find our desired expression for $\sigma(B)$. We make the substitution:

$$\beta = \frac{\sigma_o B_z}{nq}$$

(51)

where q can still be positive or negative. Our final expression for the anisotropic conductivity tensor becomes:

$$\overline{\overline{\sigma(B)}} = \frac{\sigma_o}{1 + \beta^2} \begin{bmatrix} 1 & \beta \\ -\beta & 1 \end{bmatrix}$$

(52)

To tailor this expression to the charge carriers, q must now be explicitly expressed as -e, as it is electron transport that we will consider. The anisotropic conductivity tensor becomes spatially dependent for spatially varying magnetic fields, expressed as $B_z(x,y)$, at any point (x,y) in the sensor plane. This model can thus be used to compute the response to both spatially uniform and inhomogeneous magnetic fields. Expressing the electric field in E the device as the gradient of the electric potential, ϕ, allows us to re-write equation (47) as:

$$\vec{J} = -\overline{\overline{\sigma(B)}}\ \overrightarrow{\nabla\phi}$$

(53)

We consider the continuity equation for current density:

$$\vec{\nabla} \cdot \vec{J} = 0$$

(54)

Which describes the conservation of current in the device i.e., the current leaving the device must be equal to the current entering the device such that charge is conserved. Applying this to equation (53), it results that:

$$-\vec{\nabla} \cdot \left(\overline{\overline{\sigma(B)}}\ \overrightarrow{\nabla\phi}\right) = 0$$

(55)

We can solve this equation for the electric potential at any point within the Hall cross subject to specific boundary conditions. In general, we pump current from the upper contact (electron flow is from the lower contact) using the constant current density boundary condition, requiring J at any point along the boundary to be constant and equal to the prescribed value J_0:

$$-\vec{n} \cdot \vec{J} = J_0$$

(56)

where n is the outward normal. We ground the lower contact of the cross, requiring the voltage at any point along the boundary to be equal to 0. We then apply insulating boundary conditions to all other boundaries of the device, requiring that no current can enter or leave the device through these boundaries:

$$\vec{n} \cdot \vec{J} = 0$$

(57)

It is also possible to treat the voltage probe contacts with floating point boundary conditions. In this case, a constant voltage V_0 is applied along the boundary such that the total current density J along that boundary is equal to a specific current, I_0:

$$V = V_0$$

(58)

$$\int -(\vec{n} \cdot \vec{J}) dS = I_0$$

(59)

If I_0 is set to 0, the boundary behaves as a perfect, unconnected conductor – a floating equipotential. The current density can vary locally but the total current entering or leaving a boundary will remain 0.

Once equation (55) is solved for the potential at all points in the cross, the Hall voltage is evaluated as the difference between the average voltage along the left and right voltage probe contacts of the cross.

When using this model to solve for the potential at all points within a 2DEG Hall cross in response to the presence of a magnetic particle, we use 3D values of the current density, carrier concentration and conductivity as inputs to the model, assuming a certain thickness for the 2DEG. It is also possible to use 2D values for these inputs – the results are the same as long as the dimensionality for all inputs is consistent.

2.2.2 Hall response to localised, inhomogeneous magnetic fields

The 2D computational approach discussed is commonly employed in the literature to calculate the Hall voltage response of a 2DEG Hall cross in the diffusive regime to the presence of an inhomogeneous magnetic field profile, such as that from a magnetic particle. However, the relationship between the Hall voltage and the stray field of the particle is complex and as such, equation (36), used to predict the Hall voltage response to a uniform magnetic field, no longer applies. In the following section we review the key findings reported in the literature to establish an understanding of the Hall response to inhomogeneous magnetic field profiles.

One key publication is the work of Bending and Oral [112]. In this work, the authors focus on the response of a Hall cross to the stray field profile of a superconducting flux vortex, with the field profile mathematically described using an analytical exponential approximation to the field at the vortex core, given by:

$$B(x,y) = \frac{\Phi_o}{2\pi\lambda^2} . \exp\left(-\sqrt{(x-x_0)^2 + (y-y_0)^2}/\lambda\right)$$

(60)

where λ is the penetration depth, Φ_o the magnetic flux quantum and (x_o,y_o) the coordinates of the vortex origin. The authors solve for the electrostatic potential in the Hall cross in the presence of this inhomogeneous magnetic field situated at the cross centre. Current is pumped through the cross in the X direction and the Hall voltage is measured across the vertical voltage contacts, as can be seen from the inset of Figure 8a. In Figure 8b, the potential in the active area of the cross solved for with the inhomogeneity present is shown. The field inhomogeneity is responsible for the central, pronounced kinks in the equipotential lines, indirectly demonstrating the local build-up of the Hall electric field (the potential is bent on the left and right sides due to the presence of the contacts).

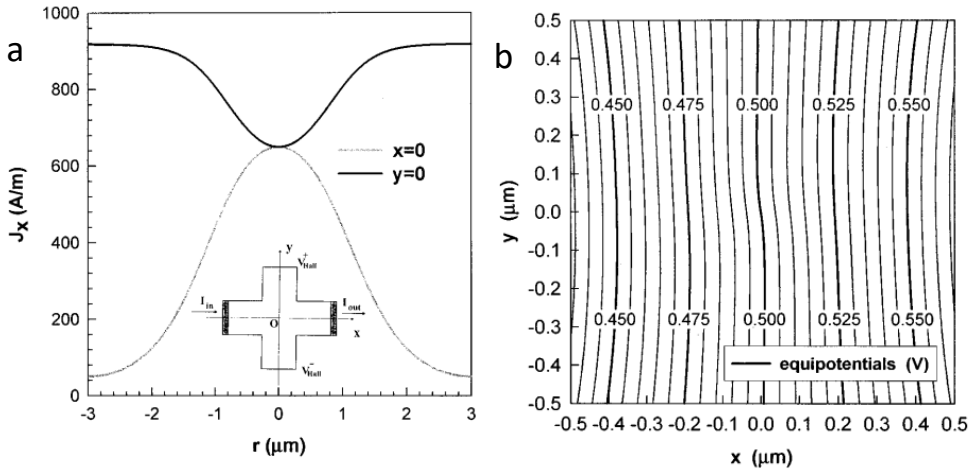

Figure 8: (a) Current density J_x along the horizontal and vertical directions within the Hall cross. (b) Potential in the cross active area, with kinks indicating the local build-up of the Hall electric field in response to a magnetic flux vortex. Reproduced from reference [112], S. J. Bending, A. Oral; Hall effect in a highly inhomogeneous magnetic field distribution. J. Appl. Phys. 15 April 1997; 81 (8): 3721–3725., with the permission of AIP publishing. Doi: https://doi.org/10.1063/1.365494

Figure 9a illustrates the y component of the electric field along a slice through the centre of the cross (x=0). Figure 9b shows the divergence of the electric field, which is directly proportional to the local charge density via Gauss' Law. Here we see that the presence of the field inhomogeneity results in the creation of a local charge dipole and a local Hall electric field, which peaks at the position of the centre of the inhomogeneity. The authors find that this Hall field gives rise to the Hall voltage detected at the contacts of the cross.

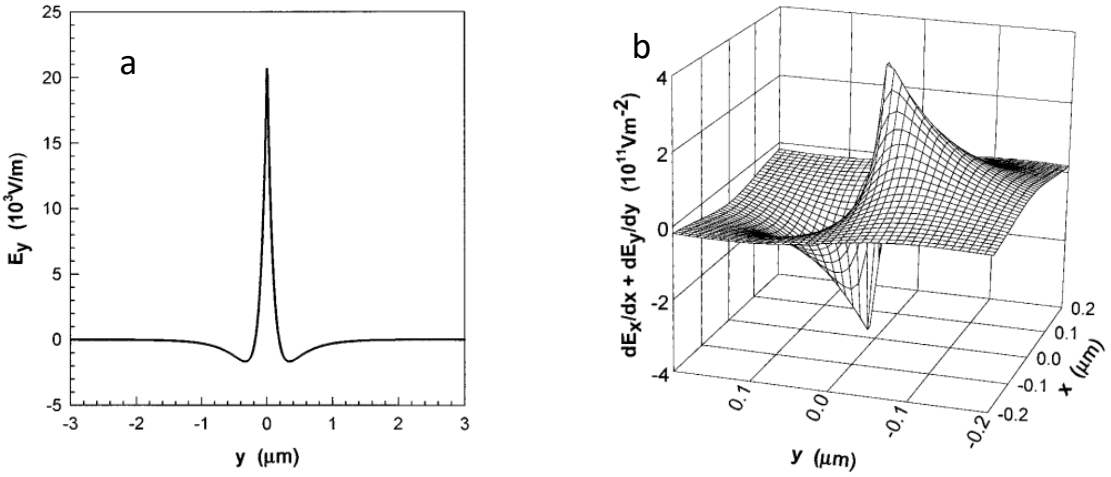

Figure 9: (a) Hall electric field and (b) dipolar charge distribution in response to the local field of a magnetic flux vortex. Reproduced from reference [112], S. J. Bending, A. Oral; Hall effect in a highly inhomogeneous magnetic field distribution. J. Appl. Phys. 15 April 1997; 81 (8): 3721–3725., with the permission of AIP publishing. Doi: https://doi.org/10.1063/1.365494

The authors attempt to analytically predict the Hall voltage response of the cross to the field inhomogeneity. They take as their starting point the analytical formula shown to accurately predict the Hall response to a local inhomogeneous field in the ballistic regime [113]:

$$V_H = \frac{< B_Z > I}{nqt} \quad (61)$$

where $<B_Z>$ is the average value of the stray field of the inhomogeneity over the geometric active area of the Hall cross, defined as the square area at the intersection of the cross arms. The authors find that in the diffusive regime

the Hall voltage calculated by their simulations is almost exactly a factor of two less than that which they would expect based on equation (61).

To explain why this analytical expression does not predict the result in the diffusive regime, the authors point out that when the injected current reaches the geometric active area of the cross, it spreads into the voltage probe arms, which does not occur in the ballistic regime. To account for the true area in which the current flows, an effective active area, double the size of the geometric active area, extending into the voltage probe arms, should be considered. The stray field of the inhomogeneity thus needs to be averaged into this larger effective active area which is inhabited by the current, resulting in the reduction in Hall response. The authors show that when this effective active area is used in the calculation of $\langle B_z \rangle$, equation (61) may be used to accurately predict the Hall response to a field inhomogeneity situated at the centre of the cross.

Finally, the authors also calculate the response function of the Hall cross to the flux vortex field profile by translating the profile along the vertical, horizontal, and diagonal directions through the cross centre. Figure 10 shows the Hall resistance (Hall voltage divided by the current through the cross) as a function of the position of the centre of the flux vortex. Along x=0, the inhomogeneity is moved vertically into the voltage probe arms, where the authors state that the Hall voltage falls off as the current density drops. Along the x=y diagonal direction, the Hall voltage falls off more slowly and increases again as the corners of the cross are approached as the current density is locally highest here. Thus, the authors show that when the flux vortex is translated away from the Hall cross centre, the Hall response varies, seemingly in correspondence with the local current density and so carrier drift velocity.

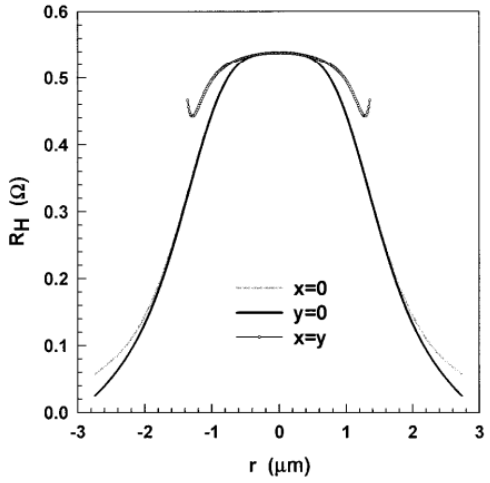

Figure 10: Hall resistance in response to a magnetic flux vortex translated in the horizontal, vertical, and diagonal directions through a Hall cross. Reproduced from reference [112], S. J. Bending, A. Oral; Hall effect in a highly inhomogeneous magnetic field distribution. J. Appl. Phys. 15 April 1997; 81 (8): 3721–3725., with the permission of AIP publishing. Doi: https://doi.org/10.1063/1.365494

Another substantial contribution to our understanding was offered in reference [111]. The authors investigate the effect on the Hall voltage response of changing the voltage probe width relative to the current probe width. They find that upon increasing the voltage probe width, the Hall voltage response (to a magnetic dot, positioned at the sensor centre) decreases, due both to the decreased average carrier drift velocity within the active area of the cross from increased current exploration of the voltage probe arms and to the decreased averaged field due to the increased effective active area. Thus, the authors conclude that the Hall voltage response depends on both the average drift

velocity of the carriers within the effective active area and the average field of the inhomogeneity into the effective active area, both of which can be varied by altering the geometry of the Hall cross.

From these works, we understand that the magnitude of the Hall response of a 2DEG Hall cross in the diffusive regime to an inhomogeneous magnetic field depends on the average value of the stray field of the inhomogeneity into the 'effective' active area of the cross, the average carrier drift velocity within the active area as well as the local carrier drift velocity at the location of the field inhomogeneity.

2.2.3 Perforated Hall sensors

The average value of the stray field of a magnetic particle over the effective active area of a Hall sensor, $\langle B_z \rangle$, drops off rapidly as the width of the active area, W, increases relative to the particle diameter, D. This occurs as more of the negatively directed stray field of the particle is captured by the sensor as W increases, as is illustrated in Figure 11a. If instead the sensor size is matched to the particle size, only the positive flux directly below the particle is captured by the sensor, resulting in an enhanced $\langle B_z \rangle$ and so Hall response. However, for the purposes of this work, measuring many particles using the same sensor is desired, ruling out the possibility of matching the sensor size to particle size. Instead, we consider novel sensor geometries with the aim of increasing the average stray field of the particle into the sensor, while maintaining a geometry that allows many particles to fit onto the surface for simultaneous measurement.

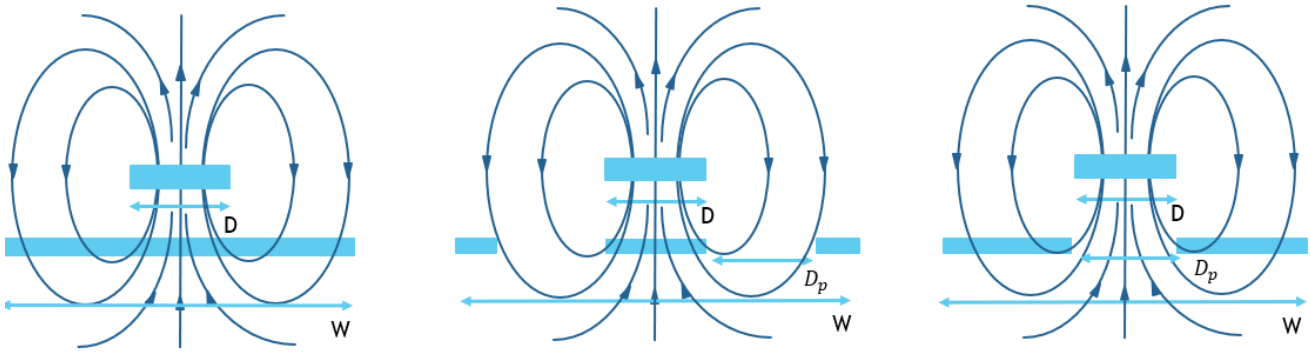

Figure 11: Magnetic disk situated above (a) a continuous Hall cross sensor, illustrating the increasing capture of the negatively directed stray field components with increasing sensor width, W, (b) a perforated Hall cross with multiple perforations surrounding the disk, illustrating how the device becomes insensitive to some of the negatively directed stray field and (c) a perforated sensor with a perforation directly below the disk, illustrating how the device can become insensitive to the positively directed stray field directly below the disk.

In Figure 11b, the basic concept of a perforated device is illustrated, in which the particle to be measured is surrounded by perforations with the aim of making the sensor insensitive to the negatively directed stray field components which reduce the overall $\langle B_z \rangle$. In Figure 11c, an alternative configuration is shown, in which only the negatively directed flux is captured by the sensor. Here, since the polarity of the magnetic field seen by the sensor is opposite to that at the continuous device, the polarity of the Hall response is expected to switch.

In addition to perforations making the device insensitive at positions for which the stray field reduces the overall $\langle B_z \rangle$, it is also expected that they should locally alter the current density, increasing it close to the perforations where the current is squeezed into narrower channels. We thus predict that the addition of perforations to the device will optimise the signal by both increasing $\langle B_z \rangle$ and the carrier drift velocity in the vicinity of the magnetic particles.

2.3 Computational Methods

Finite Element Analysis (FEA) software is often used in the design and optimisation of novel devices. Use of the software during this process can reduce the number of experiments to be run and prototypes to be built, as well as aid understanding of the physical principles governing device operation.

FEA software is built on the laws of physics, expressed as mathematical models. For time and space dependent problems, often the mathematical descriptions consist of one or several partial differential equations (PDEs) with associated boundary and initial conditions, which cannot be solved by analytical methods. To get around this, the mathematical model can be discretised to give a numerical model for the system. The numerical model is a discrete approximation of the mathematical model which can be solved by numerical methods. The solutions of the numerical model equations are approximations of the real solutions of the PDEs. The Finite Element Method (FEM) can be used to discretise such mathematical models and compute such approximations, and this is the approach taken by the COMSOL Multiphysics software.

To illustrate how we may use the FEM to discretise a mathematical model, we consider a simple 1D example, where we want to discretise the function u(x). We may approximate u(x) by the function u_H using linear combinations of basis functions ψ_i :

$$u(x) \approx u_H = \sum_i u_i \psi_i$$

(62)

where u_i are the coefficients of the functions that approximate u with u_H. Figure 12a illustrates one possible discretisation, where the chosen linear basis functions each have a value of 1 at their respective node and 0 at all other nodes, and the associated elements are equally spaced along the x-axis. In Figure 12b, an alternative discretisation is shown, whereby smaller elements are used where the gradient of u(x) is larger. This freedom in the selection of discretisation is one of the great advantages of the FEM, as the resolution with which space is discretised can vary depending on local requirements.

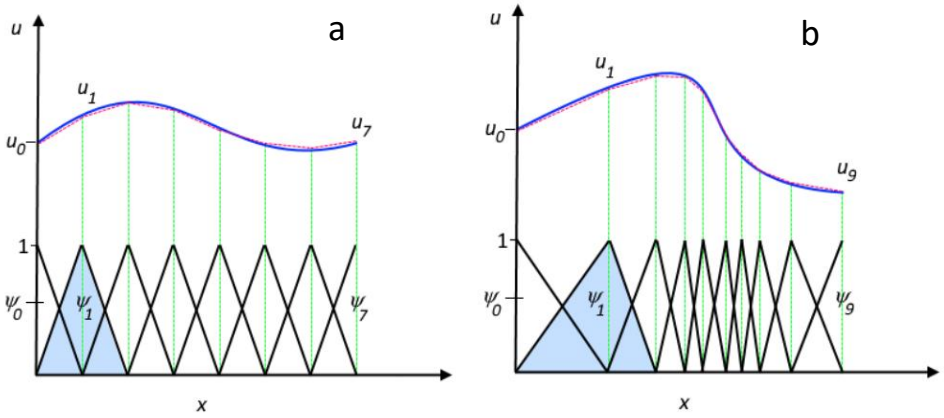

Figure 12: Illustration of basis functions used to discretise function u(x) via the FEM, showing (a) elements uniformly distributed along x and (b) smaller elements used where the slope of u(x) is large. Image credit: COMSOL, reprinted from reference [114].

For a more in-depth understanding of the FEM and how it is implemented, we refer to the COMSOL Multiphysics Cyclopaedia [114].

2.3.1 COMSOL Workflow

COMSOL Multiphysics recommends the use of a particular workflow by the user. It is the same regardless of the system to be modelled and the software is structured in such a way that following this workflow is intuitive. In this section, the main steps of the workflow are outlined and the implementation of our Hall effect model in COMSOL is illustrated.

2.3.1.1 Setting up the model environment

COMSOL initially requires several selections to be made and then presents the user with a tailored COMSOL environment. Firstly, the space dimension that the user intends to work in is selected, followed by the relevant Physics modules and interfaces. For our model, a licence was obtained for both COSMOL and the AC/DC module. We work in 2D and the 'Electric Currents' interface from the AC/DC module is added. This interface enables the computation of electric field, current and potential distributions in conductive media. Finally, the desired study types are selected which in our case is the Stationary Study option used for time independent problems.

2.3.1.2 Building the model geometry

Once the model environment has been set up, building the model geometry is often the next step. To assemble the Hall cross, the arms and contact pads were built from basic shapes and a union was formed. To add perforations, circles were added to the active area of the cross in the desired array and a difference operator was used to remove the material. The design was parameterised such that various geometrical aspects could be easily varied. This is achieved by simply adding parameters and their corresponding values under the 'Parameters' section of Global Definitions.

2.3.1.3 Creating definitions

In the Parameters section of the Global Definitions node, all the parameters which the model needs to solve for the electrostatic potential within the Hall cross are defined. In our model, this included parameters describing the 2DEG such as mobility and carrier concentration, parameters describing the model geometry and parameters describing the stray field profile of the magnetic particles such as saturation magnetisation and working distance.

For our model the most obvious definition is the Hall Voltage. We define the Hall voltage using a global variable probe and two average non-local coupling operators. An average non-local coupling operator can be used to compute the average of an expression over a boundary. This operator is used to compute the average voltage along each of the voltage probe contacts at the boundary between the 2DEG and copper pad. A Global Probe is then defined as the difference between these values and this is taken to be the Hall voltage. Boundary and Domain Probes have also been very useful in our model, enabling the calculation of integrals and averages of variables over regions and boundaries. Calculating, for example, the average stray field of a magnetic particle over the active area of the device was achieved using such a probe.

In our model, the Variables and Functions sections of the Definitions node are used to implement the different magnetic stray field profiles. From simplest to most complex, this includes the stray field of a magnetic dot, bead and disk. For the magnetic dot, we define an analytic function Dot(x,y) to describe the stray field beneath the dot according to:

$$Dot(x,y) = \begin{cases} 1, & (x-XS)^2 + (y-YS)^2 < Radius^2 \\ 0, & (x-XS)^2 + (y-YS)^2 \geq Radius^2 \end{cases} \quad (63)$$

To vary the strength of the magnetic dot, we define a parameter B_0 and create a variable $B_Z(x,y) = B_0 Dot(x,y)$. We also define parameters XS and YS to translate the position of the dot centre across the surface of the sensor. This approach is used to translate all local field profiles.

For the magnetic bead, we define an analytic function $B_Z(x,y)$ following equation (7) (the dipole approximation). We define the parameter h from equation (7) as the sum of the bead radius, half the 2DEG thickness and an independent parameter, d, which represents the distance between the bottom surface of the bead and top surface of the 2DEG.

The stray field of the magnetic disk has by far the most complex analytical formulation. To include the defining equation for the stray field of this particle, the use of a single function was not feasible. Instead, a set of functions and variables (needed for computation of the elliptic integrals) following the equations presented in section 2.1.2.4 was defined and brought together to give the final expression for the stray field $B_Z(x,y)$. As for the magnetic bead, the distance between the disk and 2DEG, (referred to as z in section 2.1.2.4), was defined as the sum of half the disk thickness, half the 2DEG thickness and the parameter d, representing the distance from the bottom surface of the disk to the top surface of the 2DEG.

2.3.1.4 Defining the physics

At the Physics node, we added the 'Electric Currents' interface. Within this node, we define the physics of the system, include the Hall effect via the anisotropic conductivity tensor and impose boundary and initial conditions. We add a Current Conservation node which we apply to the bulk of the device excluding the contacts. There is an option to provide a user defined conductivity and it is here that we include the anisotropic conductivity tensor. With the conductivity tensor defined, conduction in the bulk of the cross can now be solved for in the presence of a magnetic field $B_Z(x,y)$. A second Current Conservation node is also defined and applied to the contact pads. Here, the conductivity is set by assigning to the contact pads the material properties of copper.

In this section we also define the boundary and initial conditions. Electrical insulation is the default setting, applied to all boundaries not otherwise specified. For the voltage probes, floating potential boundary conditions are applied to the outermost boundary of the contacts, with the I_0 option set to 0. For the upper current probe arm, the normal current density boundary condition is applied to the outermost boundary of the contact. For the lower current probe arm, the ground boundary condition is applied to the outermost boundary of the contact.

2.3.1.5 Creating the mesh

There are three main considerations when choosing a mesh: the sequence type, element type, and element order. For the sequence type, we choose the user-controlled option, allowing us to specify all mesh parameters, including the minimum and maximum element size, the maximum element growth rate and the element curvature. The minimum and maximum element size define, as expected, the minimum and maximum allowed element sizes in the mesh. The maximum element growth rate defines the maximum rate at which element size can grow, from a region with a small element size to a region with large element size. The curvature limits the maximum element size along a curved boundary, with smaller values resulting in a finer mesh along curved boundaries. For the element type, the shape of the cells must be decided and for the element order, a choice between linear and quadratic must be made.

It is possible to set up multiple mesh types and apply them to specified sections of the geometry by adding multiple size nodes. The 'form union' option in the geometry node requires that all meshes continuously merge across boundaries. This is very advantageous when a geometry contains both regions requiring fine mesh resolution and regions for which a coarse mesh will suffice. For our system, we use three different size nodes: one for the active area, one for the contacts, and one for the arms. High mesh resolution is desired within the active area to resolve the rapidly varying field profiles of the magnetic particles, reasonable resolution is desired at the contacts for accurate computation of the Hall voltage, and coarse resolution is desired in the arms to decrease computation times. We employ a quadratic, free triangular mesh, which is considered standard for 2D meshes.

2.4 Experimental Methods

The experiments conducted in this project were designed to prove that the addition of perforations to a Hall cross device gives rise to the improvements in magnetic particle counting predicted by computational modelling. Various fabrication and characterisation techniques were employed to produce prototype devices and an experimental measurement rig was built with which transport measurements were conducted. This section details the experimental methods employed in the course of this work.

2.4.1 Device fabrication

2.4.1.1 Optical lithography

Optical Lithography refers to techniques which use light to create small scale patterns on the surface of a substrate. In general, the substrate is coated in a layer of resist, a light-sensitive polymer which either breaks down (positive) or hardens (negative) when exposed to light. The desired pattern is transferred to the resist, usually by shining UV light through an optical mask. The mask is often made of a transparent material (glass or quartz), with the pattern defined by sections with opaque coating (chromium). The areas of resist positioned below the chromium is shadowed while elsewhere light goes through. Direct-write lithography is also possible, whereby the optical mask is held in software, and computer-controlled optics are used to project the pattern directly onto the resist. Once exposed, the sample is soaked in a developer, a chemical which removes the sections of resist which have become soluble due to light exposure (positive) or remain soluble due to lack of exposure (negative). The pattern will then be present upon the substrate, defined in the remaining resist.

In this work, optical lithography techniques were used in the fabrication of Hall cross devices. To define the overall structure of a device, as well as to allow metallic contact pads to be added, an optical mask was custom designed in the software CleWin and produced in glass-chromium by an external company, Compugraphics. This mask was used in combination with the positive photoresist S1813, spin coated to a thickness of ~1 µm, and a mask aligner for flood exposure. Figure 13a illustrates the design corresponding to a single 100 µm x 100 µm active area Hall cross device, and Figure 13b illustrates the corresponding design for the contact pads.

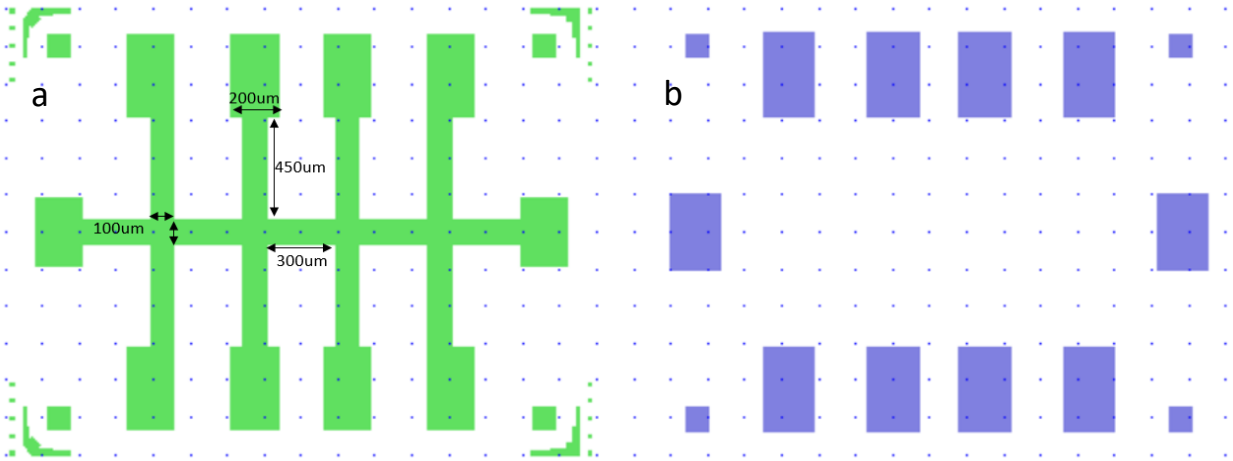

Figure 13: CleWin design corresponding to the glass-chromium optical mask, used to define the structure of the Hall crosses. (a) Hall Bar structure, (b) associated contact pads.

To add perforations to the crosses, direct-write lithography was carried out using the Microwriter ML3 Pro, by Durham Magneto Optics. A 405 nm wavelength laser directly exposed the perforations in the S1813 resist, using an uploaded CleWin file as a mask. The CleWin file contained the design corresponding to the physical optical mask, with an additional layer added, containing the desired arrays of perforations. In this case, alignment steps were carried out, to relate the positions of the devices already defined on the chip, to their positions within the CleWin file. Figure 14 shows the additional layer, in dark green, representing the perforations.

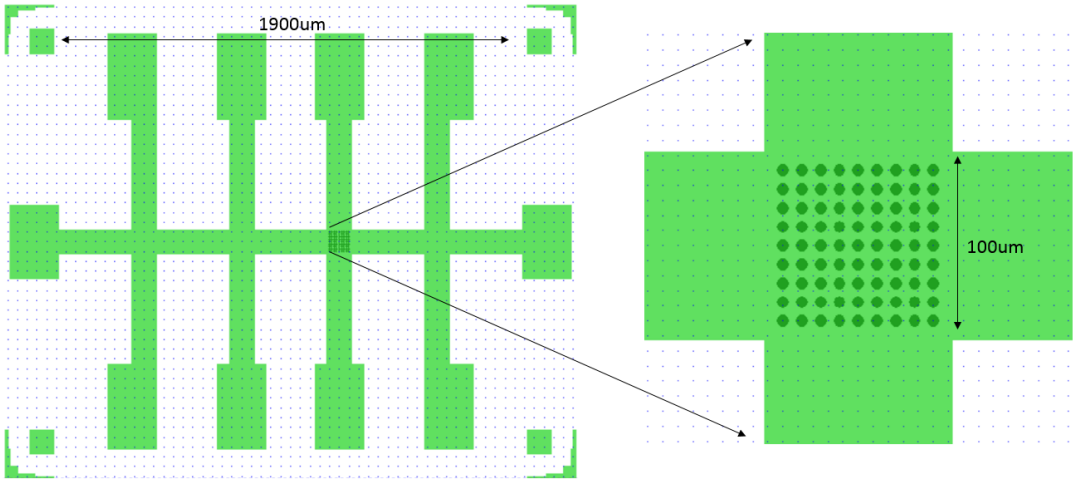

Figure 14: CleWin design file used during direct write lithography to define arrays of circles, later to become the perforations.

2.4.1.2 *Wet chemical etching*

Wet chemical etching is a process in which material is removed from a sample via a chemical reaction with a liquid etchant. Often, the etchant is composed of a chemical which oxidises the material to be removed, and an acid which dissolves the oxidised product. Etching is commonly used to define small-scale structures across the surface of a substrate in combination with photolithography. As described, a pattern can be produced in photoresist, which when exposed to etchant, protects the covered areas and allows the exposed areas to be etched away.

Etching can occur isotropically (at the same rate in all crystallographic directions) or anisotropically (at different rates in different crystallographic directions). This is determined by a combination of the crystallographic structure of the substrate to be etched and the chosen etchant. Knowledge of the expected etch profile is important, as it may limit subsequent fabrication steps, for example metallisation.

The sample to be etched is first cleaned by RF ashing and then placed in the etchant bath for a set amount of time. The sample is then washed thoroughly in deionised water and dried using a Nitrogen gun, and the etch depth measured. The process can be repeated until the desired etch depth has been achieved.

In this work, the Hall cross devices and the perforations are defined in GaAs/AlGaAs via wet chemical etching. The etchant used is acidic hydrogen peroxide (H_2SO_4:H_20_2:H_20) in the ratio 1:8:80. The etchant is prepared at room temperature. The solution is exothermal, and so is allowed to 'rest' for about 60 minutes, ensuring that the etch rate is roughly constant. The GaAs/AlGaAs is oxidised by the hydrogen peroxide (H_2O_2) and the oxidised product is subsequently dissolved by the sulfuric acid (H_2SO_4). The etching of GaAs/AlGaAs occurs anisotropically, and for this etchant, the ratio of undercut to etch depth is 0.62[115].

2.4.1.3 *DC magnetron sputtering*

Direct Current (DC) Magnetron Sputtering is a Physical Vapour Deposition (PVD) technique used in the fabrication of thin conductive films. The process involves the bombardment of a target material with ionised gas molecules, resulting in the ejection or 'sputtering' of target atoms from the surface, and subsequent deposition on the substrate surface.

The target and substrate are held in a vacuum chamber, which is first evacuated, then filled with an inert gas, usually Argon, and maintained at low pressure. An electrical circuit is set up such that the target is connected to a negative electrode and the substrate is earthed. A high electrical bias is then applied to ionise the Argon atoms via impact ionization with free electrons in the chamber. Once ionized, the Argon ions are accelerated towards the negatively charged target, causing target atoms to be ejected from the surface, and to coat the substrate positioned directly above. An arrangement of alternating polarity magnets situated below the target creates a magnetic field, which confines free electrons to the region above the target. This improves Argon ionization by increasing collision probability, thus enhancing the deposition rate.

In this work, magnetic thin films and particle arrays were produced via sputtering using a Kurt Lesker DC magnetron sputtering system. The system consists of a high vacuum chamber with six target positions and an adjacent load-lock. All targets are angled towards a rotating sample stage spinning at 20 rpm to smooth out deposition thickness. The typical base pressure of the system was ~2 to 8 x10^{-8} mbar. The thin film stacks were grown at room temperature and

under a working pressure of ~7 to 9 x10^{-3} mbar. The sputtering rate of each target was calibrated by growing a film for a set amount of time and then measuring the thickness of the resulting film using an atomic force microscope (AFM), allowing the calculation of a growth rate for each target. The growth rate could be controlled by varying the magnetron power, generally set to between 30 to 300 W, depending on the desired precision.

2.4.1.4 Electron-beam evaporation

Electron Beam Evaporation is a PVD technique used in the fabrication of thin films. The process involves the heating of a target material to its melting point with a directed electron beam, resulting in the thermal evaporation of the target and subsequent deposition on the substrate surface.

The target material, contained in a crucible, and the substrate are both held in a vacuum chamber at low pressure. The electron gun consists of a metallic filament, often Tungsten, which is heated until electrons are ejected from the surface by thermionic emission. A high voltage is applied to accelerate the electrons towards the target material, and magnetic fields are used to focus the electron beam onto the target. The electron beam heats the target to its melting point, and the material evaporates, coating the entire chamber. The rate of evaporation is monitored by a sensor, often a quartz crystal. As material is evaporated and coats the crystal, the resonant frequency of vibration changes, and the amount of material deposited within a given time can be calculated.

In this work, thin films of silicon dioxide (SiO_2) were produced using a K J Lesker Electron Beam Evaporator. The system consists of a high vacuum chamber, with a four-pocket heath containing 4 crucible positions. The substrate is attached to a rotating sample stage, usually spinning at 4 rpm to smooth out deposition thickness. Depositions are carried out at room temperature. Each growth contains a ramp up and ramp down stage, during which a shutter is placed between the substrate and the target, while the growth rate is monitored to ensure it is as desired.

2.4.1.5 Device fabrication process

In this work, all Hall cross devices were produced using GaAs/AlGaAs heterostructures with the following layer structure: GaAs(2000nm)/AlGaAs(80nm)/GaAs(10nm) on a semi-insulating GaAs substrate. A 2DEG lies below the surface, beginning at a depth of 90 nm and extending for 20 to 25 nm. A single device, as illustrated by the mask shown in Figure 13, consists of four independently contactable Hall crosses. During processing, it was planned that two out of the four crosses would have an array of magnetic particles added. The fabrication process flow is illustrated in Figure 15, showing the addition of perforations and embedded magnetic particles to a cross (a), followed by the addition of magnetic particles to the surface of a continuous cross (b).

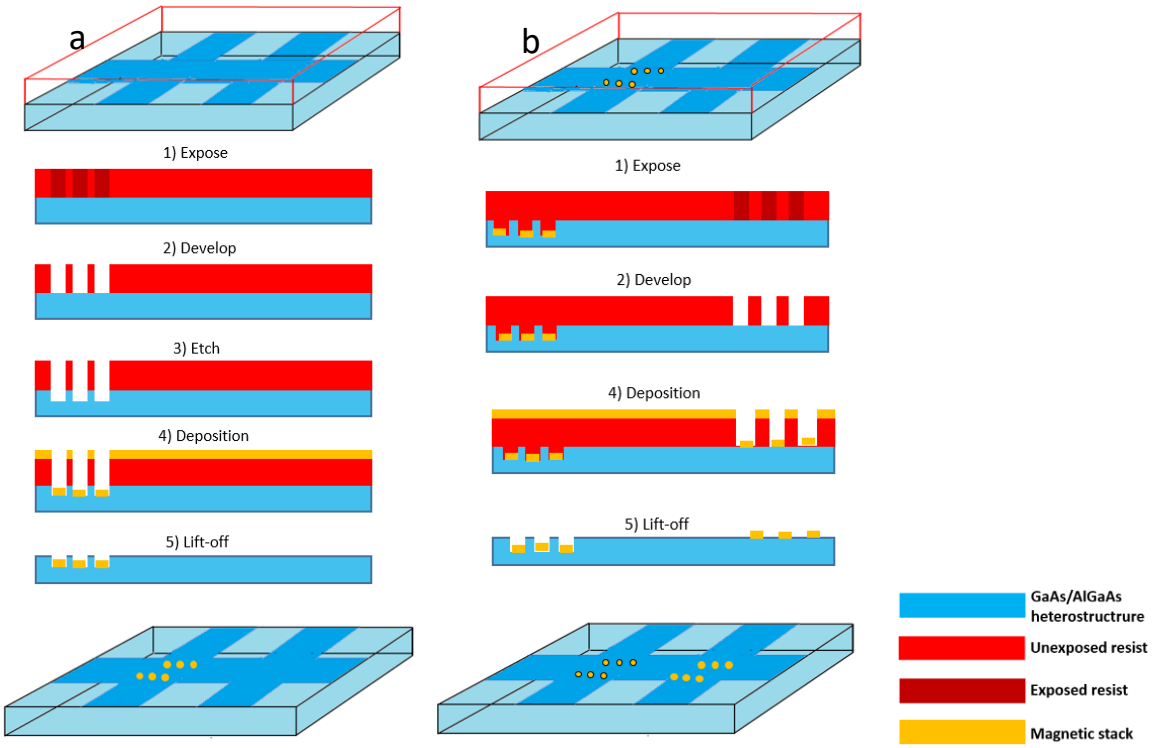

Figure 15: Illustration of the device fabrication process. (a) Fabrication of perforated device, with magnetic particles produced within the perforations. (b) Addition of an array of magnetic disks to the surface of continuous device.

The red layer in Figure 15a represents positive S1813 photoresist, which is first exposed via direct write lithography to define an array of circles. The exposed resist is developed, producing an array of perforations in the resist. Via wet chemical etching, this pattern is then transferred to the underlying GaAs/AlGaAs, where perforations in the chip are produced. To add magnetic disks embedded within the perforations, a layer of SiO_2 is first deposited via e-beam evaporation (to electrically isolate the 2DEG from the metallic disks), followed by the magnetic film via sputtering. The remaining resist is then dissolved, lifting off all deposited material outside the bounds of the perforations. The process shown in b is similar to that shown in a, without the etching step or the deposition of SiO_2.

2.4.2 Structural characterisation measurements

Following etching and deposition steps, the physical structure of the devices was investigated, to ensure that the etching depths and deposition thicknesses were as expected.

2.4.2.1 Atomic Force Microscopy (AFM)

Atomic force microscopy (AFM) is a scanning probe microscopy technique, used in this work primarily for topographic imaging. A Park XE 100 AFM was used in non-contact mode, whereby a cantilever is vibrated just above its resonant frequency using a piezoelectric element and brought close to the sample surface. Van der Waals interactions between the sample and tip result in a shift in the resonant frequency of the cantilever and a corresponding change in vibration amplitude. The change in amplitude is measured by reflecting a laser from the back of the cantilever onto a four-quadrant photodetector. A feedback loop is then used to maintain the height of the tip above the sample surface by maintaining the resonant frequency and vibration amplitude constant. Thus, in non-contact mode, the topology of a sample can be measured by recording the movements of the sample tip required to maintain constant height above it. Topographic images were processed in the software Gwyddion.

2.4.2.2 Scanning Electron Microscopy (SEM)

Scanning electron microscopy is a microscopy technique in which a beam of high energy electrons is focused to a point on a sample surface. Electrons in the incident beam interact with atoms in the sample, leading to the emission of secondary electrons, back-scattered electrons and characteristic X-rays. These interaction products are detected as the electron beam is scanned across the sample surface, providing information on both the sample topology and composition, and allowing images of the sample surface to be constructed.

SEM was used in this work to image the prototype Hall devices at various stages of fabrication. Primarily, this was to check that each step had proceeded as expected. A FEI Helios NanoLab dual-beam FIB/SEM was used. A field Emission Gun (FEG) acts as the electron source, providing a highly confined electron beam, via electron field emission. Secondary electrons are detected, to provide topographical images of sample surfaces. In general, imaging was undertaken using an accelerating voltage of 1 kV, for which a 2.5 nm resolution is quoted by the manufacturer.

2.4.3 Magnetic characterisation measurements

Magnetic characterisation measurements were used to investigate the magnetic behaviour of the fabricated magnetic thin films and disks. Polar Magneto Optical Kerr Effect (MOKE) magnetometry was primarily used to rapidly and locally investigate the switching behaviour of the films and particles. Vibrating Sample Magnetometry (VSM) was used to quantify the saturation magnetisation of the films.

2.4.3.1 Magneto-Optical Kerr Effect (MOKE) magnetometry

Plane polarised light, upon incidence to a magnetic medium, splits into a reflected and transmitted beam, both of which have been observed to become elliptically polarised, with a rotated major axis of polarisation. This phenomenon is known as the Faraday effect for the transmitted beam and the Magneto Optical Kerr Effect (MOKE) for the reflected beam, with both effects shown to depend on the magnetisation of the material.

Macroscopically, the Kerr effect is understood by means of the 3D dielectric tensor, ε, which describes the response of a medium to an electric field, E. The response is governed by the dynamics of the electrons in the medium; bound electrons are displaced from their equilibrium positions with respect to the atomic nuclei, inducing local electric dipole moments. The displacement field D, which accounts for this effect, is given by:

$$\vec{D} = \vec{P} + \varepsilon_0 \vec{E} = \varepsilon_r \varepsilon_0 \vec{E} = \varepsilon \vec{E} \quad (64)$$

where P is the polarisation density, the density of permanent and induced dipole moments in the medium, ε_0 is the permittivity of free space and ε_r is the relative permittivity of the medium. The dielectric tensor, ε, in combination with the magnetic permeability of the material, μ, governs the speed of propagation, v, of a light wave through the medium, following:

$$v = \sqrt{\varepsilon \mu} \quad (65)$$

Linearly polarised light is a superposition of equal magnitude left and right circularly polarised components. In a magnetic medium, the dielectric tensor has off-diagonal elements. The two circularly polarised components thus have different propagation velocities, resulting in each component gaining a different phase shift as it propagates through the medium. As a result, the polarization plane is rotated, with the angle by which the polarization rotates known as the Kerr angle. Both components additionally experience different absorption rates, resulting in a stronger attenuation of one component relative to the other, impacting the ellipticity, with the change known as the Kerr ellipticity [116].

MOKE Magnetometry has been widely adopted as a tool for rapid, local measurements of magnetisation dynamics in thin magnetic films. In this work, a NanoMOKE3 by Durham Magneto Optics was used. This system consists of a laser, optical components with which to linearly polarise the beam, and optical filters to enable the measurement of the Kerr angle. The system was arranged in the polar configuration, whereby the magnetisation of the sample is perpendicular to the surface, and parallel with the incident beam. A uniform magnetic field was applied to the sample via a dipole electromagnet, perpendicular to the sample surface. Here, the easy-axis switching behaviour of out of plane magnetic films was investigated, by sweeping the applied magnetic field, at a controlled frequency, and simultaneously measuring the Kerr angle. While MOKE magnetometry does not provide quantitative information regarding the sample magnetisation, switching of the magnetisation in the presence of the applied field is observed as jumps in the Kerr angle. MOKE measurements are limited to locally probing the films over the area illuminated by the beam spot, which was about 10 to 15 µm in diameter for the settings used in this work. The maximum field the system can apply is ~0.7 T, with a sweep rate in the range 2.1 to 0.005 Hz.

2.4.3.2 Vibrating Sample Magnetometry (VSM)

Vibrating Sample Magnetometry (VSM) is a technique used to investigate the magnetic behaviour of bulk magnetic samples, based on Faraday's law of induction [117],[118]. A magnetic sample is attached to a rod-shaped holder and vibrated in a direction perpendicular to an applied uniform magnetic field, B. As the sample moves, the magnetic flux, Φ_B, created by the sample into a set of surrounding, stationary pick-up coils, varies. The result of this time varying magnetic flux is the production of an EMF, V, in the pick-up coils. For a sample vibrating in the y direction while the magnetic field B is applied in the x direction, V is given by:

$$V = -N\frac{d\Phi_B}{dt} = -N.\frac{d\Phi_B}{dy}.\frac{dy}{dt} \quad (66)$$

where N is the number of turns of the coil. For a sample vibrating sinusoidally in the y direction at frequency ω and with amplitude C, its position as a function of time may be written as:

$$y(t) = Csin(\omega t) \ , \ \frac{dy}{dt} = C\omega cos(\omega t) \quad (67)$$

Putting this together, the EMF in the pick-up coils takes the form:

$$V = -N.\frac{d\Phi_B}{dy}.C\omega cos(\omega t)$$

(68)

The stray field of the sample is assumed to take the form of a magnetic dipole, given earlier in equation (7) where it was shown to be directly proportional to the magnetic moment, m. The magnetic flux into the pick-up coils is given by the integral of the dipole field over the area enclosed by the coil, S:

$$\Phi_B = \int_S B \cdot dA$$

(69)

Combining these equations, the EMF can be expressed as [119]:

$$V = G(r).m.C\omega cos(\omega t)$$

(70)

Where G(r) is a geometrical factor, related to the specific coil arrangement. The EMF produced can be measured and amplified using a lock in amplifier, focusing on the frequency of oscillation of the magnetic sample. The EMF is measured as a function of the applied magnetic field, which is generally swept at a much slower rate in comparison to MOKE magnetometry. This results in a much slower measurement of the switching behaviour of the magnetic sample but enables the quantification of the saturation magnetisation.

In this work, an EZ7 VSM by Microsense was used, in combination with a quartz rod sample holder. The maximum applied field by the system is 1.75 T, with a vibration frequency of 75 Hz. The sample is vibrated vertically, with the applied field in the horizontal direction. A background correction was applied to all measurements to remove the linear diamagnetic response of the sample holder, as well as any other systematic errors in the measurement.

2.4.4 Hall Measurements

In their most basic form, Hall effect measurements involve passing a current I through a sample in the presence of a perpendicular magnetic field B and measuring the resultant transverse voltage V_{Hall}. In the case of a uniform applied magnetic field, V_{Hall} is directly proportional to B and I and is inversely proportional to the carrier concentration, n, and sample thickness, t:

$$V_{Hall} = \frac{BI}{nqt} = R_H \frac{BI}{t}$$

(71)

Where R_H is the Hall coefficient. By measuring the V_{Hall} response as a function of applied magnetic field for a known drive current and sample thickness, R_H can be calculated from the slope of the response. From R_H, the carrier concentration, n, and indeed carrier sign may be evaluated. Often, V_{Hall} is measured in both positive (B+) and negative (B-) polarity applied field, as well as using both positive (I+) and negative (I-) polarity drive current, and these measurements are combined to remove offsets from the final Hall voltage measurement, V_{Hall}:

$$V_{Hall}(B+) = \frac{V_{Hall}(B+, I+) - V_{Hall}(B+, I-)}{2} \quad (72)$$

$$V_{Hall}(B-) = \frac{V_{Hall}(B-, I+) - V_{Hall}(B-, I-)}{2} \quad (73)$$

$$V_{Hall} = \frac{V_{Hall}(B+) - V_{Hall}(B-)}{2} \quad (74)$$

By combining measurements at opposite polarities of applied field, the offsets removed include the voltmeter and current source offsets due to improperly zeroed equipment, thermoelectric voltage offsets which occur when a temperature difference exists within a measurement setup across a junction between different materials, and the contact misalignment voltage which occurs when the contacts of a device are not perfectly electrically opposite each other. By combining measurements at opposite-polarity currents, the Nernst effect and Right-Leduc voltages are removed, both of which stem from the diffusion current which can result when longitudinal temperature gradients exist across the device.

2.4.4.1 Experimental measurement setup

A measurement platform was built with which Hall voltage measurements using the Hall bar configuration were taken. The setup was used to characterise the GaAs/AlGaAs 2DEG from which the devices were fabricated, providing estimates of the room temperature Hall coefficient, carrier concentration, conductivity and mobility. The setup was also used to measure the Hall voltage produced by arrays of magnetic disks on continuous and perforated Hall crosses.

The prototype devices used in this work are each composed of four individually contactable Hall crosses joined by a central channel, as illustrated in Figure 13. To make electrical contact to these devices, a custom sample holder was designed. The design was executed by the department electronics workshop and is shown in Figure 16a. The holder is composed of 8 electrically isolated copper pads from which electrical contact can be made to the contact pads of the device. The device is attached to the holder using rubber cement (Elmer's, no wrinkle) and contacts are wire bonded using an FS Bondtec wedge ball bonder with 25 µm diameter wire (Al-1%Si). In general, 6 connections are made; a pair across the central channel of the device, a pair across the chosen Hall cross for measurement and a final pair across the blank, continuous reference cross.

The sample holder is plugged into an 8-pin dip socket, which is wired to the 8 BNC connectors of an electrical breakout box. The dip socket is mounted on a brass rod which is used to suspend the sample between the pole pieces of an electromagnet, as shown in Figure 16b. All wires running between the sample holder and breakout box were shielded with metallic foil to reduce interference from external electromagnetic sources. The BNC sockets on the breakout box can then be connected to the desired instrumentation, either a current source or voltmeter, using BNC cables. In this work, a Keithley 2182A NanoVoltmeter is used to measure voltages in the µV range, and two Keithley 2400 sourcemeters are used to deliver currents in the µA range. The sourcemeters are operated manually by the user.

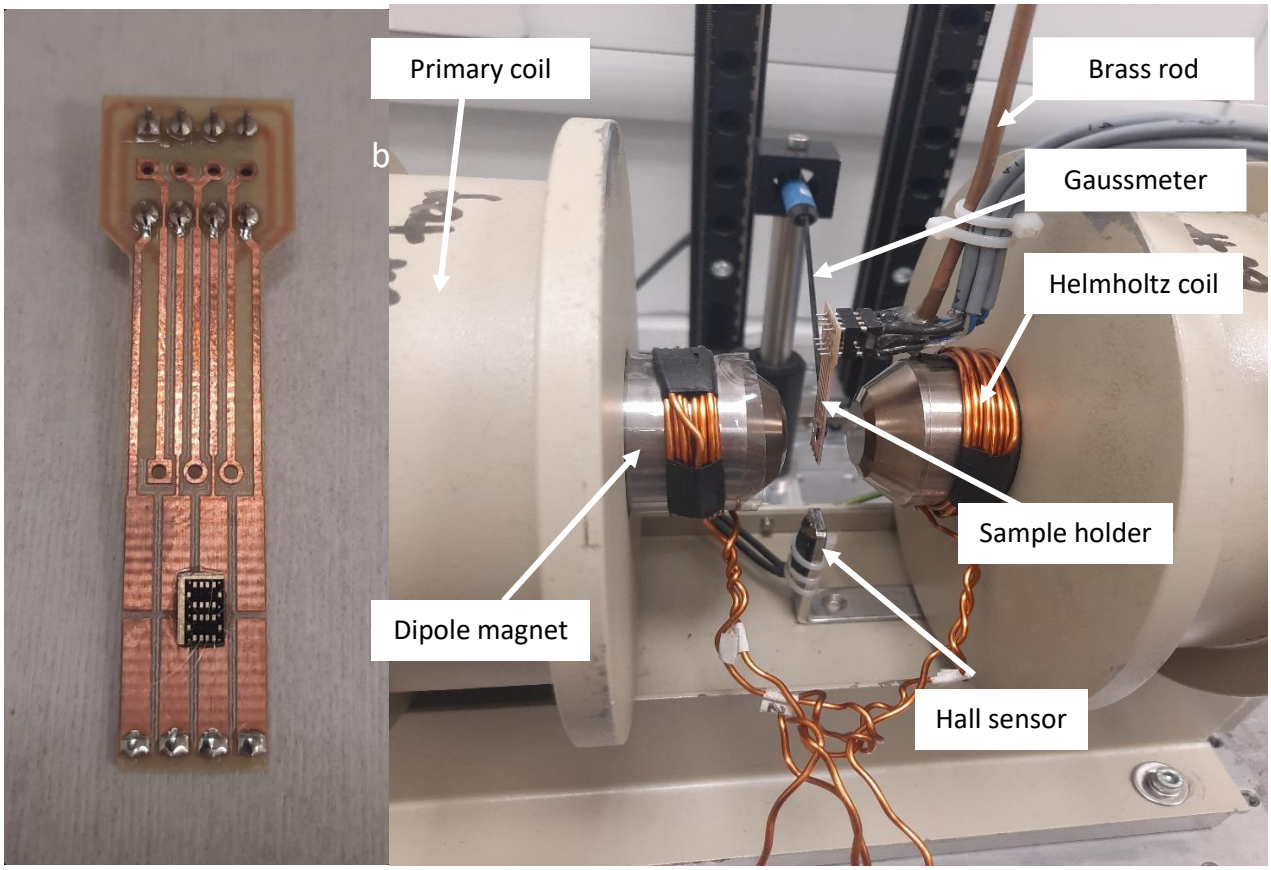

Figure 16: (a) Custom-made sample holder, with Hall cross device wire-bonded. (b) Main components of the Hall voltage measurement platform, including the electromagnet (composed of the primary coil and dipole magnet), the custom-made Helmholtz coil, gaussmeter, Hall sensor and sample holder in place.

When acquiring Hall voltage measurements as a function of applied magnetic field, a dipole electromagnet (EM) is used to controllably provide the required field. In this work, a GMW Associates 3470 45 mm Dipole Electromagnet is used. The EM was adapted from the NanoMOKE3 setup and is controlled using the associated software (LXPro) and electrical components (Controller unit, power supply, magnetic field sensor).

The EM is connected to a power supply (Kepco 20V-10A) which is in turn connected in voltage-controlled mode to an output of the NanoMoke3 controller module. A magnetic sensor (Hall sensor) is positioned below the centre of the pole pieces of the EM, as shown in Figure 16. The output of this sensor provides feedback to the system and is connected to an input of the controller module. The system is calibrated such that the magnetic field produced (measured manually by a Lakeshore 450 gaussmeter) at the central position between the pole pieces (where the sample would sit) as a result of a given voltage provided by the Kepco, is related to the voltage measured by the Hall sensor, positioned below the pole pieces.

In this work, the electromagnet was arranged to have a 13 mm pole spacing. The maximum current which may be provided by the Kepco is ±10 A, resulting in a maximum field of approximately ±0.8 T. The instructions are coded via the controller using 16 bits, meaning that the 1.6 T field range is coded over 2^{16} points. As a result, we expect to be able to control the field to the nearest 1.6 T/2^{16} = 0.244 Oe. This is the minimum step on the field setpoint. However, we are also limited by our ability to read the field value. In our system the output from the Hall sensor is a 0-5 V signal which covers approximately the full 1.6 T range, giving a sensitivity of 5 V/ 1.6 T = 312.5 µV/Oe. This is digitised by the controller using a 16 bits DAC card operating on ±10 V, with gives a resolution of 20 V/2^{16} = 305 µV, or 305/312.5 =

0.976 Oe. When applying the field using the EM and measuring it with the built-in Hall sensor, the limiting element is our ability to read the field, and the limit is 1 Oe.

Certain measurement configurations require the Hall voltage to be measured at a cross containing remanent magnetic particles in zero applied field. If we consider the average stray field from an array of magnetic particles present on the surface of a 100 µm x 100 µm Hall cross, it tends to be less than 1 Oe. Thus, the potential spurious Hall voltage generated by the improperly zeroed global field of the EM would be of comparable magnitude to the Hall voltage generated by the magnetic particles.

To improve the accuracy with which the applied field may be controlled close to 0, a pair of Helmholtz coils were designed and built. The range of field produced by the coil, and so coded over 16 bits by the controller, was greatly reduced in comparison to the EM. Each coil composing the Helmholtz pair was wound from 15 mm diameter copper wire with the aim of accepting 5 A of current without overheating, delivered by a 20V – 5A Kepco power supply. The coils were wound with a loop diameter of just over 4.5 cm, such that they could easily sit upon the pole pieces (4.5 cm diameter) of the EM, as shown in Figure 16b.

When no power is supplied to the EM, the remanent field of the pole pieces can be as large as ±30 Oe. Thus, the coils needed to be capable of at minimum producing ±30 Oe of field. From the manufacturer webpage and manual, the number of turns of coil in the EM is known to be 980 and the field produced at a drive current of 5 A with a 13 mm pole spacing was estimated to be ~0.85 T. This tells us that at a current of 5 A, roughly 8.7 Oe of field is produced per turn, and 10 turns should thus provide 87 Oe of field. The coils were thus built with 10 turns and we measured a field of 80 Oe at the centre of the pole pieces at 5 A of current. The coils were connected to the 20V - 5A Kepco, operated in voltage-controlled mode, which was in turn connected to the controller module. With ±80 Oe coded over 2^{16} bits by the controller, field control to the nearest ~0.0024 Oe is expected.

As we saw earlier, the accuracy to which the field can be controlled is also limited by the accuracy to which it can be measured, with the optimum situation occurring when these are matched. A Lakeshore 450 Gaussmeter using a High Sensitivity Probe in the 30 G range was added to the setup. In this range, the instrument resolution is stated as ±0.001 Oe by the manufacturer. The probe was placed between the pole pieces, laid against the back of the sample holder, aligned with the position of the sample, as illustrated in Figure 16. Due to the strong homogeneity of the EM field in the x direction, as presented in the manual, it is assumed that the field measured at the position of the probe is essentially equal to that at the sample. The output of the Lakeshore was connected to the input of the controller module to provide feedback.

All voltage measurements were acquired using a Keithley 2182A Nanovoltmeter (NVM). Measurement settings for the NVM were chosen to minimise electrical noise while maintaining reasonable measurement times. The measurement rate sets the integration time of the analog to digital (A/D) converter and as such, the number of voltage measurements acquired per second. The integration time is also referred to as the measurement aperture and is specified based on the number of power line cycles (NPLC) over which the measurement is averaged. Power line noise is present at 50 Hz (UK) and since it is periodic, integrating the signal over 1 PLC can reduce this contribution. The system was capable of averaging measurements over 0.1, 1 or 5PLC. According to the KNVM manual, the 2182A model

generally has a parabola-like shape for its speed-noise characteristics, with 5PLC (100 ms aperture, 10 Hz measurement rate) at the minima and 1 PLC (20 ms measurement aperture, 50 Hz measurement rate) close by, thus both are considered reasonable rate settings. In this work, a moving average digital filter was applied, with a 10 reading, 0.1% window. The 100 mV measurement range was used. With these settings, 10 nV measurement resolution is expected, as stated by the manufacturer.

The output of the NVM is connected to the controller module and displayed in the LXPro software. Within a single measurement cycle, the LXPro software interfaces with the EM to apply the desired magnetic field sequence, while simultaneously interfacing with the NVM to collect 1000 voltage data points. The LXPro measurement frequency thus dictates the timeframe over which the field sequence is applied and in general, the measurement frequency was set to either 0.06 Hz in combination with a NVM rate of 1PLC or 0.012 Hz in combination with a NVM rate of 5PLC.

2.4.4.2 Measurement types

Here, the Hall voltage measurement types and corresponding setup configurations for the measurement of arrays of magnetic disks are described.

2.4.4.2.1 Hall gradiometry

Hall gradiometry is a measurement technique developed to allow the Hall signal produced by an array of magnetic particles situated on the active area of a Hall cross to be measured as a function of applied field [120],[121]. Without the gradiometer, the Hall voltage produced by the array of particles is dominated by the Hall voltage response to the applied magnetising field. With the gradiometer, the response to the applied global field is effectively zeroed and the response to the particles is isolated.

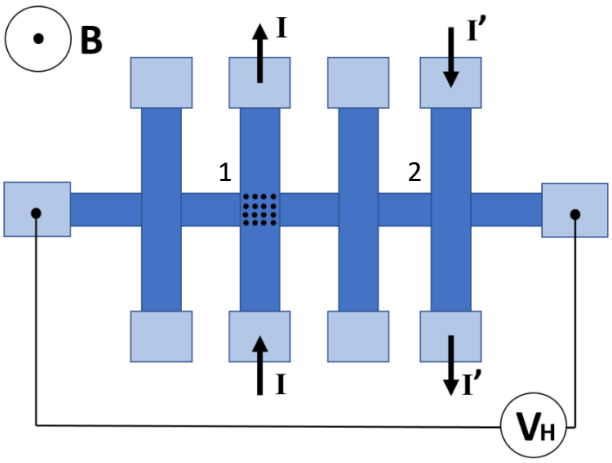

Figure 17: Schematic of the Hall bar configuration, arranged for measurement of the Hall voltage using Hall gradiometry.

A current of equal magnitude and opposite direction is driven through two crosses on the same device, as shown in Figure 17. The magnetic particles to be measured are situated on cross 1, while cross 2 is blank. In response to a global uniform field B, each cross produces a Hall voltage of equal magnitude and opposite direction ($V_{1,B}$ and $V_{2,B}$, where $V_{1,B}$ = - $V_{2,B}$). At cross 1, an additional Hall voltage, $V_{1,particles}$, is produced, due to the presence of the stray field of the magnetised particles. The Hall voltage is measured across the main channel of the device such that it is the sum of the Hall voltages produced at cross 1 and cross 2:

$$V_{Hall} = \left(V_{1,B} + V_{1,particles}\right) + V_{2,B} = V_{1,particles}$$

(75)

Hall gradiometry was used in this work primarily for non-remanent measurements. Here, the EM was used to sweep an applied field to beyond the switching field of the magnetic particles. The balanced gradiometer zeroes the response of the device to the global field, such that the V_{Hall} response to the particle array is isolated and the hysteresis loop is extracted. The hysteresis loop of the magnetic disks used in these experiments is highly recognisable, thus such measurements give us confidence that the measured V_{Hall} signals are indeed due to the magnetic particles. Hall gradiometry also offers a measurement approach applicable to non-remanent particles.

To make this measurement, the contacts across which the Hall voltage is to be measured (the main bar of the device) were connected to the NVM via BNC connections to the breakout box and the output of the NVM connected to an input of the controller module. The contacts across which the current was to be driven (one cross with magnetic particles, one blank cross) were connected to two floating current sources via BNC connections to the breakout box. The current through each cross was set manually. The EM, controlled by the LXPro software, provided the required field sequence (swept between ±2000 Oe).

Due to differences between crosses, it cannot be assumed that the response of the device to a global field will be perfectly zeroed by driving opposite polarity currents of exactly equivalent magnitude. The desired drive current I was applied to the cross with magnetic particles and initially also to the blank cross. A field was swept in a range below the switching field of the particles, and the Hall response recorded. The current through the blank cross, I', was then varied until the slope of the V_{Hall} vs field response was flat, at which point the gradiometer was balanced.

2.4.4.2.2 Remanent measurements

During a remanent measurement, the magnetisation direction of the array of magnetic particles to be measured was set by a field pulse larger in magnitude than the switching field of the particles. The V_{Hall}^{+} response to the stray field of the particles was then measured in zero applied field. The magnetisation was then set in the opposite direction via an oppositely directed magnetic field pulse and V_{Hall}^{-} was recorded in zero field. The V_{Hall} signal of the array is calculated as:

$$V_{Hall} = \frac{V_{Hall}^{+} - V_{Hall}^{-}}{2}$$

(76)

The system was set up to operate both the EM and the Helmholtz coils together. The high field pulses needed to set the magnetisation state of the magnetic particles was provided by the EM, while the zero-field section of the measurements employed the Helmholtz coils to ensure accurate zeroing of the field.

3. COMSOL Simulations

The COMSOL model used in this work was created in collaboration with Dr Pierre Roy of the Hitachi Cambridge Laboratory.

In this chapter, the computational simulations conducted using COMSOL, set up as described in section 2.3, are discussed. Firstly, the code was benchmarked against publications in which the detection of uniform global fields [110] as well as local, inhomogeneous field profiles [111] were modelled. The model was also verified in the experimentally relevant situations of single super-paramagnetic bead detection [85] and super-paramagnetic bead array enumeration [80], again by comparison against published computational results. Details of the verification are presented in Appendix A and agreement between our calculations and the published literature is always better than 5%. The authors of publications [85] and [80] claim to have validated their model against experiments [109][122] showing agreement to within 10-20%. The checks carried out to ensure that the simulation results reached a stable state with respect to various computational parameters such as meshing are shown. Then, the model Hall cross system upon which our simulations primarily focus is presented. This model system was explored, first in its continuous form (non-perforated sensor) to assess the capability of the continuous device for the detection and enumeration of magnetic particles. The main limitations are found to be low magnitude single particle Hall voltage signal and the inhomogeneity of the signal as a function of position.

The model perforated device was then explored and the superiority of this device design for the enumeration of magnetic particles was demonstrated. The addition of perforations is shown to both increase the magnitude of the single particle Hall voltage signal and to improve the homogeneity of the signal as a function of position when particles land either aligned with the perforations or diagonally between four perforations. Perforations are shown to increase the average stray field of the particles onto the sensor, and this is thought to be the central mechanism responsible for the increase in Hall signal. Their presence also drastically alters the current density distribution, which is known to impact the Hall response. In addition, we suggest that the improvement in the homogeneity of the averaged stray field of the particles within these subsets of positions is primarily responsible for the improvement in signal homogeneity.

Having explored the improvements towards magnetic particle counting attained by perforating Hall cross devices, simulations were used to aid the design of prototype experimental devices. Magnetic disks were focused upon, and a large parameter space was explored, including varying the magnetic particle and perforation diameter, perforation spacing and lay-out and Hall cross active area size. Finally, features of an experimental prototype device which are not accounted for in the model were considered. This includes the rounding of the Hall cross corners due to lithography resolution limitations and a potential mismatch between particle and perforation diameters. Reduction in the Hall voltage signal due to these effects was explored to understand how the experimental results can be expected to differ from those of the model system.

3.1 Introduction to the model system

To demonstrate the limitations of continuous, large area Hall cross sensors for magnetic particle counting, as well as the improvements offered by our perforated device design, we focussed primarily on a single Hall cross system. For this model system, we used a cross with an active area of 100 µm x 100 µm and arms of length of 150 µm terminated by copper pads. The current density was $1x10^8$ A/m^2, equivalent to a current of 250 µA for a 25 nm thick 2DEG. This current entered the device from the upper current probe arm where a constant current density boundary condition was applied, while the lower current probe arm was grounded. Floating point boundary conditions were applied to the left and right voltage probe arms. The Hall voltage was calculated as the average voltage along the boundary between the 2DEG and copper pad for the left arm, minus the same calculated for the right arm. The carriers were electrons with a carrier concentration n of 9.21 $x10^{22}$ m^{-3}. The mobility µ was 0.9012 m^2/Vs and the conductivity was defined as the product of n, µ and the absolute value of the carrier charge, q (1.602 $x10^{-19}$ C).

For the corresponding model perforated device, a 7x7 array of perforations was added to the active area. One perforation was positioned at the centre, surrounded by a square array of perforations, 6 µm in diameter with centre-centre distances of 12 µm. Figure 18 shows a schematic of the devices, in the continuous (a) and perforated (b) forms.

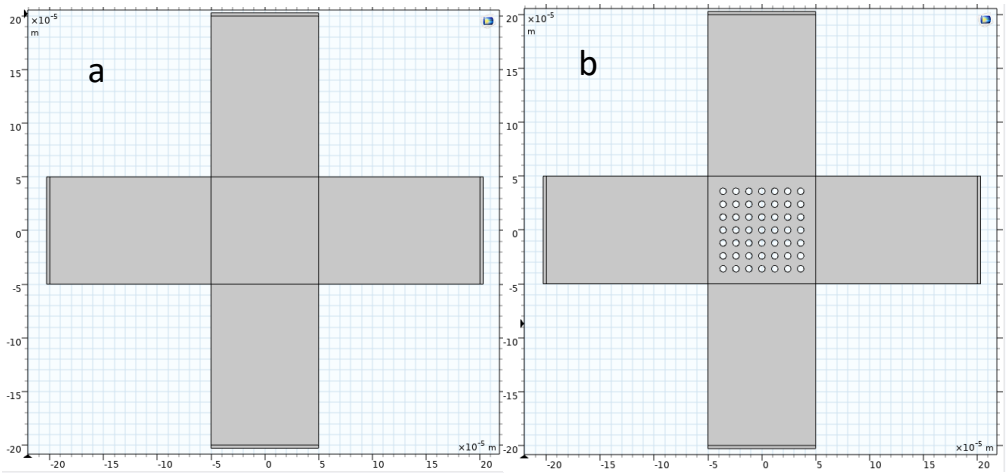

Figure 18: Schematics of the Hall devices modelled. (a) Model system: 100 µm x 100 µm continuous cross with 150 µm long arms. (b) Corresponding perforated cross, with a 7x7 array of 6 µm holes with 12 µm centre to centre distance.

For the magnetic particles, cylindrical disks and spherical beads of 6 µm diameter were modelled. The disks and beads were designed to have the same magnetic moment, with field profiles described as outlined in previous sections. The saturation magnetisation, M_S, of the disks was 0.2 $x10^6$ A/m, with a thickness of 20 nm and a corresponding moment of 1.13 $x10^{-13}$ Am^2. For the magnetic beads, a saturation magnetisation, M_S, of 1000 A/m was used to equate moments. The distance between the central plane of the particles and the central plane of the 2DEG was set to be the sum of half the 2DEG thickness (12.5 nm), half the particle thickness, and 90nm. This corresponds to a particle sitting directly on top of a 2DEG which begins 90 nm below the surface of the material and extends 25 nm, as is the case in GaAs/AlGaAs wafers produced at our department by collaborator Dr. Chong Chen of the Semiconductor Physics group. We refer to a particle in this configuration as being at a working distance of 90 nm. For the perforated cross, simulations were also run in which the particles were placed within the perforations, situated at the level of the 2DEG

(central plane of particle and 2DEG overlapping). In this case, we refer to the particles as being embedded within the perforations, and the central plane of the 2DEG and the particles coincide.

The response of the sensor to the field profile of a magnetic dot was also explored in the course of this work to aid our understanding of the system. As described in section 2.3.1.3, a magnetic dot is defined by a field B_0 inside the radius of the dot and zero outside. The field B_0 was set here to a value of 4.18 mT, corresponding to the maximum stray field of an equivalent 6 μm disk at the sensor.

In the following sections, we use this model system to demonstrate the superiority of our perforated device design by comparing the Hall voltage generated by magnetic disks and beads immobilised upon a continuous and perforated Hall cross with the same current through each device. We quantify the improvements to the device, discuss the central mechanisms at play and optimise the device design. While the parameters chosen to describe the model system are not likely to exactly match the parameters of the experimental prototype to follow, those describing the 2DEG are considered experimentally realistic values for a GaAs/AlGaAs 2DEG at room temperature. GaAs/AlGaAs Hall devices were fabricated by departmental collaborators (Dr Chong Chen) and characterised at an early stage of the project to establish these values. The parameters describing the magnetic disk are also considered experimentally realistic for magnetic disks produced in-house (as will be presented in following experimental section). We thus expect the predictions made to provide a reasonable estimation of experimental device performance.

3.2 Preliminary checks

Several preliminary checks were carried out to ensure that our simulations accurately represent the operation of a Hall cross device such that our results may be used to make reliable predictions. It was ensured that the results do not rely on the mesh used or choices made when building the model which may change when moving to an experimental device. This includes certain geometric choices, such as the length of the arms included in the simulations as well as the choice of boundary conditions used to represent experimental device operation.

3.2.1 Mesh analysis

The mesh used to discretise the system dictates both the accuracy of the results and the computation time required, with a high-resolution mesh yielding more accurate data at the cost of long run times. When choosing a mesh, a balance between the two is sought. There comes a point past which continuing to enhance the resolution of the mesh fails to significantly impact the results. Mesh independence is then said to have been reached, and this mesh can be used to provide accurate data with the shortest possible computation time.

For our system, we employed a quadratic, free triangular mesh. We used three different size nodes; one for the active area, one for the contacts, and one for the arms. We wanted high mesh resolution within the active area to resolve the rapidly varying field profiles of the magnetic particles, reasonable resolution at the contacts for accurate computation of the Hall voltage, and coarse resolution in the arms to decrease computation times.

The mesh is defined by several parameters. The growth rate dictates how fast the mesh from one section of the structure can grow, to fit with a mesh from another section. The curvature limits the maximum element size along a curved boundary, with smaller values resulting in a finer mesh along curved boundaries, and the maximum and

minimum cell sizes define the size range into which the mesh elements must fit. If the growth rate is low (minimum value is 1), the maximum cell size is usually the most important parameter in defining the mesh resolution. These parameters are input to COMSOL, which then generates the mesh for the user.

The mesh independence study was conducted by calculating the Hall voltage response, V_{Hall}, to 13 magnetic disks simultaneously placed on the cross active area: 9 at the centre in a 3x3 square array and one in each of the 4 corners, as a function of the various mesh parameters. 13 disks were used to give a total V_{Hall} signal which was well above the computational noise, and which captured the behaviour across the active area. The study was conducted using magnetic disks, as these have the most rapidly varying field profile of the magnetic structures that will be used in our work, and thus should have the most demanding resolution requirements. We ran the mesh analysis for the particles at the closest working distance that we expect to use in each case – embedded within the 2DEG for the perforated case, and 90nm above the 2DEG for the continuous case.

For the perforated cross, due to the presence of the array of perforations, the simple mesh generated by COMSOL within the active area was high in resolution for a large range of mesh parameters. In this case, the mesh analysis was performed for particles embedded within the perforations, as well as positioned diagonally between the perforations, at a working distance of 90nm.

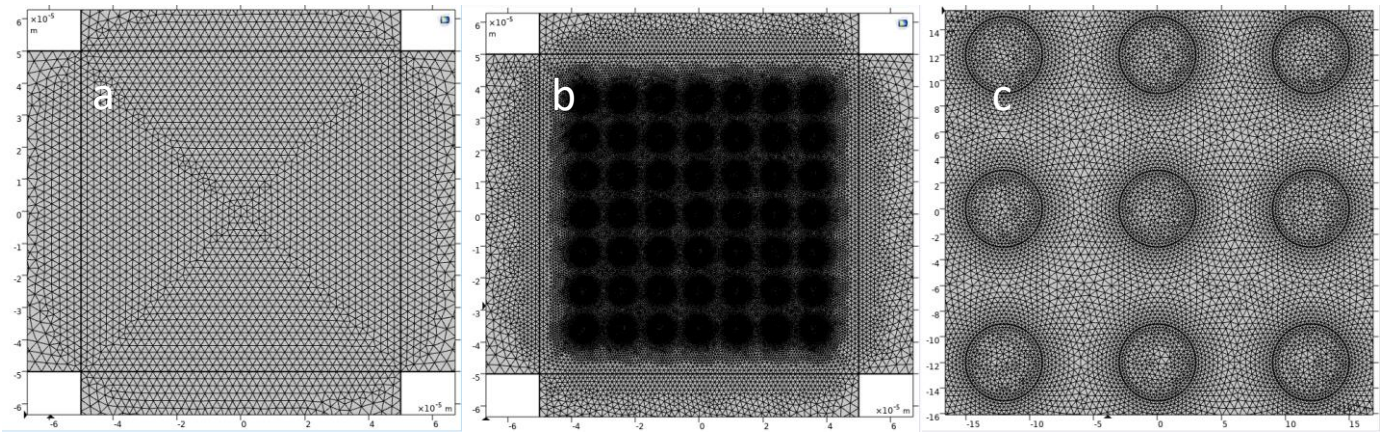

Figure 19: Automatically generated meshes for a 100 µm x 100 µm continuous cross. (a) simple mesh. (b) mesh obtained when creating an array of 6 µm circles in the positions where the perforations would be in the case of the perforated device (phantom circles). (c) zoom of the central area in (b).

For the continuous cross, two different meshing options within the active area were investigated. The first was a simple mesh, as illustrated in Figure 19a, in which the maximum cell size primarily determines the mesh quality, and the mesh is consistent across the active area. The second is produced by defining an array of circles within the active area in the positions corresponding to the perforations of an equivalent perforated device (phantom circles), as illustrated in Figure 19b and c. With these structures present, the generated mesh is forced to be well resolved around the circles. This mesh is useful when we intend to simulate particles sitting at the positions of the circles, which is often done to compare the response of the continuous and perforated crosses. We performed the mesh independence study with both the simple mesh and with particles aligned with the phantom circles.

The details of the investigation are presented in Appendix B. In brief, we tested mesh independence for 3 mesh parameters: the maximum cell size in the active area, the minimum cell size in the active area and the maximum cell

size in the arms, which were empirically found to be the most important parameters in defining the mesh. The study was carried out by calculating V_{Hall} while varying these parameters separately to determine the value below which V_{Hall} was within 2% of its value at the finest mesh investigated. The results are summarised in Table 1.

Device type	Mesh type	Max cell size (µm), active area	Min cell size (µm), active area	Max cell size (µm), arms
Continuous	simple	0.3	0.1	10
Continuous	phantom holes	10	0.1	10
Perforated, disks embedded	simple	10	0.5	10
Perforated, disks between perforations	simple	0.4	0.1	10

Table *1*: *Summary of mesh parameters for which mesh independence is reached.*

We find that the mesh parameters required for the results to reach mesh independence can differ depending on whether we are dealing with the continuous or perforated device, and indeed as a function of where the particle sits on the sensor (embedded within a perforation or positioned diagonally between them). These values represent the meshing parameters that will provide accurate results with the shortest possible computation times. In all our computational work, we ensure that the mesh parameters used are below these values.

3.2.2 Arm length and boundary condition analysis

We expect that the response of the device to a magnetic particle situated within the active area will vary as a function of the arm length of the cross. As the voltage probe arms are elongated, the current distribution in the junction is expected to change, and as a result, so too is the Hall voltage response. We also expect that experimentally, the cross fabricated will have arms much longer than those used in the simulations. The longer the arms included in our simulations, the more computation time required. Thus, it is important to establish the minimum arm length at which the Hall voltage becomes constant, and to run our simulations for such a geometry.

In addition, we have a reasonable amount of choice regarding the boundary conditions (BCs) that we may apply to the device to simulate experimental operation. Firstly, the device is most likely to operate in constant current mode, which, as discussed in the introduction, can be simulated using constant current density (J), or floating point (FP) constant current BCs applied to the current probe arm. In addition, for the voltage probe arms, we have a choice of either insulating (ins) or floating-point BCs, as well as the option to add metallic contact pads (contacts/no contacts). We are aiming to model a realistic experimental device and thus ideally, would like to ensure that our choice of BCs does not impact the results.

We approached this by calculating the Hall voltage, V_{Hall}, as a function of arm length, for all the different BC combinations that could be used to model device operation. We repeated this for both the model continuous and perforated crosses and did so for both a global uniform field of strength 0.01 T and a set of 13 magnetic disks, organised again in a 3x3 square array at the cross centre, and with one in each of the 4 corners, with a working distance of 90 nm in both cases. The details of the study are presented in Appendix C and Table 2 summarises the results.

In brief, we find that the minimum arm lengths at which the V_{Hall} results, calculated with all possible boundary condition combinations, converge to within 1%, varies depending on whether the cross is continuous or perforated, and whether a global field or the field of magnetic particles is being applied.

Device type	Applied field	Arm Length (W)
Continuous	Magnetic Disks	1.5
Continuous	Uniform 0.01T Field	1.5
Perforated	Magnetic Disks	1
Perforated	Uniform 0.01T Field	2

Table 2:Summary of minimum arm length for which arm length independence is reached.

For simulations involving magnetic disks, a minimum arm length of W is required for a perforated device, and 1.5W for a continuous device. At the expense of computation time, we decide to use the longer arm length of 1.5W in both cases, to keep the global geometry consistent. When a global field is to be applied, a minimum arm length of 1.5W is needed for the continuous device, and 2W for the perforated device. Again, to keep the global geometry consistent, we decide to use the longer arm length of 2W in both cases. We also decide that the boundary conditions we will use will be FP on the voltage probes, and constant J on the current probes. These boundary conditions will be used for all studies from this point onwards, unless otherwise stated. Furthermore, we found that the arm lengths required for arm length independent results is not impacted by the size or the arrangement of perforations within the active area or by the active area width.

3.2.3 Additional considerations

When running simulations to explore the operation of continuous and perforated Hall cross devices, we make two assumptions. Firstly, we run our simulations with no global field present, implicitly assuming that the perforated and continuous sensors respond in the same way to a global uniform field and that the superposition of this field will not impact the response of the devices to magnetic disks. Secondly, we run our simulations with a single particle present upon the sensor at a time, assuming that the total signal from a collection of particles is equal to the sum of single particle signals. Experimentally, the detection of any non-remanent magnetic particle will require the application of a global field to magnetise the particles and multiple particles will be present upon the sensor simultaneously. It is therefore important to verify that our assumptions hold true.

3.2.3.1 Superposition of a uniform field

We compared the responses of the model perforated and continuous Hall crosses, with parameters as described in section 3.1 (each operated with a drive current of $1x10^8$ A/m^2) to a global uniform magnetic field, as shown in Figure 20, where the inset shows the percentage difference between device responses. This difference is much less than 1% and we thus conclude that the perforated and continuous sensors respond identically to a global uniform field. We later use this result to allow the experimental characterisation of the properties of the 2DEG at both perforated and continuous devices.

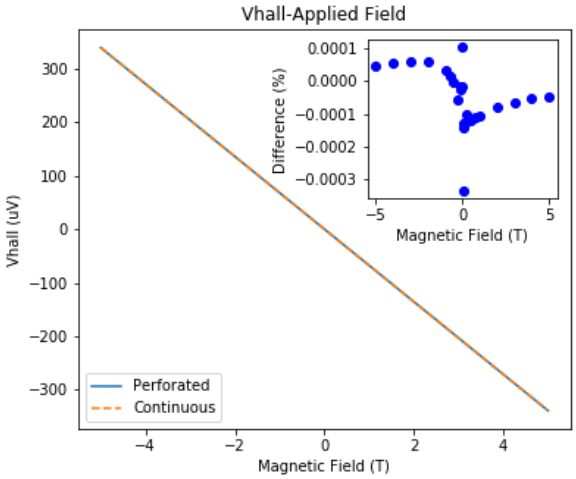

Figure 20: Hall voltage response of the model continuous and perforated devices to an applied global uniform field. Inset shows the percentage difference between both responses, illustrating that the response of a Hall cross is essentially unaffected by the addition of perforations.

To check that the application of a background uniform magnetic field does not change the response of the perforated Hall cross to magnetic disks, we calculated the V_{Hall} response of the model perforated device to a 6 µm magnetic disk present upon the sensor, both in isolation and with a superimposed global uniform field (0.001 T, 0.01 T, 0.1 T and 1 T). We calculated the V_{Hall} response maps for all available particle positions in which the disk is aligned 90 nm above the perforations (7x7 array of available positions), firstly with the superimposed background field and secondly without. We also calculated the response of the Hall cross to the background field alone. We subtracted the response of the cross to the background field alone from the first response map and calculated the percentage difference between this map and the second map calculated previously. The result (not shown here) is a maximum percentage difference of 2%. We thus conclude that the superposition of a global uniform field does not significantly impact the response of the perforated Hall cross to a magnetic disk, and simulations may be run without a background global field.

3.2.3.2 Multiple particles at once vs sum of single particle contributions

To verify that the Hall voltage response to any combination of particles is equivalent to the sum of the corresponding single particle contributions, we calculated the Hall voltage response of the model perforated and continuous Hall crosses to a collection of 6 µm diameter disks using two different approaches. In the first approach, we placed a single particle at a given position, calculated the response of the sensor and repeated the process for all positions of interest. These single particle Hall voltages were then summed up to give the total signal of the particle collection. In the second approach, we placed a collection of N particles simultaneously upon the sensor. This was achieved by generating the applied stray field from the particle collection (by summing the individual magnetic field profiles of the magnetic disks placed at the positions of interest) and then conducting a single calculation to extract the V_{Hall} response.

In Figure *21*a, we show the total V_{Hall} as a function of particle number calculated via both approaches for the perforated and continuous sensors. As the particle number increases, particles are added to the collection in rings, from the centre of the active area outwards. It is immediately evident that the datasets calculated using the second method perfectly cover the datasets calculated using the first approach. The complete equivalence between both computation methods

is confirmed in (b), where we show the percentage difference between the two sets of results. We thus conclude that either approach may be used to calculate the Hall voltage response of the devices to a collection of magnetic particles.

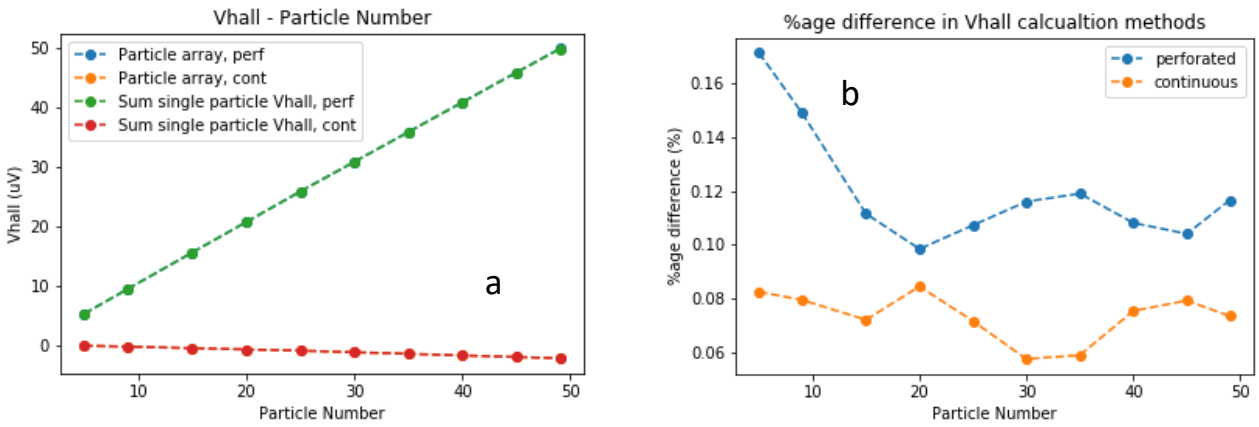

Figure 21: (a) V_{Hall} response to an array of disks present on the continuous and perforated (aligned configuration) sensors, as a function of particle number, calculated with all particles present upon the sensor simultaneously, and as the sum of single particle signals. (b) Percentage difference in V_{Hall} between both approaches as a function of particle number.

3.3 Continuous Hall cross

With the validity and the basic parameters and conditions for the COMSOL simulations established, we used this tool to study the performance of Hall sensors. Figure 22 shows the V_{Hall} response of the model continuous cross (100 µm x 100 µm active area) to a 6 µm magnetic bead (a) and disk (b) translated across the sensor surface at a working distance of 90 nm. We generated the maps by placing a single magnetic particle at a given position, calculating the V_{Hall} response, and plotting the result at the corresponding position on the map (2D grid of 41x41 points, with 3.5 µm spacing). The maps extend an additional 20 µm into each of the cross arms and the outline of the active area is indicated as a dashed square.

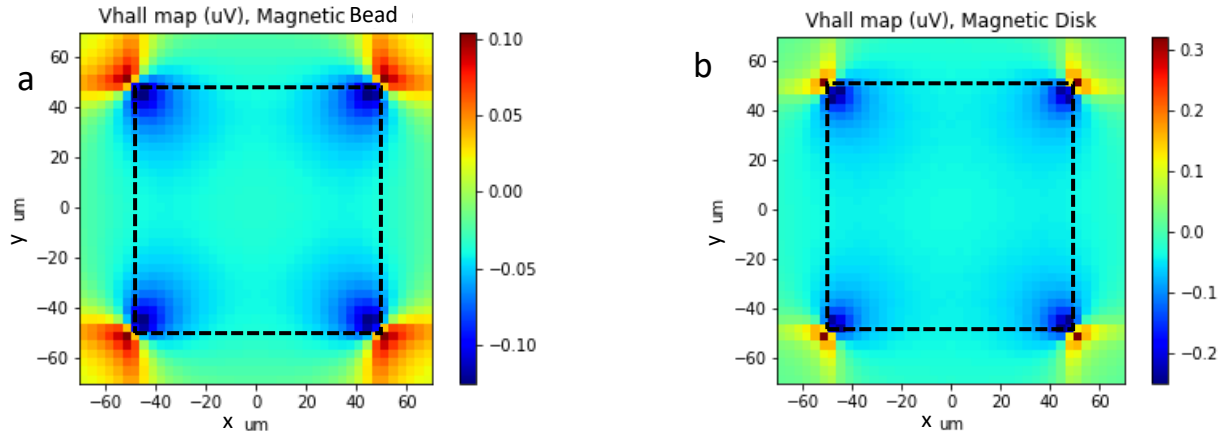

Figure 22: Heat map representing the V_{Hall} response of the model continuous Hall cross to a magnetic (a) bead and (b) disk, placed at different positions 90 nm above the sensor. The dashed line indicates the outline of the active area.

The signal is highly inhomogeneous, with regions of high V_{Hall} close to the corners of the active area and a low V_{Hall} region at the centre. For an ideal particle counter, the Hall voltage response as a function of particle position must be perfectly homogeneous. This means that the signal from a particle landing anywhere on the active area regardless of position must be identical. The total Hall voltage generated by any collection of particles could then be divided by the

single particle signal to exactly yield the number of particles present on the sensor. In addition, the Hall response to a single particle must be as large as possible, to achieve the best signal to noise ratio during experimental device operation.

To assess device performance, some metrics are required which reflect the strength of the single particle signal and the homogeneity of the sensor. The former is straightforward; it is the average single particle Hall voltage. The latter requires a little more analysis of the results to emerge, which we illustrate here with the 6 µm disks.

We considered magnetic disks placed at positions equivalent to the perforations of the model perforated device. The particle positions considered are separated by a single particle diameter (6 µm) edge to edge, forming a 7x7 array. This makes comparing our results directly against an equivalent perforated device straightforward.

In Figure 23a, we present the Hall voltage map for the 7x7 array of disks positions. To create the map, a single disk was placed upon the cross and the Hall voltage response was calculated. The result was then plotted at the corresponding position within the map. The positions are indexed, from (0,0) in the top left corner, to (6,6) in the bottom right corner, with the positions and associated indices illustrated in Figure 23b.

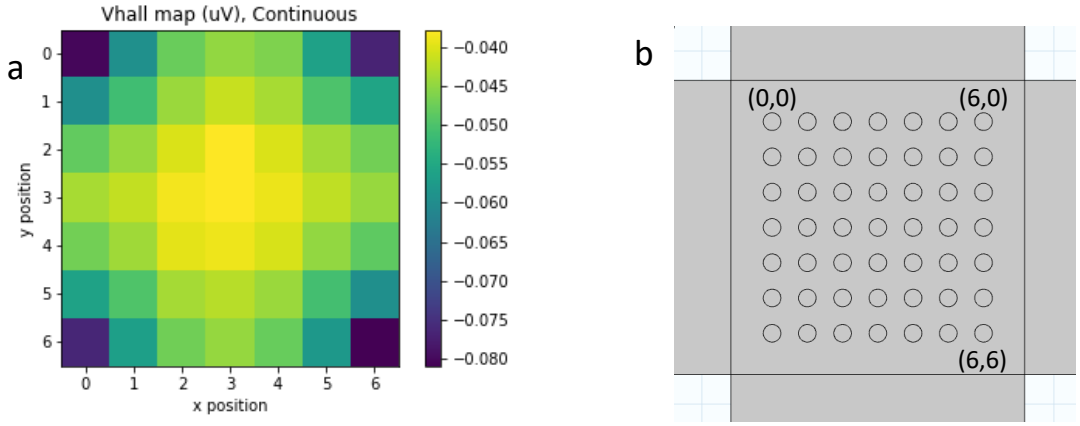

Figure 23: (a) Hall voltage map generated by placing a magnetic disk at different discrete lateral positions across the active area of the continuous sensor. The positions of the disks and the position's indices are illustrated in (b).

To count the number of magnetic disks present on the Hall cross device, the total V_{Hall} signal produced by the particle collection is measured and divided by the average single particle signal, V_{av}. An ideal device would be capable of counting any number of particles, from a single particle up to the maximum number of 49, with a maximum uncertainty of ±1 particle. We tested whether this was possible for this device and set of particle positions. In Figure 24a, the single particle signal is plotted as a function of position index, with V_{av} indicated by the green line. In Figure 24b, the absolute value of the difference between V_{Hall} and V_{av} is plotted as a function of position index. Here, the (column, row) indexation of positions illustrated in Figure 23b was mapped onto a single index running across columns, then rows: an index of 1 corresponds to the (0,0) position, 7 corresponds to (6,0), 8 corresponds to (1,0) etc., through to 49 for position (6,6).

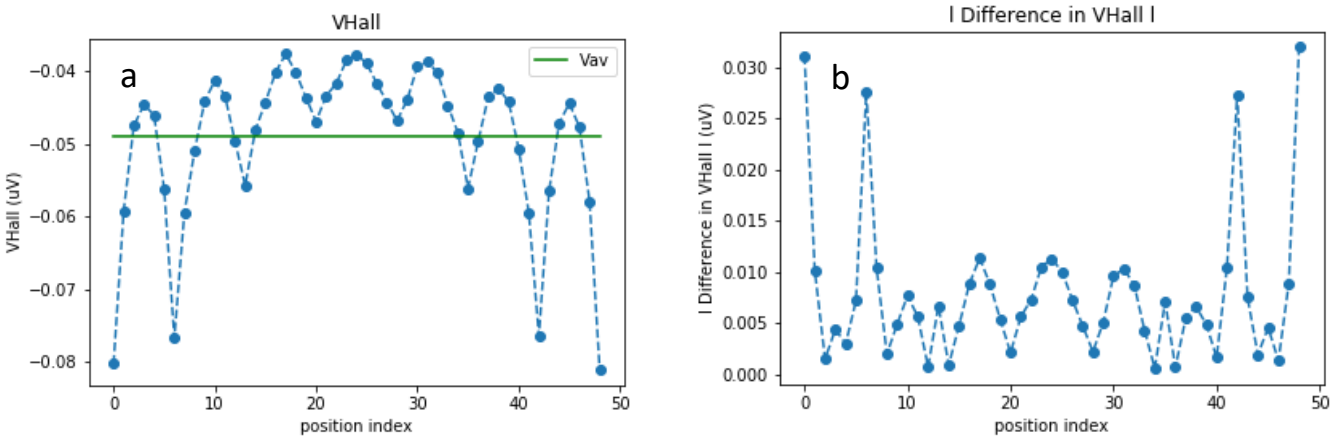

Figure 24: (a) The single particle V_{Hall} signal plotted as a function of particle position index, with the average single particle signal, V_{av}, in orange. (b) Absolute value of the difference between V_{Hall} and V_{av} as a function of particle position index.

Next, we arranged the single particle Hall voltage signals in ascending order (most to least negative) and calculated the total signal due to N particles by summing N consecutive single particle Hall voltages following this order. We plotted the total Hall voltage as a function of N, as shown by the blue curve in Figure 25a. The orange curve shows the results when the single particle Hall voltage signals are added in descending order. We also calculated the ideal total Hall voltage for the N particles by multiplying N by V_{av}, as shown by the green curve.

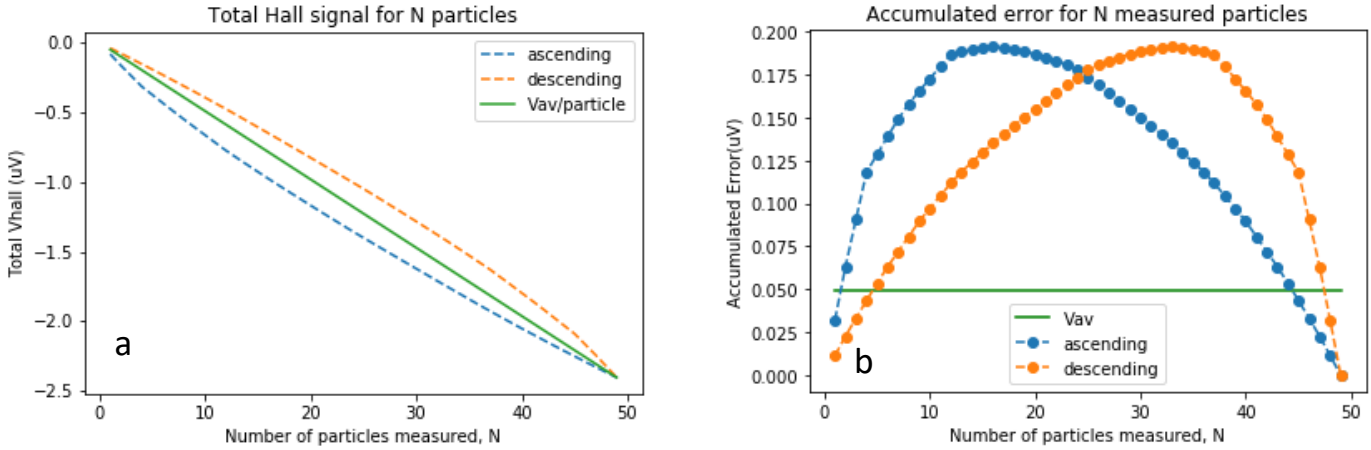

Figure 25: (a) Hall voltage due to N particles, as a function of N. The blue curve shows the single particle signals summed in descending order, and the orange curve in ascending order. The ideal V_{Hall} for N particles is shown in green, if all particles had V_{Hall} equal to V_{av}. (b) Maximum possible accumulated error as a function of N.

By calculating the difference between the ideal total V_{Hall} (NV_{av}) and the V_{Hall} calculated by summing the N largest magnitude Hall voltage signals, we calculated the maximum possible accumulated error due to the worst-case scenario of all N particles landing upon the sensor at positions for which the V_{Hall} signal is greater in magnitude than V_{av}. The absolute value of this accumulated error is shown as the blue curve in Figure 25b. This error initially increases in magnitude with increasing particle number, peaking roughly when one third of the available positions have been filled. As we saw in Figure 24a, there is a distribution of particles with V_{Hall} signals above and below V_{av}. Roughly 30% of V_{Hall} signals are above V_{av} (in magnitude), consistent with the accumulated error peaking when roughly 30% of positions are filled. As more particles are added beyond this point, the single particle V_{Hall} signals included in the sum are less than V_{av} (in magnitude) and the accumulated error starts to drop, falling to zero as all positions are filled.

We may also calculate the maximum accumulated error due to the (other) worst-case scenario of all N particles landing upon the sensor at positions for which the V_{Hall} signal is less than V_{av} (in magnitude). The absolute value of this accumulated error is shown as the orange curve in Figure 25b. Here, when particles are added in descending order, the maximum accumulated error occurs when ~70% of positions are filled, again consistent with the V_{Hall} signal distribution.

We progressed with this analysis by removing from the dataset the particle position for which the V_{Hall} signal was furthest from V_{av}. With the remaining dataset, a new V_{av} was calculated and as before, the single particle V_{Hall} signals were added in ascending order (or descending order – both lead to the same result), and the absolute value of the accumulated error was calculated as a function of N. We assessed whether the accumulated error for any N exceeded V_{av} in magnitude and if so, the process was repeated, removing a new particle position from the dataset at each iteration until no value of N led to an accumulated error larger in magnitude than V_{av}. The results for the remaining particles are shown in Figure 26. The number of particle positions remaining, N_0, in this case is 33 out of a total of 49. We see that the total V_{Hall} curves calculated in ascending and descending order of V_{Hall} are both closer to the NV_{av} line (a) and the accumulated error for this set of 33 particles positions always remain lower in magnitude than V_{av} (b). We conclude that if particles are restricted to landing only at the remaining 33 positions, particles can now be counted with an accuracy of ±1 particle.

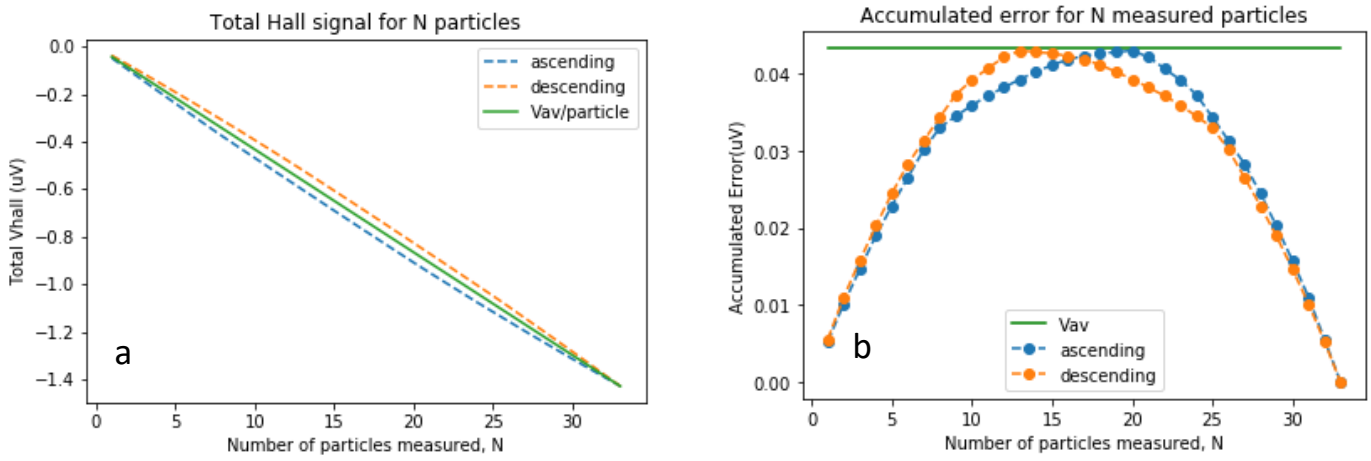

Figure 26: (a) Total Hall signal calculated as single disks are added onto remaining N_0 measurable positions on the sensor in descending (orange curve) and ascending (blue curve) order of V_{Hall}. The perfect case where each particle contributes by the same amout to the total Hall voltage, NV_{av}, is illustrated by the blue line. (b) Corresponding accumulated error versus N. The black horizontal line indicates the average single particle signal from the set.

With the remaining (N_0) 33 positions, we plotted a V_{Hall} map, as shown in Figure 27a. The V_{Hall} results at the positions which were removed from the dataset during analysis were left as blank white boxes. The subset of positions for which the data is presented correspond to the positions at which particles may land. No matter how many other particles land, or in what configuration they land, these particles can be measured to an accuracy of ±1 particle. Positions within this dataset are referred to as 'measurable' (to within error of ±1 particle) and this term of 'measurability' of positions will be used with this meaning in the rest of this thesis. The Hall voltage for both measurable and not measurable positions are shown in Figure 27b as a function of position index, with the measurable positions highlighted in orange, the non-measurable positions highlighted in blue and V_{av} indicated by the dashed green line.

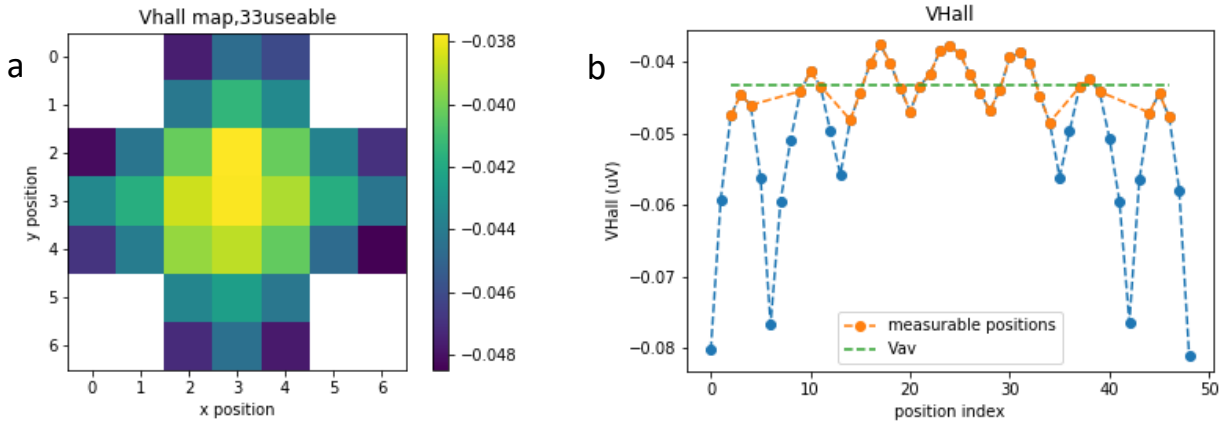

Figure 27: (a) V_{Hall} map of the measurable positions only, calculated using magnetic disks on the continuous Hall cross. The data-set shown here is a subset of the data shown in Figure 23a. Positions that are not measurable were left blank. (b) V_{Hall} versus position index for measurable positions (orange) and non-measurable positions (blue). The green dotted line shows the final average single particle signal V_{av} for the remaining position.

Obvious figures of merit to characterise device performance with regard to homogeneity now emerge: the number of measurable particles N_0 and the ratio of measurable particles with respect to the total number of available positions N_0/N_{total}. Together with the average single particle signal V_{av}, calculated for the measurable positions only, these provide us with a way of assessing the performance of a given sensor geometry. Clearly, device performance is optimised when both parameters are maximised. For our model continuous Hall cross, 33 magnetic disks out of 49 (or 67%) can be measured to ±1 disk accuracy, each with an average signal of -43.3 nV.

We performed the same analysis for magnetic beads, and we find that 35 magnetic beads out of 49 (or 71%) can be measured to ±1 bead accuracy, each with an average signal of -38.8 nV. The corresponding Hall voltage map for the measurable particle positions can be seen in Appendix D. The results for beads and disks on the continuous Hall cross are compiled in Table 3.

Particle type	N_{total}	N_0	N_0/N_{total} (%)	V_{av} (nV)
Magnetic disks	49	33	67.3	-43.3
Magnetic beads	49	35	71.4	-38.8

Table 3: Summary of the main parameters describing the efficiency of the model continuous sensor for magnetic particle counting, including the number of particles measurable to an accuracy of ±1 particle, N_0, the fraction of particle positions which are measurable and the average signal of the measurable particles, V_{av}, for magnetic beads and disks.

3.4 Perforated Hall cross

Figure 28 shows the V_{Hall} response maps for the model perforated sensor (100 µm x 100 µm active area, 7x7 array of 6 µm diameter perforations) to a 6 µm magnetic bead (a) and disk (b) translated across its surface at a working distance of 90 nm. The parameters are the same as those used to generate Figure 22.

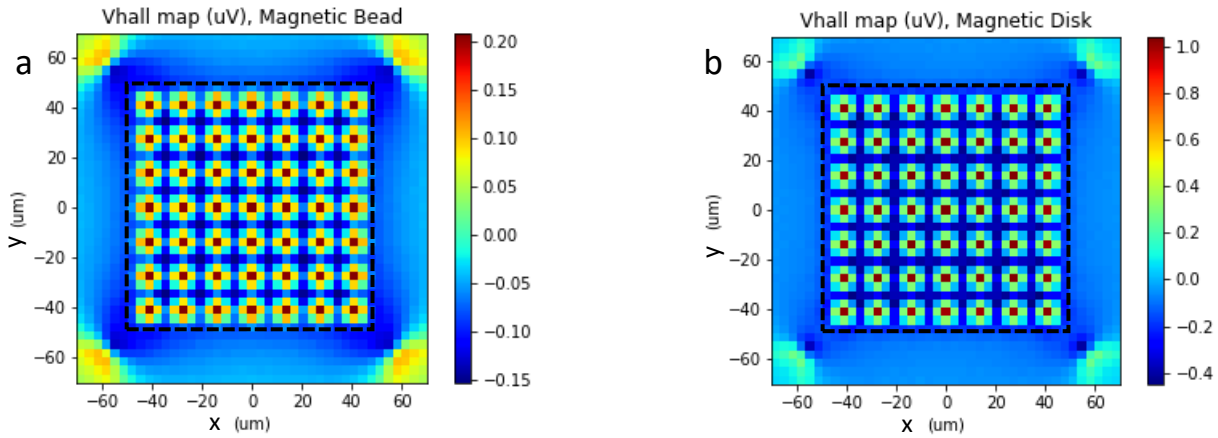

Figure 28: Heat map representing the V_{Hall} response from a magnetic bead (a) and disk (b) placed at different positions 90 nm above the model perforated sensor.

In this case, the signal as a function of position appears even more inhomogeneous than in the continuous case, with a larger range of Hall responses within the active area and even changes in polarity. However, we also notice that at specific subsets of positions, the magnitude of the Hall signal is much larger on the perforated device and appears consistent within these subsets of positions.

Figure 29 shows a close-up of the response map around the central perforation of the cross for (a) the bead and (b) the disk. The Hall response was calculated within a 12 µm x 12 µm area (2D grid of 41x41 points, with 0.3 µm spacing). The largest magnitude Hall response occurs when the magnetic particles are positioned directly above a perforation, with a V_{Hall} of ~1 µV for the disk and ~0.2 µV for the bead. The polarity of this signal is opposite to that produced by the continuous cross and is consistent with a negatively directed stray field. In addition, there is a secondary peak in signal magnitude with a V_{Hall} of ~ -0.4 µV for the disk and ~ -0.1 µV for the bead, which occurs in the 4 corners of the response maps and corresponds to when particles are situated between 4 perforations. In this case, the polarity of the signal is consistent with a positively directed stray field.

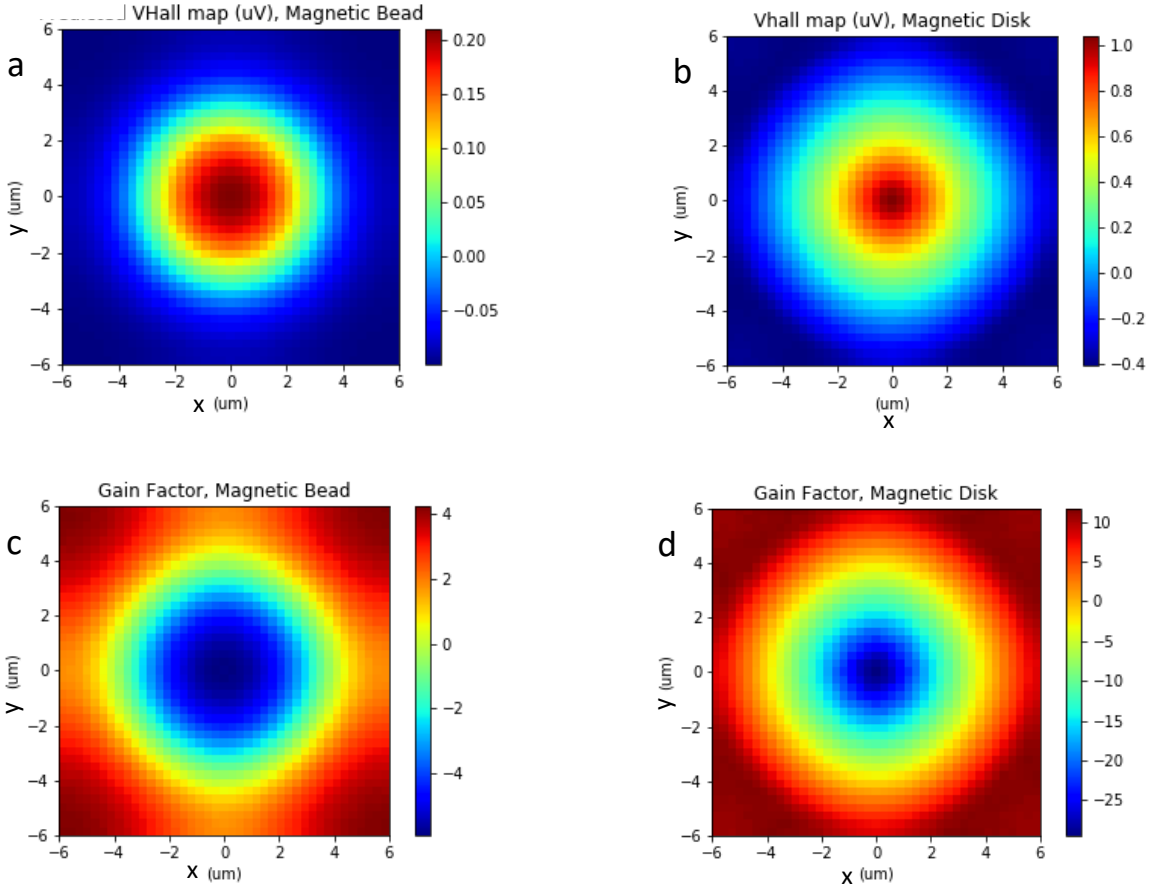

Figure 29: Heat map of V_{Hall} response versus position of a perforated model sensor to a single magnetic (a) bead and (b) disk, within a 12 µm x 12 µm area centred on the central perforation. (c) and (d) show the gain in signal magnitude, calculated as the response maps shown in (a) and (b) divided by the equivalent maps calculated at the continuous cross.

Figure 29 (c) and (d) show the signal gain for the bead and disk, calculated by dividing the response maps shown in (a) and (b) by the equivalent response maps calculated at the continuous device. Here, for the magnetic beads we see a 6-fold gain in signal magnitude when the beads are aligned above a perforation and a 4-fold gain when at the diagonal position between 4 perforations. For the disks, the equivalent gains are a factor of 30 when aligned with the perforations and 10 when at the diagonal positions. For particles landing upon the sensor within these subsets of positions, the gain in signal magnitude is substantial.

The same homogeneity analysis was performed with the perforated sensor as was shown for the continuous Hall cross. We separately considered the two subsets of positions which provide substantive gains in signal strength: when particles are aligned with the perforations and when they are placed diagonally between 4 perforations.

We first calculated the V_{Hall} signal at the 7x7 array of available positions (corresponding to the 7x7 array of perforations) when the particles are aligned with the perforations. This is the situation illustrated in Figure 30b. The results will be compared against those previously calculated on the continuous device with particles placed in the same 7x7 array of positions (see Figure 30a). As described in the case of the continuous sensor, we analysed the Hall voltage maps to assess the number of particles countable to within ±1, i.e., the number of measurable particles N_o, and the average single particle signal, V_{av}.

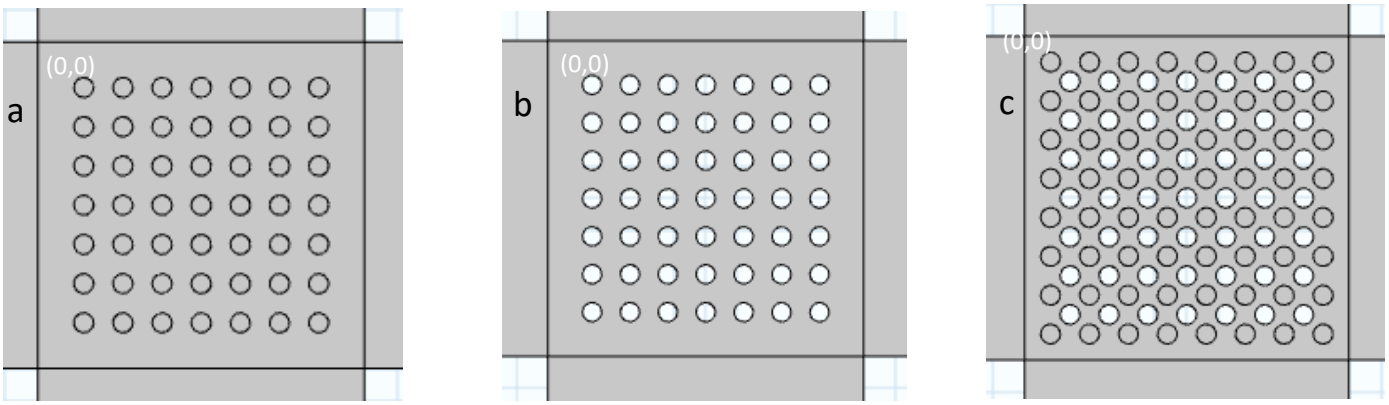

Figure 30: Schematics of the active area of (a) the model continuous Hall cross, with considered particle positions indicated by circles, (b) the model perforated Hall cross and (c) the model perforated Hall cross, with the circles indicating the considered particle positions when investigating particles placed at the diagonal positions between perforations.

Figure *31*a shows the V_{Hall} response map for disks situated at all measurable positions, in this case aligned with the perforations, at a working distance of 90 nm. Figure *31*b displays the accumulated error as a function of particle number N. The total accumulated error is much less than the average signal of one particle, meaning that in this case, all 49 particle positions are measurable, while on the equivalent continuous cross, only 33 positions were measurable. The improvement in signal strength is perhaps even more striking. Here V_{av} is calculated to be 1.02 µV, a factor of 23.5 times larger than that of the equivalent continuous device (-43.3 nV). The simultaneous increase in N_o and V_{av} constitutes a significant enhancement in device capability towards magnetic particle counting.

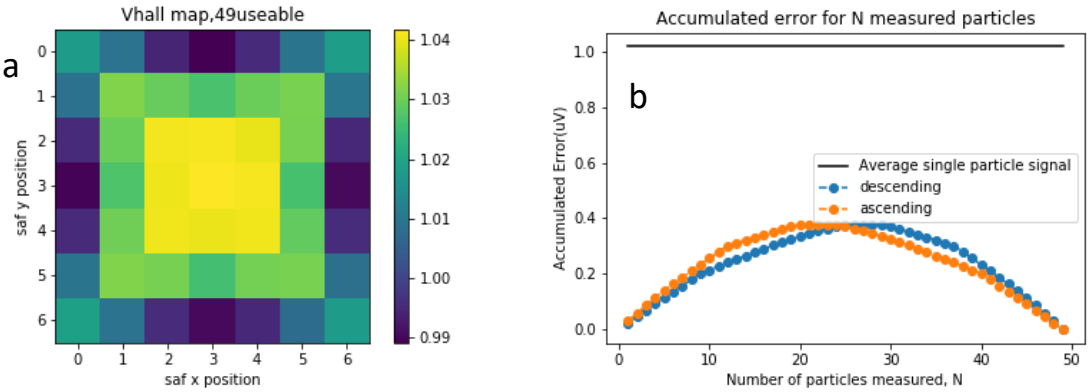

Figure 31*: (a) V_{Hall} map for magnetic disks aligned with perforations at a working distance of 90 nm. (b) Accumulated error versus N. The black horizontal line indicates the average single bead signal from the set.*

It is possible to use the perforations as a method via which to bring the magnetic disks closer to the active layer of the Hall cross. This would involve landing the magnetic disks within the perforations and arranging the depth of the perforations such that the disks could sit with their central plane aligned with the central plane of the 2DEG. In doing so, we expect to increase the stray field of the particle onto the 2DEG and thus the Hall response. We also investigated the response when the disks are positioned with their central plane aligned with the central plane of the 2DEG (we refer to the particles as being embedded within the perforations) and find that the number of measurable particles remains 49 while, as expected, the average single particle signal increases to 1.13 µV, now a factor of 26 times larger than that of the equivalent continuous device.

We also investigated the homogeneity of the signal for the configuration in which the particles are positioned diagonally between the perforations (see Figure 30c). For this configuration, an array of 8x8 available particle positions

was considered, with the outermost ring of particle positions falling outside of the array of perforations. It is worth pointing to the fact that this array of positions is offset compared to when the particles are aligned with the perforations (or where the particles were in the case of the continuous sensor). We find that these outer positions are not measurable, and the number of measurable particles is 36 out of 64. If the homogeneity improvement over the continuous device is only marginal for the diagonal configuration (for the equivalent continuous device with an 8x8 offset array of available positions, 35 are usable) the average single particle signal is now 0.38 μV, a factor of 9.4 times larger than that of the equivalent 8x8 configuration on the continuous device.

We also investigated the case in which an additional ring of perforations was added to the cross to surround the array of 8x8 particle positions considered. The perforations extend beyond the bounds of the active area and thus cannot be added to the four corners without significantly altering the global geometry of the cross. In this case, we find that 57 positions out of 64 are measurable, with an average single particle signal of 0.417 μV, a factor of 10.3 times larger than the continuous device, offering a significant improvement both in terms of homogeneity and signal strength when particles land at the diagonal positions between perforations.

We tabulate all the results for the magnetic disks in Table 4. The Hall voltage response maps and accumulated error figures that were not shown here can be found in Appendix D.

	N_{total}	N_o	V_{av} (μV)
Perforated, 7x7 disks, aligned, 90 nm	49	49	1.02
Perforated, 7x7 disks, embedded	49	49	1.13
Continuous, 7x7 disks, 90 nm	49	33	-0.0433
Perforated, 8x8 disks, 7x7 perforations, diagonal, 90 nm	64	36	0.38
Perforated, 8x8 disks, 9x9 perforations, diagonal, 90 nm	64	57	0.417
Continuous (offset), 8x8 disks, 90 nm	64	35	-0.0404

Table 4: Summary of the main parameters characterising the performance of the perforated and continuous model Hall cross for counting magnetic disks.

We repeated the same analysis for the magnetic beads. The associated Hall voltage maps can be found in Appendix D and a summary of the results is given in Table 5.

	N_{total}	N_o	V_{av} (μV)
Perforated, 7x7 beads, aligned, 90 nm	49	49	0.203
Perforated, 7x7 beads, embedded	49	49	0.574
Continuous, 7x7 beads, 90 nm	49	35	-0.0388
Perforated, 8x8 beads, 7x7 perforations, diagonal, 90 nm	64	36	0.158
Perforated, 8x8 beads, 9x9 perforations, diagonal, 90 nm	64	57	0.174
Continuous (offset), 8x8 beads, 90 nm	64	39	-0.0448

Table 5: Summary of the main parameters characterising the performance of the perforated and continuous model Hall cross for counting magnetic beads.

The impact of the perforations on homogeneity is clearly overall very positive. For the configuration in which the particles are aligned with the perforations, a 50% increase in homogeneity (number of measurable particles) is seen for the disks and 60% for the beads. In the configuration in which the particles are situated diagonally between perforations, when an additional ring of perforations is added, an increase in homogeneity of 40% for the disks and

45% for the beads is seen. Without this additional ring of perforations, the homogeneity is close to equivalent for the perforated and continuous devices with respect to magnetic disks and has worsened for magnetic beads.

In terms of signal strength, however, the improvement brought about by the addition of perforations is a lot clearer. The largest gains are seen for the magnetic disks with a ~23-fold increase in signal for particles aligned with perforations, further increasing to a ~25-fold increase as particles are moved into the perforations to the level of the 2DEG. For the magnetic beads, the gains across the board are more modest. When aligned with the perforation, a 5-fold increase in signal magnitude is seen, however this becomes a 15-fold increase when the beads are embedded within the perforations. Across configurations, the signal and the signal improvement are greatest for the disks, and the configuration in which the particles are embedded within the 2DEG is optimum for both the disk and bead.

The addition of perforations to a Hall cross device improves both the signal magnitude and the signal homogeneity for magnetic disks and beads positioned either aligned with a perforation or diagonally between perforations. For a 6 μm disk at 90 nm working distance, where V_{av} increases from ~ -0.04 μV to ~1 μV with the addition of perforations to the sensor, or for a bead where the signal increases from -0.04 to 0.2 μV, we calculated that such an improvement would be achieved by reducing the size of the active area from 100 μm to ~18-20 μm. With the edge-to-edge distance used here, only one particle would fit in such a sensor, instead of 49.

3.5 Understanding the system

As discussed in section 2.2.2, the Hall voltage response of a 2DEG Hall cross in the diffusive regime to the presence of an inhomogeneous magnetic field profile situated at the centre of the Hall cross has been successfully predicted using an adaptation of the basic Hall voltage formula:

$$V_{Hall} = \frac{I < B_z >}{nqt} \quad (77)$$

where $<B_Z>$ is the value of the magnetic field profile averaged into an effective active area twice the size of the geometric active area, extending into the voltage probe arms of the device. This effective active area accounts for the fact that the current driven in the device spreads into the voltage probe arms upon reaching the cross junction. This results in an average carrier drift velocity within the active area and so corresponding Hall voltage response which is a factor of 2 less than if this current expansion was not possible.

Figure 32a shows the Hall voltage response of the model continuous Hall cross to the presence of a magnetic disk as a function of position, calculated using equation (77) over the same area (140 μm x 140 μm) as the equivalent response map shown in Figure 22b. While the range of V_{Hall} values agree well, the symmetry of the map is clearly not well reproduced by equation (77).

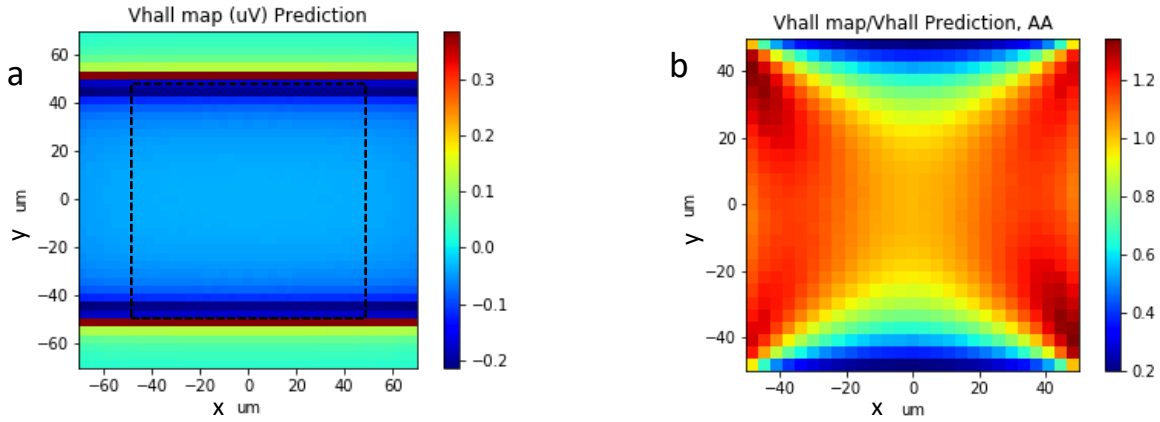

Figure 32: (a) Heat map representing the V_{Hall} response from a magnetic disk placed at different positions 90 nm above the model continuous sensor, calculated using equation (77) with $<B_Z>$ calculated over the effective active area (twice the size of the geoemtric active area which is shown as a dotted black square, and extending in the horizontal direction) (b) Heat map of V_{Hall} calculated with COMSOL divided by V_{Hall} calculated using equation (77).

In Figure 32b, we focus on the active area (100 µm x 100 µm, highlighted by dashed lines in a), showing the V_{Hall} response calculated by COMSOL divided by that predicted by equation (77). We find that equation (77) accurately predicts the response at the centre (within 2%), over-estimates the V_{Hall} response into the current (vertical) probe arms (up to 80%) and underestimates the response into the voltage probe (horizontal) arms (20-30%). The more pronounced disagreement when the disk is translated in the vertical direction is expected to be because the disk more rapidly approaches the boundary of the effective active area used to calculate the average field $<B_Z>$ in this direction, pushing the limits of equation (77). In the horizontal direction, the effective active area extends into the voltage probe arms such that this boundary is much less rapidly approached.

We would like to understand better the other factors responsible for the symmetry of the V_{Hall} response map shown in Figure 22b. To deconvolute the effect of the changing averaged stray field from other factors at play, we calculated the same V_{Hall} response map using the field profile of a 6 µm diameter magnetic dot of the same field strength as the maximum field strength of the 6 µm magnetic disk (4.18 mT). Since the field profile of the magnetic dot does not extend beyond its diameter, the averaged field of the dot into the effective active area $< B_Z>$ is perfectly constant while the dot is fully enclosed inside the effective area, and so is the V_{Hall} response calculated using equation (77). In Figure 33 we show the V_{Hall} response map calculated by COMSOL (a) and this map divided by the V_{Hall} response map predicted by equation (77) (b) within the active area of the cross.

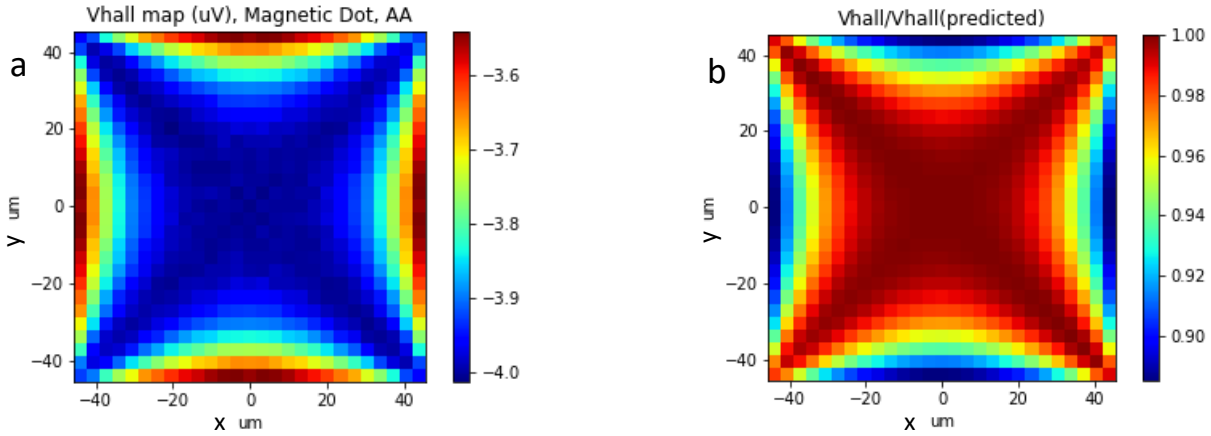

Figure 33: (a) Heat map representing the V_{Hall} response of the model continuous sensor to a magnetic dot of strength 4.18 mT and diameter 6 µm, calculated using COMSOL. (b) Ratio between the COMSOL value of V_{Hall} and the value calculated using equation (77).

The response predicted by COMSOL is not uniform as a function of position. It is highest at the centre and at the corners and decreases in magnitude towards each of the four arms of the cross. The agreement between COMSOL and equation (77) is better for the magnetic dot than it was for the disk, with most positions now showing agreement to within 4%. This suggests that the averaged field plays a central role in defining the V_{Hall} response and that the stronger breakdown in agreement seen for the disk is likely due to its far extending field profile which crosses the boundaries of the effective active area and pushes the limits of the approximation.

However, beyond this, the V_{Hall} response map calculated by COMSOL does have some structure that is not yet explained. In the literature [112] it is suggested that local variations in current density are the central cause of the variations in V_{Hall} as a local, inhomogeneous field profile is translated from the cross centre. Figure 34a shows a map of the y component of the current density, J_y, within the active area of the cross, normalised by the value of J_y at the cross centre and Figure 34b shows line slices through this map along x=0 and y=0 to better illustrate the changes in J_y with position. J_y decreases between the centre and the edge of the voltage probe arms (x) and increases between the centre and the edge of the current probe arms (y), while the V_{Hall} response decreases when the dot moves from the centre along x and y (see Figure 33a). The main features of the COMSOL V_{Hall} response thus cannot be directly explained by local variations in current density.

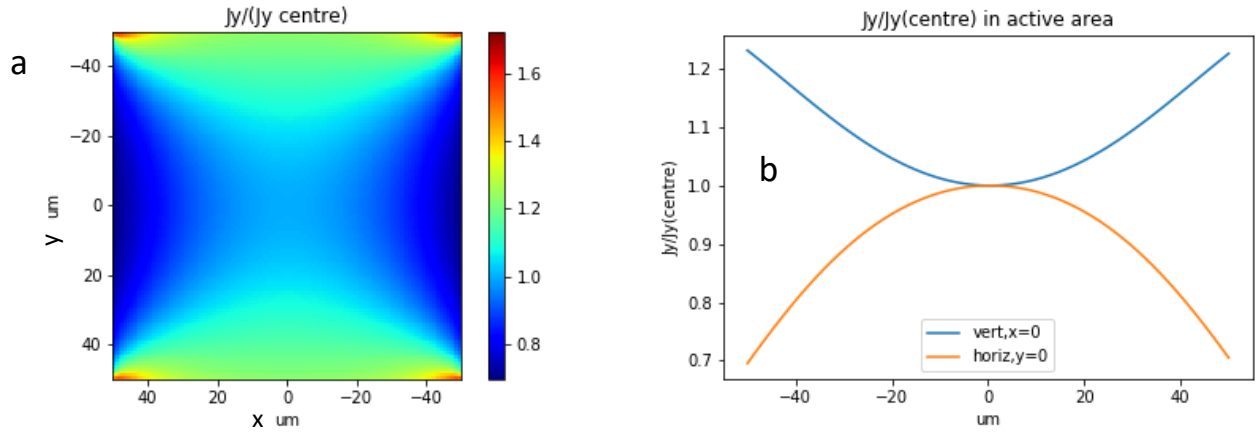

Figure 34: (a) Y component of the current density, J_y, within the cross active area, normalised to its value at the cross centre. (b) Line slices through the map shown in (a), along the vertical (x=0) and horizontal directions (y=0).

However, given the highly localised nature of the Hall voltage response (as discussed in section 2.2.2), it may not be fully measured due to the relative position of the Hall cross voltage probes and the magnetic field dot as it is translated vertically from the cross centre (from position B to A or C, in Figure 35a). To explore this, we calculated the Hall voltage as the difference between the average voltage along the full length of the cross on the left and right sides (green boundaries shown in Figure 35b, as opposed to along the boundaries of the voltage probe contacts only (red boundaries) as has always been done. We present the results in Figure 35b, normalised by the value at the cross centre.

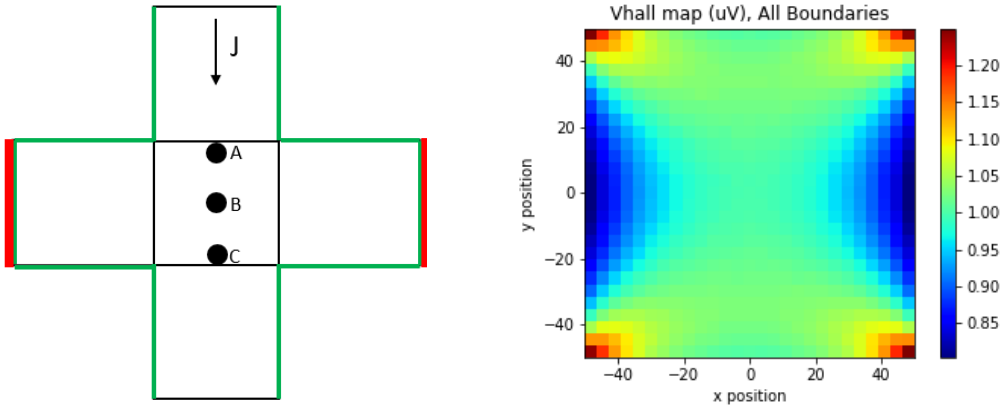

Figure 35: (a) Heat map showing Hall voltage response of the continuous cross to the field profile of a magnetic dot, calculated as the difference between the total voltage along the left side of the cross, minus the total voltage along the right side of the cross. The map has been normalised by the voltage value calculated at the cross centre. The resemblance in form with respect to Figure 34a is striking. (b) Illustration of the boundaries along which the average voltage is calculated, for standard Hall voltage calculation (red) and calculation shown in a (green).

When calculated in this manner, the resemblance between this map and the current density map shown in Figure 34a is striking. We find that as before, the Hall voltage response decreases into the voltage probe arms with decreasing current density. More interestingly, the V_{Hall} response now increases with the increasing current density towards the current probe arms. V_{Hall} also increases in the corners, where the current density is locally enhanced. Thus, while the local variations in current density do not provide an analytical description for the variation in Hall response with position, this is rather compelling evidence that the local current density does have a significant impact on the Hall response.

Given that it was is not possible to analytically describe the signal as a function of position for the simple case of the continuous cross, we do not expect to find an analytical description for the change in signal brought about by the addition of perforations either. However, we have identified the averaged stray field as an important player in defining the Hall response and we hope that equation (77) can be used to qualitatively predict the trends in Hall voltage with position for the perforated cross. To investigate this, we used equation (77) to calculate the Hall voltage response of the model perforated sensor to a 6 µm diameter magnetic bead and disk at a working distance of 90 nm, within the 12 µm x 12 µm area located at centre of the cross. The effective active area into which the particle stray field was averaged was taken to be the same rectangular effective active area used for the continuous cross, minus the areas removed by the perforations. The results are presented in Figure 36 as line slices along the horizontal (y=0), vertical (x=0) and diagonal (x=y) directions through the centre of this area. We display both the results calculated by equation (77) and COMSOL (from Figure 29) and show the results for the bead (a) and disk (b).

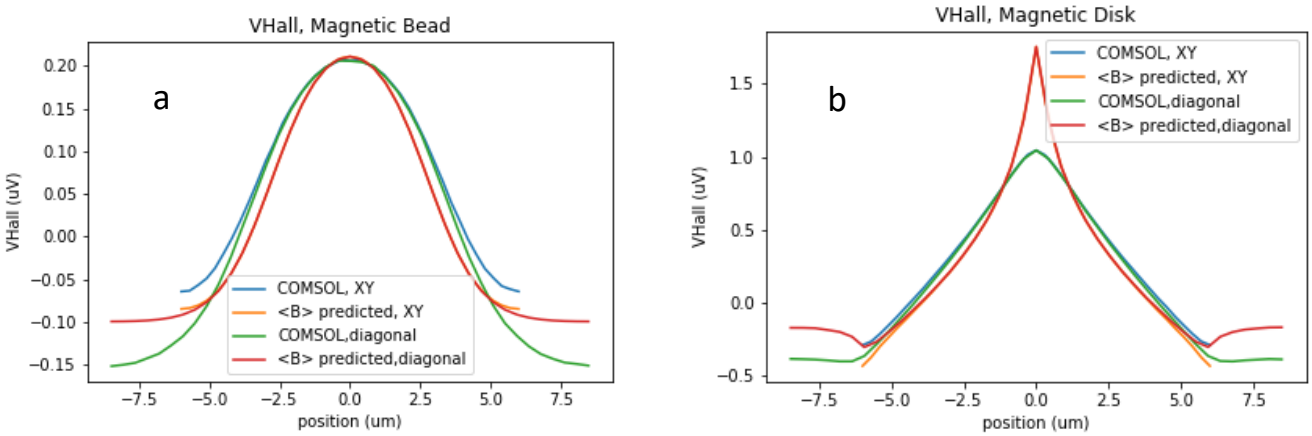

Figure 36: V_{Hall} response around the central perforation of the model perforated Hall cross, calculated by COSMOL and equation (77) along x=y=0 (XY) and x=y (diagonal) for (a) a bead and (b) a disk.

For the magnetic bead, equation (77) predicts the location of the two peaks in signal magnitude – when the bead is located aligned with a perforation and diagonally between 4 perforations. For the disk, equation (77) successfully predicts the peak in signal when the disk is aligned with the perforation but predicts that the secondary peak should occur when the disk is situated laterally between two perforations, with the diagonal position having a marginally smaller signal magnitude. Equation (77) also over-estimates the COMSOL response when the disk is aligned with the perforation and under-estimates when the disk is in the diagonal position.

Figure 37 shows the V_{Hall} response of the model perforated Hall cross to the presence of a bead (a) and a disk (b) in the diagonal position as a function of perforation radius. The V_{Hall} response calculated by COMSOL (blue) and equation (77) (orange) match for a perforation radius of 0 i.e., a continuous cross, as expected. As the perforations increase in radius, agreement clearly becomes worse, however the trend in V_{Hall} with perforation diameter is clearly well reproduced by equation (77).

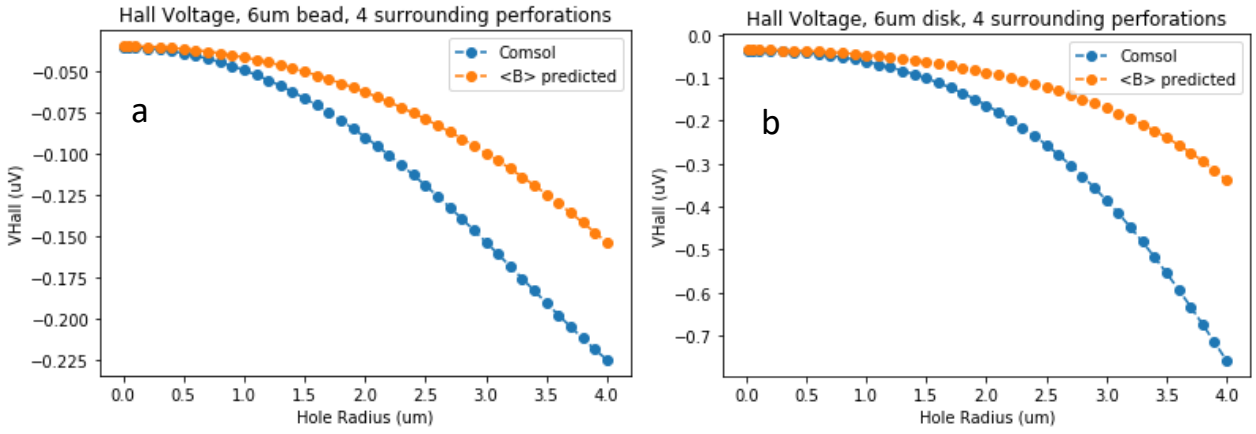

Figure 37: Hall voltage response to a single magnetic bead (a) and disk (b) as a function of perforation radius, for a magnetic particle situated diagonally between 4 perforations.

Figure 38 shows the same when the bead (a) and disk (b) are aligned with the perforation. Once again, the general trends are predicted by equation (77) – with increasing perforation diameter, V_{Hall} initially decreases in magnitude, changes polarity, and then increases in magnitude before reaching a maximum.

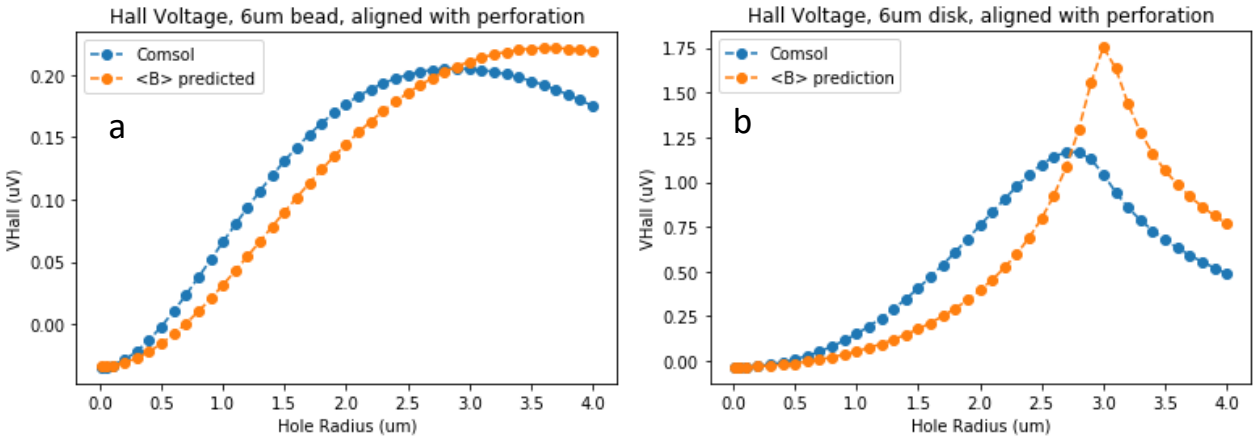

Figure 38: Hall voltage response to a single magnetic bead (a) and disk (b) as a function of perforation radius, for the magnetic particle situated aligned above a perforation.

Whereas equation (77) could reproduce the signal generated by the presence of a particle at the centre of a continuous sensor, the addition of perforations clearly results in equation (77) becoming a less valid approximation. However, we have little reason to assume that the effective active area into which the stray field should be averaged is the same for the perforated cross as for the continuous cross. The effective active area for the continuous device was chosen to account for the fact that the average current density and so average carrier drift velocity within the geometric active area was roughly a factor of 2 less than that pumped into the cross (due to expansion into the voltage probe arms). In Figure *39*, we show the impact of the addition of perforations on the current density distribution within the cross active area as a pixel-by-pixel ratio between the J_y for the perforated device and the J_y for the continuous device. The regions in red have increased by up to a factor of 2.3 as the current impinging upon the active area is squeezed between perforations. The regions in blue have decreased by over a factor of 10 as the current impinging upon the active area is blocked by the perforations.

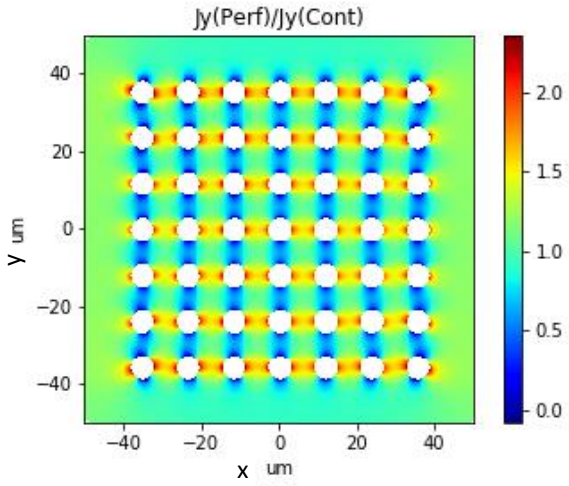

Figure 39: Pixel-by-pixel division of the y-component of the current density map for the perforated sensor by the y-component of the current density map for the continuous sensor, showing the local changes in current density caused by the addition of perforations.

While it is difficult to assess how these changes in current density will impact the Hall response, clearly the average carrier drift velocity within the active area will be altered, suggesting that the relevant effective active area for field averaging will change. In addition, we understand that the Hall response is also a function of the local current density

at the position at which the magnetic particle is situated, which again will take a different value in the perforated device than in the continuous device.

Finally, to investigate the change in signal homogeneity with the addition of perforations, we directly compared the single particle Hall voltage signal as a function of position index for the perforated and continuous devices. As can be seen from Figure 40a, the variations in V_{Hall} with particle position are of comparable magnitude for the continuous and perforated devices. The dashed lines represent the average V_{Hall} signal across all available particle positions, and in b, we show the difference between this average value and the V_{Hall} value at each available position. Here, we may see even more clearly that the magnitude of the V_{Hall} fluctuations about the mean are comparable, and in fact even larger in magnitude for the perforated device, with the standard deviation in V_{Hall} being 0.17 µV and 0.11 µV for the perforated and continuous devices respectively.

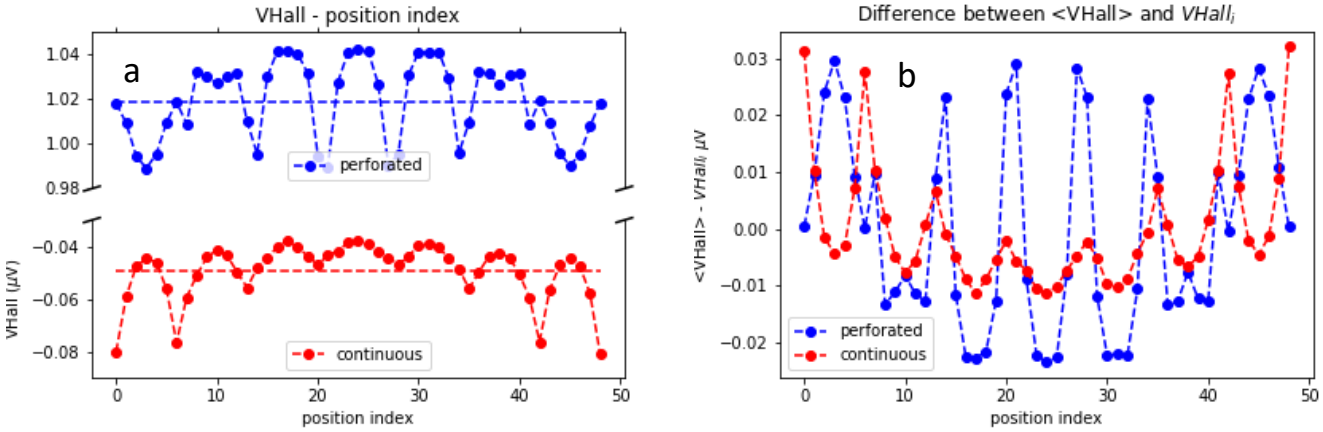

Figure 40: (a) Single particle Hall voltage and (b) difference between the Hall voltage signal as a function of particle position ($V_{Hall\ i}$) and the average Hall signal over all available positions ($<V_{Hall}>$), as a function of position index for the continuous and perforated devices.

However, the fluctuations in Hall signal with particle position are much smaller relative to the average Hall voltage signal in the case of the perforated device. Thus, while the magnitude of the accumulated error for a given number of particles may be comparable for the continuous and perforated devices, relative to the signal of a single particle, the accumulated error will be much smaller in the perforated case. As a result, more particles are required before the accumulated error exceeds the average single particle signal, leading to increased number of measurable particles in the perforated case.

3.6 Device design optimisation

The model Hall cross system has enabled us to demonstrate the improvements offered by the addition of perforations to a large area Hall cross sensor towards the goal of counting magnetic particles. It has allowed us to explore the mechanisms responsible for these improvements and provided an estimate of the Hall voltage signals that can be expected experimentally. However, no optimisation has yet been carried out to test whether the response of the perforated Hall cross can be further improved. Here, we explore variations to the model perforated Hall cross in search of device designs which optimise the magnitude of the single particle signal, V_{av}, in combination with the number of measurable particles, N_o. There is a huge potential parameter space to explore, which we must restrict somehow. This optimisation study is therefore by no means exhaustive, but rather shows the great potential of perforated Hall

devices. Of primary interest in this study is the effect of varied active area size, particle/perforation size and perforation arrangement on the embedded configuration.

While magnetic beads are commercially available and widely accepted by the community, working with magnetic disks offers many advantages for the purposes of a proof of principle experimental device. Firstly, our research group has extensively developed its capability to fabricate magnetic disks with tuneable magnetic properties. Secondly, it is possible to fabricate the disks directly on top of the sensor in any desired arrangement, making direct comparison of experimental and computational results straightforward. Thirdly, the gain factors predicted for the single particle Hall signal of magnetic disks are larger than for the beads while the number of measurable particles is comparable, providing a larger signal. In addition, we have shown that the configuration in which the magnetic disks are aligned with the perforations gives the best performance. We therefore conducted these studies for magnetic disks aligned with the perforations in all cases.

3.6.1 Perforation spacing, number and arrangement

We began our optimisation process by investigating the effect of the perforation spacing. We calculated the V_{Hall} response of the model perforated cross (100 µm x 100 µm active area, 7x7 array of 6 µm perforations with edge-to-edge perforation spacing of 6 µm) to a model 6 µm magnetic disk at a working distance of 90 nm, aligned with the perforations, as a function of edge-to-edge perforation spacing. For a given spacing, we calculated the single particle V_{Hall} response at all available particle positions within the array and analysed the V_{Hall} response maps to extract the number of measurable particles N_0 and the average single particle signal V_{av}. Figure 41 shows V_{av} (a) and the total number of measurable particles N_0 (b) as a function of the perforation spacing.

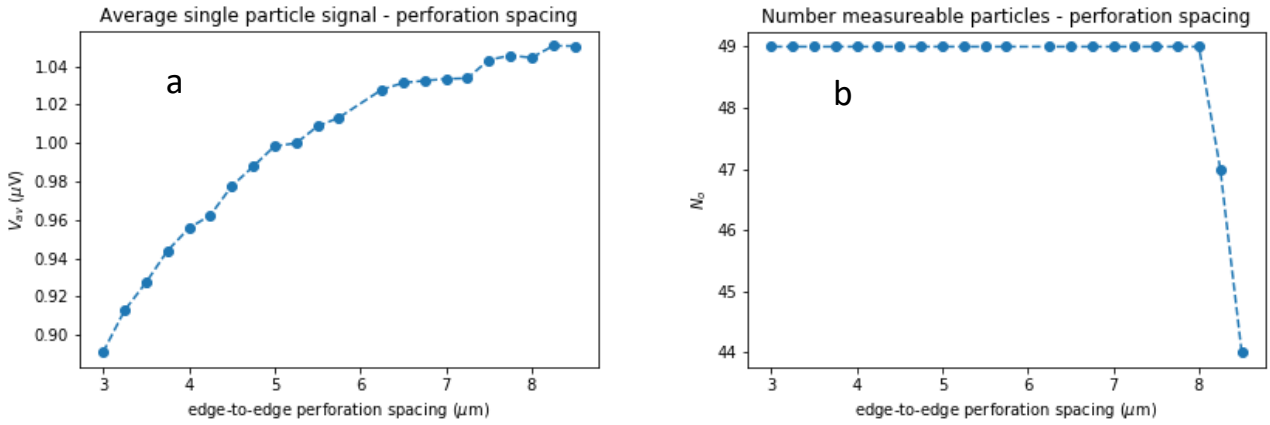

Figure 41: (a) Average single particle signal V_{av} and (b) number of measurable particles N_0 as a function of the edge-to-edge perforation spacing.

We find that there is very little variation in V_{av} or N_o as a function of perforation spacing. The number of measurable particles remains 49 across the majority of investigated spacings, decreasing by at most 10% for the largest spacing considered (perforations overlap with active area boundaries for spacings much beyond this). V_{av} increases marginally with increasing perforation spacing, with a gain in V_{av} of only 4% found for the largest perforation spacing considered relative to the standard spacing of 6 µm. We thus conclude that significant improvements in device performance are not attained by varying the perforation spacing from the standard value of 6 µm, as has been used thus far.

However, as the perforation spacing decreases it becomes possible to fit additional rings of perforations within the active area. To investigate whether the addition of further perforations is beneficial to device performance, we studied the response of devices with increasing numbers of perforations. For each new geometry studied we calculated, as described above, the V_{Hall} response map (to the presence of the model 6 µm magnetic disk at a working distance of 90 nm, aligned with the perforations) as well as V_{av} and N_o.

For the device geometries studied, we set the distance from the active area boundary edge to the edge of the outermost perforation in the array to be 6 µm (one perforation diameter). The perforation edge-edge spacing was then set to the value required to maintain this 6 µm edge boundary while fitting the intended array of perforations, with the constraint that the perforation array must be centrally located within the active area with one perforation present at the centre. This allowed us to simulate Hall cross geometries with perforation arrays of size 7x7, 9x9, 11x11 and 13x13. We also included in this study perforation arrays of size 8x8, 10x10 and 12x12, applying the above criteria however no longer requiring a perforation to align with the active area centre. The results of this study are shown in Figure 42, where (a) shows V_{av} and (b) N_o as a function of edge-edge perforation spacing. Here, the largest spacing of 7.67 µm corresponds to the 7x7 array of perforations, with the smallest spacing of 0.83 µm corresponding to the 13x13 array of perforations.

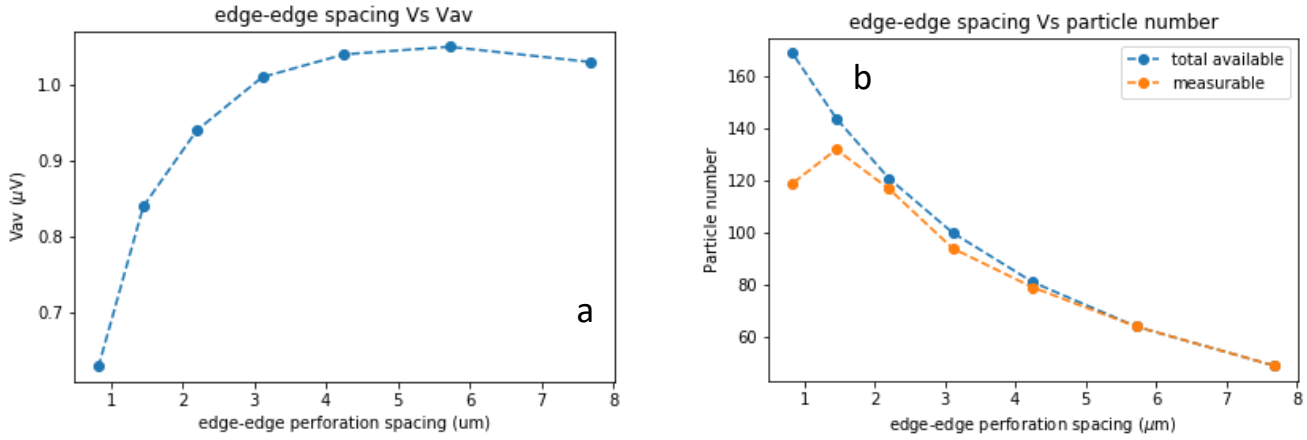

Figure 42: (a) V_{av}, (b) N_0 as a function of edge-to-edge perforation spacing, with the number of perforations increasing as the spacing decreases. Results shown for arrays as large as 13x13 at a spacing of 0.83µm down to 7x7 at a spacing of 7.67 µm.

The variation in V_{av} is reasonably small as the perforation array size increases from 7x7 to 11x11 (varies from 1.03 to 0.94 µV, loss of 9 %), however beyond this, V_{av} begins to drop off significantly (decreases to 0.63 µV, loss of roughly 40% by 13x13 array). Naturally, as the edge-to-edge spacing decreases and the perforation array size increases, the number of available particle positions increases, and we find that the number of measurable positions increases also.

Thus, we conclude that decreasing the edge-to-edge perforation spacing and increasing the number of perforations improves device performance up to a point. Increasing the array size from 7x7 to 11x11 increases the number of measurable particles from 49 to 117 (increase of ~140%) at a minor cost to the average single particle signal (reduction by 9%). For array sizes beyond this, the improvement in the number of measurable particles is minor, while V_{av} begins to drop significantly. Thus, the performance of the model device can be improved, however a balance must be struck between increasing the number of particles the device can measure, while maintaining a high single particle Hall voltage signal.

We also investigated whether the addition of perforations to the arms of the Hall cross offers any improvement. We considered 3 configurations – perforations added to the voltage probe arms only, to the current probe arms only and to both simultaneously. For each configuration we added perforations to the Hall cross one row at a time. For each new geometry, we generated the V_{Hall} response map for the magnetic disks aligned with the central 7x7 array of perforations and analysed the data to extract V_{av} and N_o. We find that N_o remains 49 for all geometries considered, and Figure 43 shows V_{av} as a function of the number of additional rows of perforations normalised by V_{av} for the model perforated cross (no additional perforations in the arms) when perforations are added to the voltage probe arms(a), to the current probe arms (b) and to both (c).

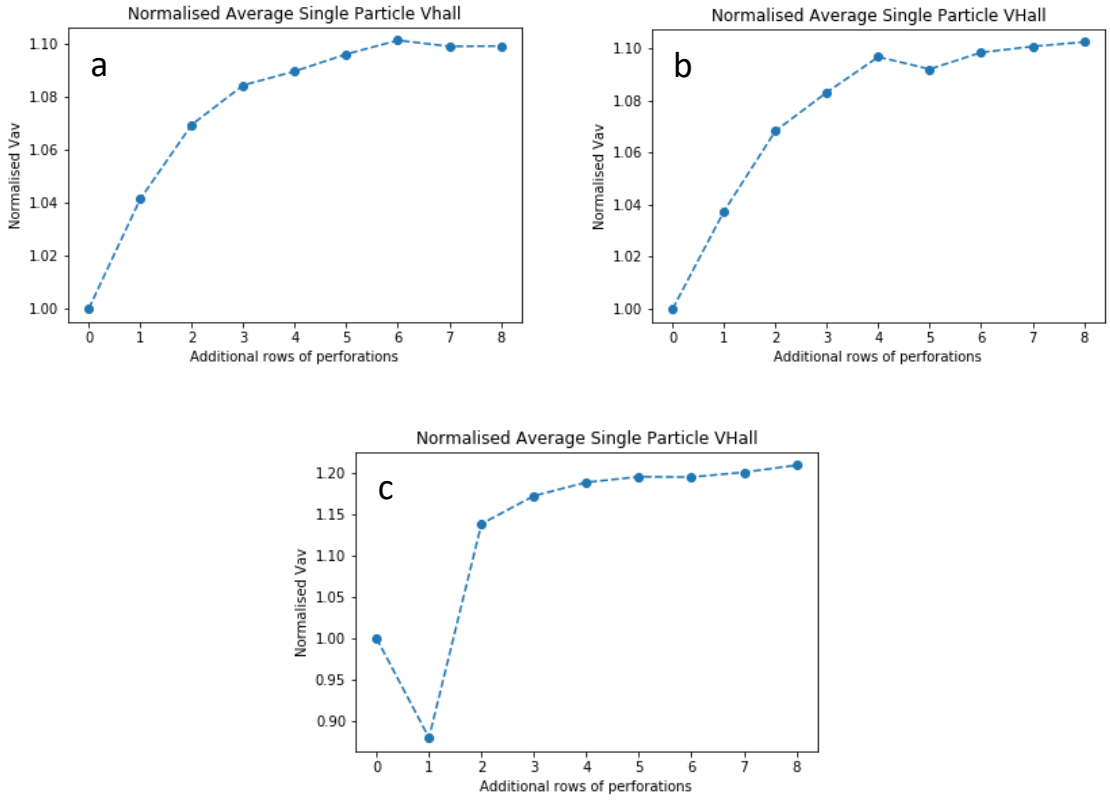

Figure 43: Single particle Hall signal as a function of the number of additional rows of perforations, added to (a) the voltage probe arms, (b) the current probe arms and (c) both, normalised by the Hall single when there are no additional perforations.

For the configurations in which additional perforations were added to the voltage and current probes arms separately, we find an improvement in V_{av} of ~10% by the addition of 8 rows of perforations. The signal increases most rapidly with the addition of the initial rows and appears to saturate by the 8^{th} row. When perforations were added to both the voltage and current probe arms simultaneously, we see an increase in signal magnitude of ~20% when 8 additional rows have been added. The literature [112] has indicated that changes to the geometry of the Hall cross arms can result in changes to the relevant effective active area into which the stray field of a particle should be averaged, and correspondingly the Hall voltage response. Thus, it appears here that the addition of perforations to the Hall cross arms may be altering the relevant effective active area, and as a result, enhancing the signal. This improvement by

20% in single particle signal at no cost to the number of measurable particles offers a significant improvement in device operation.

3.6.2 Perforation/particle diameter for a set active area width

We investigated the effect of varying the particle/perforation diameter on a 100 µm x 100µm active area Hall cross. The perforation spacing was maintained at one particle diameter edge to edge, and a boundary of at least one particle diameter was consistently left between the edge of the perforation array and the edge of the sensor. Within these constraints, as many perforations as possible were fitted within the active area. For each perforation/particle diameter, we calculated the response map for the continuous sensor, perforated sensor with a working distance of 90 nm and the perforated sensor with the particles embedded in the perforations. The results for 6 µm disks are shown in Figure 44, 5 µm disks in Figure 45, 4 µm disks in Figure 46, 3 µm disks in Figure 47 and 2 µm disks in Figure 48. All response maps presented are restricted to the measurable positions.

The symmetry of the Hall voltage maps was exploited to allow us to calculate the upper half of the maps only – see Appendix E for a justification. This became necessary due to the increased computation times with increased particle numbers.

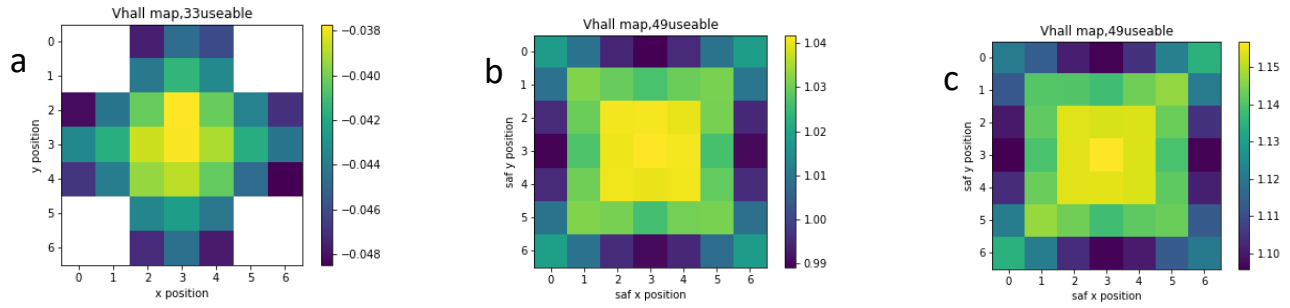

Figure 44: 6 µm disks. Measurable particle array for (a) the continuous sensor, (b) the perforated sensor for disks with a working distance of 90 nm and (c) the perforated sensor with disks embedded in the perforations.

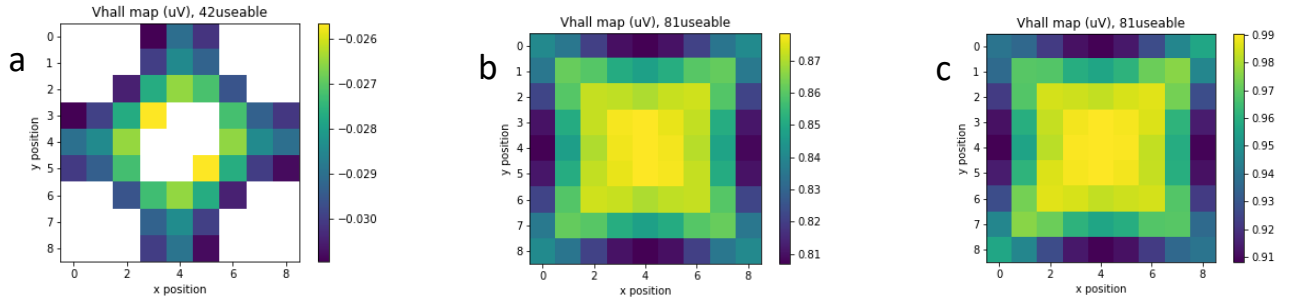

Figure 45: 5 µm disks. Measurable particle array for (a) the continuous sensor, (b) the perforated sensor for disks with a working distance of 90 nm and (c) the perforated sensor with disks embedded in the perforations.

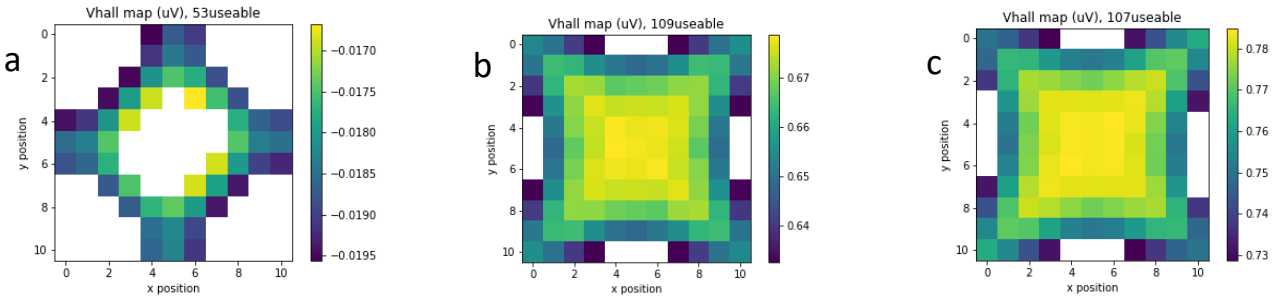

Figure 46: 4 µm disks. Measurable particle array for (a) the continuous sensor, (b) the perforated sensor for disks with a working distance of 90 nm and (c) the perforated sensor with disks embedded in the perforations.

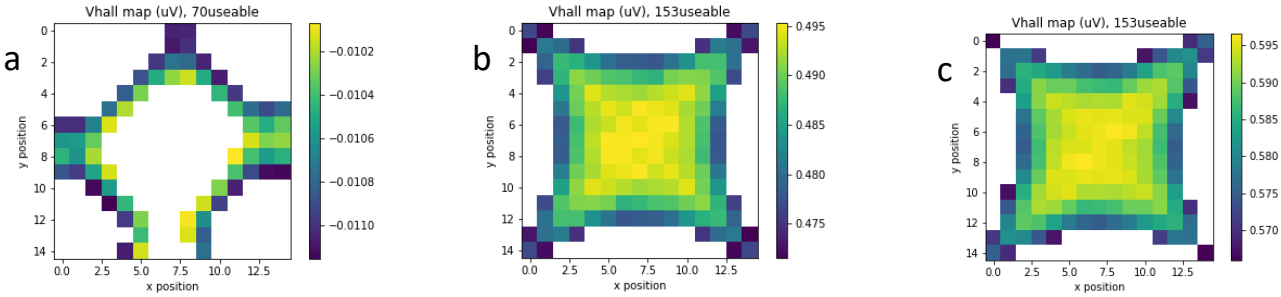

Figure 47: 3 µm disks. Measurable particle array for (a) the continuous sensor, (b) the perforated sensor for disks with a working distance of 90 nm and (c) the perforated sensor with disks embedded in the perforations.

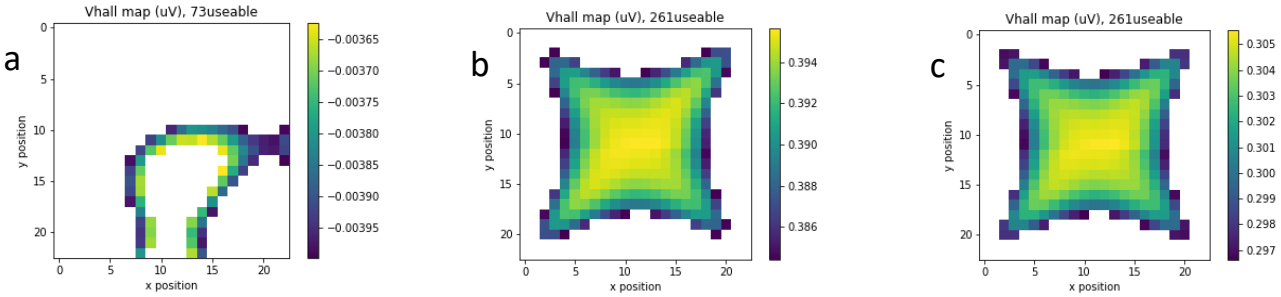

Figure 48: 2 µm disks. Measurable particle array for (a) the continuous sensor, (b) the perforated sensor for disks with a working distance of 90 nm and (c) the perforated sensor with disks embedded in the perforations.

For both perforated Hall crosses with particles at 90 nm and embedded, V_{av} decreases with decreasing particle diameter (see the overall range of V_{Hall} in the maps), as does the fraction of particle positions which are measurable (see the evolution of the ratio of white to coloured pixels). In these two cases, the measurable positions are located within the central area of the cross, with positions towards the edges of the active area becoming increasingly unmeasurable for smaller particle diameters. For the continuous Hall crosses, V_{av} also decreases with decreasing particle diameter and the homogeneity deteriorates much more dramatically. The positions which were found unmeasurable include the corners of the cross as well as the central area.

Figure 49a shows V_{av} as a function of particle/perforation diameter for the continuous and both perforated crosses. In Figure 49b, V_{av} for the perforated device is divided by the same for the continuous device to highlight the gain in signal magnitude brought about by the addition of perforations.

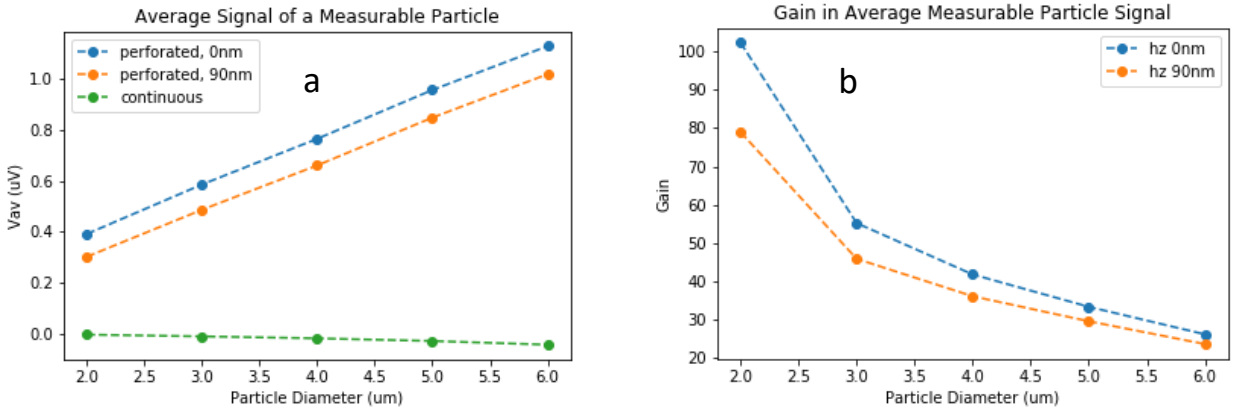

Figure 49: (a) V_{av} for 100 µm x100 µm continuous and perforated devices filled with particles of varying diameters, as a function of the perforation/particle diameter. (b) Gain in V_{av} from the addition of perforations.

As expected, the average signal per particle decreases with the diameter of the particles. However, the gain factor increases dramatically as the particle diameter decreases. The gain of 20-30 that was shown for the 6 µm diameter particles/perforations increases to a factor of 80-100 for the 2 µm particles. The improvements towards magnetic particle counting offered by the addition of perforations to the Hall cross are even more pronounced the smaller the particle/perforation diameter. We also notice that the extent to which the gain factor is further enhanced by taking a particle from the sensor surface to embedded within a perforation increases as particle diameter decreases.

Figure 50a shows the number of measurable particles for the continuous and perforated crosses as a function of particle diameter. The total number of available positions is also plotted for reference. Naturally, as the particle diameter decreases, more particles fit within the 100 µm x 100 µm active area such that the total number of available positions increases. The number of measurable particles generally also increases with decreasing particle diameter, while the fraction of measurable particles decreases, as shown in Figure 50b.

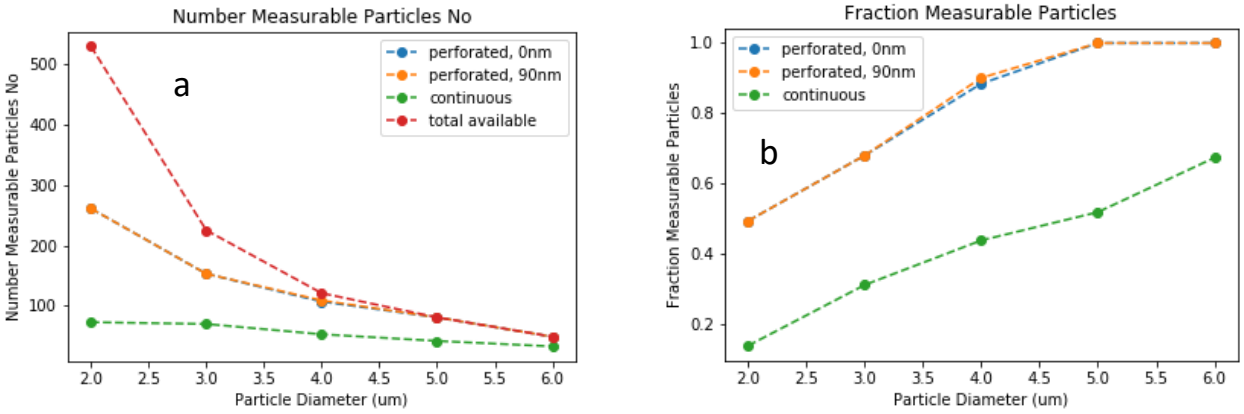

Figure 50: (a) Number and (b) fraction of measurable particles for the model 100um x100um active area continuous and perforated devices, as a function of the perforation/particle diameter.

Although it is promising that the improvements in terms of gain offered by perforating Hall cross devices increase as the particle diameter decreases, it is important to remember that it comes at the expense of the single particle signal, which decreases with decreasing particle size.

3.6.3 Active area width for a set particle/perforation diameter

We investigated the V_{Hall} response of continuous and perforated Hall crosses of varying active area size to arrays of 2, 4 and 6 µm diameter magnetic disks. For each disk diameter, the smallest active area considered was that which just fit a 3x3 array of particles with one particle diameter edge-to-edge spacing and with a boundary between the edge of the outermost perforation and the active area of one diameter. The Hall voltage was calculated for a single disk at all available particle positions and the resulting Hall voltage maps were analysed as in the previous sections to extract V_{av} and N_0. The active area size was increased in steps such that for each new active area considered, an additional ring of particles/perforations was added with the same geometric constraints as for the 3x3 array. Constant current density ($1x10^8$ A/m^2) was maintained across geometries. The symmetry of the Hall voltage maps was exploited to allow us to calculate only the upper half of the response maps (see Appendix E).

Figure 51a shows V_{av} for the continuous and perforated crosses (particles embedded in the perforations indicated by square data markers and at 90 nm working distance indicated by circular data markers) for the 2, 4 and 6 µm disks/perforations as a function of the cross active area width. As expected, for both the continuous and perforated devices, V_{av} decreases dramatically as the active area width increases, with the rate of decay most rapid for the smallest diameter particles. For the continuous device, the single particle Hall signal is found to be directly proportional to the inverse of the active area width squared, while for the perforated device the single particle Hall signal is found to be directly proportional to the inverse of the active area width. In Figure 51b, V_{av} calculated at the perforated sensor is divided V_{av} calculated at the continuous sensor. The gain in V_{av} increases linearly as the active area width increases over most active area widths studied, and the rate of increase of the gain is found to increase as the particle diameter decreases.

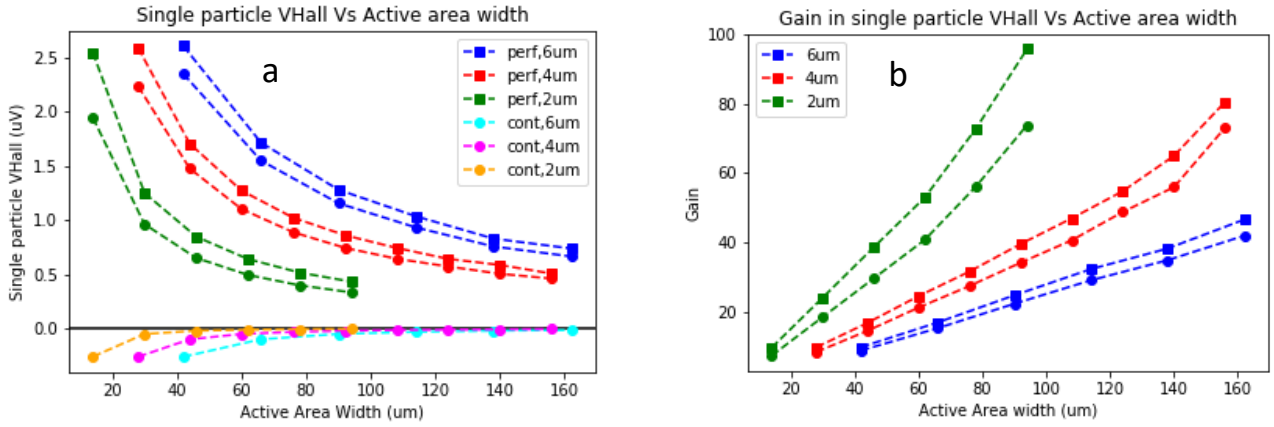

Figure 51: (a) V_{av} as a function of increasing Hall cross active area width for the perforated and continuous crosses with particles of diameter 2,4 and 6 µm. (b) Gain in V_{av} due to addition of perforations. Square symbols correspond to embedded particles, circles correspond to particles at 90 nm working distance.

Figure 52 shows N_0 as a function of active area width for (a) the continuous and (b) the perforated crosses. In (c) we divide the number of measurable particles at the perforated cross by that at the continuous cross to calculate the gain.

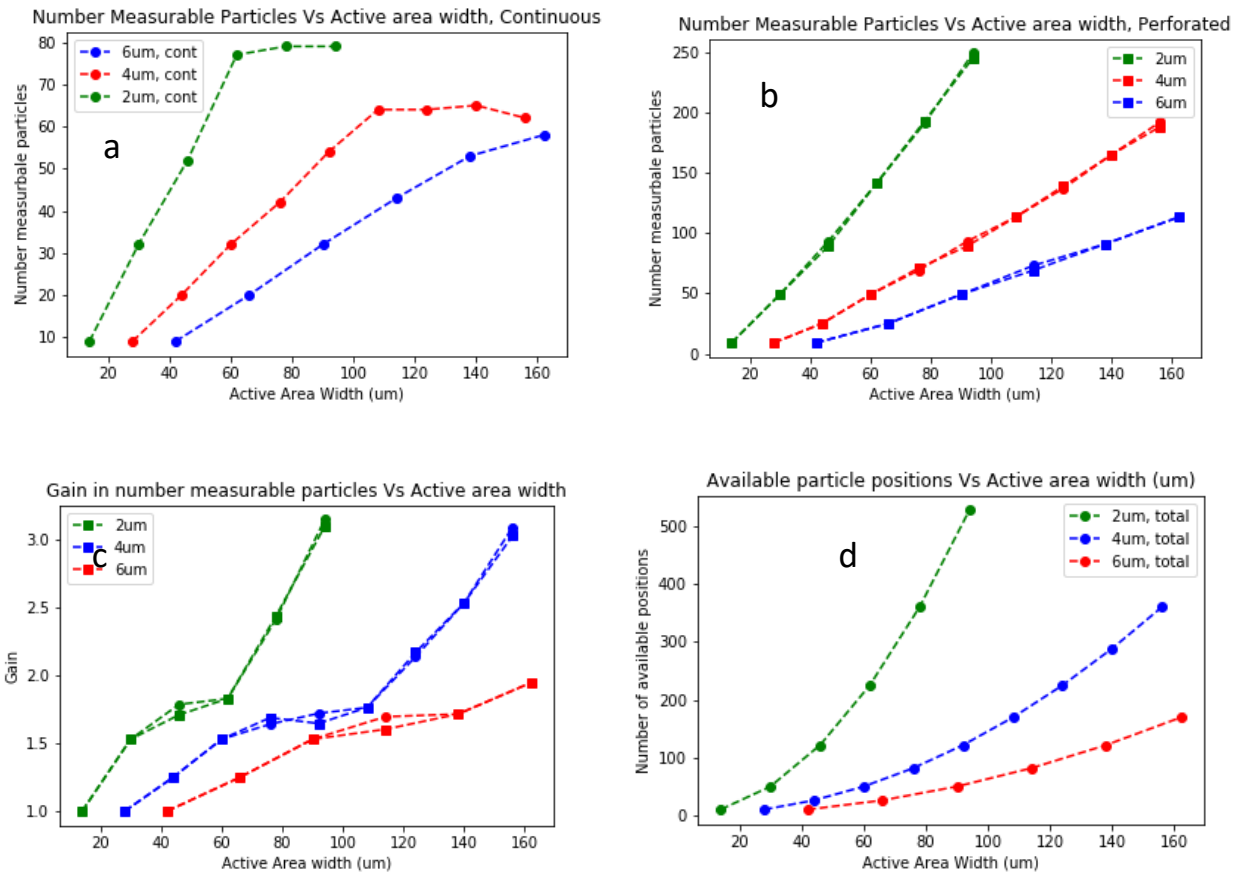

Figure 52: N_0 on (a) continuous and (b) perforated Hall crosses as a function of active area width, for different perforation/particle diameters. (c) Gain in N_0. Square symbols correspond to embedded particles, circles correspond to particles at 90 nm working distance. (d) Total number of available particle postiions.

For the continuous sensor, N_0 first increases with increasing active area width and then saturates, despite the total number of available particle positions continuing to increase, as can be seen from (d). For the perforated crosses, N_0 increases for all active area widths considered. Thus, we see the gain in N_0 with the addition of perforations initially increase gradually with increasing active area width and then increase rapidly when N_0 on the equivalent continuous cross saturates. Once again, we see that for a given active area width, the gain is greatest for the smallest diameter particles.

3.7 Considerations for comparing computational and experimental results

Experimental devices are likely to differ from the ideal devices modelled in our simulations. Firstly, magnetic disks are modelled as having the same diameter as the perforations into which they are embedded. Experimentally, this is not likely to be the case for several reasons. When the perforations are etched into the material, it is likely that this process will damage the 2DEG along the perimeter of the perforation, creating a thin depletion region which will not respond to the magnetic field of the particle. Estimates for the probable thickness of this depletion region are ~25nm[123]. In addition, the magnetic disks will be deposited into the perforations following the deposition of an insulating layer to electrically isolate the 2DEG from the metallic disks. The insulating layer is generally 100-200 nm thick and may coat the inner walls of the perforations. This would effectively narrow the width of the perforations into which the magnetic

layers are deposited, resulting in the diameter of the disks being smaller than the diameter of the perforations. Thus, the perforations may be larger and the disks smaller in diameter in the experimental devices than presently modelled.

To understand the effect this could have on the response of the perforated Hall cross to embedded magnetic disks, we calculated the Hall voltage due to the presence of a single magnetic disk of decreasing radius aligned with the central perforation of the model perforated Hall cross. The radius of the disk was decreased from the ideal size of 3 µm by at maximum 150 nm. We conducted this study for perforations of several radii, from the ideal case of 3 µm (no depletion layer) to 3.1 µm (100 nm depletion layer). The V_{Hall} results are shown in Figure 53a, with the legend referring to the perforation radius. In Figure 53b, we show the same data normalised by the V_{Hall} response when the disk radius is the ideal value of 3 µm in order to highlight the change in signal with decreasing disk radius.

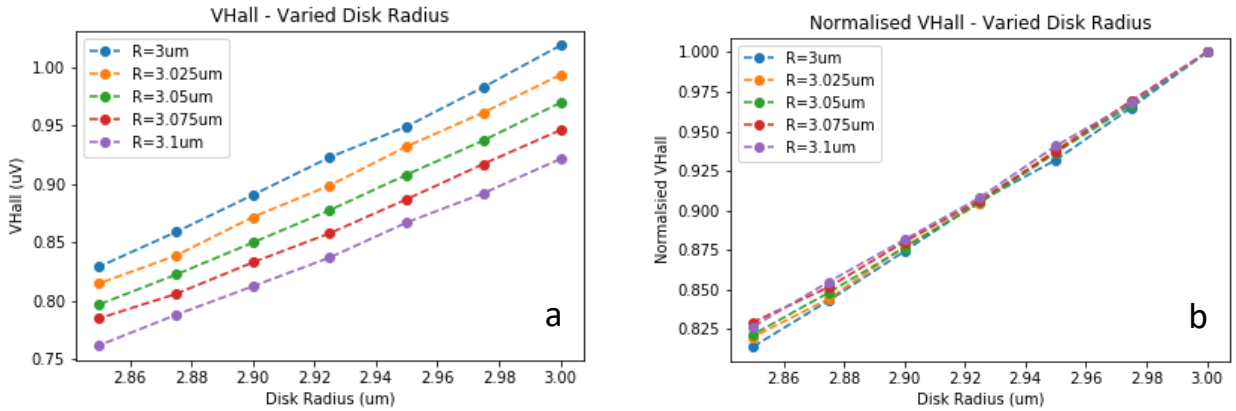

Figure 53: (a) Hall voltage response of the model perforated Hall cross to a single particle embedded within the central perforation, as the disk radius is decreased and for different perforation radii. (b) The same, normalised by the Hall voltage response of a disk with 3 µm diameter.

We see that for all perforation radii, decreasing the radius of the magnetic disk by 150 nm causes a decrease in Hall voltage response of 17.5%. Increasing the radius of the perforation relative to the disk gives at worst (for an increase of 100 nm) a decrease in Hall voltage by 10%. We consider it likely that both effects will occur to some degree in experimental devices, and we note that a non-negligible reduction in the Hall voltage response is possible.

Secondly, our current model does not account for the fact that the experimental devices will not have sharp corners due to lithographic resolution limitations. The corners of the Hall crosses will be rounded, which is likely to perturb the current density and affect the Hall voltage response. We defined a new Hall cross geometry with rounded corners, shown in Figure 54.

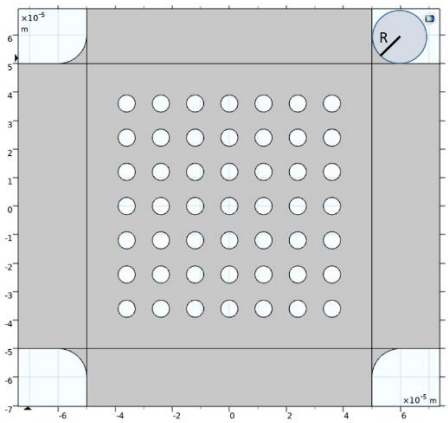

Figure 54: Schematic illustrating the perforated Hall cross geoemtry with rounded corners.

We investigated rounding by up to a radius of 10 µm. For each new geometry, we calculated the V_{Hall} response at all available particle positions for disks aligned with perforations at a working distance of 90 nm and extracted V_{av} and N_0. We saw a maximum a decrease in signal strength of 5% for the 10 µm radius corner and N_0 remained at 49 for all geometries. We conclude that corner rounding has little to no effect on performance of Hall sensors.

3.8 Conclusions

In this computational work, we have demonstrated that the geometry of large area Hall cross devices can be optimised for magnetic particle counting via the addition of an array of perforations to the active area. This geometric alteration results in improved single particle signal as well as homogeneity as a function of particle position. These enhancements are found when magnetic particles land within certain subsets of positions relative to the perforations, with optimum performance demonstrated when particles land aligned with the perforations, followed by diagonally between perforations. Gains in signal strength of over an order of magnitude are shown, with signal homogeneity, characterised by the number of particles deemed measurable to within an error of ±1 particle, increasing by ~50%.

Due to the complexity of the system, an analytical description of these improvements was not found, however the central mechanisms at play were identified. We suggest that the increased average stray field of a particle into the sensor due to the addition of perforations is the central cause for the improvement in signal strength. We find that the variation in the average stray field of the particle into the sensor as a function of position is reduced with the addition of perforations, which we suggest is responsible for the improvement in signal homogeneity.

With the superiority of the perforated Hall cross demonstrated and a basic understanding of the system established, further optimisation of the perforated geometry was carried out. A large parameter space exists which had to be restricted, however the number and arrangement of perforations was explored, as well as the perforation/particle size and the Hall cross active area size. Several modifications were found to further improve performance, including reducing the perforation to perforation spacing such that increased particle numbers could be measured for a given active area size, as well as adding more perforations into the arms of the cross to further enhance the signal strength. Finally, we considered how an experimental device may differ from the ideal devices modelled. To this end, the impact of Hall cross corner rounding due to optical lithography resolution limitations was investigated, as well as the impact of a possible mismatch between perforation and particle diameter when realistic fabrication protocols for the perforations and particles are considered. It was found that the effect of the former was essentially negligible (signal reductions of 5%) while the latter has the potential to significantly impact the response.

4. Experimental Results

The GaAs/AlGaAs wafers used in this work were provided by Dr. Chong Chen of the Semiconductor Physics group at the University of Cambridge. The fabrication of the Hall cross structures and etching of the perforations was conducted by Dr. Georgios Stefanou of the Semiconductor Physics group at the University of Cambridge.

The experiments conducted in this work were designed to prove that the addition of perforations to a Hall cross device offers the improvements towards magnetic particle counting predicted by simulations. To this end, Hall cross devices were designed and fabricated such that on a single device the Hall signal could be measured on a continuous cross with magnetic disks, a perforated cross with embedded magnetic disks, and a continuous, blank (reference) cross. For the purposes of proof of principle experiments, the Hall voltage response, V_{Hall}, due to an array of remanent magnetic particle was measured. Hall gradiometry measurements were also conducted to extract the hysteresis loops of the arrays, providing confirmation that the signal from the remanent measurements was indeed due to the magnetic particles. Magnetic particles of diameter 3, 4 and 6 µm were fabricated and measured, to allow comparison with simulation predictions across a range of particle sizes.

In this section, the various fabrication steps involved in the production of the Hall cross devices are described. The engineering of the magnetic films from which the particles were fabricated is outlined and the magnetic and structural characterisation of the particles is shown. Characterisation of the 2DEG at room temperature is also presented. Focusing initially on a device with 6 µm particles/perforations, the V_{Hall} response of the perforated cross as a function of drive current was collected using the remanent setup, and the method by which the data was analysed is presented. Hall gradiometry measurements were also used to extract the hysteresis loop of the particle arrays. These measurements were also collected for devices with particles of diameter 3 and 4 µm, and the results were compared with simulations. Best agreement is shown for 6 µm magnetic disks (within 32%) and agreement is found to decrease with decreasing particle diameter. Potential explanations for the discrepancy and trend are offered.

The results of the V_{Hall} measurements made at the continuous cross with magnetic particles are also presented. It was initially intended that these results would be compared directly against those of the perforated cross, to demonstrate the predicted improvement in signal, however the results do not match that expected from simulations, most strikingly in terms of polarity. A potential explanation is offered and supported by a combination of COMSOL simulations and experimental measurements. It is hypothesised that the magnetic particles, fabricated directly on top of the GaAs with an underlayer of gold, have resulted in the depletion of carriers from the 2DEG directly below the metallic islands. As a result, the depleted islands act somewhat like perforations, somewhat enhancing the magnitude of the signal and causing the polarity to switch.

4.1 Device Fabrication

4.1.1 Basic Hall cross structure

The GaAs/AlGaAs wafers used in this project were grown using Molecular Beam Epitaxy (MBE) by Dr. Chong Chen of the Semiconductor Physics research group at the University of Cambridge. The structure is

GaAs(2000nm)/AlGaAs(40nm)/GaAs(10nm). The 2DEG occurs starting at a depth of 90 nm and is 25 nm in thickness. The definition of the Hall cross structures in the GaAs/AlGaAs wafer, deposition of ohmic contacts, etching of perforations and spin coating of resist was conducted by Dr. Georgios Stefanou of the Semiconductor Physics research group at the University of Cambridge.

To define the Hall cross devices, roughly 1 µm of the positive photoresist S1813 was spin coated upon the GaAs/AlGaAs wafer. The wafer was exposed to UV light, through the optical mask described in section 2.4.1.1, using a mask aligner. The material intended to form the Hall cross devices remained protected following resist development. Wet chemical etching was then used to etch the exposed GaAs/AlGaAs to a depth of roughly 190 nm, to define the Hall cross devices, and the remaining resist was stripped by soaking the wafer in acetone. To add ohmic electrical contacts, roughly 1 µm of photoresist S1813 was again spin coated on the chip. The associated contact pad design of the optical mask was aligned with the Hall cross devices using a mask aligner, and the areas of resist at which contacts were desired were exposed. Following resist development, GeAuNi was deposited by evaporation and annealed, to ensure electrical contact was made to the 2DEG. For this, AuGeNi was evaporated and lift-off of the GeAuNi deposited upon the resist was carried out by soaking the chip in acetone. The sample was then loaded into a rapid thermal annealer and the chamber was flooded with H_2 (5 %) and N_2 (95 %) for 2 minutes. The sample was annealed to 430°C for 80 seconds (with an intermediate step at 150°C for 30 seconds). With the device structures defined, roughly 1 µm of resist S1813 was again spin coated upon the chip, now ready for the addition of perforations.

4.1.2 Addition of perforations

To perforate the Hall cross devices, a combination of direct write lithography and wet chemical etching was used. The Microwriter ML3 was used to optically expose arrays of circles in the photoresist S1813 coating the chip via direct write optical lithography. The arrays of circles were defined as a layer in the digital optical mask created using the software CleWin. Alignment markers were used to align the software mask with the pattern of Hall bars fabricated on the chip, such that the arrays of circles were exposed at the appropriate positions (centrally located within the selected cross active areas).

The appropriate exposure dose was decided upon by using a test sample with the same resist, spun to the same thickness and exposing and developing arrays of circles using a range of doses. By viewing the developed circles, structures with diameters as close as possible to that requested and with ideal circular shapes were searched for, and the corresponding dose was considered optimum. This led to the selection of a dose of 300 mJ/cm^2, using a 405 nm wavelength laser with 0.6 µm resolution. Following exposure and resist development, circular areas of GaAs/AlGaAs were left unprotected by resist, to be later etched to form perforations.

Arrays of circles of diameter 3, 4 and 6 µm were created and each diameter value was repeated 4 times on the chip, with one device used for calibration of the etch rate. For each diameter value, two of the four corresponding devices were fabricated to have arrays with the maximum number of circles that would fit into the active area (100 µm x 100 µm), with an edge to edge spacing of one diameter and a boundary between the array edge and the active area edge of one diameter. For the 3, 4 and 6 µm diameter circles, this resulted in arrays of 15x15, 11x11 and 7x7 circles, respectively. In addition, for each diameter value, two devices were fabricated with a reduced circle-to-circle spacing,

to fit an additional ring of circles into the active area. Figure 55 shows optical micrographs of (a) the chip as it was received from Dr. Stefanou, as well as developed arrays of circles of each diameter.

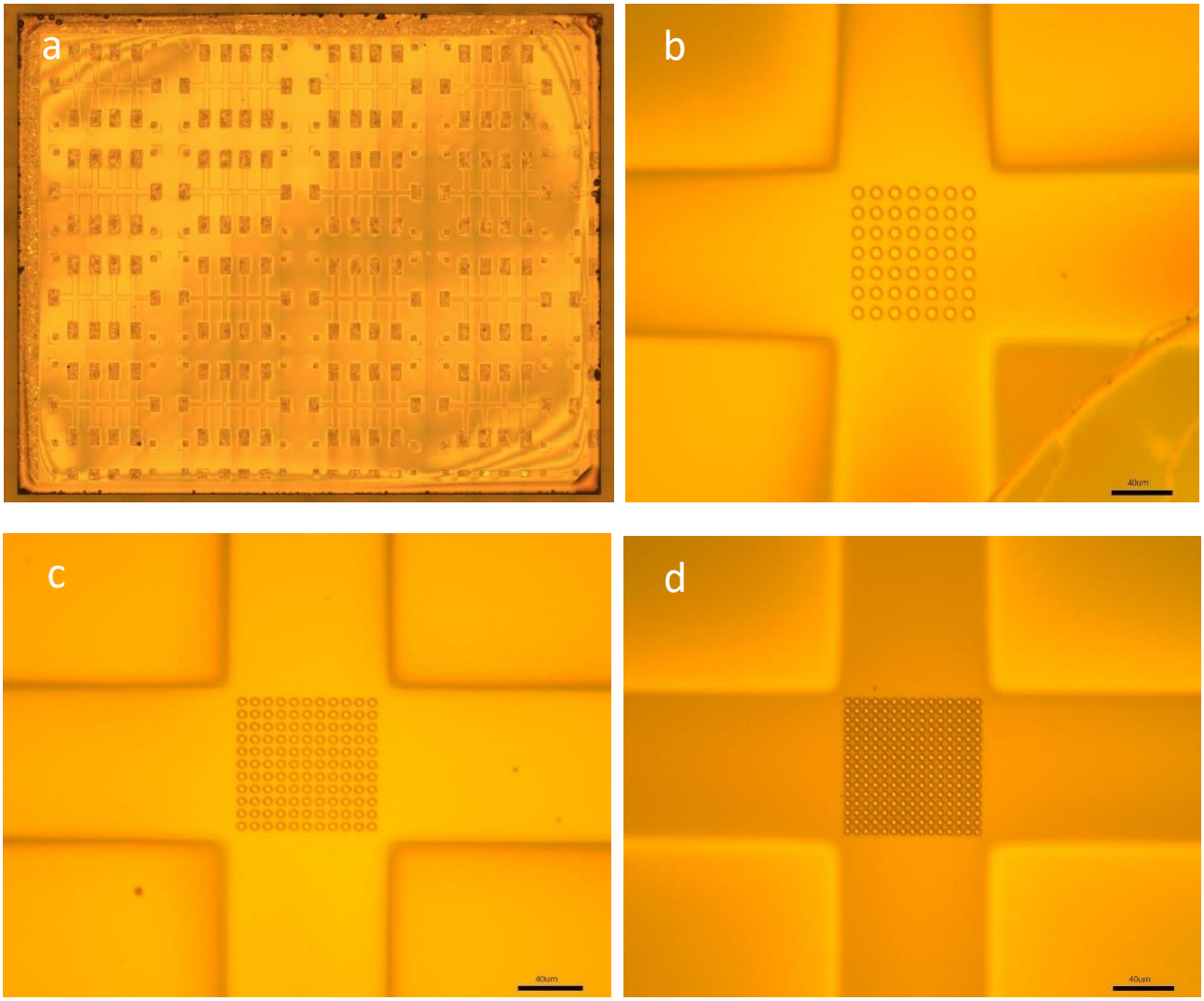

Figure 55: Optical micrographs of (a) the chip as it was received from Dr Stefanou, and following the exposure and development of arrays of circles of diameters (b) 6 μm, (c) 4 μm and (d) 3 μm.

Following exposure and resist development, the perforations in the devices were fabricated via wet chemical etching using sulfuric acid/hydrogen peroxide (H_2SO_4:H_20_2:H_20) in the ratio 1:8:80, as described in section 2.4.1.2. The 2DEG was known to be present below the surface of the GaAs/AlGaAs wafer, starting at a depth of 90 nm and extending an estimated 25 nm to a depth of 115 nm. To ensure that the perforations would extend through the full thickness of the 2DEG, an etch depth of at least 130 nm was aimed for.

The resist present on the chip was required for the following fabrication step in which the magnetic disks were fabricated embedded within the perforations. Thus, it was not possible to strip the resist and verify the depth of the perforations using a more accurate measurement approach than the profile-meter. At the same time however, accurate knowledge of the perforation depth was required to establish the thickness of insulator (SiO_2) which would need to be deposited into the perforations prior to the addition of the magnetic layers. A balance was desired between enough material to electrically isolate the metallic disks from the 2DEG while not increasing the working distance by any more than necessary due to the expected reduction in V_{Hall} signal magnitude with increasing distance.

Due to problems with the department scriber, devices could not be scribed from the main chip to allow resist development on a single sacrificed device and the exact etch depth to be verified directly using AFM before material deposition. Instead, test experiments were conducted to assess the reliability of the etching process on which we would ultimately have to rely for the actual device. Resist was spun on a GaAs/AlGaAs chip using the same well-defined procedure as would be used on the chip containing the devices. Arrays of circles of 6, 4 and 3 μm diameter as well as large (70 μm x 70 μm) squares were exposed in the resist and developed. The resist thickness was estimated using the profile-meter by measuring the depth of the large squares developed in the resist. The chip was then etched, and the etch depths before resist stripping were measured using the profile-meter. The difference between the latter measurements and the previously measured resist thickness was used as an estimate for the etch depth. For the purpose of our tests, the resist was then stripped and the actual etch depth re-measured using AFM. This allowed us to confidently estimate the etched depth on the actual GaAs/AlGaAs chip containing the devices at 160 nm.

4.1.3 Addition of magnetic disks

Arrays of magnetic disks were added to the Hall cross devices. Magnetic disks were chosen as they can be easily produced in-house with tuneable magnetic properties and can be easily fabricated at the desired sizes and positions, enabling direct comparison of experimental results against simulations. Ferromagnetic particles were chosen, as they allow both remanent measurements and Hall gradiometry measurements to be conducted. To produce the arrays of magnetic disks, a magnetic stack was sputtered onto the chip while resist with the desired array of exposed and developed circles was present. This process was used to sputter magnetic particles directly into the etched perforations and onto the surface of continuous crosses.

4.1.3.1 Addition of magnetic disks embedded in perforations

The magnetic stacks used in this work are composed of metallic layers and are thus capable of conducting current. For the purposes of enhancing the V_{Hall} response to the magnetic disks, the distance between the 2DEG and the particle should be minimised. However, it was feared that should the particles be embedded at the level of the 2DEG within the perforations, the drive current of the device may flow through the particles. It was therefore decided that a layer of insulating material would be added to ensure electrical isolation of the perforated 2DEG from the embedded metallic magnetic disks. SiO_2 was chosen as it was available within the facilities of the department.

To maximise the V_{Hall} response of the device to the arrays of magnetic disks, the magnetic properties of the film from which the disks were fabricated were optimised. There are several properties which are of importance, and which can be tuned by careful engineering of the magnetic film structure. These are high remanence, high moment, high anisotropy, sharp magnetic reversal and controllable coercivity. An ideal hysteresis loop for such a film is shown in Figure 56.

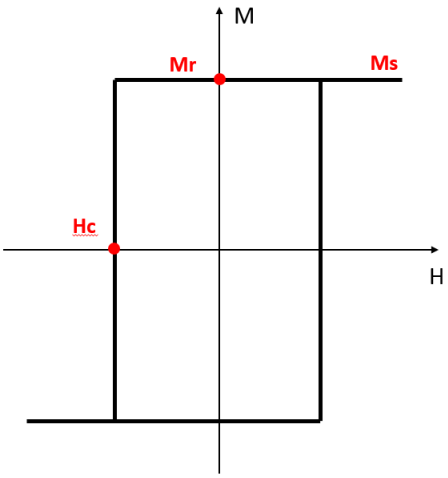

Figure 56: Ideal hysteresis loop of magnetic disks to maximise V_{Hall} response.

The first property is high remanence, to obtain as high a signal as possible during remanent measurements. Full remanence occurs when the magnetic film remains saturated in a magnetising field of zero. Remanence can be quantified by taking the ratio of M_r, the remanent magnetisation, to M_s, the saturation magnetisation, with a ratio of 1 indicating full remanence. M_r and M_s are labelled on the ideal loop of Figure 56. Then, because the magnitude of the stray field of a magnetic disk is directly proportional to the disk's magnetic moment, optimising the moment of the magnetic film from which the disks are made will optimise the V_{Hall} response. The moment can be increased by increasing the saturation magnetisation, M_s, of the magnetic film, or for a given M_s, increasing the magnetic volume of the film. The third important property the magnetic films should possess is a high perpendicular anisotropy. In the devices used for these experiments, the current runs along the central channel of the device and the Hall voltage response is measured perpendicular to the direction of current flow, in the device plane. Thus, for an applied field to create a deflection of charge carriers which results in a Hall voltage, the field must be in the z direction. A strong and perpendicular magnetic anisotropy axis is therefore important for the associated stray field to be fully translated into electron deflection and a measured V_{Hall}. Finally, as long as the magnetic particles are highly remanent, the sharpness of the magnetic switching behaviour is not of primary importance. However, several advantages come with sharp magnetic reversal and controllable coercivity. Firstly, a sharp transition occurring at a known switching field produces a highly recognisable hysteresis loop. The extraction of such a loop from Hall gradiometry measurements can be used to corroborate remanent measurements and give confidence that the V_{Hall} response is indeed due to the magnetic particle arrays. Secondly, to switch the magnetic state of the disks, the switching field must be applied by the EM. In being able to control the field at which switching occurs, it can be ensured that this field can be easily produced by the EM without excessive heating. The sharpness of magnetic reversal can be quantified by the ratio of H_{NUC}, the nucleation field, to H_{SAT}, the saturation field, with a value of 1 indicating ideal, sharp switching. For non-ideal films, the nucleation field is the field at which switching starts to occur, and the saturation field is the field at which the magnetisation saturates.

Films made from the Co/Pt system, and indeed the family which includes Pd and CoFeB, can be engineered to have strong remanence, strong perpendicular magnetic anisotropy and sharp switching. A wealth of knowledge about this system has been built over the years, with investigations focusing primarily on applications in perpendicular magnetic

recording, and much research focused on optimising the system for the same properties as desired in this work [124][125][126].

It is important to understand the magnetic reversal behaviour of Co/Pt thin films to understand how to optimise their design. It has been shown [100] that in Co/Pt films magnetic reversal is nucleation limited. This means that magnetic reversal occurs via the nucleation of reverse domains, and subsequent propagation of these domains through the film. Nucleation sites tend to be defects at which the coercivity is reduced relative to the bulk, and reverse domains occur when it becomes energetically favourable to form a domain wall to reduce the Zeeman energy of the film in a reverse applied field. Domain propagation can occur rapidly when a single or small number of domains nucleate and spread through the film. This reversal behaviour is ideal, as it gives sharp switching and full remanence. Surface and edge roughness can produce pinning sites, at which domains become trapped. The result is a smoother magnetic transition and a higher H_C due to the pinning sites slowing domain propagation.

The magnetic reversal behaviour of Co/Pt films changes with the volume and arrangement of magnetic material. If a high moment is desired, the volume of Co can be increased to increase the moment of the film, and this can be done both by increasing the volume within a single Co/Pt layer, and/or by adding multiple repeats of this motif to the film. To maintain strong PMA, the thickness of Co within a single motif is limited. On the lower end, the percolation limit defines the thickness at which the film is too thin to make a continuous layer. On the upper end, the thickness of a single layer is limited by the onset of the spin reorientation transition (SRT). At this thickness, the interface anisotropy is no longer larger than the shape anisotropy, and in plane magnetisation becomes energetically favoured, resulting in a loss of PMA [98].

This upper limit applies to a single Co/Pt layer, however multilayers composed of multiple repeats can be formed. Here, the different magnetic layers are ferromagnetically coupled, resulting in sharp and collective switching. This occurs because Co/Pt multilayers exhibit an oscillatory interlayer coupling, which changes with Pt thickness but is always ferromagnetic [127]. While the total magnetic volume is increased with increasing numbers of repeats, each layer still has a ratio of interface to volume anisotropy that favours PMA. The number of repeats is still limited however, as increasing the magnetic volume increases the total demagnetising energy of the film. As repeats are added, the energy of the multilayer can be reduced via the formation of stripe domains. Magnetisation reversal begins to occur via the formation, propagation and annihilation of these stripe domains. This results in decreased nucleation fields and slanted reversal. Thus, to maintain ideal magnetic reversal behaviour (full remanence and sharp switching), the volume of magnetic material (and so magnetic moment) of the film is limited, and compromises must be found.

Within the Cowburn group, Dr. Mike Stanton extensively investigated CoFeB/Pt films for use in the production of magnetic particles for magnetic self-assembly in fluids. In his PhD thesis [128], Dr Stanton optimised the magnetic stack towards the same properties as are sought in this work. For our purposes, films must be grown on SiO_2, and the fabrication techniques used to produce particles from films differ, however Dr Stanton's thesis offers a great starting point for our optimisation.

He began by optimising the moment of a single CoFeB/Pt repeat by increasing the thickness of CoFeB, finding the upper SRT limit to occur at 1.6 nm. All films were grown on a Ta buffer layer and Pt seed layer, in which the low

thickness of Ta ensures it remains amorphous and promotes the growth of 111 Pt, which maximises the PMA of the film. He went on to construct multi-layers, with the aim of creating a film with more than 1.6 nm of CoFeB. He found from the literature [127], [100] that 5x repeat multilayers give the best compromise between maximum total CoFeB thickness and an ideal square hysteresis loop. Using this as a starting point, he produced 5x repeat multilayers, with different thicknesses of CoFeB within the individual layers. He found that the maximum moment, strongest PMA and sharpest switching occurred for 5x repeat of 0.5 nm to 0.6 nm CoFeB. For thicknesses beyond this, the switching behaviour was seen to change from sharp and nucleation limited, towards the formation and propagation of stripe domains.

We used the findings of Dr. Stanton as our starting point. Films were deposited on Si chips, as well as Si chips coated with roughly 100 nm of e-beam evaporated SiO_2. All films investigated had an underlayer of Ta (2 nm), followed by Pt (6 nm). A reasonably tight parameter space was investigated, centred around the [CoFeB(0.5-0.6nm)/Pt(0.855nm)]x5 recipe, shown to have the most ideal properties. Films in which the number of CoFeB/Pt repeats was varied were produced, with a CoFeB thickness primarily of 0.5 nm. Polar MOKE was used to measure the easy axis hysteresis loops of these films, as presented in Figure 57. The blue curves represent the MOKE data collected for the films deposited on Si, with the orange showing the same for the films deposited on Si + SiO_2. Both films were grown by magnetron sputtering during the same sputtering run, so any change in the magnetic behaviour can be attributed to the presence or absence of the SiO_2 underlayer.

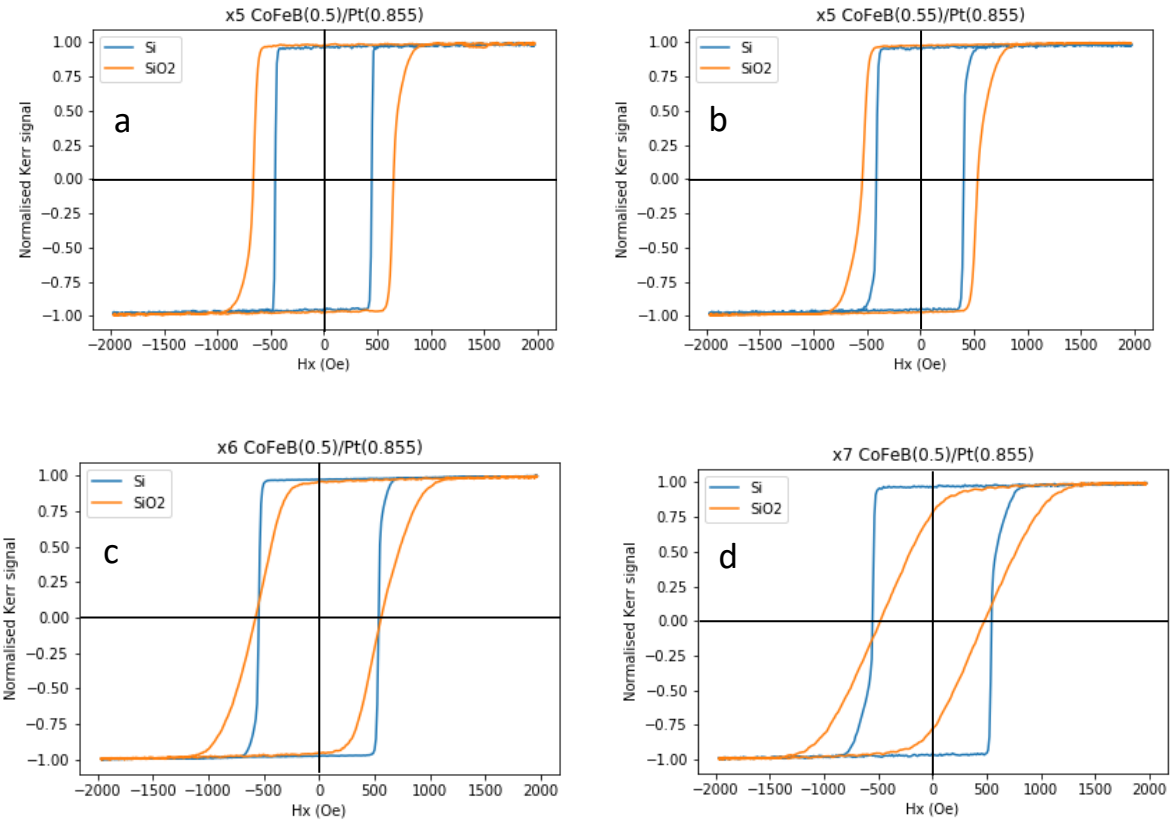

Figure 57: Polar MOKE easy axis hysteresis loops for magnetic films composed of [CoFeB/Pt] repeats, deposited on silicon chips and silicon chips with a 100 nm underlayer of e-beam evaporated SiO_2. Study centres on [CoFeB(0.55nm)/Pt(0.855nm)]x5 recipe, optimised by Dr. Stanton.

As the volume of magnetic material increases (from a to d in Figure 57), the switching behaviour of the film is clearly altered. These changes are reasonably minor for samples grown on Si and follow trends reported in the literature[100].

Magnetic reversal moves from nucleation limited towards stripe domain formation, indicated by the slanted switching which begins to emerge. However, full remanence is maintained for all samples. For the films grown on SiO_2, the underlayer clearly has a substantial effect on the switching behaviour. As the magnetic volume increases, full remanence is lost, the nucleation field is drastically decreased and switching sharpness is strongly reduced. The behaviour is likely due to the impact of the roughness of SiO_2. Slanted reversal generally comes about because of high pinning, suggesting that the rough SiO_2 likely introduces many pinning sites when used as an underlayer. The loss of full remanence and reduction in nucleation field can also be explained by increased numbers of defects, giving rise to many nucleation sites with a large spread in nucleation field.

SiO_2 clearly negatively impacts the magnetic behaviour of the CoFeB/Pt films, in particular as the volume of magnetic material is increased. The film we decided to use is:

Ta(2nm)/Pt(6nm)/[CoFeB(0.55nm)/Pt(0.855nm)]x4/CoFeB(0.55nm)/Pt(3nm)

of Figure 57(b). This magnetic film has a total thickness of CoFeB of 2.75 nm and total thickness overall of 17.2 nm. While the film stack with 5 repeats of 0.6 nm CoFeB is also fully remanent and contains a larger volume of magnetic material than the selected film stack, it was considered too close to losing remanence.

Following the first round of lithography and etching, magnetic particles were fabricated in the perforations. The expected perforation depth was 160 nm (see section 4.1.2), with the 2DEG expected to extend from 90 nm to 115 nm below the surface of the GaAs/AlGaAs. It was decided that 30 nm of insulating material should be placed between the upper surface of the 2DEG (90 nm) and the lower surface of the deposited magnetic particles, to ensure electrical isolation. Thus, the perforations needed to be filled by insulating material to bring the perforation depth from 160 nm to 60 nm, a thickness of 100 nm of SiO_2 in total. The magnetic disks would then be deposited, beginning at 60 nm below the surface of the GaAs/AlGaAs (or 30 nm above the top surface of the 2DEG), and extending 17 nm. This would mean that following the addition of the SiO_2 and magnetic disks, the perforations should be measured to have a depth of 43 nm.

The resist used for etching was left intact on the chip and SiO_2 was deposited via e-beam evaporation. This deposition was followed by magnetron sputtering of the magnetic stack. The chip was then soaked in acetone for 15 minutes and then sonicated for 5-10 seconds, to lift off the magnetic film and SiO_2 deposited outside the bounds of the perforations.

4.1.3.1.1 Structural characterisation

Structural characterisation of the deposited magnetic particles was carried out using SEM and AFM. SEM images enabled us to visually inspect the quality of the fabrication, while AFM was used to measure the topography of the device surface, providing information on the relative position of the particles and 2DEG.

SEM images of the magnetic disks formed within the perforations are shown for perforation/particle diameters of 3 (Figure 58), 4 (Figure 59) and 6 µm (Figure 60). In each case, (a) shows a large-scale image and (b) shows a close-up.

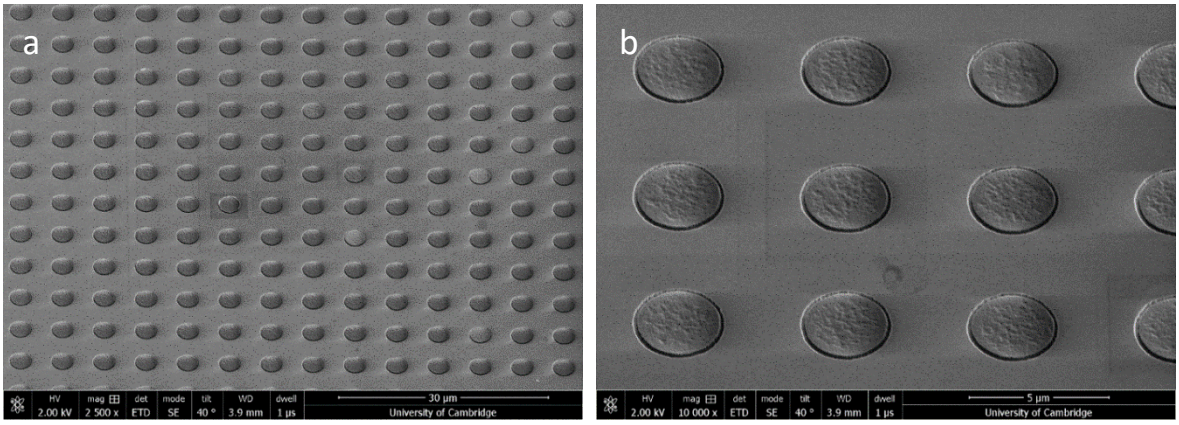

Figure 58: SEM image of 3 µm diameter magnetic disks fabricated in perforations.

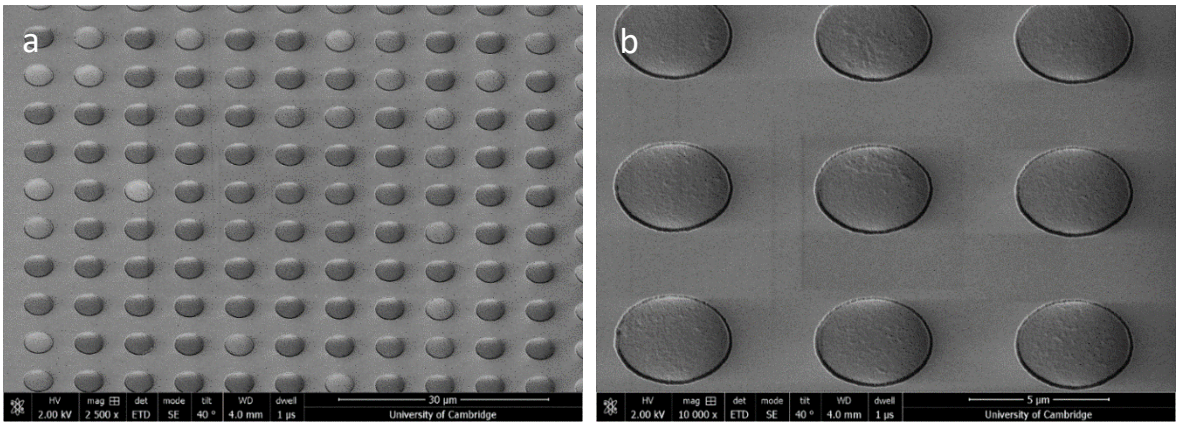

Figure 59: SEM image of 4 µm diameter magnetic disks fabricated in perforations.

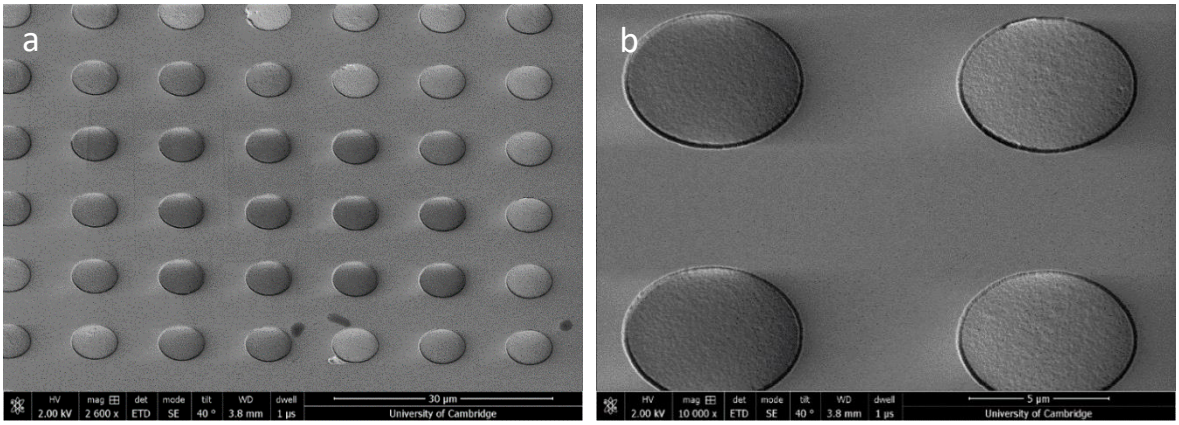

Figure 60: SEM image of 6 µm diameter magnetic disks fabricated in perforations.

We see that for all particle/perforation diameters, the circular shape has been well produced. The images are used to extract the particle diameters, and the average values, calculated over several images for each diameter, are presented in Table 6. As can be seen from this table, the measured sizes match well with the intended sizes.

Intended Size (µm)	3	4	6
SEM measured size (µm)	2.9 ± 0.1	4.0 ± 0.1	6.1 ± 0.1

Table 6: Diameter of the magnetic disks deposited within the perforations, intended and as measured from SEM images.

SEM images were also acquired following each fabrication step, enabling us to identify potential problems in the fabrication process. SEM images following the deposition of SiO_2 revealed issues with its deposition. It was found that for several devices, the SiO_2 deposited was highly non-uniform and textured, as shown in Figure 61a, b and c, which would likely negatively impact the magnetic properties of the particles grown directly on top. This did not occur in

such a pronounced way on all devices of the chip, and care was taken to conduct Hall voltage measurements using devices for which the SiO_2 deposition appeared most uniform.

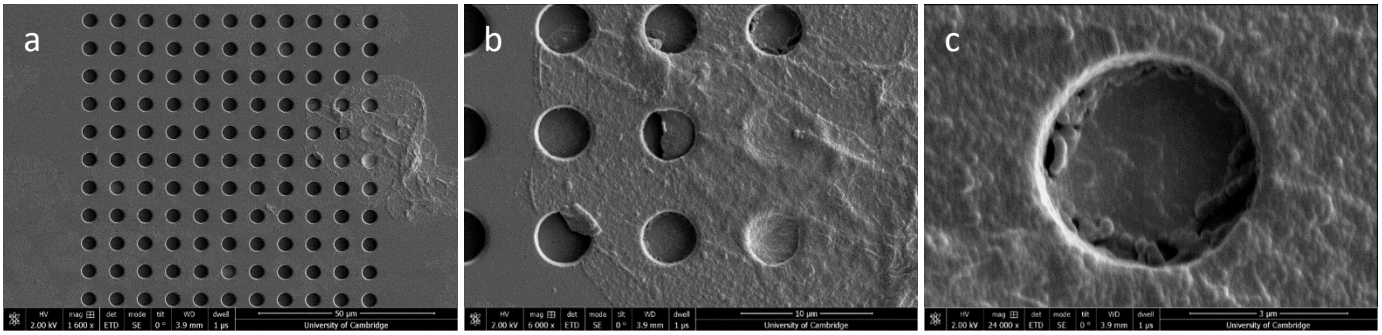

Figure 61: SEM images of an array of perforations onto which SiO_2 and magnetic stack were deposited. Images post metallisation presented for image clarity, however images pre metallisation were also taken and the same was seen. SiO_2 evaporated non-uniformly, with thick and rough areas forming across the chip. A wide field image of entire array is shown in (a), and zoomed images in (b) and (c).

In Figure 62, SEM images following the completion of all fabrication steps for the 6 µm particles are shown. Here, skirts of material can be seen around the particle edges. While sonication successfully removed these skirts for most particles, the thickness can be estimated from these images as ~150 nm. Since only ~17 nm of magnetic material is deposited, this suggests that the deposited SiO_2 must coat the inner walls of the perforations to form these structures. The magnetic material deposited on top will thus be deposited into a perforation with a physical radius smaller by roughly 150 nm than intended.

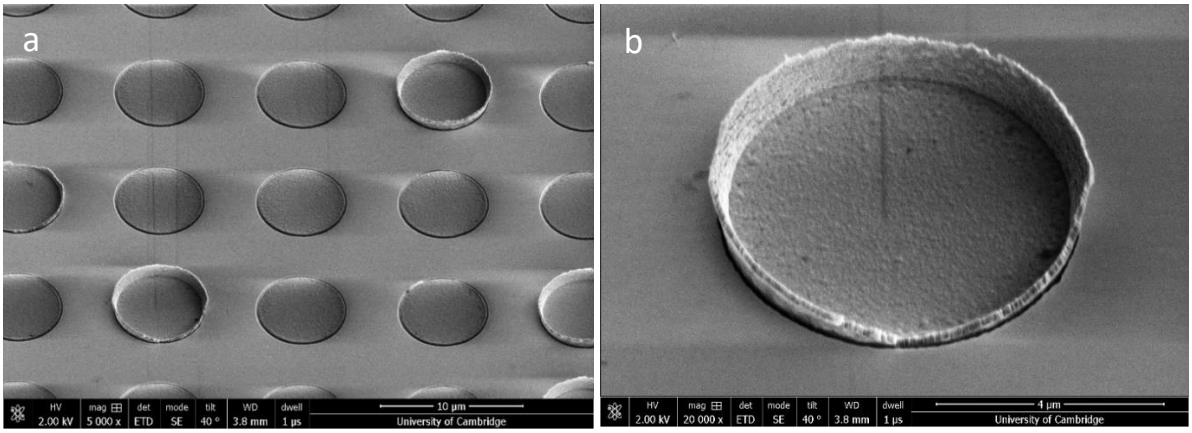

Figure 62: SEM images of 6 µm magnetic disks fabricated within perforations, showing a ~150nm thick layer of SiO_2 coating the inner walls of the perforations.

In addition to the problems shown with deposition uniformity, the e-beam evaporator also had issues with consistently growing the desired thickness of material, sometimes missing the target by a factor of 5. The thickness of SiO_2 depositions on all chips containing devices had to be closely monitored by also placing a chip dedicated to measuring the deposited SiO_2 thickness in the evaporation chamber. Unfortunately, this was experienced by all users of the system and no solution was found to improve the consistency during this work.

AFM measurements were taken to gain a better understanding of the particle structure. In Figure 63, 3D images of particles of each diameter are shown. Here, we see that the particle surfaces are rough and structured, with peaks around the circumference of the particles due to material coating the inner walls of the perforations during deposition.

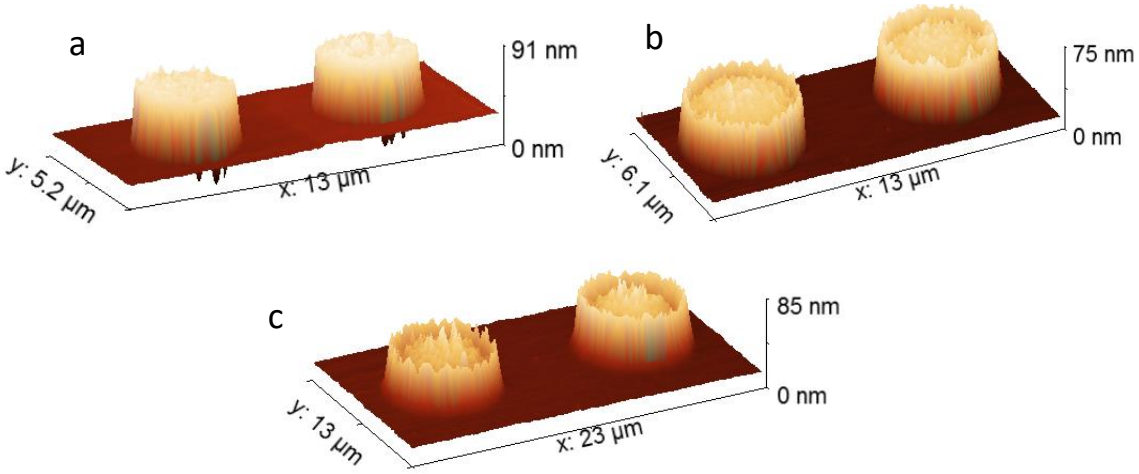

Figure 63: 3D AFM scans of the particles fabricated embedded within the perforations. Particles of diameter (a) 3 µm, (b) 4 µm and (c) 6 µm are shown.

AFM measurements were taken across all particle sizes (four measurements per diameter value) and analysed using the software Gwyddion. An AFM scan (a) and line slice through the centre of the scan (b) are shown for particle/perforation diameters of 3 (Figure 64), 4 (Figure 65) and 6 µm (Figure *66*). We notice the roughness of the particle surface, the physical gap between perforation edge and particle edge.

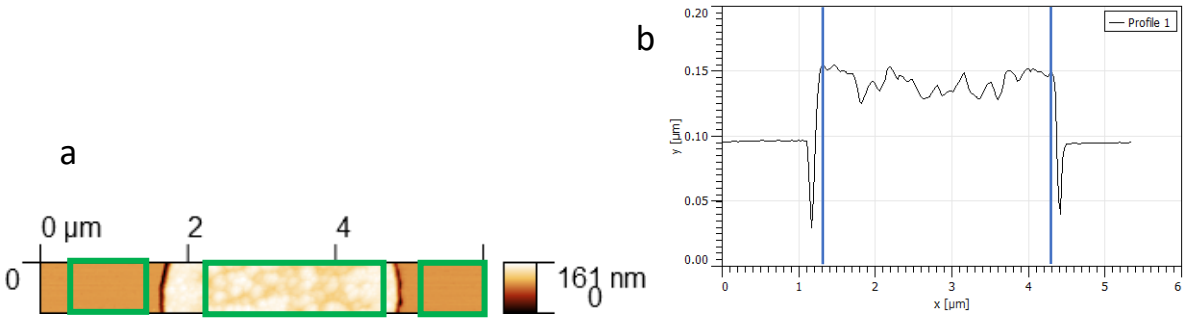

Figure 64: AFM data for 3 µm diameter disks. (a) shows 2D scan, (b) shows 1D slice. The blue vertical lines indicate the positions of the tips of the edge peaks used for measuring the particle diameter.

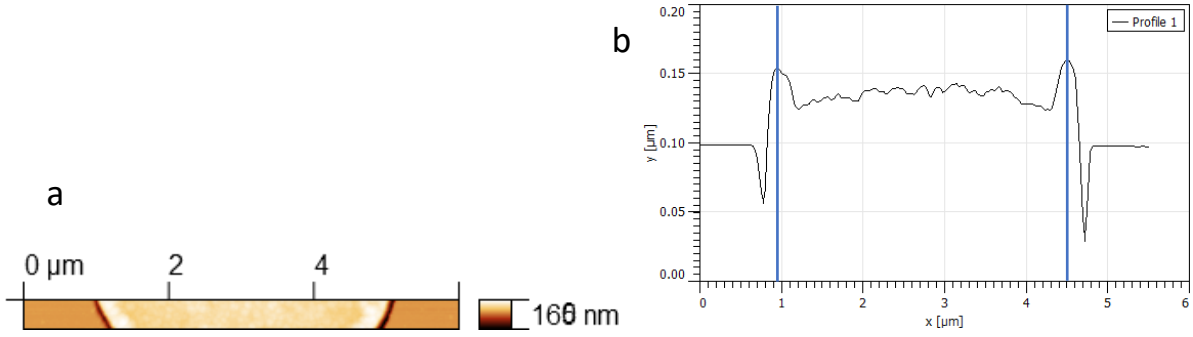

Figure 65: AFM data for 4 µm diameter disks. (a) shows 2D scan, (b) shows 1D slice. The blue vertical lines indicate the positions of the tips of the edge peaks used for measuring the particle diameter.

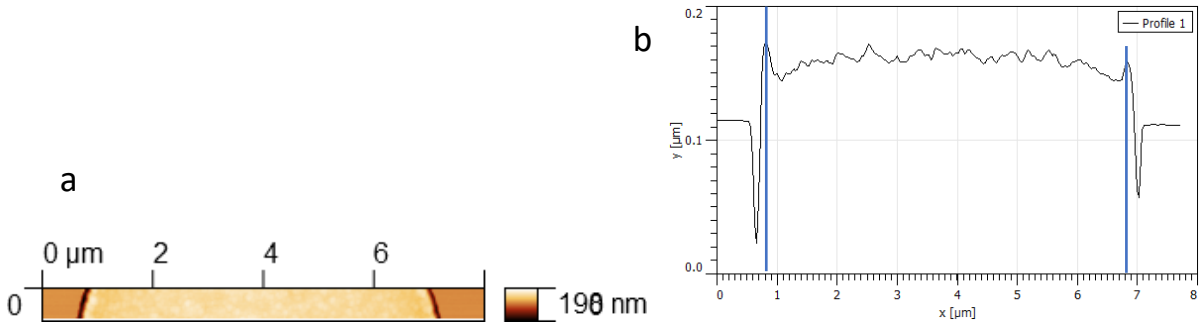

Figure 66: AFM data for 6 µm diameter disks. (a) shows 2D scan, (b) shows 1D slice. The blue vertical lines indicate the positions of the tips of the edge peaks used for measuring the particle diameter.

These scans were used firstly to calculate the height of the particle surfaces above the GaAs/AlGaAs chip surface. Using Gwyddion, an average height value can be calculated within a highlighted area of the AFM scan. The average height of the area surrounding the particles was calculated using a flat portion of the GaAs/AlGaAs area on each side of the scanned particle, and these two values averaged. The average height was also calculated within the central area of the particle, excluding the peaked ridge around the particle circumference. The relevant areas used are highlighted in green in the AFM scan for the 3 µm diameter disk shown in Figure 64a. These two values were subtracted, to give an estimate of the height between the particle surface and the GaAs/AlGaAs chip surface.

As previously mentioned, the thickness of SiO_2 deposited was systematically monitored by placing a Si chip with a cross drawn in marker pen beside the sample chip during the e-beam evaporation of SiO_2. While the intended thickness was 100 nm for this particular run, placing the bottom of the particle surface 30 nm above the top surface of the 2DEG, the SiO_2 thickness was measured to be 182 nm on average. The expected etch depth of the perforations is 160 nm, meaning that SiO_2 was expected to protrude 22 nm above the GaAs/AlGaAs chip surface. The magnetic films grown are 17 nm thick, meaning that the expected height to be measured by AFM between the top surface of the disks and the GaAs chip surface is 39 nm. Table 2 shows a compilation of the AFM results where we see good agreement between the measured and expected heights. The issue with unpredictable SiO_2 deposition also caused the bottom surface of the particles to be 112 nm above the top surface of the 2DEG, rather than the intended 30 nm.

We also used these line slices to estimate the particle diameters. The diameter was calculated as the distance from the tip of the edge peak on one side of the particle, to the tip of the edge peak on the other, as illustrated by the blue lines on the figures. These slices suggest that there is a gap between the edge of the perforation and the edge of the particle. We also estimated the size of this gap for all particle size and compile the results in Table 7.

Intended particle diameter (µm)	3	4	6
Measured particle diameter (µm)	3.1 ± 0.2	4.0 ± 0.2	6.2± 0.2
Expected height of particle top surface above substrate (nm)	39		
Measured height of particle top surface above substrate (nm)	47 ± 11	47 ± 11	45 ± 10
Measured gap between perforation and particle edges (nm)	196± 100	208± 100	200± 100

Table 7: Summary of the averaged results of AFM measurements on magnetic disks fabricated on the perforated devices, including measurement of the particle diameters, heights and gaps between the particle and perforation edges.

We see that all height measurements fall within the uncertainty bound of each other. Thus, from these measurements we calculate an average height of 46 ± 11 nm across all particle diameters. This result is consistent with our expectation (39 nm), based on the actual thicknesses of the SiO_2 and magnetic stack deposited, and the measured etch depth. For

comparison with magnetic particles on a continuous Hall cross, particles would ideally be at the same height relative to the 2DEG. Thus, a 27 nm underlayer of material is required between the magnetic particle and GaAs/AlGaAs surface of the continuous crosses to equate particle working distances across devices.

4.1.3.1.2 Magnetic characterisation

Magnetic characterisation of the deposited magnetic particles was carried out using Polar MOKE and VSM. During the e-beam evaporation of SiO_2 and sputtering of magnetic material, a Si chip was kept alongside the main device chip, such that a film of the magnetic material with the same SiO_2 underlayer was produced. Polar MOKE was used to extract the easy axis hysteresis loop of this film as well as of the magnetic particles. The magnetic particles could not be measured directly via VSM, as there was not enough magnetic material to produce a measurable signal. Instead, the film was measured by VSM to extract the saturation magnetisation, M_S, and this value was assumed to also represent the M_S of the magnetic particles.

Polar MOKE measurements of the easy axis hysteresis loops of the magnetic particle arrays were taken. Due to the localised nature of MOKE measurements, with a laser spot size of ~10 µm, it was possible to focus on single particles in the case of larger diameters (6 µm) and collect data averaged over several particles for the smaller diameters (3 and 4 µm). In Figure 67, the data from all disk sizes as well as the film are overlaid. Clearly, the smaller the particle diameter, the lower the coercivity and nucleation field.

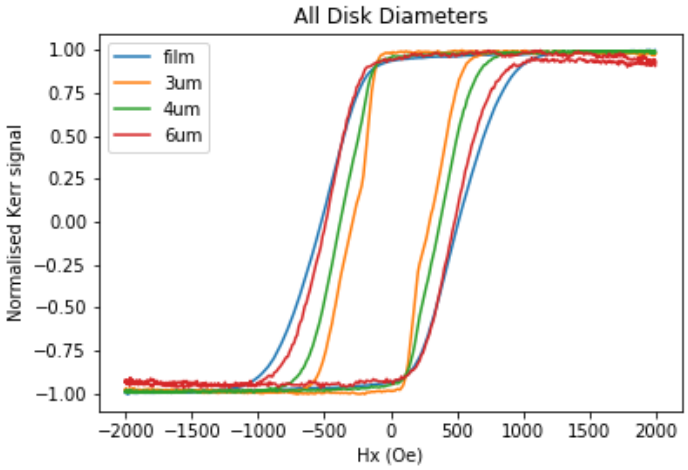

Figure 67: Overlaid easy axis polar MOKE hysteresis loops for film and particles of various diameters.

The trends seen here are different to those reported by Dr Stanton and generally reported in the literature [129][130]. Often it has been observed that as particle size decreases, coercivity increases and remanence is maintained. This is generally understood to be because in nucleation limited magnetic reversal, only a few nucleation sites are needed within the entire film for switching to occur. Patterning small particles from such films means that for any singular particle, the probability that it has a nucleation site is small. This results in an increased coercivity for the particle relative to the film, and a spread in H_{NUC} over the array. While decreasing coercivity has been seen with decreasing

particle size, this is reported only when the particles are fabricated using ion milling, which damages the particle edges, and only for particle diameters less than ~200 nm [131].

In the case of our particles, decreasing coercivity with decreasing particle size suggests that in going from film to particle, many additional nucleation sites are introduced. A loss in switching sharpness and full remanence is also seen, which could indicate an increased numbers of pinning sites. We saw earlier that even for films, the presence of SiO_2 as an underlayer likely introduced many pinning and nucleation sites. Here, the SiO_2 was deposited into the perforations and coated the inner walls. Thus, the magnetic films were likely deposited onto a roughly bowl-shaped underlayer of SiO_2. In this case, it seems plausible that this could result in high numbers of pinning/nucleation sites being introduced at the particle edges. As particles decrease in size, the edge to volume ratio increases, perhaps explaining why the impact of going from film to particle is most pronounced here for the smallest particles.

The easy axis hysteresis loop of the magnetic film associated with the magnetic disks was also measured using VSM and the saturation magnetisation M_S of CoFeB was measured at 1.28 $x10^6$ A/m, in agreement with other values found in the literature in the 1.1 to 1.3$x10^6$ A/m range [126][128].

4.1.3.2 Addition of magnetic disks to the surface of continuous Hall crosses

Arrays of magnetic disks were also fabricated on the surface of continuous crosses. To allow for a fair comparison of the V_{Hall} signal with that measured at equivalent perforated crosses, the magnetic particle arrays should be identical. The magnetic particles should thus be composed of the same magnetic layer structure and sit at the same working distance relative to the 2DEG. It should also be ensured that the particle diameters match well with those of the equivalent perforated crosses, such that the amount of magnetic material present is equal in both cases.

As seen previously, for the working distance of the particles on the continuous crosses to be equivalent to that of the perforated crosses, a 27 nm spacer layer between the particles and sensor surface was required. The particles on the perforated crosses were grown on an underlayer of SiO_2, which had a noticeable impact on the magnetic properties. Using SiO_2 again here would produce particles of equivalent magnetic behaviour and allow exactly the same fabrication protocols to be used. However, due to the unreliability of the e-beam evaporator, it was considered likely that the intended thickness would not be achieved, risking reducing the Hall signal of the particles to below the detection threshold of the measurement setup (due to the V_{Hall} reduction with increasing working distance) if a larger amount of material than intended was deposited.

Alternative options were therefore sought, and metallic underlayers which could be grown using the sputterer system were investigated. The magnetic stack optimised previously for use in fabrication of the magnetic disks was grown on underlayers of SiO_2, GaAs, Au and Ta. We hoped to find a metallic underlayer which would not disrupt the important magnetic properties, primarily M_S, remanence and PMA, and which could be deposited accurately with a thickness of 27 nm. In Figure 68, the MOKE easy axis hysteresis loops are shown for the magnetic stack grown on each of these underlayers on top of Silicon chips.

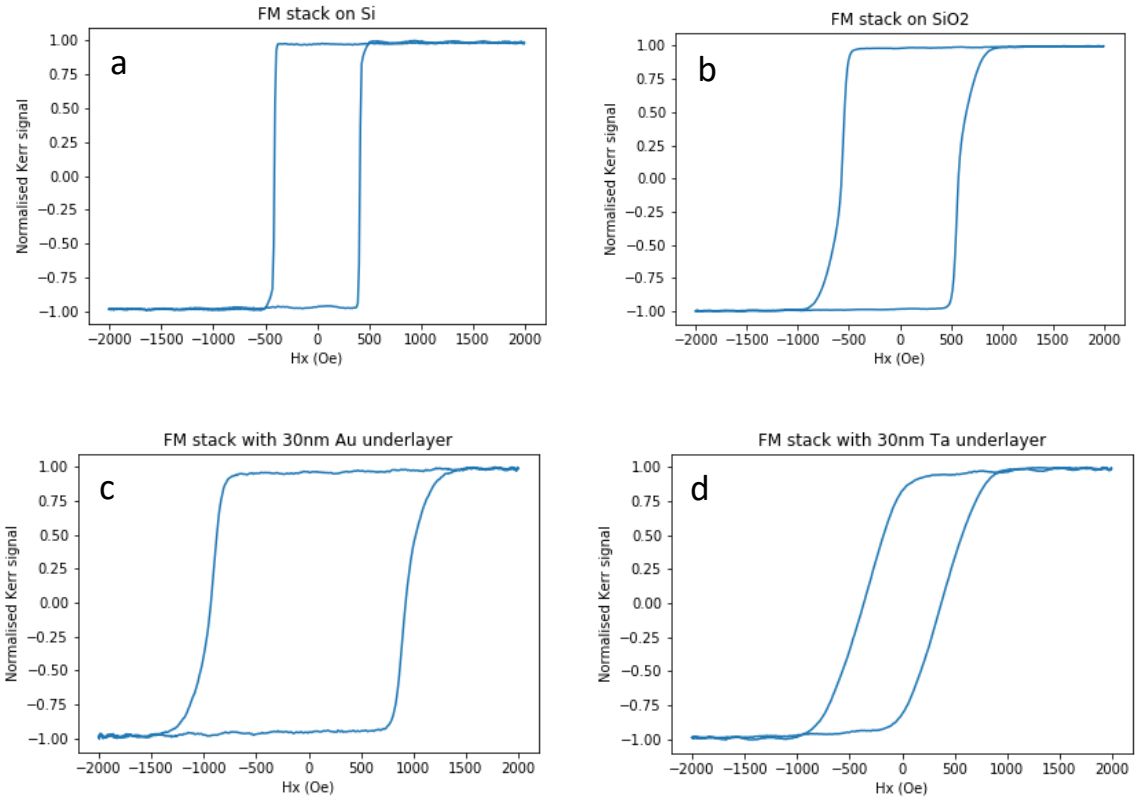

Figure 68: Polar MOKE easy axis hysteresis loops of magnetic film [CoFeB(0.55nm)/Pt(0.855nm)]x5 grown on different underlayers: (a) directly on Silicon wafer (b), with 180 nm SiO_2 (c), with 30 nm gold and (d) with 30 nm Tantalum underlayers.

The film grown on Ta is not fully remanent and therefore cannot be used. The use of gold as an underlayer also clearly alters the magnetic properties: the coercivity increases from around 600 Oe on SiO_2 to 900 Oe on gold. However, full remanence and switching sharpness are maintained. VSM measurements did not show a significant difference in the M_S of films grown on Si, SiO_2 and Au, and thus the gold underlayer was chosen.

To fabricate the particles upon the surface of continuous crosses, ~1 µm of S1813 photoresist was spin coated on the chip and arrays of circles were exposed via direct write lithography using the microwriter ML3 on the selected cross active areas. Dose testing was conducted to optimise the dose, and again 300mJ/cm^2 was used, with a 405 nm wavelength laser with 0.6 µm resolution. The resist was developed and 30 nm of gold followed by the magnetic stack was sputtered onto the chip. The chip was soaked in acetone for 15 minutes and then sonicated for 5-10s, to lift off all material deposited upon the resist, leaving behind the desired arrays of magnetic disks.

4.1.3.2.1 Structural characterisation

Structural characterisation of the deposited magnetic particles was carried out using SEM and AFM. SEM images of the magnetic disks formed on the surface of continuous Hall crosses are shown for particle diameters 3 (Figure 69), 4 (Figure 70) and 6 µm (Figure 71). In each case, (a) shows a large-scale image and (b) shows a close-up. It is clear from these images that large skirts of material are present around the edges of the particles. This is due to the sputtered material coating the inner walls of the resist perforations. Some of this material has been ripped away during sonication, while some has remained attached to the disks.

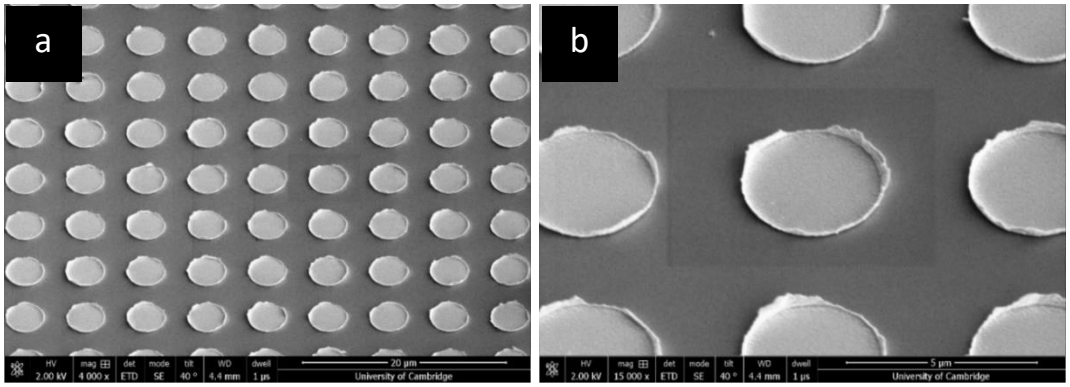

Figure 69: SEM image of 3 μm diameter magnetic disks grown on the surface of a continuous Hall cross.

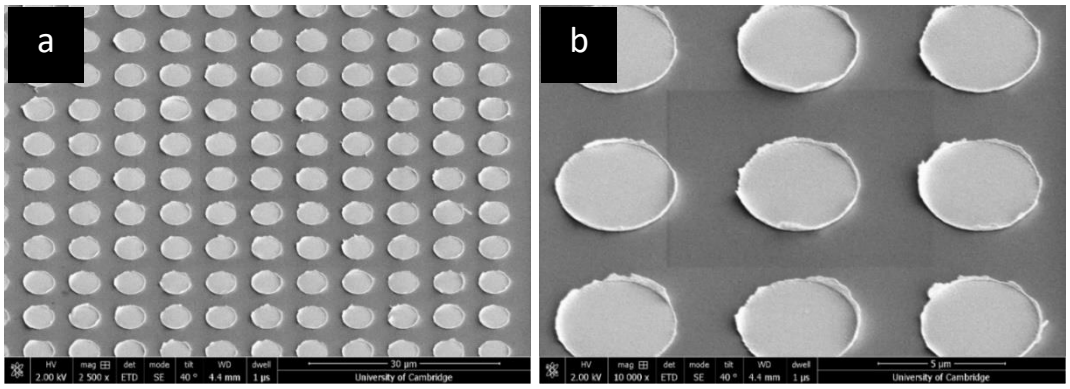

Figure 70: SEM image of 4 μm diameter magnetic disks grown on the surface of a continuous Hall cross.

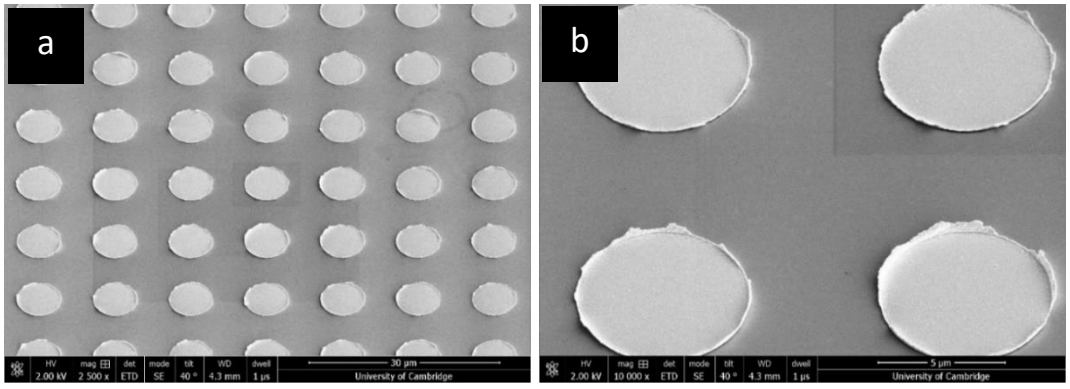

Figure 71: SEM image of 6 μm diameter magnetic disks grown on the surface of a continuous Hall cross.

The SEM images also reveal that the diameters of the magnetic particles are significantly larger than intended. From several images, the average diameters were estimated and compiled in Table 8.

Intended diameter (μm)	3	4	6
SEM measured diameter (μm)	3.5 ± 0.2	4.6 ± 0.2	6.7 ± 0.2

Table 8: Diameter of the magnetic disks deposited upon the continuous crosses, as measured from SEM images.

The larger than intended particle diameters likely resulted from over-exposure of the resist. As mentioned, dose testing was executed, however it is possible that the resist thickness on the chip was substantially different to that on the dose test chips due to human error. The result is that more magnetic material is present upon the continuous crosses than the equivalent perforated crosses. This means that directly comparing the V_{Hall} signal will not provide a fair comparison. However, the experimental V_{Hall} data gathered using the perforated and continuous crosses can still be compared directly with COSMOL predictions, accounting for the true particle diameters.

In Figure 72, a wide-field image of a single device is shown. Here, three crosses with magnetic particles can be seen. Cross (a) was fabricated initially, but due to fabrication issues, was never measured. Cross (d) was used as the continuous, blank reference cross, to measure the background signal in the absence of magnetic particles. Cross (b) is the continuous cross with magnetic particles, and cross (c) is the perforated cross with magnetic particles.

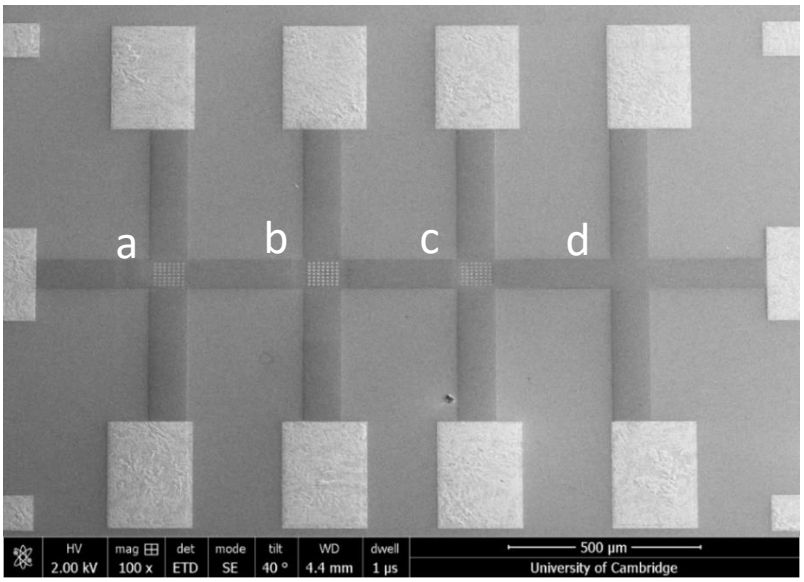

Figure 72: SEM image of entire Hall cross device. Arrays of magnetic particles present embedded in perforations (a) and (c). Array of magnetic particles present at the surface of continuous cross (b) and continuous, blank reference cross (d).

AFM measurements were also conducted. In Figure 73, 3D AFM scans of particles of each diameter are shown. In comparison to the AFM images taken of the particles formed on the perforated device shown in Figure 63, the skirts are clearly more pronounced. The presence of the skirts negatively impacts the quality of the AFM scans as the tip struggles to resolve such sharp changes in topography.

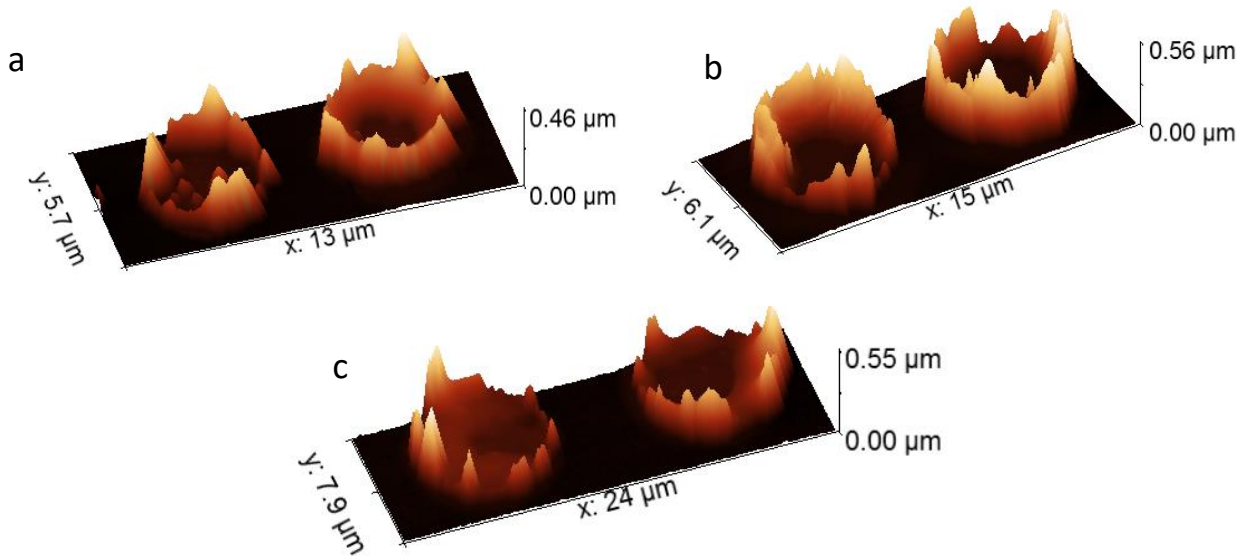

Figure 73: 3D AFM scans of the particles fabricated on the surface of continuous Hall crosses. Particles of diameter (a) 3 µm, (b) 4 µm and (c) 6 µm are shown.

The AFM scans were also used to estimate the height of the skirts. For each particle size, four AFM images were taken and analysed using the software Gwyddion. An AFM scan is shown for particles of diameter 3 (Figure 74), 4 (Figure 75) and 6 µm (Figure *76*). In (b), a line slice through the centre of the images shown in (a) can be seen. From the line slices,

the maximum height of the skirts was estimated, with the results compiled in Table 9. It was found that the particle diameters could not be accurately measured using AFM, as the skirts inflated the measurements.

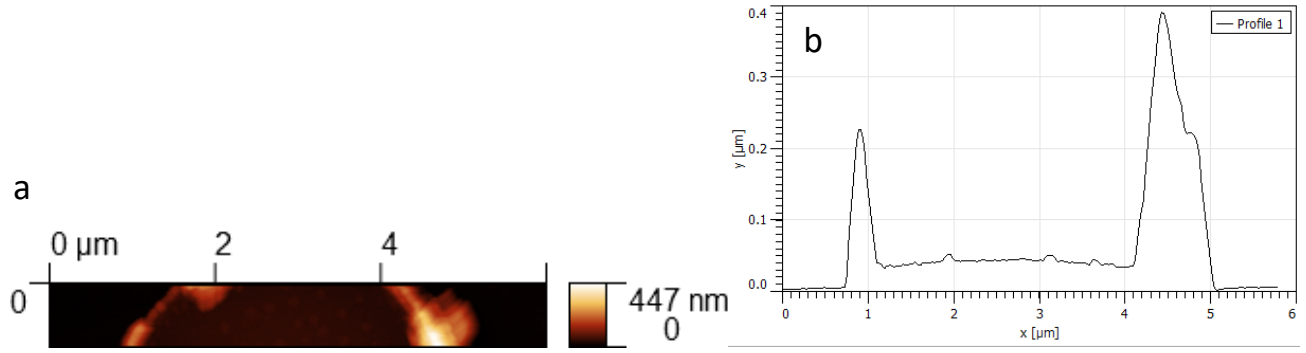

Figure 74: AFM data for 3µm diameter disks. (a) shows 2D scan, (b) shows 1D slice.

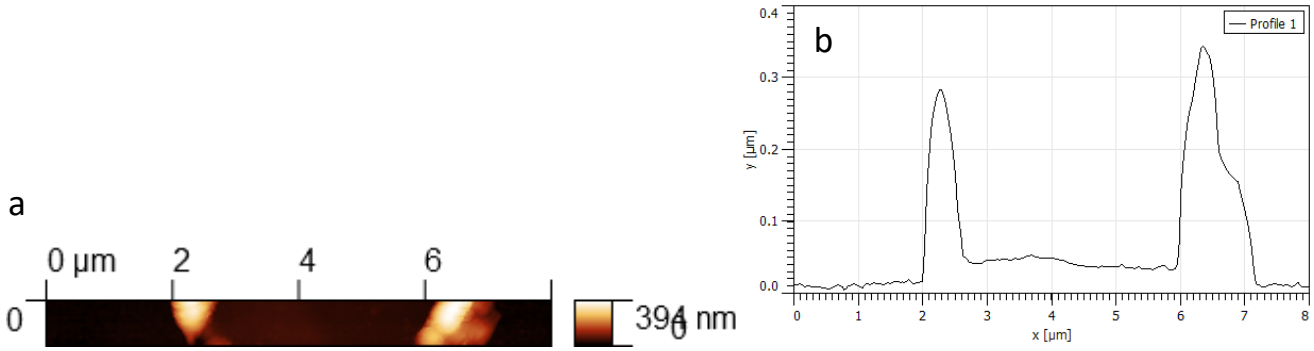

Figure 75: AFM data for 4µm diameter disks. (a) shows 2D scan, (b) shows 1D slice.

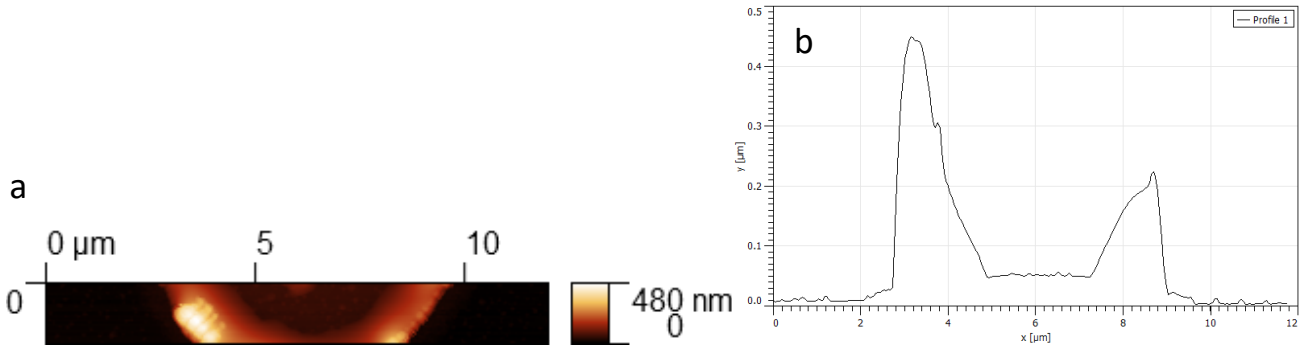

Figure 76: AFM data for 6µm diameter disks. (a) shows 2D scan, (b) shows 1D slice.

Intended particle diameter (µm)	3	4	6
Maximum skirt height (nm)	300	250	450

Table 9: Maximum skirt heights measured via AFM scans, for magnetic disks fabricated on the surface of continuous Hall crosses.

It is hard to predict the potential effect of the presence of the skirts on the Hall signal. One possibility is that the films composing the skirts maintain the magnetic properties of the films/disks, including remanence and PMA. In this case, the easy axis of magnetisation would be perpendicular to the film plane and thus lie in the X-Y plane. The magnetisation state would not be switched via the application of an external magnetic field in the z direction, and we would thus not expect a V_{Hall} contribution to the remanent measurements.

It is also possible that PMA would be lost, and the easy axis of magnetisation would change to in plane. In this case, the magnetisation state could be switched via the application of an applied field in the z direction. It is possible that if

the magnetic properties were affected enough to result in the loss of PMA, that remanence may also be lost, in which case again, we would not expect a V_{Hall} contribution to the remanent measurements.

In the worst-case scenario of remanent magnetic skirts, with in plane magnetisation that can be switched by a magnetic field applied in the z direction, then we expect the V_{Hall} response of the continuous Hall cross to the disks to be enhanced, due to the additional magnetic volume, providing a larger stray field in the z direction.

4.1.3.2.2 Magnetic characterisation

Magnetic characterisation of the deposited magnetic particles was carried out using Polar MOKE and VSM. During sputtering of magnetic material, a Si chip was kept alongside the main device chip, such that a film of the magnetic material atop the same gold underlayer was produced. Polar MOKE was used to extract the easy axis hysteresis loop of this film, as well as of the magnetic particles of each diameter. The magnetic particles could not be measured directly via VSM, as there was not enough magnetic material to produce a measurable signal. Instead, the film was measured by VSM to extract the saturation magnetisation, M_S and this value was assumed to also represent the M_S of the magnetic particles.

In Figure 77, polar MOKE measurements of the easy axis hysteresis loop of the magnetic particle arrays are shown for all disk sizes as well as for the film. The effect of going from film to particle, and indeed the effect of particle diameter, appears much less pronounced in comparison to the disk arrays fabricated on SiO_2 within the perforations.

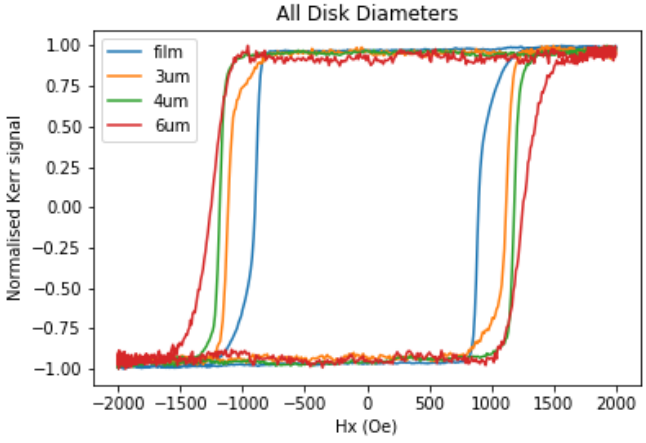

Figure 77: Polar MOKE hysteresis loops for magnetic disks deposited on continuous cross, overlaid for all diameters and film.

Here, full remanence is maintained and coercivity is increased for all particle sizes relative to the film. As a function of particle size, coercivity decreases with decreasing diameter and the switching sharpness is largely unchanged. Overall, these trends are rather different to those seen for the disks grown on the perforated device with the underlayers of SiO_2 where remanence and the switching sharpness diminished as the particle diameter decreased. The coercivity drops as particle diameter drops in both cases, however this effect was much more pronounced for the particles on the perforated device.

The primary difference is the underlayer, with 30 nm of gold here and 180 nm of SiO_2 previously. It is possible that the gold introduces fewer nucleation sites than SiO_2, resulting in higher H_c and remanence being maintained. H_C does decrease as the particle diameter decreases however, suggesting that nucleation sites are introduced at the particle

edges, having more of an effect as the edge to volume ratio increases. It is also possible that the differences in underlayer thickness is playing a role. For the SiO_2, 180 nm is deposited while only 30 nm for the gold. This larger extent of side-wall coating with the SiO_2 underlayer likely results in the formation of a more pronounced bowl-shaped underlayer, and larger roughness around the circumference of the particles.

The easy axis hysteresis loop of the magnetic film associated with the magnetic disks was measured using VSM. Here the M_S of CoFeB was estimated to be 1.19×10^6 A/m, in good agreement with that measured for the film associated with the magnetic particles deposited on SiO_2 on the perforated cross.

4.1.4 Device fabrication conclusions

Overall, the fabrication of the devices proceeded reasonably well however, several improvements could be made should this work lead to further research and a subsequent round of samples be fabricated. Firstly, the coating of the inner walls of the perforated resist by the materials being deposited to form the magnetic particles negatively impacted the particles in several ways. In the case of the particles formed within the perforations, a ~150 nm thick layer of SiO_2 was measured (likely 180 nm, corresponding to the SiO_2 deposition thickness). This layer firstly reduces the diameter of the magnetic particles which can be deposited within the perforations, and we suspect that the rough SiO_2 layer present around the particle circumference negatively impacts the magnetic properties of the particles and is perhaps responsible for the reduction in coercivity with decreasing particle diameter. In the case of the particles fabricated on the continuous crosses, large skirts of material were found around the particle edges, which may result in a larger than expected Hall voltage response. To improve upon this, a resist with an undercut sidewall profile when developed can be used, preventing deposited material from coating the inner walls of the resist. Such a profile occurs for negative photoresists and can even be produced for the positive photoresist S1813 used in this work by soaking the resist in chlorobenzene. This hardens the resist surface, resulting in faster development for resist closer to the substrate surface, and the formation of the desired resist side-wall profile.

In addition, the need for SiO_2 negatively impacted the fabrication. Issues with the e-beam evaporator system resulted in less-than-optimum SiO_2 quality as well as highly variable deposition thicknesses. The underlayer also clearly negatively impacted the magnetic behaviour of the films and particles. To get around this, it is possible to either use a different insulator layer (deposited using a functioning deposition system!) and carefully selected to impact the magnetic behaviour of the films/disks to a lesser degree. It may be possible, if the inner walls of the resist and perforations are no longer coated in material during deposition, to directly deposit the magnetic layers into the perforations, at a depth appropriately below the level of the 2DEG, thus using air as the insulating layer. Perhaps even better, would be to use the shallow mesa etching technique, as opposed to the deep etch that is presently being used. In this work, the etch goes through the 2DEG to ensure full depletion. It has been shown [132] that it is not necessary to etch through the 2DEG, but that etching to a shallower depth, above where depletion is required, can achieve the same. In this case, an insulating layer would exist in the form of GaAs/AlGaAs between the 2DEG and the magnetic disk, negating the need for any additional insulating layers. This has also been shown to be beneficial in reducing damage to the 2DEG that occurs when etched through. This damage causes the formation of a depleted layer around the circumference of the perforations. From the literature [123], we expect a depletion region of ~25 nm from the

damage caused by wet chemical etching. Moving to the shallow etch method could potentially avoid the formation of this dead layer.

Nevertheless, 15 Hall cross devices were fabricated using the methods described above, each of which had a perforated cross with magnetic disks, a continuous cross with magnetic disks, and a continuous, blank reference cross. Here, we compile the results of the characterisation measurements and translate them into input parameters for the COMSOL simulations which will be shown later in this chapter to predict the Hall voltage response of the experimental devices.

Firstly, we consider how the magnetic disks are modelled in COMSOL. The magnetic stack layer structure of the disks is given by Ta(2nm)/Pt(6nm)/[CoFeB(0.55nm)/Pt(0.855nm)]x4/CoFeB(0.55nm)/Pt(3nm). The total thickness of the stack (excluding the Ta and Pt under and capping layers) is 6.17 nm, with a CoFeB thickness of 2.75 nm. We model the magnetic disks as a 6.17 nm thick disk in which the moment of the CoFeB layers is diluted, so that:

$$M_{disk} = \frac{m_{disk}}{V_{disk}} = \frac{M_{CoFeB}V_{CoFeB}}{V_{disk}} = M_{CoFeB} \times 0.445705 \quad (78)$$

M_{CoFeB} was measured to be 1.28e6 A/m for the perforated device, giving M_{disk} as 0.5705×10^6 A/m and 1.19×10^6 A/m for the continuous device, giving M_{disk} as 0.5314×10^6 A/m.

The working distance (distance between central plane of particle and 2DEG) on the perforated crosses is the distance from the GaAs chip surface to the central plane of the 2DEG, plus the distance from the GaAs chip surface to the lower surface of the magnetic disk, calculated as the measured particle height minus the known thickness of deposited magnetic material, plus the underlayer of Pt and Ta upon which the magnetic layers are deposited, plus half the thickness of the disk – see Figure 78 a, i.e., 142.9 ± 11 nm.

For the particles on the continuous crosses, the working distance is the distance from the GaAs chip surface to the central plane of the 2DEG, plus the thickness of the gold underlayer, plus the underlayer of Pt and Ta, plus half the thickness of the disk – see Figure 78 b, i.e., 143.6 ± 11 nm.

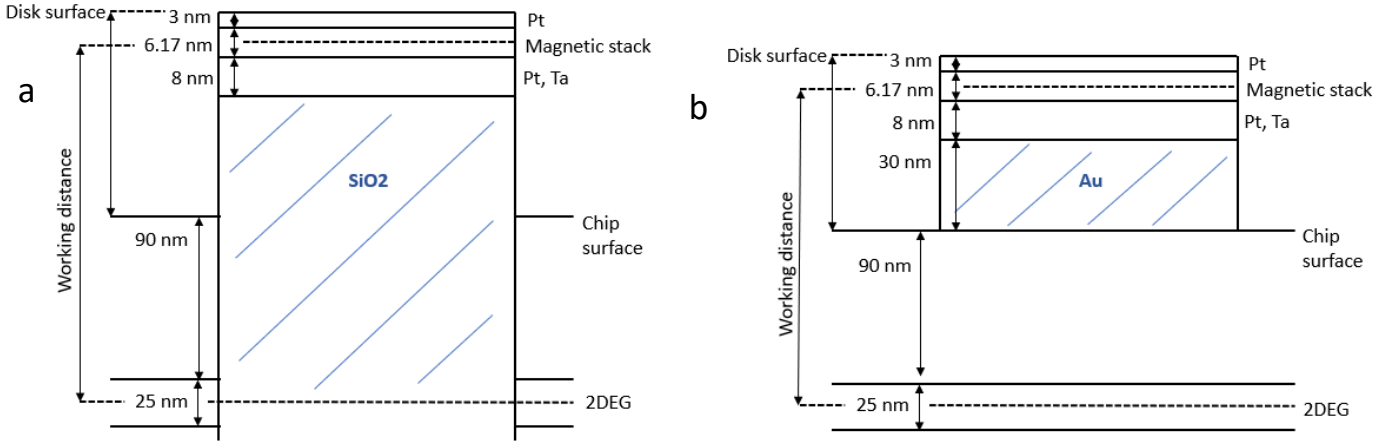

Figure 78: Schematic (not to scale) describing the geometry of the disks when (a) above/embedded in a perforation and (b) above a continuous Hall sensor.

In Table *10*, we compile the results of the structural and magnetic characterisation measurements of the magnetic disks fabricated within the perforations of the perforated devices and in Table *11* we show the same for the continuous device.

Intended disk diameter (µm)	3	4	6
Measured disk diameter by SEM (µm)	2.9 ± 0.1	4.0 ± 0.1	6.1 ± 0.1
Measured disk diameter by AFM (µm)	3.1 ± 0.2	4.0 ± 0.2	6.2 ± 0.2
Average disk diameter (µm)	3.0 ± 0.2	4.0 ± 0.2	6.2 ± 0.2
Particle to perforation edge spacing (nm)	196 ± 100	208 ± 100	200 ± 100
Height of disk surface above chip surface (nm)	47 ± 11	47 ± 11	45 ± 10
M_{CoFeB} (A/m)	1.28×10^6		
M_{disk}(A/m)	0.5705×10^6		
Working distance (nm)	142.9 ± 11		

Table 10: Summary of the structural and magnetic characterisation measurements of magnetic disks fabricated within the perforations of perforated devices.

Intended diameter (µm)	3	4	6
Measured diameter by SEM (µm)	3.5 ± 0.2	4.6 ± 0.2	6.7 ± 0.2
M_{CoFeB} (A/m)	1.19×10^6		
M_{disk}(A/m)	0.5314×10^6		
Working distance (nm)	143.6		

Table 11: Summary of the structural and magnetic characterisation measurements of magnetic disks fabricated on the continuous devices.

4.2 2DEG Characterisation

The 2DEG was characterised using a combination of Hall and resistance measurements carried out at a drive current of 50 µA and the results were used as inputs in all COMSOL simulations against which experimental measurements are compared.

In the experiments presented in the following sections, three Hall cross devices were used for all measurements. Each device contained perforations/particles of a different diameter (3, 4 and 6 µm). Here, the results of the characterisation of the perforated and the blank, continuous cross from each of the three devices is shown. A 50 µA current was pumped through the relevant cross while an orthogonal applied field, B, was swept by the EM (between ±0.2 T). This measurement was carried out for both positive and negative currents and these results were combined to remove offsets from the V_{Hall} measurement. The results are shown in Figure 79a for all characterised devices.

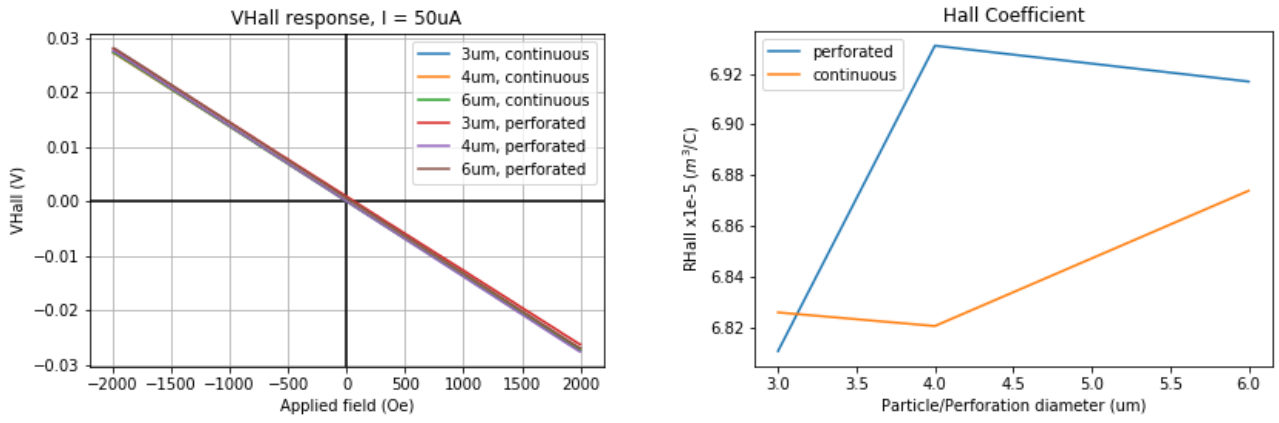

Figure 79: (a) Hall voltage versus applied field response of perforated and continuous Hall crosses, from the characterised devices containing perforations of diameter 3, 4 and 6 µm. (b) Hall coefficient extracted from the data shown in (a).

A straight line was fitted to each V_{Hall} versus field dataset, and the slope was extracted. From this, the Hall coefficient, R_H, and carrier concentration, n, were calculated following:

$$\frac{V_{Hall}}{B} = \left(R_H \frac{I}{t}\right) \quad (79)$$

$$R_H = \left(\frac{1}{nq}\right) \quad (80)$$

In Figure 79b we show the extracted Hall coefficient for all characterised devices. The maximum difference in measured Hall coefficient between continuous and perforated crosses of the same device is 2%, demonstrating that the addition of perforations has negligible effect on the response of the Hall cross to a uniform applied field. This was expected from COMSOL simulations shown in section 3.2.3.1.

To measure the resistivity of the 2DEG, a 50 µA current was injected along the central channel of a device and the longitudinal voltage, V_L, was measured across a pair of contacts along the central channel. Measurements were carried out using both positive and negative current and combined to calculate the longitudinal resistance R_L according to:

$$R_L = \frac{V_L(I^+) - V_L(I^-)}{I^+ - I^-} \quad (81)$$

This measurement was repeated using a different pair of contacts along the central channel and the average longitudinal resistance was calculated. To calculate the resistivity, the longitudinal resistance was multiplied by the dimensions of the channel, following:

$$\rho_{bulk} = \frac{R_L w t}{b} \quad (82)$$

Where t is the 2DEG thickness (25 nm), b the distance between contacts used for the longitudinal voltage measurement (500 µm), and w is the channel width (100 µm). The measurements were taken on a single device, where no magnetic material and no perforations were present between the contacts used for the measurement. The resistivity extracted here is used for all devices fabricated from the same 2DEG chip and was found to be 6.52×10^{-5} Ωm.

From the measurements of the resistivity and carrier concentration, the carrier mobility was also estimated following:

$$\mu = \left(\frac{1}{nq\rho}\right)$$

In Table 12 we compile the values of the Hall coefficient, carrier concentration and mobility at a drive current of 50 µA. We present the average value of these results across devices, for the perforated and continuous crosses

separately. Given the agreement between values for the perforated and continuous crosses, we used the average values as the inputs for COMSOL simulations in which experimental devices are modelled.

	R_H (m^3/C)	n (m^{-3})	μ (m^2/Vs)
Continuous	6.85×10^{-5}	9.125×10^{22}	1.0495
Perforated	6.86×10^{-5}	9.119×10^{22}	1.0502
Average	6.855×10^{-5}	9.122×10^{22}	1.0498

Table 12: Average Hall coefficient, carrier concentration and mobility, measured across devices for the perforated and blank continuous crosses under 50 μA driving current. Final values of the same parameters, taken as input parameters for COMSOL simulations, also included.

4.3 Hall voltage measurements of array of 6 μm magnetic disks

To measure the Hall voltage response of perforated and continuous crosses to arrays of magnetic disks, both the remanent and Hall gradiometer approaches, as outlined in section 2.4.4.2, were employed. The data gathered using the different approaches was compared to assess the relative accuracies and to establish confidence in the results. Here, the Hall voltage response, V_{Hall}, of a perforated and continuous Hall cross to the presence of a 9x9 array of 6 μm diameter magnetic disks is presented in detail. All measurements were acquired from the same Hall cross device.

4.3.1 Remanent measurements

The response of a Hall cross to the presence of 6 μm diameter remanent magnetic disks in the absence of applied magnetic field was measured in what is referred to as the remanent measurement approach. As was outlined in section 2.4.4.2.2, the magnetisation direction of the array of magnetic disks was set by a field pulse, larger in magnitude than the switching field of the disks. The Hall voltage response to the stray field of the disks was then measured in zero applied field. The magnetisation was subsequently set in the opposite direction via an oppositely directed magnetic field pulse, and the measurement repeated. Combining these two measurements, the V_{Hall} signal of the disk array was calculated as

$$V_{Hall} = \frac{V_{Hall}(B_{FM}+) - V_{Hall}(B_{FM}-)}{2} \quad (83)$$

where the notation $V_{Hall}(B_{FM}\pm)$ refers to the Hall voltage response due to the stray field of the ferromagnetic disks magnetised in the positive and negative directions, in accordance with the applied field pulses. $V_{Hall}(B_{FM}+)$ and $V_{Hall}(B_{FM}-)$ are expected to be opposite in polarity due to the oppositely directed stray field in each case. In this approach, it must be ensured that the magnetic field onto the sensor during measurement is due to the stray field of the magnetic particles only. Two options were developed to minimise the V_{Hall} response to non-zero background fields resulting from imperfect field control close to 0 or stray fields emanating from magnetised components of the setup.

The first approach involved relying on the EM to set the direction of magnetisation of the disks, and on the custom-built Helmholtz coils to accurately provide a period of zero applied field directly afterwards. In fact, more important than having a perfectly zeroed applied field, is that the field returns to the same value following each pulse. Any Hall voltage response due to an imperfectly zeroed applied field, B_{offset}, will not contribute to the final V_{Hall} measurement, if B_{offset} is present during the measurement of both $V_{Hall}(B_{FM}+)$ and $V_{Hall}(B_{FM}-)$.

During each measurement, the magnetic field at the sample was recorded via the Lakeshore Hall probe such that the difference in B_{offset}, ΔB, between the two remanent measurement sections could be calculated. Knowing the response coefficient α of the device to an applied field, we estimated the V_{Hall} signal contribution caused by ΔB according to:

$$V_{error} = \alpha \frac{\Delta B}{2}$$

(84)

In addition, a blank, continuous reference cross was present on each device, such that a background V_{Hall} measurement in the absence of magnetic particles could be acquired. Via background subtraction of this measurement, any V_{Hall} signal contribution due to the presence of local magnetic fields which might not be picked up by the Lakeshore Hall probe could also be accounted for.

The second approach involved setting up the gradiometer to nullify the V_{Hall} response to any difference in B_{offset} between the two remanent measurement sections. The applied field during each measurement was again recorded using the Lakeshore Hall probe and the response of the gradiometer as a function of applied field, when the gradiometer was considered balanced, was recorded prior to each measurement. Thus, the contribution to the measured V_{Hall} due to a combination of unwanted applied fields and imperfect balancing of the gradiometer could be estimated using equation (84).

4.3.1.1 Without the gradiometer

The EM and custom-built Helmholtz coils were used to apply a magnetic field pulse sequence, as shown in Figure 80a. Here, a large pulse was applied to set the magnetisation state of the particles, followed by a period in which the applied field was set to zero. A second magnetic field pulse sets the magnetisation of the disks in the opposite direction, followed by a second remanent measurement section, in which again the only field at the sensor should be the stray field of the magnetic disks, oppositely directed in this case.

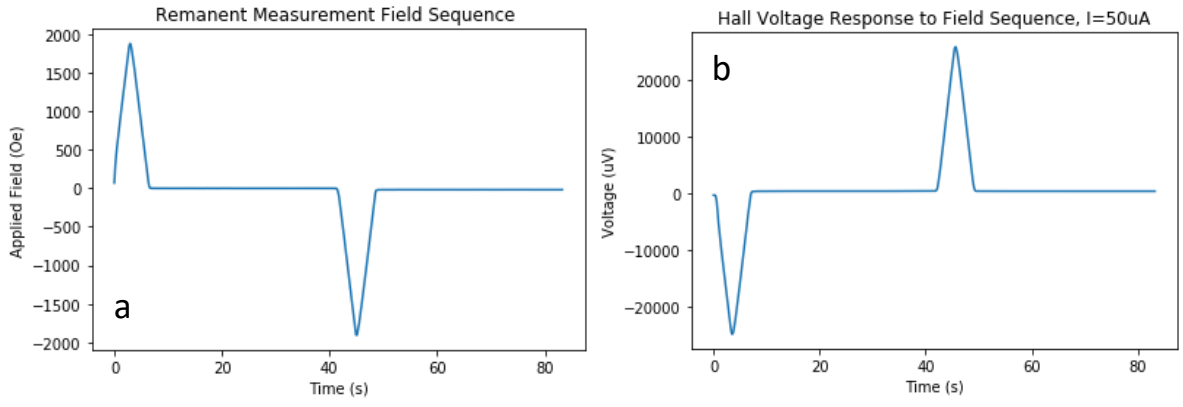

Figure 80: (a) Applied field pulse sequence for remanent measurements, (b) Hall voltage response of a perforated cross with 6 μm magnetic disks, drive current 50 μA, to the field sequence shown in (a).

The V_{Hall} response of the Hall cross to the magnetic pulse sequence is shown in Figure 80b. The presented data was collected at the perforated cross, through which 50 μA of current was driven, with the voltage measured across the main bar of the device. Clearly the first positive polarity field pulse produced a negative polarity V_{Hall} response.

This first field pulse set the magnetisation of the disks parallel with the field direction, and so during the following remanent section of the measurement, the stray field $B_{FM}+$ emanating from the disk was also positive in polarity. For the continuous cross, we thus expected the generated $V_{Hall}(B_{FM}+)$ to be negative and equal to $-|V_{Hall}(B_{FM})|$. Following the second field pulse, the magnetisation of the disks was set in the negative direction, with a corresponding negatively directed stray field $B_{FM}-$. The Hall response $V_{Hall}(B_{FM}-)$ of a continuous cross should then be positive in polarity and equal to $|V_{Hall}(B_{FM})|$. By calculating V_{Hall} as the difference in the measured Hall voltage between the first and second remanent measurement sections, we expected the calculated V_{Hall} to be negative in polarity, following:

$$V_{Hall} = \frac{V_{Hall}(B_{FM}+) - V_{Hall}(B_{FM}-)}{2} = \frac{-|V_{Hall}(B_{FM})| - |V_{Hall}(B_{FM})|}{2} = -|V_{Hall}(B_{FM})|$$

(85)

For the perforated cross, the opposite polarity V_{Hall}' is expected, as indicated by equation (86). This is because the direction of the stray field falling onto the sensor is opposite to the direction of magnetisation of the disks (and the magnetising pulse sequence) due to the presence of the perforation. This expectation makes intuitive sense, as is illustrated in Figure 81 and was previously discussed in section 2.2.3, and the switch in signal polarity with the addition of perforations was predicted by COMSOL simulations.

$$V_{Hall}' = \frac{V_{Hall}'(B_{FM}+) - V_{Hall}'(B_{FM}-)}{2} = \frac{|V_{Hall}'(B_{FM})| - (-|V_{Hall}'(B_{FM})|)}{2} = |V_{Hall}'(B_{FM})|$$

(86)

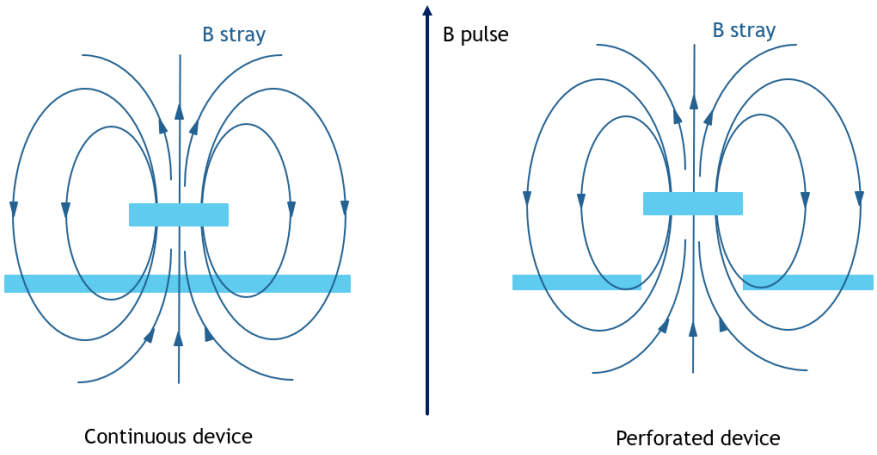

Figure 81: Illustration of the direction of stray field onto a (a) continuous and (b) perforated sensor, for magnetic disks magnetised in the positive direction by a positively directed field pulse.

To calculate the Hall voltage response at the perforated cross due to the array of magnetic disks, the data shown in Figure 80b was analysed. The data between each pulse ending and the next pulse beginning is shown in red in Figure 82a. Clearly, the device was still responding to the changing field while into the remanent section of the measurement. This is likely due to the large V_{Hall} response caused by the magnetising field pulses requiring some time to settle, and the rapidly changing field inducing some EMF in the device. As a result, all data in these remanent sections was not fit for use in the calculation of V_{Hall}. A region of data was selected within the remanent section in which the voltage appeared to have stabilised. It was found that the higher the drive current, the further into the remanent section this occurred. Thus, the section of data fit for analysis was determined at the highest drive current used for measurement,

and this same section was consistently analysed across all measurements. This subset of data is plotted in blue in Figure 82a, and again in Figure 82b, isolated from the discarded data. The time required for the stabilisation of the voltage response limited the frequency at which the measurements could be conducted. When the NVM measurement aperture was set to 0.2 ms (1PLC) and the LXPro measurement frequency set to 0.06Hz, it was found that for reasonable drive currents, the voltage had not yet stabilised. This led to the selection of the 10 ms NVM measurement aperture (5PLC) and a 0.012 Hz LXPro measurement frequency. 50 single shot measurements were taken and averaged, giving a corresponding measurement time of ~70 minutes.

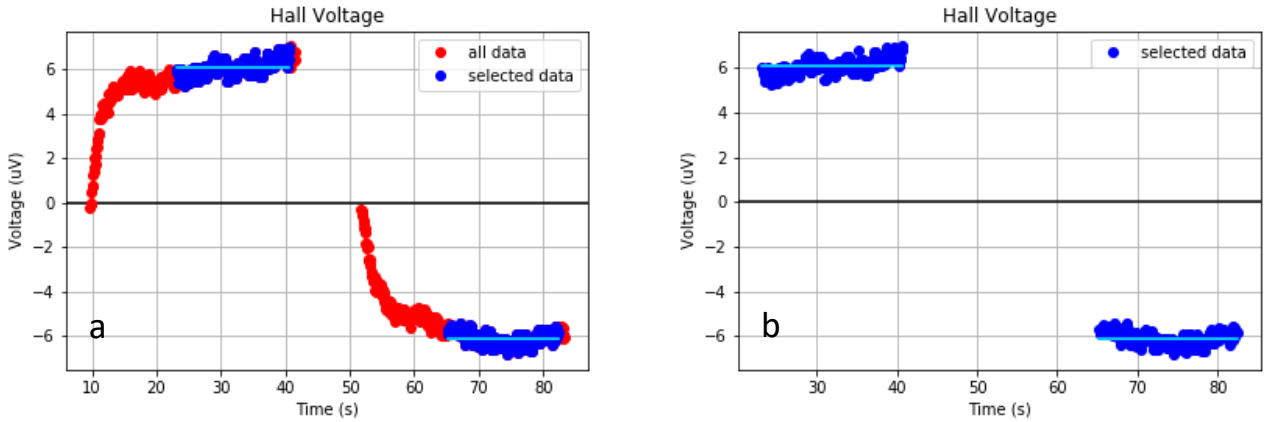

Figure 82: Hall Voltage response in between magnetic field pulses for a perforated cross in the presence of an array of 6 μm magnetic disks, showing all data (a) and data used for analysis (b).

Using these sections of the remanent measurement, $V_{Hall}(B_{FM}+)$ and $V_{Hall}(B_{FM}-)$ were calculated as the average voltage following the first and second field pulses, respectively. The V_{Hall} response due to the magnetic disk array was then calculated following equation (83). The calculated polarity of V_{Hall} was positive, in agreement with our expectations for a perforated cross. The standard deviation in the voltage during each remanent measurement section was calculated, and the error in V_{Hall} calculated as the standard deviations, combined in quadrature, and divided by 2, following standard error analysis. For the perforated cross with an array of 6 μm disks, we find V_{Hall} = 6.1 ± 0.2 μV at a drive current of 50 μA. The applied field during the remanent measurement sections was monitored and the result shown in Figure 83. Here, the field was not measured to perfectly return to zero, or to the same value following each pulse.

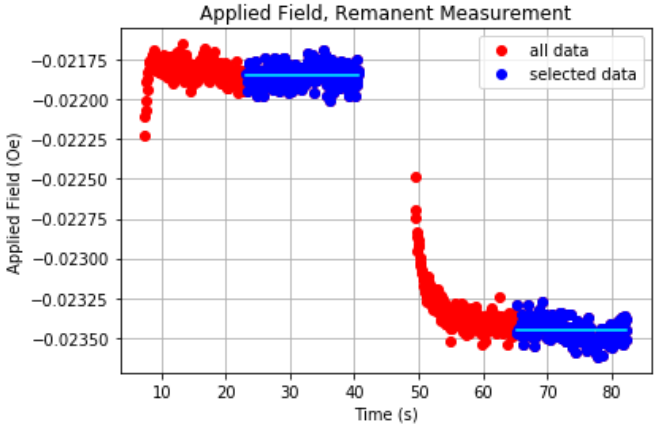

Figure 83: Magnetic field measured by the Lakeshore Hall probe to be present following magnetic field pulses during the remanent sections of measurement.

The difference in applied field between remanent measurement sections, ΔB, was estimated to be 0.0016 Oe. This is consistent with our expectations based on the previously demonstrated field control to a precision of 0.003 Oe. The response of the perforated Hall cross to a uniform applied field with 50 µA of drive current was estimated to be 13.7 µV/Oe (from device characterisation data, as shown in Figure 79a). From equation (84), we estimated the contribution to V_{Hall} due to ΔB to be -0.011 µV. We expect a negative polarity contribution, as a more positive field is present during the first remanent measurement than the second.

For the continuous cross with magnetic disks, the same measurement approach and data analysis were employed. In Figure 84a, we present the Hall voltage response to the field sequence shown in Figure 80a. The 50 µA current was driven in the same direction as for the perforated cross and thus the global response was of the same polarity, as expected. In Figure 80b, we focus on the Hall voltage response recorded during the remanent sections of the measurement and used for analysis.

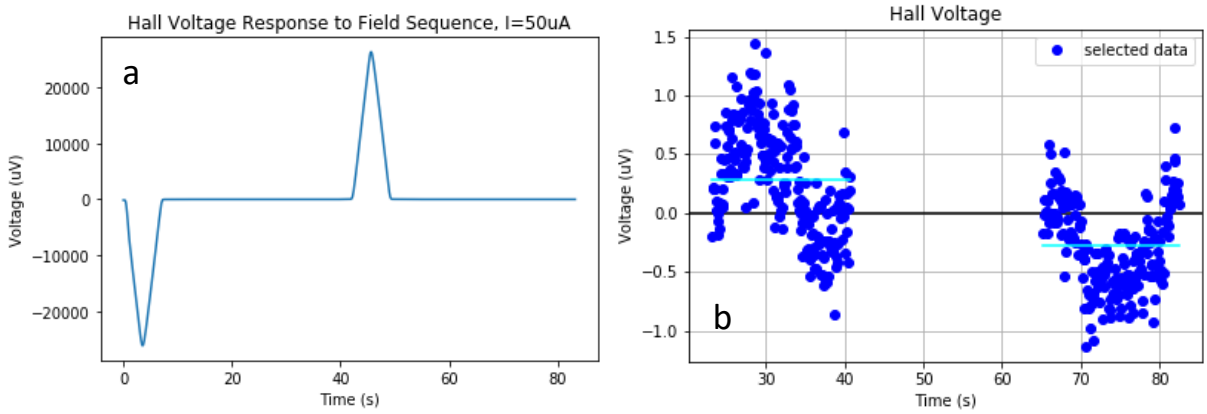

Figure 84: (a) Hall Voltage response of continuous cross with 6 µm magnetic disks, drive current 50µA, to the field sequence shown in Figure 80(a), (b) Hall Voltage response in between magnetic field pulses showing data used for analysis.

Here, the voltage level during each remanent section was near identical in magnitude, however a positive polarity V_{Hall} was calculated, as in the case of the perforated cross. This suggests that the V_{Hall} response was caused by a field opposite in polarity to that of the magnetising pulse sequence. This is not consistent with our expectations for the response of a continuous cross to the magnetic disks. For the continuous cross with an array of 6 µm disks, we find V_{Hall} = 0.3 ± 0.3 µV at a drive current of 50 µA. The applied field during the remanent measurement sections was monitored, as shown in Figure 85, and the difference, ΔB, was again found to be 0.0016 Oe, giving a corresponding error voltage of -0.011 µV.

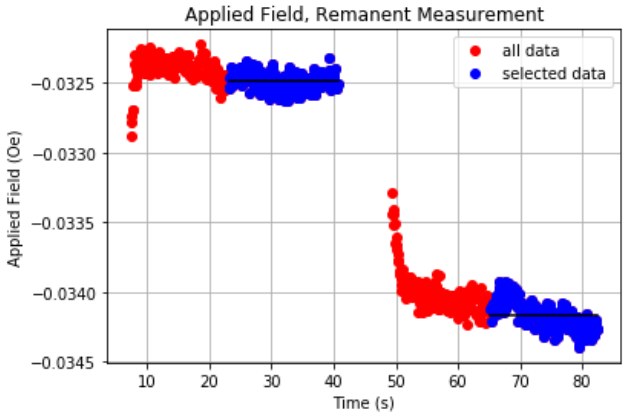

Figure 85: Magnetic field measured by the Lakeshore Hall probe to be present following magnetic field pulses during the remanent sections of measurement.

For the continuous cross with no magnetic disks, the same measurement approach and data analysis were employed. In this case, because no magnetic particle was present, the difference in voltage between remanent levels should be zero. In Figure 86, we present the V_{Hall} response to the pulse sequence shown in Figure 80a. Again, we ensured that the 50 µA current was driven in the same direction as for the other crosses. In Figure 86b we focus on the Hall voltage response recorded during the remanent sections of the measurement and used for analysis.

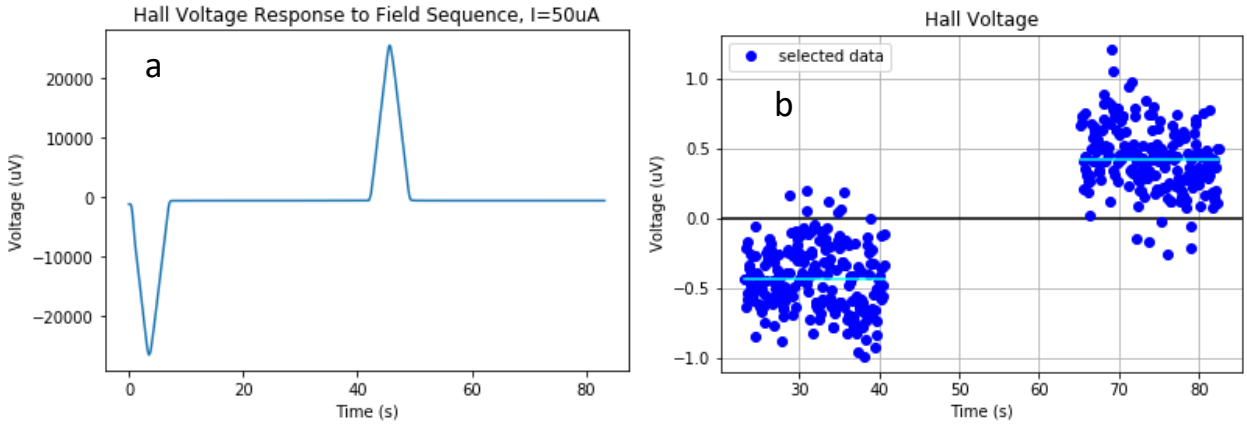

Figure 86: (a) Hall Voltage response of continuous, blank cross, drive current 50µA, to the field sequence shown in Figure 80(a), (b) Hall Voltage response in between magnetic field pulses showing data used for analysis.

In this case, the voltage levels during each remanent section were again close to equivalent in magnitude, however a negative polarity V_{Hall} was calculated. For the blank reference cross, we find V_{Hall} = - 0.4 ± 0.2 µV at a drive current of 50 µA. The polarity is consistent with the field applied during remanent measurement sections due to lack of field

control, as shown in Figure 87. However, the measured ΔB was again 0.0016 Oe, with a corresponding error voltage of -0.011 μV, which is not large enough to explain the result of -0.4 ± 0.2 μV.

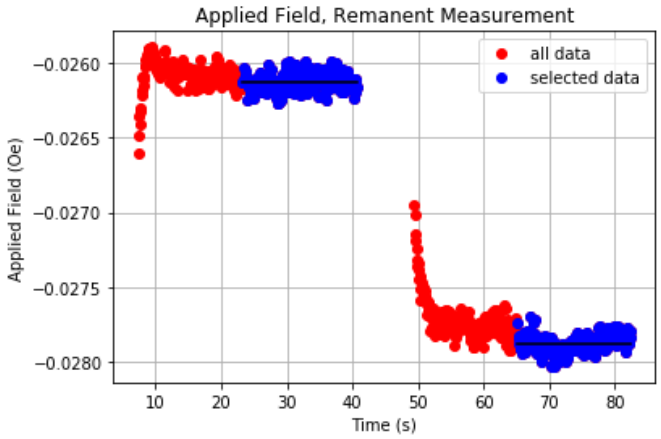

Figure 87: Magnetic field measured by the Lakeshore Hall probe to be present following magnetic field pulses, during the remanent sections of measurement.

To further investigate the source of this Hall voltage response, we estimated the difference in applied field, ΔB, needed to produce the measured response at the blank reference cross, and found it to be 0.06 Oe. It is consistent with some element of the measurement setup magnetising with the applied pulse sequence, resulting in an applied field 0.06 Oe higher following the first pulse than the second. This local field was not measured by the Lakeshore Hall probe. We repeated the measurement with the magnetic field pulse sequence applied in the opposite direction and find that the polarity of V_{Hall} changes. This is consistent with something magnetising within the setup following the applied field pulse sequence and rules out the possibility that the voltage simply drifts in time, leading to the second voltage measurement being consistently elevated relative to the first. In Figure 88, we show the Hall voltage measured at the blank continuous reference cross, as a function of drive current, using the original (orange) and reversed (green) pulse sequences.

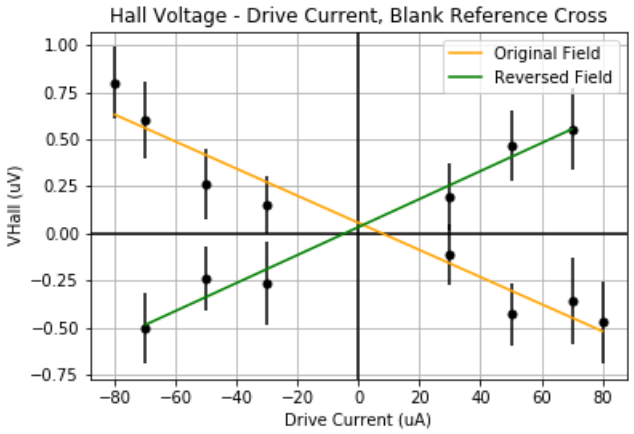

Figure 88: Hall voltage versus drive current, collected using remanent measurement approach without gradiometer, on continuous, blank reference cross, with magnetic field pulse sequence applied in usual direction, and reversed.

For each of the Hall crosses, the V_{Hall} response was calculated using the remanent measurement approach as a function of drive current. The results are presented in Figure 89a, with linear fits superimposed on the data. Clearly, the array of magnetic disks on the perforated cross (red dots) gives the largest V_{Hall} response, and the polarity is consistent with our expectations. For the continuous cross (pink dots), the V_{Hall} response to the array of magnetic disks is much lower

(factor of ~9) in magnitude than the perforated cross, however the polarity of the response is not consistent with simulations. It is also not explained by the possibility of a local field due to some element of the setup magnetising, or inaccurate field control close to 0, as the background response measured at the blank, continuous reference cross (orange dots) is of opposite polarity. Possible explanations for the unexpected polarity of the Hall signal from the continuous cross will be discussed in more detail in section 4.5.2. In Figure 89b, we subtract the slope of the data measured at the blank reference cross from the data calculated at the perforated and continuous crosses. Here, we assume that the V_{Hall} response measured at the blank reference cross was due to a background field present at all crosses.

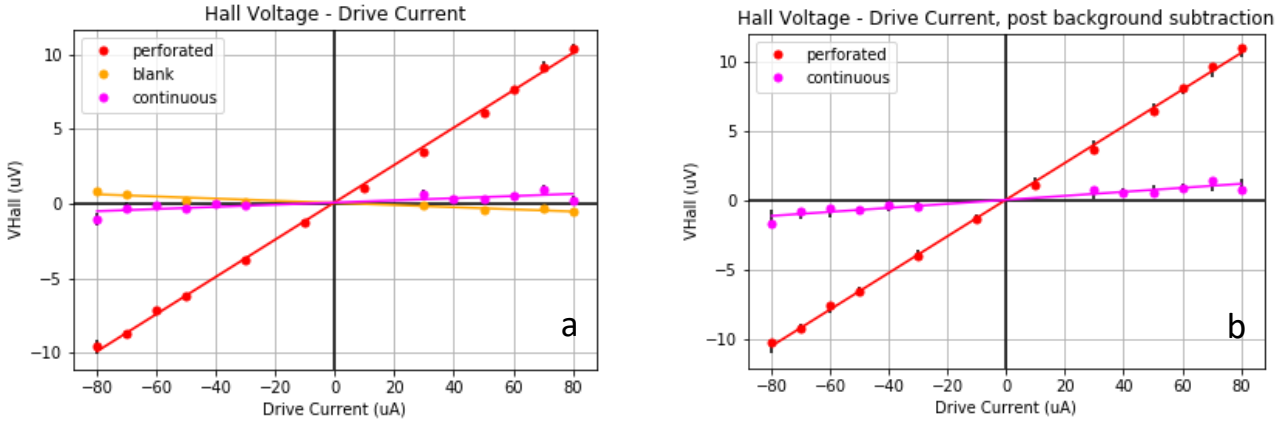

Figure 89: (a) Hall voltage versus drive current, collected using the remanent measurement approach without the gradiometer, for the perforated cross with 6 µm magnetic disks, continuous cross with 6 µm magnetic disks and continuous, blank reference cross. (b) Same data for the perforated and continuous crosses after background subtraction of the slope of the continuous blank reference cross.

Each data point was calculated following equation (83), by combining measurements at positive and negative particle stray field. Thus, the current source and voltmeter offsets, thermoelectric offset, and the contact misalignment offset discussed in section 2.4.4 are expected to be removed from V_{Hall}. The remaining offsets (the Nernst effect and Right-Leduc voltages) can be removed by combining measurements at positive and negative polarity current, which will be carried out at a later stage of the analysis. However, we expect that these offsets drift in time and given the 70-minute acquisition time per measurement, combining positive and negative polarity current data is not expected to be effective at removing these offsets.

Finally, the measured difference in applied field, ΔB, between remanent measurement sections is shown in Figure 90a for each cross. From our knowledge of the cross response to applied uniform field as a function of drive current, we calculated the expected associated error voltage, as shown in Figure 90b. Firstly, we point out that these values are much less (over an order of magnitude) than the error voltages associated with the voltage level fluctuations (generally between 0.1 and 0.8 µV). Secondly, we notice that these values are much less (approaching 2 orders of magnitude) than the Hall voltage response measured at the continuous blank reference cross, which we concluded likely results from components of the system magnetising following the applied pulse sequence. Thus, we consider the error in Hall voltage due to lack of field control close to 0 to be essentially negligible in comparison to the errors associated with voltage fluctuations and the response to magnetised system elements.

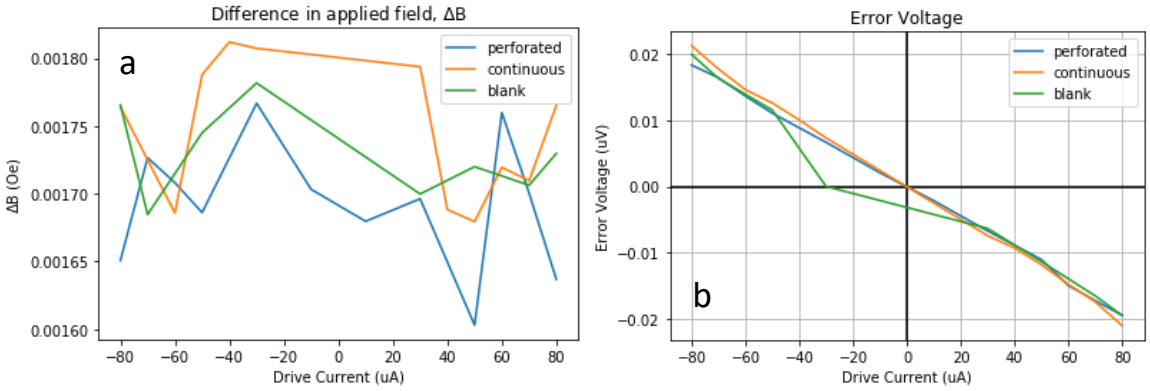

Figure 90: (a) Measured difference in applied field between the two remanent sections of the measurement, (b) corresponding error voltage, due to cross response to measured difference in field.

4.3.1.2 With the gradiometer

The remanent measurements were also taken using the gradiometer. Here, current was passed through the cross of interest and simultaneously through the blank, continuous reference cross in the opposite direction. A magnetic field of 200 Oe amplitude (less than the switching field of the particles) was swept and the V_{Hall} response recorded. The current through the blank cross was varied until the V_{Hall} response as a function of applied field appeared to have a slope of zero and the gradiometer was then considered balanced. The same magnetic field pulse sequence as used in the previous section was applied and the V_{Hall} response of the gradiometer recorded and analysed. The current though the cross of interest was driven in the same direction as for measurements taken without the use of the gradiometer, so the V_{Hall} response is expected to be consistent in polarity with the data presented in the previous section.

The results for the perforated cross with a drive current of 50 µA are shown in Figure 91. In Figure 91a, we see the V_{Hall} response as a function of applied field when the gradiometer was considered balanced. The current through the blank cross was controlled manually, with current increments not always precise enough to achieve a perfectly flat response. The response slope is calculated to be 0.012 ±0.001 µV/Oe, 3 orders of magnitude lower than the 13.7 µV/Oe response slope for the cross without the gradiometer. We expect that the response of the gradiometer to unwanted magnetic fields is reduced by the same factor (assuming said field is present at both crosses).

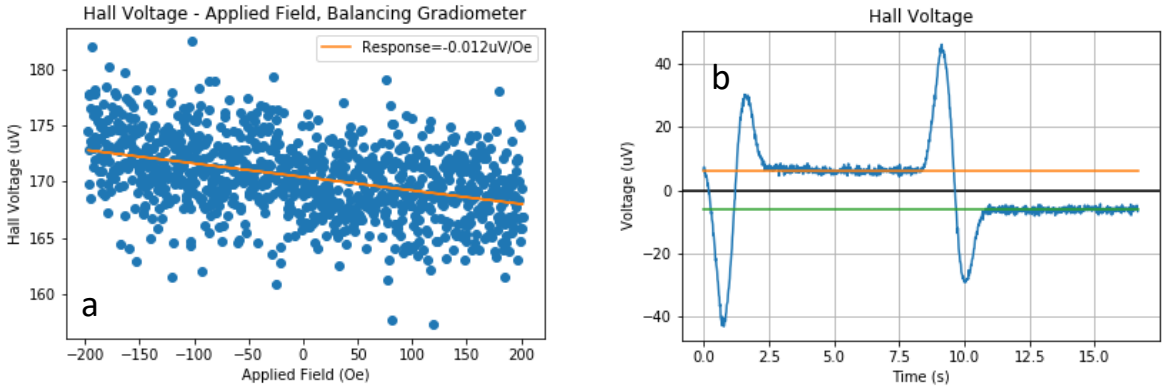

Figure 91: (a) Response of the gradiometer when considered balanced to applied field of ±200 Oe, (b) Hall Voltage response of perforated cross with 6 µm magnetic disks to remanent measurement pulse sequence, when balanced gradiometer is set up.

The Hall voltage response of the cross to the applied magnetic field pulse sequence when the gradiometer was balanced is presented in Figure 91b. With the response of the cross to the magnetic pulses essentially nullified, the

difference in voltage levels between remanent sections can be immediately seen, as highlighted by the orange and green lines. The dual polarity spikes in the V_{Hall} response prior to each remanent section is likely due an EMF induced in the device due to the changing field.

In Figure 92a, we present the data collected between applied field pulses in red, with the data used for analysis highlighted in blue. Using these sections of the remanent measurement, $V_{Hall}(B_{FM}+)$ and $V_{Hall}(B_{FM}-)$ were calculated as the average voltage following the first and section pulses, respectively. The V_{Hall} response due to the magnetic disk array was then calculated following equation (83). The polarity of V_{Hall} was positive, in agreement with our expectations for a perforated cross. The standard deviation in the voltage during each remanent measurement section was also calculated, and the error in V_{Hall} was calculated as the standard deviations, combined in quadrature, and divided by 2, following standard error analysis. For the perforated cross with an array of 6 µm disks, we find V_{Hall} = 6.2 ± 0.5 µV at a drive current of 50 µA.

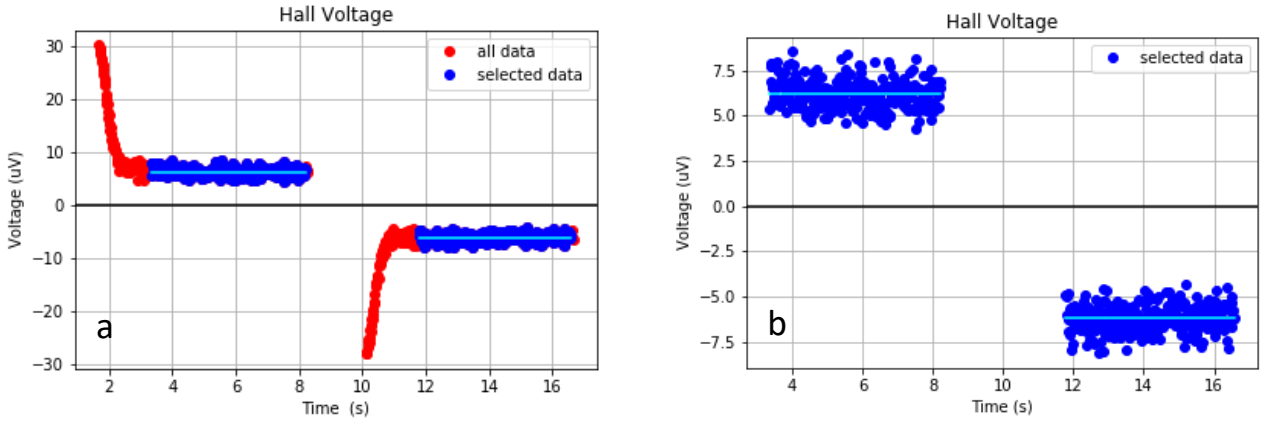

Figure 92: Hall Voltage response in between magnetic field pulses, on continuous cross, with 6 µm magnetic disks, with gradiometer balanced, showing all data (a) and data used for analysis (b).

Using this setup, much less time is required for the voltage response following the field pulses to stabilise. This allows larger sections of the remanent measurements to be used in analysis, and the measurement frequency to be increased, compared to the approach without the gradiometer. Here, we use a measurement frequency of 0.06 Hz in combination with the NVM rate setting of 1PLC and the total time required for the acquisition of 50 single shot measurements is 14 minutes, giving a decrease in measurement time by a factor of 5.

The results for the continuous cross with magnetic particles and a drive current of 50 µA are presented in Figure 93. Figure 93a shows the V_{Hall} response as a function of applied field when the gradiometer was considered balanced. The response slope is calculated to be 0.001 ±0.001 µV/Oe, ~4 orders of magnitude lower than the 13.7 µV/Oe response slope for the cross without the gradiometer. We expect the response of the gradiometer to unwanted magnetic fields to be reduced by the same factor (assuming said field is present at both crosses). The Hall voltage response of the cross to the applied magnetic field pulse sequence when the gradiometer was balanced is presented in Figure 93b.

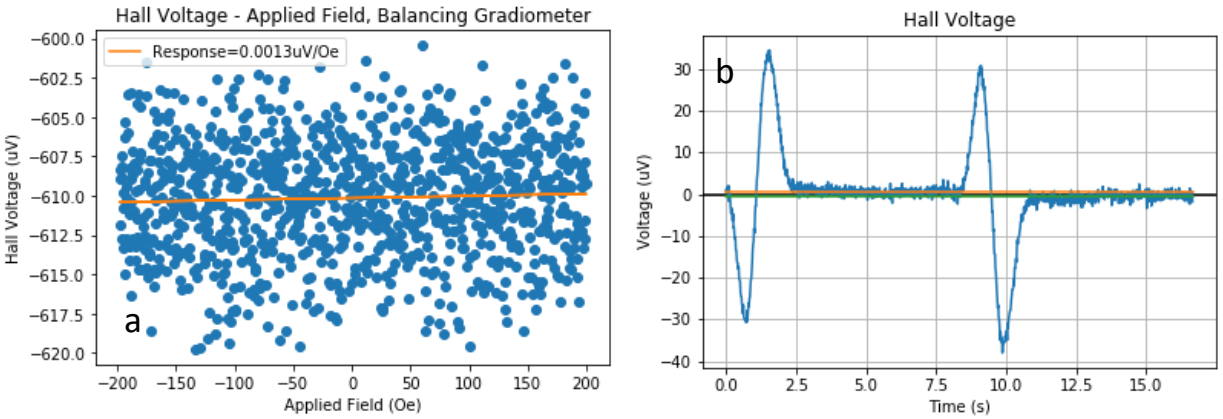

Figure 93: (a) Response of the gradiometer when considered balanced to applied field of 200 Oe amplitude, (b) Hall Voltage response of continuous cross with 6 µm magnetic disks to remanent measurement pulse sequence, when balanced gradiometer is set up.

Figure 94a shows the data collected between applied field pulses in red, with the data used for analysis highlighted in blue. The Hall voltage was calculated to be positive in polarity, as for the perforated device, and consistent with results collected without the gradiometer. For the continuous cross with an array of 6 µm disks, we find V_{Hall} = 0.6 ± 0.7 µV at a drive current of 50 µA.

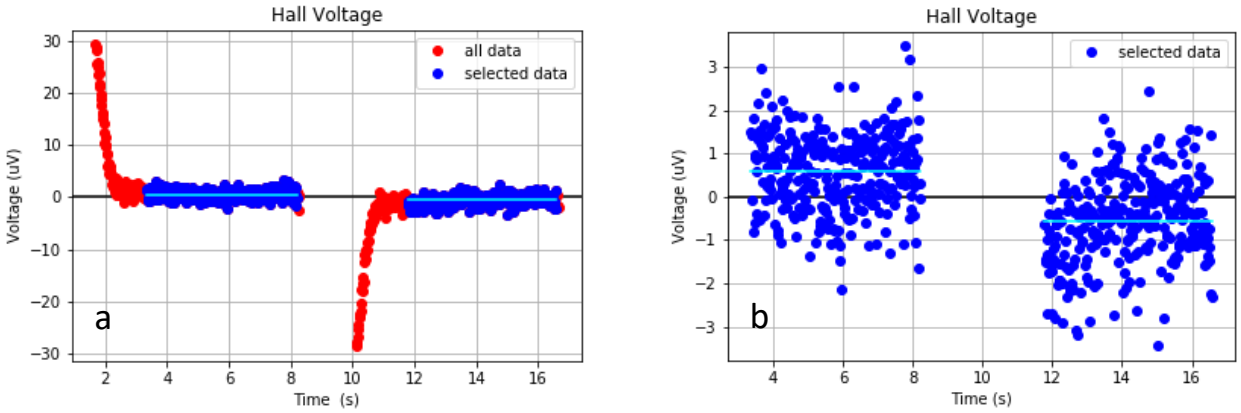

Figure 94: Hall Voltage response in between magnetic field pulses, on continuous cross, with 6 µm magnetic disks, with gradiometer balanced, showing all data (a) and data used for analysis (b).

Figure 95 shows the V_{Hall} results measured as a function of drive current. Again, the response to the disks on the perforated cross is larger in magnitude (by a factor of ~9) than the continuous cross. The polarity of the responses is consistent with that measured without the use of the gradiometer.

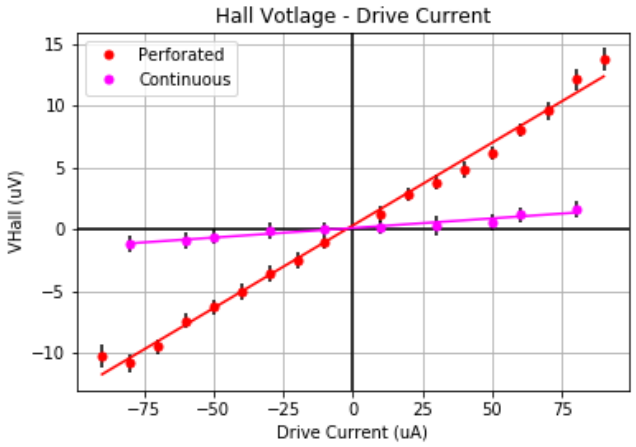

Figure 95: Hall voltage versus drive current data, collected using the remanent measurement approach, with balanced gradiometer, for the perforated and continuous cross with 6 µm magnetic disks.

Figure 96a shows the response of the gradiometer when considered balanced for the presented measurements (shown as a function of drive current). The response fluctuates between positive and negative polarity as for each measurement, the gradiometer had to be manually re-balanced, and there is a roughly 50-50 probability that the disbalance will be in either direction. In Figure 96b we show the measured ΔB due to imperfect field control for each measurement taken using the gradiometer.

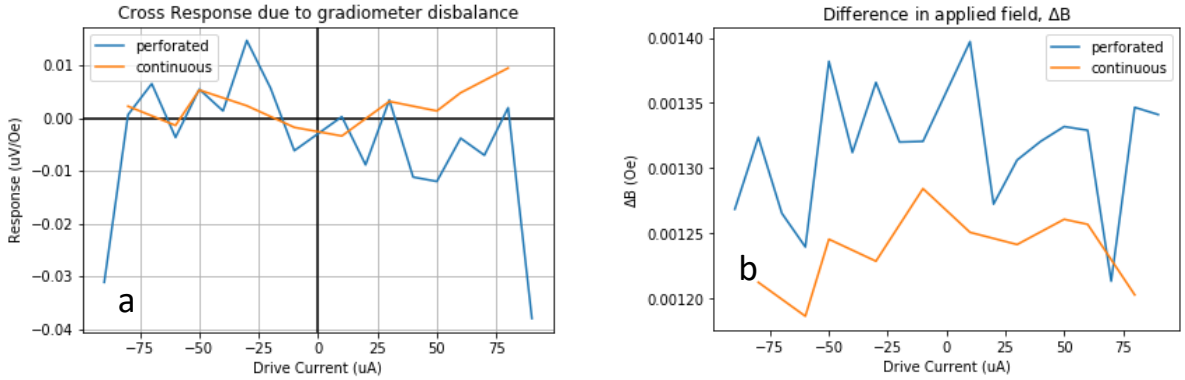

Figure 96: (a) The response of the balanced gradiometer to applied magnetic field, (b) measured difference in applied field between the two remanent sections of the measurement.

The expected error voltage due to imperfect field control (from Figure 96b) in combination with imperfect gradiometer balancing (from Figure 96a) is shown in Figure 97a. In Figure 97b, we show the expected error voltage due to the measured ΔB of 0.06 Oe, calculated by multiplying the data shown in Figure 96a by 0.06 - thought to be due to components of the system magnetising. We point out that the units on the vertical scales of both figures are nV. We thus expect that the gradiometer reduces the Hall response to unwanted background fields to values beyond the detection limits of the setup (voltage fluctuation errors in 0.1 to 0.8 µV range in general).

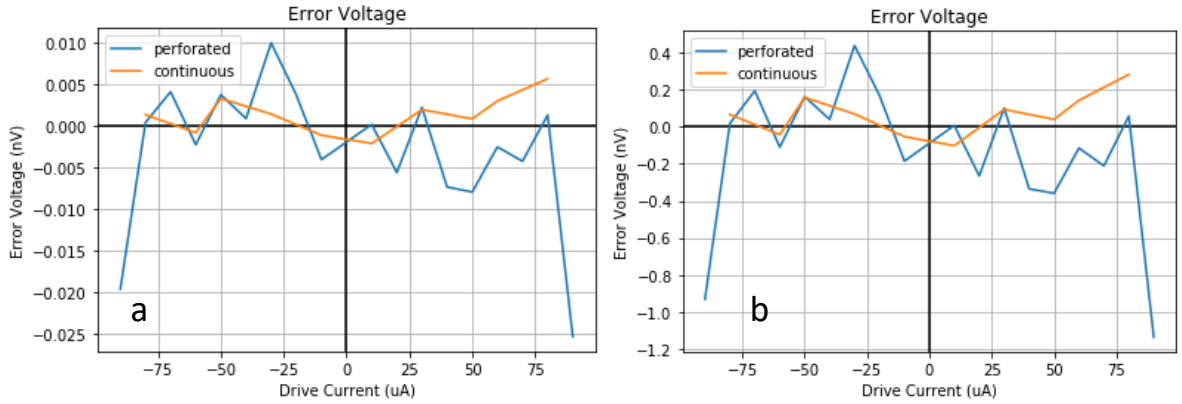

Figure 97: Error voltage due to imperfect balancing of gradiometer in combination with (a) imperfect field control (measured ΔB versus drive current from Figure 96a) and (b) 0.06Oe ΔB estimated as being present, due to magnetised setup elements.

4.3.2 Hysteresis loop measurements

The gradiometer set-up was also employed to extract the hysteresis loop of the array of 6 μm diameter magnetic disks. In this approach, a magnetic field larger than the saturation field of the disks was swept while the Hall voltage was measured across the main bar of the device. Current was driven through the cross of interest and simultaneously through the continuous blank reference cross in the opposite direction, such that the gradiometer was balanced. In this configuration, the Hall voltage response due to any magnetic field which was present at both crosses in the gradiometer was zeroed and the Hall voltage response to the magnetic disk array as a function of the applied field was isolated and measured. The extracted hysteresis loops were normalised and compared with the same measured using MOKE. Agreement in the measured magnetic switching behaviours is taken as corroboration of the fact that the Hall signal is produced in response to the magnetic disks.

When conducting these measurements, the slowest measurement frequency offered by the system (0.006 Hz measurement frequency in combination with NVM rate setting of 5PLC) gave the best results (meaning that it produced a hysteresis loop that required the least amount of post-processing). At this frequency, 2.5 hours was required for the acquisition of 50 single-shot measurements for averaging. With these settings, the switching behaviour of the disks was reasonably clear, however post-processing of the loops was usually required. This was carried out using the LXPro software of the NanoMoke3, designed to remove offsets and artefacts from hysteresis loops acquired using MOKE. The loops were processed, such that by eye, they were deemed to best resemble a hysteresis loop (constant voltage response with a slope of 0 at/above applied fields for which the particles have saturated, loops closed at both ends).

This data was collected as a function of drive current and the processed loops used to calculate the Hall voltage due to the particle array. As before, the average voltage when the particles were magnetised by positive applied field, $V_{Hall}(B_{FM}+)$, was calculated, as was the average voltage when the particles were magnetised by negative applied field, $V_{Hall}(B_{FM}-)$. The Hall voltage due to the particle array, V_{Hall}, was calculated following equation (83). The error was again calculated as the standard deviation of each voltage measurement, combined in quadrature and divided by 2. This error was considered an underestimate however as, often, a range of processing parameters produced acceptable hysteresis loops leading to different values for V_{Hall}. Thus, for each measurement, the data was analysed once using the processing parameters which gave the 'best' hysteresis loop and twice more, using the parameters which gave

loops just on the bounds of acceptable, to estimate the minimum and maximum possible V_{Hall}. The previously calculated error was added to the minimum and maximum V_{Hall} values, and a range of uncertainty estimated. When presenting the results, the Hall voltage calculated from the 'best' loop is shown, and the error bars extend asymmetrically, to cover the discussed V_{Hall} range.

Because of the large amount of data processing involved, any quantitative data resulting from these measurements will be used with caution. However, as we will see, the quantitative agreement between the V_{Hall} values extracted using this method and the V_{Hall} values measured using the remanence methods is very good, and the qualitative agreement between the hysteresis loops obtained using this method and the corresponding MOKE loops is compelling confirmation that the signal we measure is indeed due to the presence of the particles.

Here, we show the results of the Hall voltage measurements taken at the perforated Hall cross using the hysteresis measurement approach. We ensured that the current though the cross of interest was driven in the same direction as for all previous measurements, such that the polarity of the V_{Hall} response was expected to be consistent. For lower drive currents (10 µA and 30 µA), as shown in Figure 98a and b, the signal magnitude was small, and the artefacts relatively large. There was thus a large range of processing parameters that were considered reasonable.

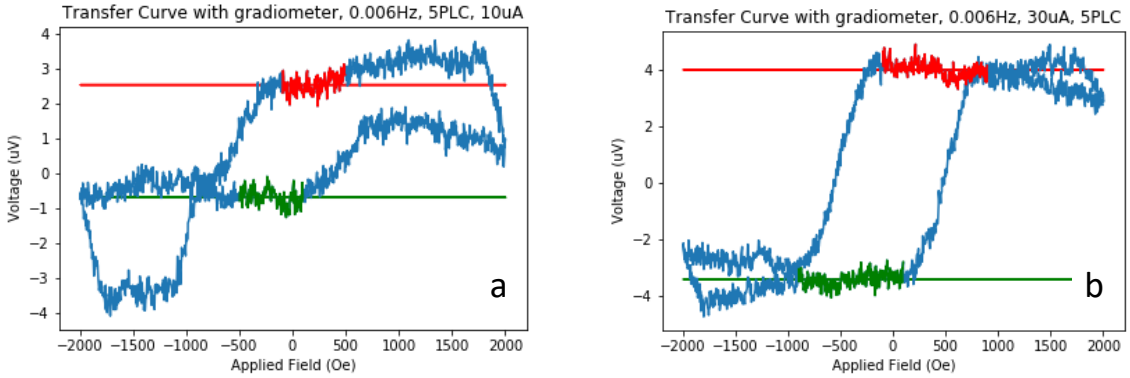

Figure 98: Processed hysteresis loops acquired using balanced gradiometer, for perforated cross with 6 µm magnetic disks, at a drive current of (a) 10 µA and (b) 30 µA.

For higher drive currents (80 µA), the magnitude of the signal was large relative to the noise, however it appears that the system was unstable, as can be seen from Figure 99.

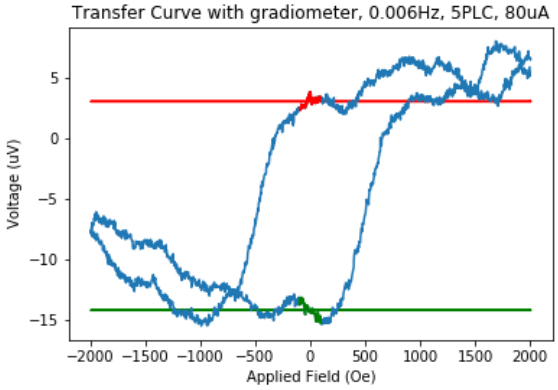

Figure 99: Processed hysteresis loop acquired using balanced gradiometer, for perforated cross with 6 µm magnetic disks, at a drive current of 80 µA.

A compromise seemed to exist at 50 µA to 70 µA, where little post-processing of the loops was required, as shown in Figure 100a and b.

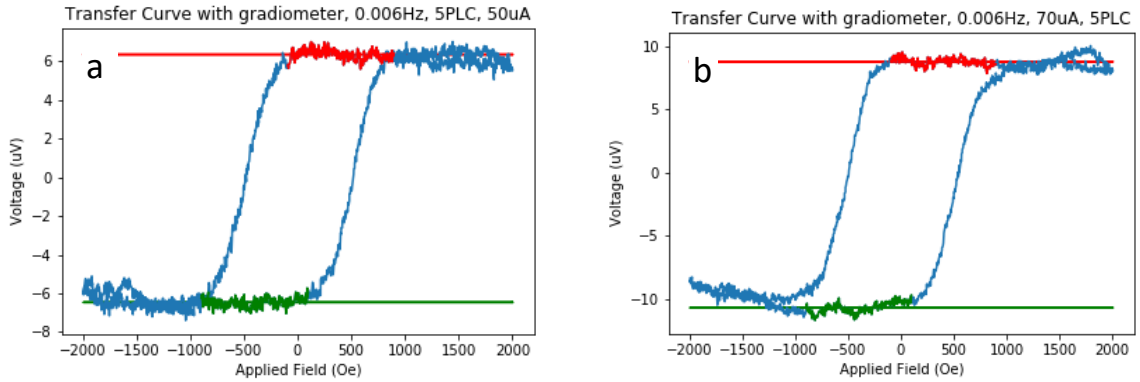

Figure 100: Processed hysteresis loops acquired using balanced gradiometer, for perforated cross with 6 µm magnetic disks, at a drive current of (a) 50 µA and (b) 70 µA.

The data collected at a drive current of 50 µA was compared with the MOKE data for the disk array in Figure 101. Here, the switching behaviours clearly match very well, confirming that magnetic particles are indeed being measured.

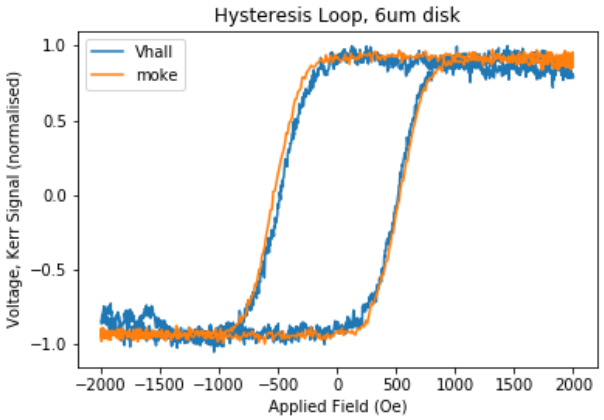

Figure 101: Hysteresis loop acquired using gradiometer V_{Hall} measurements (blue), and MOKE measurement (orange), showing excellent agreement.

Finally, we used these measurements to calculate the V_{Hall} response as a function of drive current, as shown in Figure 102. When the applied field was positive in polarity, the V_{Hall} response was positive in polarity. This is consistent with the remanent measurements, where a positive field pulse resulted in a negative V_{Hall} response to the global field, but a positive V_{Hall} response to the particle array, due to the perforations. The polarity of these results is thus consistent with those taken using other measurement approaches, and with simulation predictions.

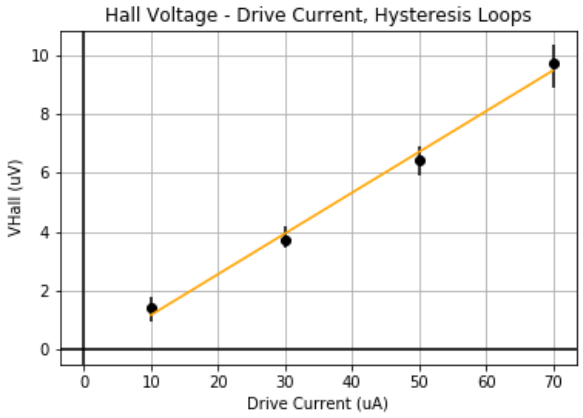

Figure 102: Hall Voltage versus drive current data, acquired at perforated cross with 6 µm magnetic disks, from hysteresis loop measurements taken using the gradiometer setup.

For the continuous cross, it was found that the hysteresis measurements could not be acquired. Figure 103 illustrates the data collected on the continuous cross at a drive current of 50 µA, overlaid with the corresponding hysteresis loop acquired using MOKE. No processing parameters were found which satisfactorily resulted in a hysteresis loop, matching the MOKE loop in form, and from which V_{Hall} could be calculated.

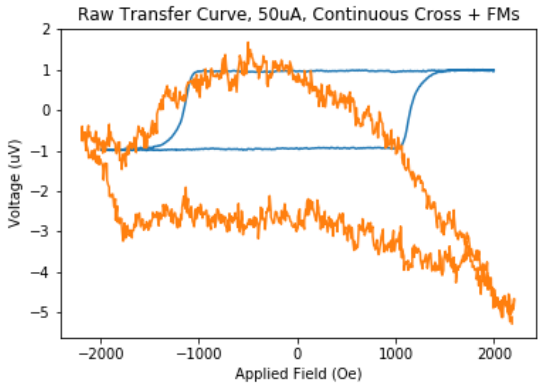

Figure 103: Processed hysteresis loop acquired using balanced gradiometer, for continuous cross with 6 µm magnetic disks at a drive current of 50 µA (orange). The corresponding MOKE hysteresis loop is overlaid for comparison (blue).

4.3.3 Comparison of approaches

The results from the different measurement approaches are compared in Figure 104. We show the data collected at the perforated cross using the remanent measurement approach, with (blue) and without (red) the gradiometer. For the data collected without the gradiometer, the slope of the data collected on the blank continuous reference cross was subtracted. The data collected using the hysteresis loops are also included (black), and the results from the three approaches demonstrate great agreement within the bounds of experimental error. We also show the data collected at the continuous cross using the remanent measurement approach, with (green) and without (pink) the gradiometer. Once again, for the data collected without the gradiometer, the slope of the data collected on the blank continuous reference cross was subtracted, and the results agree well within bounds of experimental error. As mentioned previously, the polarity of the Hall response on the continuous cross does not match our expectations (i.e., the Hall voltage response of the continuous cross to the magnetic disks should be opposite in polarity to that of the perforated

cross, since the polarity of the stray field falling upon each sensor is opposite) and this will be discussed further in section 4.5.2.

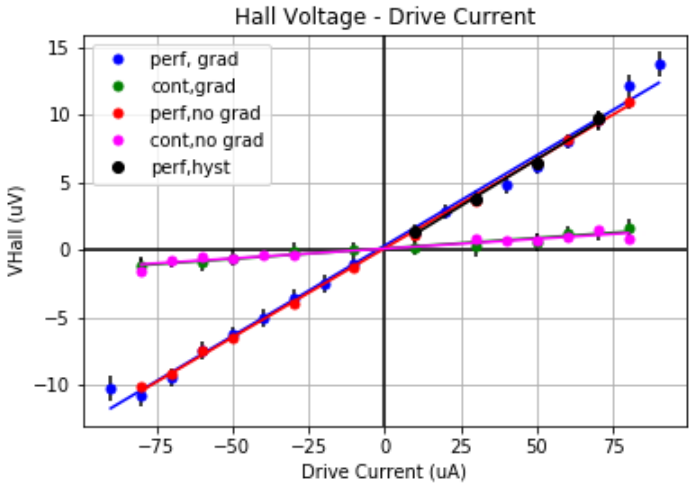

Figure 104: Comparison of Hall voltage versus drive current data for both the perforated and continuous crosses with 6 µm magnetic disks, acquired using all measurement approaches.

In Table 13, the slopes extracted from Figure 104 are presented. The measurement approach is indicated in the first column, with (Rem, NG) referring to remanent approach without the gradiometer, (Rem, G) referring to the remanent approach with the gradiometer and (Hyst) referring to the hysteresis measurement approach.

Measurement approach	Perforated	Continuous
Slope (Rem, NG) µV/µA	0.132	0.0145
Slope (Rem, G) µV/µA	0.134	0.0157
Slope (Hyst) µV/µA	0.138	-

Table 13: Summary of the slope of the Hall voltage versus drive current measurements for the various measurement approaches, in response to an array of 6 µm magnetic disks.

The average slope for the perforated cross is 0.135 µV/µA and 0.015 µV/µA for the continuous cross. These slopes will later be compared with COMSOL predictions.

Figure 105 shows the signal to noise ratio (SNR) as a function of drive current for (a) the perforated and (b) continuous crosses. The SNR is presented for data collected using the remanent measurement approach with (blue) and without (orange) the gradiometer, and from the hysteresis measurements (black). Focusing on the perforated cross, the remanent measurement approach without the gradiometer shows the best SNR, with a maximum of ~30. The SNR for the remanent measurements conducted with the gradiometer, and the hysteresis measurements, are similar, showing maximum values of ~14 and 11 respectively. It appears that the SNR peaks between 50 µA and 70 µA, for all approaches. For measurements conducted above 80 µA (not included) the single shot Hall voltage measurements, 50 of which were consistently acquired per measurement for averaging, began to fluctuate largely in magnitude and vary in polarity. It was thus concluded that the measurements were unstable above 80 µA of drive current. For the continuous cross, the maximum SNR is again seen for the remanent measurements conducted with the gradiometer, here showing a maximum of 4. As the signal magnitude is substantially smaller (roughly an order of magnitude), we expect a correspondingly decreased SNR.

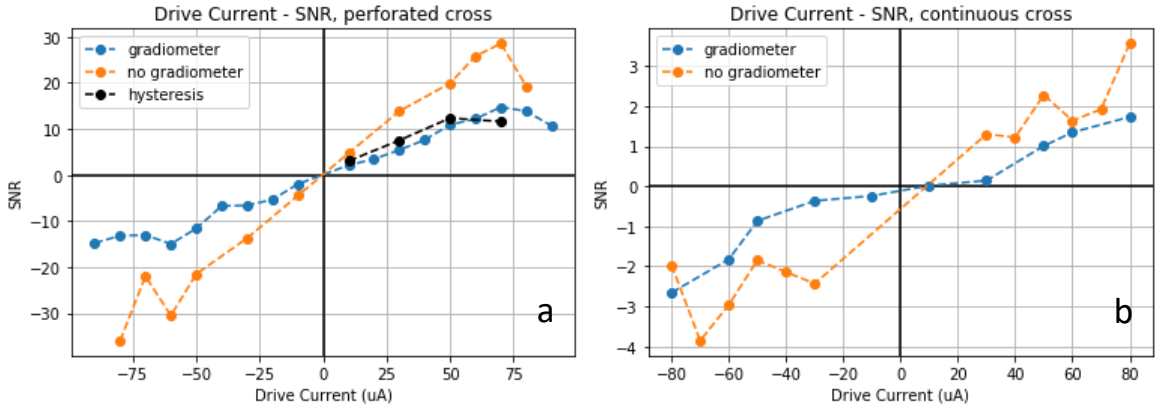

Figure 105: Signal to noise ratio (SNR) for data collected using all measurement approaches in response to the 6 μm magnetic disk array, at (a) the perforated and (b) the continuous Hall cross.

While the remanent measurements conducted without the gradiometer show optimum SNRs, we point out that these measurements require 70 minutes to run, and an additional measurement to be conducted upon the blank continuous reference cross for background subtraction, giving a total measurement time of 140 minutes. The same measurements conducted using the gradiometer require only 14 minutes, providing a 10-fold improvement in measurement speed. The SNR of these measurements could likely be improved by using slower measurement frequencies (5PLC), if desired. The hysteresis measurement approach, while slowest (2.5 hrs) and showing the worst SNR, is the only approach that can be used to measure non-remanent particles.

We focus on the Hall voltage measurements collected at drive currents for which the SNR is optimum. Using these data, we calculated the average Hall voltage signal per particle and expressed the error in the measurement in terms of particle number. In Table *14*, we present the results for the perforated cross for each measurement approach. The Hall voltages calculated at positive and negative polarity current were averaged to give the final V_{Hall} result and the associated error ΔV_{Hall}. The average V_{Hall} signal per particle was then calculated by dividing this result by the number of particles present (81 for the 9x9 array measured here). From the average single particle signal, the error in the Hall voltage was expressed as a number of particles. For the hysteresis approach, measurements were acquired only at positive polarity current. From this table we see that the error in terms of number of disks is at best ±3 disks for the remanent measurement without the use of the gradiometer. The error increases to ±5 disks for the remanent approach with the gradiometer, and ±7 for the hysteresis measurements.

Approach	I (μA)	V_{Hall} (μV)	ΔV_{Hall} (μV)	V_{Hall}/disk (μV)	Error (disks)
Rem, NG	50	6.51	0.22	0.080	3
Rem, NG	70	9.46	0.27	0.117	3
Rem, G	50	6.26	0.39	0.077	6
Rem, G	70	9.47	0.49	0.117	5
Hyst	50	-	-	0.079	7
Hyst	70	-	-	0.117	8

Table 14: Hall Voltage response to the 6 μm disk array, and the associated error expressed as number of particles. Results compiled for the perforated cross, for all measurement approaches.

Table 15 tabulates the results for the continuous cross for each measurement approach. In this case, the error in terms of number of disks is at best ±21 disks for the remanent measurement without the use of the gradiometer. The error

increases to ±27 disks for the remanent approach with the gradiometer, and the disks were unmeasurable with the hysteresis approach.

Approach	I (μA)	V_{Hall} (μV)	ΔV_{Hall} (μV)	V_{Hall}/disk (μV)	Error (disks)
Rem, NG	50	0.65	0.23	0.008	29
Rem, NG	80	1.20	0.30	0.015	21
Rem, G	50	0.58	0.44	0.0072	62
Rem, G	80	1.42	0.46	0.017	27

Table 15: Hall Voltage response to the 6 μm disk array, and the associated error expressed as number of particles. Results compiled for the continuous cross, for all measurement approaches.

In all cases, the best accuracy was achieved using the remanent measurement approach without the gradiometer. This corresponded to a measurement error of ±3 disks for the perforated cross and ±21 disks for the continuous cross, 7 times worse. Thus, overall, we conclude that the remanent measurement approach without the gradiometer offers the best accuracy and so will be the primary approach used to measure the Hall voltage response to particles of other diameters in following sections. The remanent approach with the gradiometer demonstrates reduced accuracy, however an improvement in measurement speed by a factor of 10, and so will be used when quick and/or corroborative measurements are needed. The hysteresis measurements, while slowest and offering the worst accuracy, will be used primarily to confirm that the measured Hall voltage signal is due to the magnetic disks.

While we aimed to compare signals from the perforated and continuous crosses directly to verify that the signal enhancements suggested by COMSOL are seen experimentally, we refrain from making such a comparison at this point. Firstly, the diameters of 'equivalent' disks are significantly different, such that a fair direct comparison cannot be made. However more strikingly, the polarity of the signal measured at the continuous cross does not match our expectations, suggesting that something experimentally is occurring which we have not accounted for in our simulations. The results for the continuous and perforated crosses will instead be compared independently with predictions from COMSOL later in this chapter and explanations explored. However, we have seen in this section that the perforated cross clearly offers enhanced signal magnitude and improved measurement resolution in terms of the uncertainty in the number of disks present on the Hall cross.

4.4 Other disk diameters

The Hall voltage responses, V_{Hall}, of perforated and continuous Hall cross to the presence of 4 and 3 μm diameter disks were also measured. Having previously discussed the methods of data analysis for all measurement approaches, only the analysed results are shown. We focus upon measurements taken using the remanent approach without the gradiometer as this was shown to have the best SNR. Hysteresis measurements with the gradiometer were also conducted to extract the hysteresis loops of the magnetic particle arrays and establish confidence that the measured Hall signals are due to the presence of the magnetic particles.

Figure 106 shows the V_{Hall} results as a function of drive current for the perforated (red) and continuous (magenta) crosses (with the background measurement conducted on the blank, continuous reference cross subtracted). The results are shown for the 4 μm (a) and 3 μm diameter disks (b).

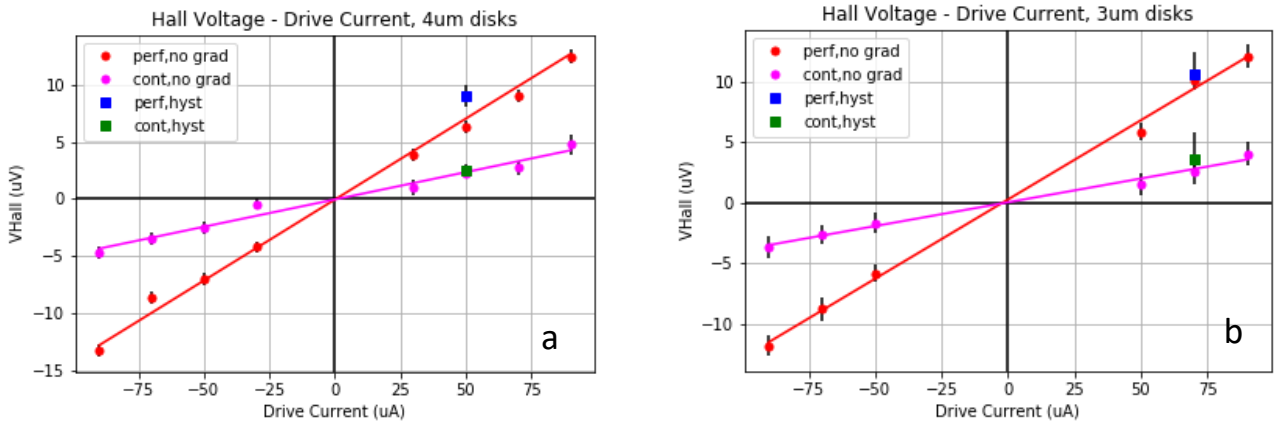

Figure 106: Hall voltage measurements as a function of drive current, for perforated and continuous devices, in response to an array of 4 µm (a) and 3 µm (b) diameter particles.

The results for the perforated crosses are systematically larger in magnitude than the continuous crosses, and the positive polarity of the results matches both our expectations for a perforated cross and that measured for the perforated cross with 6 µm disks. For the continuous cross, the polarity of the results is not consistent with our expectations, however it is consistent with that measured for the continuous cross with 6 µm disks. While lower in magnitude than the perforated cross, the difference is less pronounced (factor of ~3) than seen for the 6 µm disks. The single data points, plotted as squares in blue (perforated) and green (continuous), are the results calculated from measurement of the hysteresis loops of the array. We present the hysteresis loops for the perforated and continuous crosses with 4 µm disks (a,b), and 3 µm disks (c,d) in Figure 107. In each case, we normalise the data and overlay it with the same acquired using MOKE.

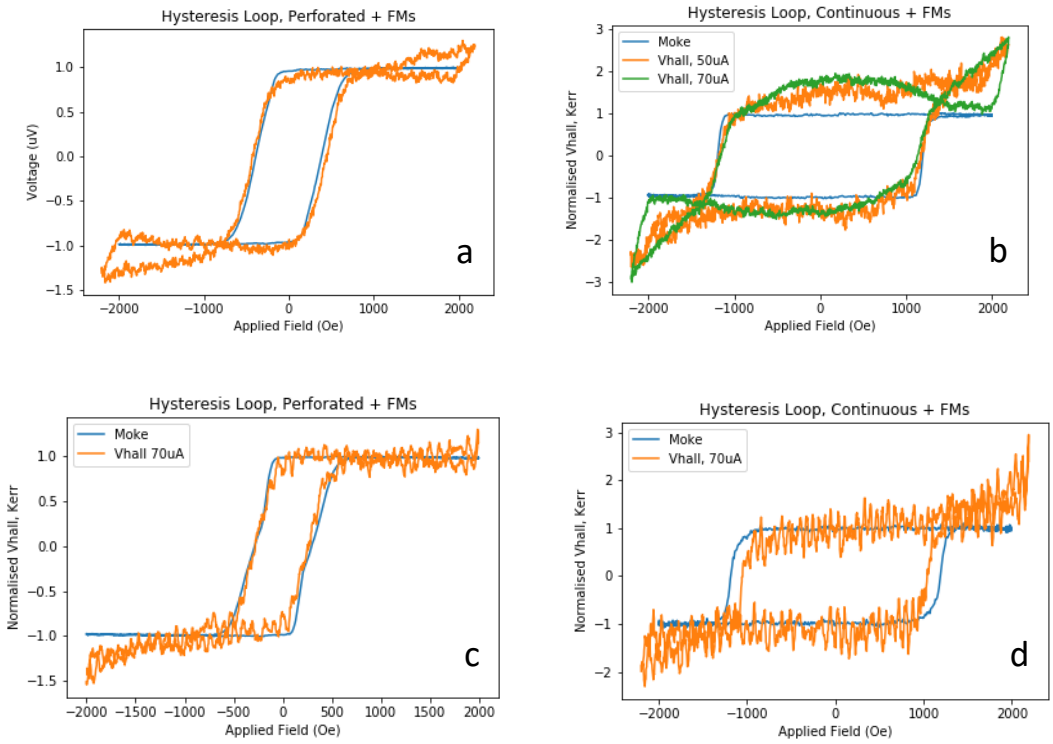

Figure 107: Hysteresis loop measurements taken for the 4 µm disks at the perforated (a) and continuous (b) cross, and for the 3 µm disks at the perforated (c) and continuous (d) cross.

For the perforated crosses, the magnetic switching behaviours measured using the Hall effect and MOKE clearly match very well. The response is positive in polarity for positive applied field, giving a positive V_{Hall}. For the continuous cross, the magnitude of the signal is clearly small relative to the noise and artefacts. While a large amount of post-processing was required, the switching fields measured agree well with those measured via MOKE and the data does resemble a hysteresis loop. We take this as evidence that the measured signal at the continuous cross was indeed due to the magnetic disks. The polarity of the response is the same as for the perforated device, providing further evidence for this unexpected signal polarity.

Here, we focus upon the Hall voltage measurements collected using the remanent measurement approach without the gradiometer at drive currents for which the SNR was maximum. We averaged the Hall voltage responses calculated at positive and negative polarity drive currents to calculate a final Hall voltage response and associated error voltage. From this, we calculated the average Hall signal per particle and expressed the error in the measurement in terms of particle number. The results are shown in Table *16* for the 4 µm disks and in Table 17 for the 3 µm magnetic disks.

	I (µA)	V_{Hall} (µV)	ΔV_{Hall} (µV)	V_{Hall}/disk (µV)	Error (disks)
Perforated	70	8.83	0.39	0.052	8
Perforated	90	12.85	0.41	0.076	6
Continuous	70	3.07	0.42	0.0182	24
Continuous	90	4.75	0.50	0.0281	18

Table 16: Hall Voltage response to the 4 µm disk array, and the associated error expressed as number of particles. Results compiled for the perforated and continuous cross.

	I (µA)	V_{Hall} (µV)	ΔV_{Hall} (µV)	V_{Hall}/disk (µV)	Error (disks)
Perforated	70	9.45	0.45	0.0327	14
Perforated	90	11.9	0.47	0.0413	12
Continuous	70	2.57	0.44	0.0089	50
Continuous	90	3.86	0.52	0.0133	40

Table 17: Hall Voltage response to the 3 µm disk array, and the associated error expressed as number of particles. Results compiled for the perforated and continuous cross.

The baseline error voltage is roughly constant (~0.4-0.5 µV) across devices of different disk diameter, as well as across continuous and perforated devices. The signal per particle decreases with decreasing disk diameter, meaning that the error in the measurement of particles of smaller diameter is equivalent to larger numbers of disks. Across all disk diameters considered, the single particle Hall signal is larger for disks of equivalent diameter at the perforated crosses than the continuous, and the error in the measurement in terms of number of disks smaller. We remember that the diameters of the disks on the continuous device are significantly larger than those on the perforated device, biasing the comparison to the advantage of continuous devices. Thus, we conclude that we do see significant improvements in device performance with the addition of perforations.

4.5 Comparison of experimental and computational results

Here, we simulate the Hall voltage response of the perforated and continuous Hall cross devices for all disk/perforation diameters and compare the experimental and computational results.

4.5.1 Perforated Hall crosses

For the perforated cross, two simulations were run for each particle/perforation diameter. In the first, the ideal experimental configuration was modelled in which the disk diameter exactly matched the perforation diameter and the corners of the cross were perfectly square. The disks were 6.17 nm thick with an M_S of 0.5705×10^6 A/m and a working distance of 142.9 nm. The disk diameters used in the simulations corresponded to the average measured values from SEM and AFM, as tabulated in Table *10*. The properties of the 2DEG (carrier concentration, mobility) corresponded to those tabulated in Table 12 following 2DEG characterisation, and all simulations were run at a drive current of 50 µA (current density of 2×10^7 A/m^2). The single particle signal was calculated for all disk positions upon the active area and summed to give the total signal of the disk array.

In the second, a more experimentally realistic adaptation of the above was modelled. Firstly, we saw in section 4.1.3.1.1, evidence that the disks are smaller and the perforations larger in diameter than intended. Both effects were shown in section 3.7 to reduce the Hall voltage response of the perforated device to a magnetic disk. SiO_2 was seen in SEM images to coat the inner walls of the perforations, thus reducing the area into which the magnetic particles are deposited, and so their size. The thickness of material was estimated from SEM images to be roughly 150 nm. The thickness of SiO_2 deposited was more accurately estimated via AFM to be 180 nm, which is regarded as the more realistic estimate (the thickness deposited on the side walls should be roughly the same as that deposited on the substrate since it was an evaporation process). In addition, AFM scans showed a roughly 200 nm gap between the particle edge and the perforation edge, and the literature related to deep mesa etching through a 2DEG suggests that a depletion layer is likely to have formed around the circumference of the perforations due to damage caused by the etching [133]. We have no way to measure the thickness of this depletion zone, however our best estimate from the literature is 25 nm [123]. To account for these issues, our simulations decreased the radius of the modelled disks by 180 nm and increased the radius of the modelled perforations by 200 + 25 = 225 nm. Secondly, we rounded the corners of the Hall crosses. Due to the resolution limitations of optical lithography, the experimental devices appear to have corners rounded with a radius of roughly 10 µm (estimated from optical microscopy images of the Hall crosses). While corner rounding was shown in section 3.7 to reduce the Hall response of the cross to magnetic particles by at most 5%, we still consider the effect worth including.

The results of these simulations are shown in Figure 108, overlaid with the experimental results for each particle size. To produce these plots, the calculated Hall voltage for the array was normalised by the drive current used in the simulations (50 µA) and then scaled by the currents used experimentally. The blue data, labelled COMSOL, shows the predicted results using the ideal model and the green data, labelled COMSOL adjusted, shows the predicted results when the discussed experimental factors have been included in the model.

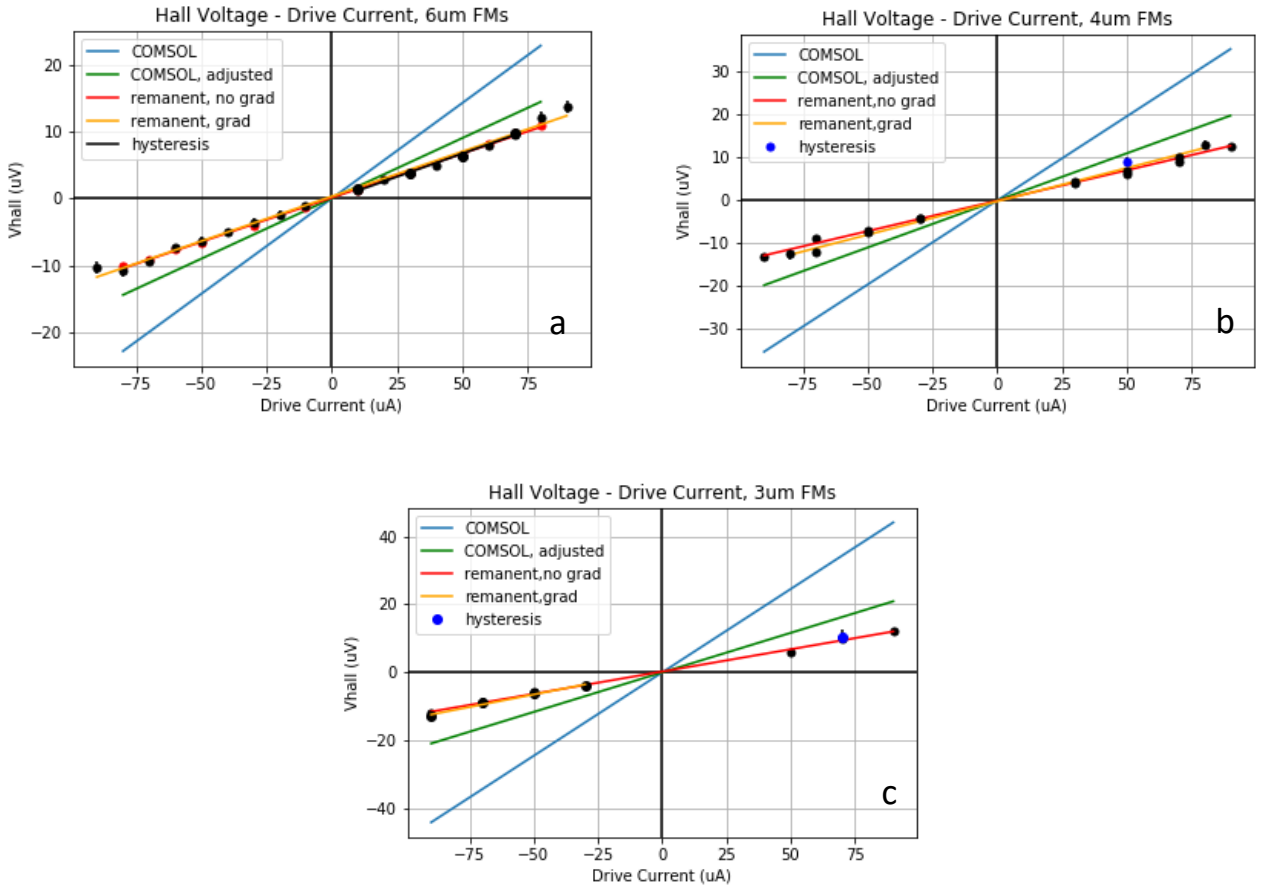

Figure 108: Comparison of experimental data and COMSOL predictions for perforated crosses with magnetic particles of diameter (a) 6 µm, (b) 4 µm and (c) 3 µm.

For all diameters, the results from the ideal COMSOL model over-estimate the experimental results. The agreement is vastly improved by using the more experimentally realistic model, as expected. To assess the level of agreement, we compared the slope of the Hall voltage vs drive current response as measured experimentally and predicted by COMSOL, using both the ideal and adjusted models. In Figure 109a, we show the slope as a function of disk diameter, and in Figure 109b, we show the percentage difference between the computational and experimental results. Best agreement is seen for the 6 µm diameter particles, with a 32% difference with respect to the experimental data. This difference increases as the particle diameter decreases, to 40% for 4 µm disks and 60% for 3 µm disks.

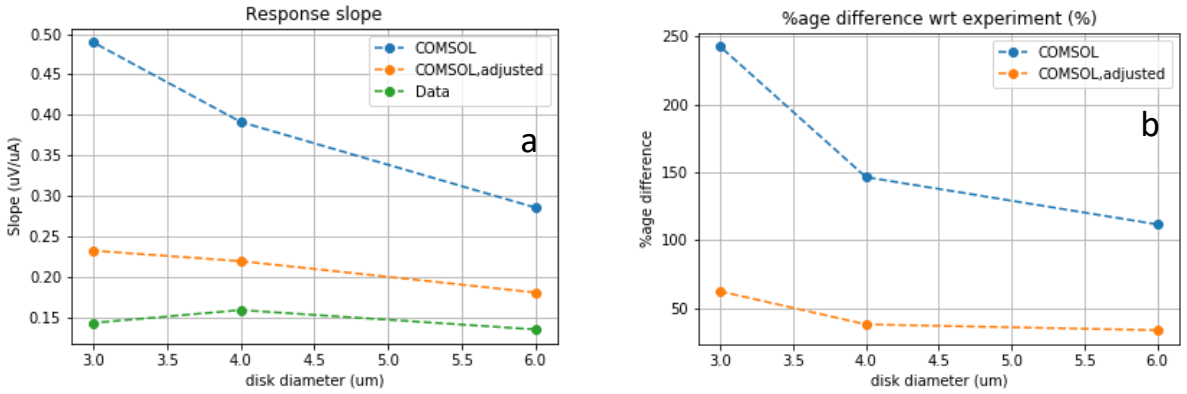

Figure 109: (a) Slope of the Hall voltage vs drive current response, as measured experimentally and calculated by COMSOL using the ideal and adjusted models. (b) Percentage difference between slope predicted by COMSOL with respect to that measured experimentally.

In the adjusted model, the particle and perforation diameters simulated are our best estimates, however there is a reasonable amount of uncertainty in these values. Firstly, as mentioned, we have no way to verify the thickness of the dead layer surrounding the perforations. In addition, the figures used for the thickness of SiO_2 and the extent of the particle to perforation edge gap are also estimates. If we have underestimated these numbers, the impact of that underestimation on the agreement between experimental and computational results will be most pronounced for the smallest diameter particles. The same can be said for the working distance used; if the disks are further from the 2DEG than simulated, again this will have the largest impact on the agreement between experimental and computational results for the smallest particles. We demonstrate this in Figure 110, by simulating the Hall voltage response for a single particle situated at the centre of the perforated cross, as these parameters are varied.

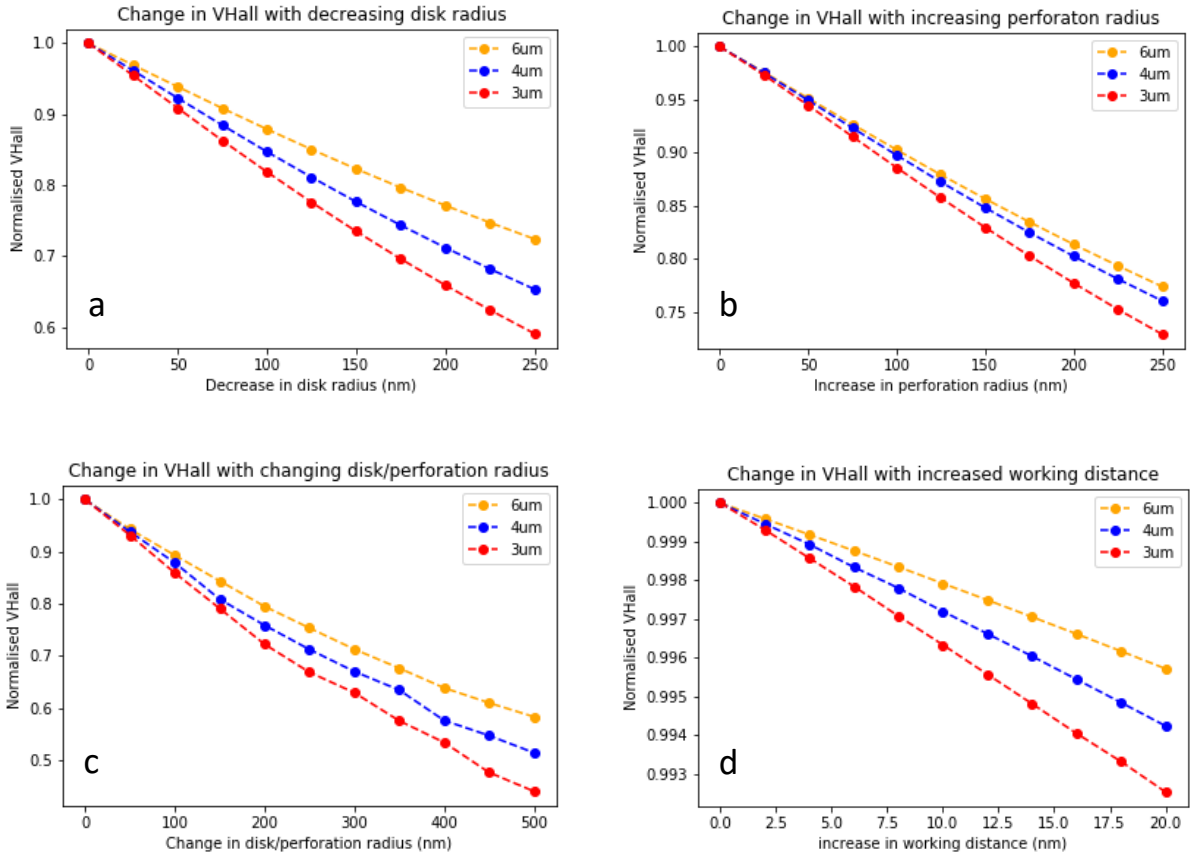

Figure 110: Change in Hall voltage response of a perforated Hall cross to single magnetic disk situated at the cross centre as a function of (a) decreasing disk radius, (b) increasing perforation radius, (c) simultaneous increase of perforation radius and decrease of disk radius, (d) increasing working distance.

In Figure 110a, we show the change in Hall voltage as the diameter of the disk is decreased relative to the perforation. The results are normalised by the Hall voltage response when the disk diameter is equal to the perforation diameter. In Figure 110b, we show the same, as the diameter of the perforation is increased relative to the disk, and in Figure 110c, we show the same, as both the diameter of the disk is decreased and simultaneously the diameter of the perforation is increased. The change in each diameter is the same as simulated in a and b (0 to 250 nm) with the summed distance between disk and perforation edges plotted on the x-axis. In Figure 110d, we show the change in Hall voltage as the working distance is increased. For a given change in working distance or particle/perforation diameter, the impact upon the calculated Hall voltage response is greater the smaller the particle diameter. Thus, if we have underestimated these parameters, the disagreement between computational and experimental results is

expected to be most pronounced for the smallest particles. It should be noted that while changing the relative dimensions of the disk and perforations has a non-negligible impact on the results, changing the working distance does not, with variations of less than 1% observed up to a change of working distance of 20 nm.

From the disagreements shown between experimental and computational data, we consider it likely that we have underestimated the particle-perforation edge to edge distance. We also note that the results are directly proportional to the M_S value used in simulations, which again has its own associated measurement uncertainty. We are confident in the experimental results presented, having attained the same results within experimental error (within 0.1 to 0.8 µV range in general) using 3 different measurement approaches. We are also confident in our simulations, having verified them extensively against the literature. In publications describing the agreement between their predictions and experimental data, comparisons within 20% are quoted, which was what we hoped for. Thus overall, we conclude that we have achieved reasonable agreement between experimental and computational results and provided experimental evidence of an enhanced signal due to the added perforations.

4.5.2 Continuous Hall crosses

For the continuous cross, the ideal experimental configuration was modelled for each particle size in which the disk diameters were as measured via SEM (Table *11*), the impact of the skirts was not considered, and the corners of the crosses were perfectly square. The disks were modelled as 6.17 nm thick with M_S of 0.5314e6 A/m and a working distance of 143.6 nm, as described in Table *11*. The properties of the 2DEG (carrier concentration, mobility) corresponded to those tabulated in Table 12 following 2DEG characterisation, and all simulations were run at a drive current of 50 µA (current density of 2×10^7 A/m^2). The single particle signal was calculated for all disk positions upon the active area and summed to give the total array signal.

In Figure 111 the results of these simulations are shown overlaid with the experimental results for each particle size. To produce these plots, the calculated Hall voltage for the array was normalised by the drive current used in the simulations (50 µA) and scaled by the currents used experimentally.

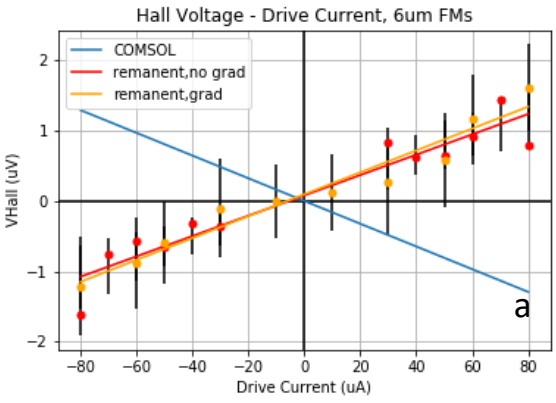

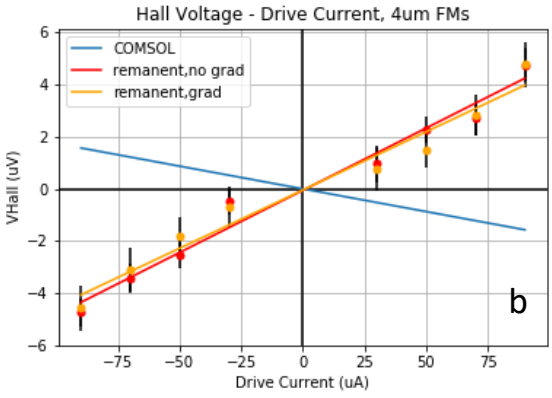

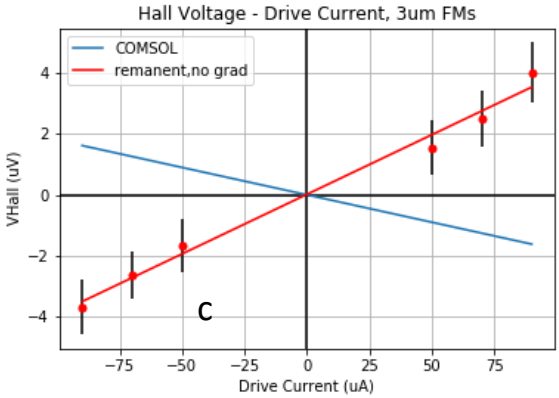

Figure 111: Comparison of experimental data and COMSOL predictions for continuous crosses, with magnetic particles of diameter (a) 6 µm, (b) 4 µm and (c) 3 µm.

It is immediately clear that across all particle diameters, the signal magnitude measured experimentally either agrees well with or is larger than that predicted by COMSOL. But, however good (or bad) the agreement in the signal magnitude is between simulations and experiments, the disagreement in polarity points to a more profound issue which must be addressed. This has been highlighted throughout the analysis and occurs consistently for all particle diameters.

As was highlighted in section 4.1.3.2.1, skirts of material up to 450 nm in height were found to have formed around the disk edges. We used COMSOL to model a 3D magnetic disk with a ring of magnetic material mimicking the skirt, with magnetisation in the z-direction, parallel with that of the disk, but found no evidence of a flip in the polarity of the Hall response with the addition of the skirt. The possibility that there is so much additional magnetic material present that the field beneath the particles is high enough to cause the Hall voltage response to change polarity via the mechanisms discussed in section 2.2.2 is highly unlikely, as fields of ~1 T are needed for such effects to emerge, far greater than the stray field of magnetic particles, even with very large additional material in the skirts.

A more realistic explanation for the observed change in polarity is the possibility that the magnetic disks grown directly on top of the GaAs wafer upon an underlayer of gold cause the depletion of charge carriers in the 2DEG directly below. If local depletion zones exist below the disks, they could theoretically act like quasi-perforations and the Hall cross could produce a Hall voltage response with polarity matching that found on the corresponding perforated crosses.

This idea was explored using COMSOL simulations. For each particle diameter, a simulation was run in which a single particle was placed at the centre of a continuous 100 µm x 100 µm active area Hall cross. The parameters used were the same as those used to model the experimental devices. An array of circles was defined at the positions corresponding to where disks would sit. These circles were designated a different material from the rest of the cross, with mobility kept the same as for the bulk and conductivity defined as the product of the mobility, electron charge and carrier concentration. The carrier concentration in the circles, n_{LOCAL}, was then decreased such that the 2DEG was locally depleted. Figure 112a shows the Hall voltage due to a single particle at the centre of the continuous cross in the presence of these local depletion zones as a function of n_{LOCAL}. The results are calculated for the experimentally measured disk diameters and labelled by the ideal diameters for simplicity.

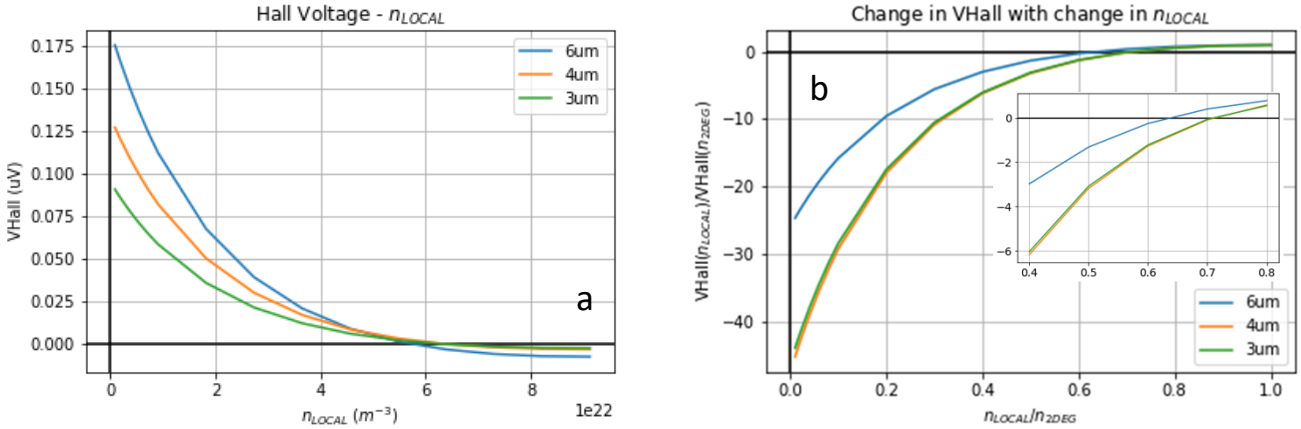

Figure 112: (a) Hall voltage due to a single magnetic disk at the centre of the sensor, in the presence of local depletion zones of carrier concentration given by the x-axis, n_{LOCAL}. (b) Same data, normalised and plotted as a function of n_{LOCAL}/n_{2DEG}. Inset: zoom of the data close to the polarity change.

Figure 112b shows the same data, normalised by the Hall voltage calculated when there is no depletion, as a function of n_{LOCAL}/n_{2DEG}, where n_{2DEG} is the carrier concentration in the rest of the 2DEG. As n_{LOCAL} decreases from the bulk 2DEG value, the Hall voltage first changes polarity and then increases in magnitude. The inset of Figure 112 (b) shows that local depletion of 25-40% is enough to cause the signal to switch polarity. Further decreases in n_{LOCAL} then rapidly give rise to an increased signal magnitude relative to that which we would expect from the continuous cross.

We do not have the possibility to directly measure n_{LOCAL}. However, its existence can be detected when measuring the response of a continuous cross with magnetic disks present to a globally applied magnetic field. From the Hall response as a function of applied field, an effective value of the carrier concentration at the cross can be calculated, n_{EFF}, from equations (79) and (80). We carried out this characterisation in COMSOL by sweeping a global magnetic field, measuring the Hall voltage response of the cross discussed above, where depletion zones of concentration n_{LOCAL} were defined, and extracting the slope of the Hall voltage versus applied field curve. For a given value of n_{LOCAL}, we used this data to calculate n_{EFF}. We repeated this calculation for different values of n_{LOCAL}, representing depletion zones with different extents of depletion. Figure 113a shows the simulated Hall voltage vs applied field responses of a cross with 6.7 µm diameter depletion zones present in a 9x9 array for various values of n_{LOCAL}/n_{2DEG} and Figure 113b shows the calculated n_{EFF}/n_{2DEG} as a function of n_{LOCAL}/n_{2DEG}.

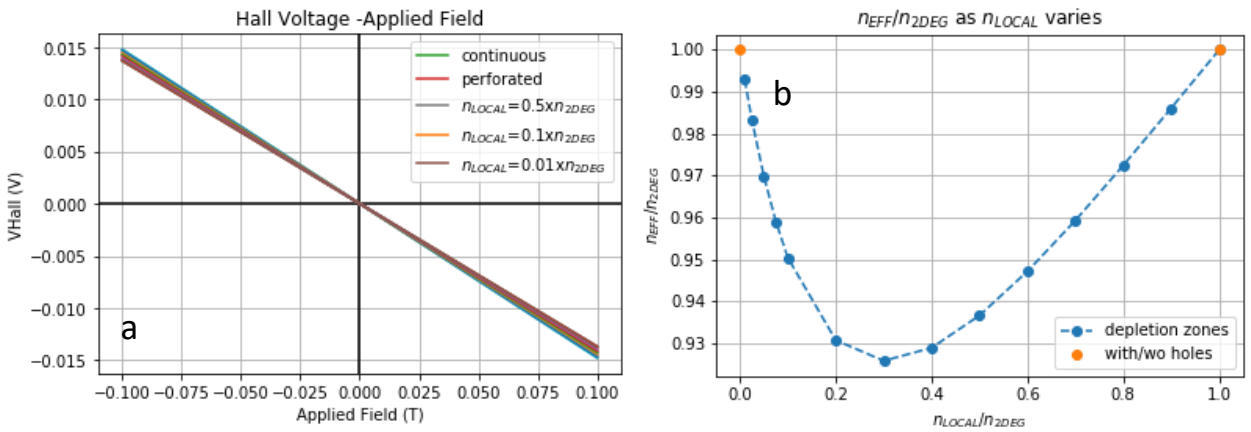

Figure 113: COMSOL characterisation of the continuous cross with depletion zones of varying carrier concentration, n_{LOCAL}. (a) Hall voltage versus applied field data for various n_{LOCAL},(b) the corresponding n_{EFF}/n_{2DEG} vs n_{LOCAL}/n_{2DEG}.

The data point at $n_{LOCAL}/n_{2DEG} = 0$ highlighted in orange was calculated using a fully perforated cross, and the data point at $n_{LOCAL}/n_{2DEG} = 1$ was calculated using a continuous cross. We see that in both these cases, n_{EFF} is equal to n_{2DEG}, whereas n_{EFF} is less than n_{2DEG} for all intermediate cases, by at most 7%. The results for other disk diameters are shown in Figure 114a.

We performed the same characterisation experimentally by measuring the Hall response of continuous crosses with magnetic disks present at a drive current of 50 µA. The corresponding effective carrier concentrations, n_{EFF}, were extracted using equations (79) and (80) for each disk diameter. The same characterisation was performed on the perforated and continuous, blank crosses previously (shown in section 4.2). The values of n_{EFF} obtained for the perforated and blank, continuous sensors were averaged, yielding an experimental value for n_{2DEG}. n_{EFF}/n_{2DEG} is shown as a function of disk diameter for the continuous crosses with magnetic disks in Figure 114b (green), together with the carrier concentrations measured on the continuous, blank cross (orange) and perforated cross (blue) of the corresponding devices, also normalised by n_{2DEG}. For all disk diameters, the carrier concentrations measured on the perforated crosses are in very good agreement with those measured on the continuous, blank crosses, and both are systematically higher than those measured at the continuous cross with magnetic disks. Here, n_{EFF} is on average 4% lower than n_{2DEG}. In Figure 114a, this corresponds to an n_{LOCAL} at around 70% of n_{2DEG}, or a 30% depletion in local carrier concentration, certainly very close to the 25-40% range numerically determined to be able to cause a change in the polarity of the V_{Hall} signal.

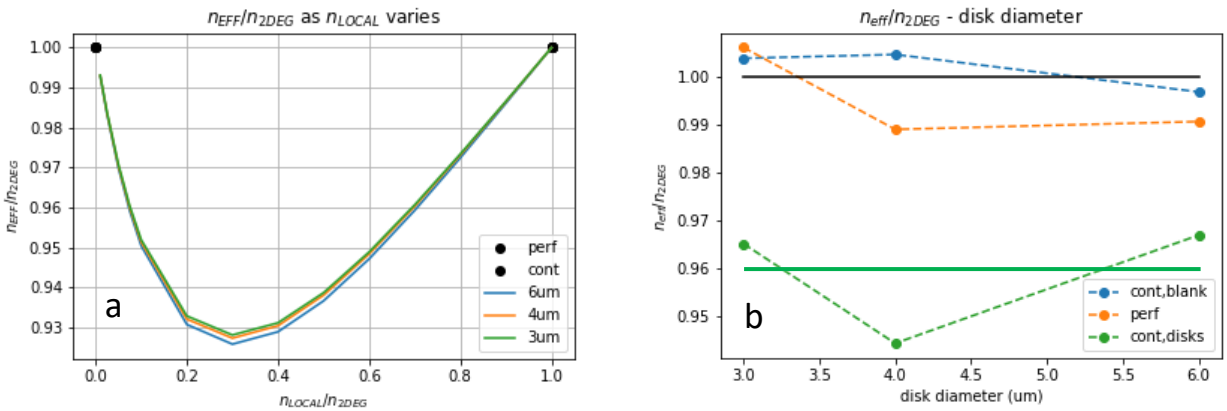

Figure 114: (a) n_{EFF}/n_{2DEG} vs n_{LOCAL}/n_{2DEG} calculated using COMSOL for particles of all diameters. (b) n_{EFF}/n_{2DEG} vs disk diameter measured experimentally on continuous sensors with magnetic disks (green). The carrier concentrations for the corresponding perforated (blue), and blank continuous reference (orange) crosses are also shown, normalised by their average, taken as n_{2DEG}.

We also observed that in addition to the change in polarity, the magnitude of the experimental V_{Hall} signal was larger than expected. Gain increases above 1 (or below -1, if the polarity change is included) are expected for depletion levels in the range of 35 to 50% (see inset of Figure 112b), still very close to the 30% we determined. However, furthering this analysis by comparing the exact experimental gain in signal with the computed expected gain from Figure 112b would prove pointless considering the simplicity of the computational model used and the accuracy of our experimental measurements on continuous crosses.

This effect has been reported in the literature. [90] found that the deposition of gold on top of a AlGaN/GaN 2DEG causes a 28% decrease in the carrier concentration directly below the gold. This was attributed to the formation of a Schottky barrier at the interface and the large work function of gold. This decrease in n_{LOCAL} is not far from that which

we measure, or that which we require to explain the polarity of our resultsfgvvvvvvvvvvvt In addition, where researchers look to measure the Hall voltage response of 2DEG Hall crosses to arrays of metallic magnetic particles, a metallic layer is often first deposited to coat the active area of the cross prior to the addition of the particles. In much of the literature, this step is not justified in any detail, with most authors simply mentioning that they would like the flexibility to be able to alter the carrier concentration in the 2DEG via gating the metallic layer[134][121]. However, in these works, the authors do not find the unexpected signal polarity that we find here. Finally, in [135] the authors add a metallic layer to coat a 2DEG heterostructure Hall cross before the addition of an array of metallic particles, and state that the purpose is to create an equipotential surface. Thus, we are optimistic that should the experiment be repeated, the addition of a metallic layer to fully coat the active area surface could remove the local depletion zones, and so allow us to produce a fully continuous Hall cross with magnetic disks.

In a realistic device for the counting and detection of magnetic disks in a medical context, again we would not expect to see this effect as the disks would land upon the surface from solution, covered with chemical and biological coatings, and such intimate contact between interfaces as to allow Schottky barrier formation would not be expected.

4.6 Conclusions

In the course of this experimental work, we successfully measured arrays of 3, 4 and 6 µm diameter magnetic disks on perforated Hall crosses using remanent and hysteresis measurement approaches. While these measurement approaches are not very precise, they allow us to estimate the strength of the Hall signal. When our computational model is adjusted to simulate experimentally realistic devices, we find agreement to within 32% for the 6 µm magnetic disks. The level of agreement decreases with decreasing disk size, to at worst 60% for the 3 µm disks, however we have shown that the factors responsible for the disagreement are most impactful for the smallest diameter disks, explaining this trend.

The measured Hall signal at the equivalent continuous crosses does not agree with the results of our simulations, most importantly in terms of signal polarity. We have explored potential explanations for this and provided computational and experimental evidence that the observed polarity change is consistent with the creation of localised carrier-depleted regions underneath the particles, causing the continuous sensors to act like hybrid devices, where ‘effective’ perforations are in the process of emerging. This has occurred as the magnetic particles were deposited directly onto the surface of the GaAs/AlGaAs wafer with an underlayer of gold, which locally depletes the carriers of the 2DEG directly below. The extent of the local depletion was estimated from experimental measurements to be in the region of 25-40%, which was found to encompass the depletion value required to explain the change in polarity of the experimental results.

Overall, we did not directly demonstrate the gain in signal strength from the addition of perforations, as measurements on a fully continuous Hall cross for comparison could not be made. However, we did demonstrate that the Hall signal at the perforated crosses is in reasonable agreement with our simulations when adjusted to represent realistic experimental devices. We find this to be good evidence to support the fact that our model is capturing all the physics of the perforated devices, such that the gain in signal should be demonstrated by repeating the fabrication of the continuous Hall crosses. Finally, we note that the partially perforated Hall crosses offer a simpler fabrication

approach for perforation formation in comparison to wet chemical etching. However, the strength of the Hall voltage response is smaller than on the equivalent perforated device, and so we do not expect that etched perforations will be replaced by circular gold pads in any future iterations of the devices.

5 Conclusion and outlook

The main objective of this thesis was to explore whether the performance of large area Hall cross sensors could be optimised via geometrical alterations towards the goal of counting large numbers of magnetic particles with single particle resolution.

To this end, extensive simulations were conducted which demonstrated that the addition of an array of perforations to the active area of Hall cross devices enhanced their capabilities for magnetic particle counting by simultaneously increasing the magnitude of the single particle Hall voltage response and improving the homogeneity of the response as a function of particle position. As a result, a larger number of particles could be measured to an accuracy of ± 1 particle using a single sensor with a higher signal per particle. These improvements were offered when particles landed either aligned with the perforations or centrally located between 4 perforations, with the former offering optimum performance. The gains in signal magnitude were further improved by embedding the magnetic particles within the perforations, aligning their central plane with the central plane of the 2DEG. In the case of the model Hall cross devices focused upon in this work (100 μm x 100 μm active area for the detection of 6 μm diameter particles), gains in signal strength with the addition of a 7x7 array of 6 μm diameter perforations were shown to be over an order of magnitude for both magnetic disks and beads in the embedded configuration and increases in the number of measurable particles per sensor (to an accuracy of ± 1 particle) of 50% were demonstrated.

Our results suggest that the central cause of the enhancement in single particle Hall signal is the enhanced averaged stray field of a particle into the sensor. In addition, by considering the averaged stray field of a particle as a function of position, we showed that the variation in this value was much reduced by the addition of perforations, which we expect is responsible for the improvements in signal homogeneity. We also highlighted the large changes in the current density distribution brought about by the addition of perforations. While it is difficult to quantify how these changes impact the Hall response, we expect that they both alter the relevant effective active area for field averaging and contribute to the Hall response as a function of position, thus constituting a secondary factor responsible for the change in device response with the addition of perforations.

We performed a limited optimisation study focused on the response of perforated Hall sensors to magnetic disks aligned with perforations while varying some geometrical parameters. We found that device performance could be further optimised in several ways. Firstly, reducing the perforation to perforation spacing such that more perforations and so more particles could fit within a given cross active area increased the number of measurable particles at almost no cost to the signal magnitude. Secondly, adding additional perforations into the arms of the cross increased the average single particle signal by 20% at no cost to the number of measurable particles. The effect of active area size and particle/perforation size was also investigated. We found that for a given cross active area, decreasing the particle/perforation diameter resulted in increased numbers of measurable particles (more fit into the active area). The single particle signal decreased, but the gain in signal magnitude from the addition of perforations increased when compared to the equivalent continuous device. In addition, for a given particle size, as the Hall cross active area increased, the gain in the number of measurable particles and the gain in single particle Hall signal increased. In other

words, perforating the device is more effective at improving device performance as the size of the particles decrease with respect to the size of the Hall cross active area. This constitutes a very promising trend in the context of applying this technology to magnetic immunoassays, as reducing the magnetic label towards the size of the biomarker to be captured is considered advantageous.

With our basic understanding of the system established and the superiority of the perforated Hall cross for magnetic particle counting demonstrated computationally, we aimed to validate our predictions by comparison with experiments. To this end, experimental prototype devices were fabricated and the Hall voltage response to arrays of 6, 4 and 3 μm diameter disks was measured. Measurements were conducted using the remanent measurement approach, with and without a gradiometer, as well as via the hysteresis measurement approach. The measurements conducted at the perforated devices showed good agreement with computational results when the model was adjusted to include an experimentally realistic spacing between the particle and perforation edges, accounting for some realities of the device fabrication process. The best agreement was seen for the 6 μm magnetic disks, where computational results agreed with experimental results to within 32%. 81 disks were measured with an uncertainty as low as ±3 disks. The agreement of experimental and computational results worsened with decreasing disk diameter, however the impact of the particle – perforation spacing was also shown to worsen with decreasing disk diameter, explaining the trend. We also found that the measurement uncertainty increased with decreasing disk diameter; while the baseline error voltage remained roughly constant, it was equivalent to a larger number of smaller diameter disks. We measured 169, 4 μm disks with ±6 disks accuracy and 289, 3 μm disks with ±12 disks accuracy.

The results measured at the continuous devices did not agree with computational results, most strikingly in terms of signal polarity. The Hall response of these devices was found to be consistent with the behaviour of Hall crosses at which perforations had partially formed due to the local, partial depletion of the 2DEG directly below the magnetic disks. We proposed that this occurred due to the formation of a Schottky barrier at the GaAs/AlGaAs – gold interface beneath each deposited magnetic disk and supported this hypothesis using a combination of simulations and experimental measurements.

In the future, if additional iterations of the devices were built, we would firstly implement several changes to the fabrication process to produce Hall crosses closer to the ideal devices modelled in COSMOL. Firstly, for the perforated devices, we would investigate the shallow mesa etching technique, to deplete the 2DEG where perforations are required without etching through and potentially damaging the 2DEG. This would obviate the need for the deposition of an insulating layer between the metallic disks and 2DEG, simplifying the fabrication process. We would also work with photoresist with an overhang side-wall profile, to prevent deposited material from coating the inner walls of the resist and perforations. Finally for the continuous devices, we would deposit a uniform metallic layer over the active area of the Hall cross (ideally, one which does not impact the underlying 2DEG without the application of a bias voltage) before the deposition of the magnetic disks. We expect that this would allow us to fabricate Hall crosses at which reference measurements can be conducted, allowing us to directly demonstrate device improvement due to the addition of perforations. We would investigate ways to reduce the measurement noise, perhaps using AC lock-in detection techniques, to improve measurement uncertainty and push the experimental system towards single disk

resolution. Finally, in order to move towards a more realistically useful device, adapting the set-up for the accurate detection of non-remanent magnetic particles such as SAF disks or Dynabeads should be investigated.

In conclusion, we hope to have conveyed how promising these new perforated Hall devices are for the detection of single magnetic tags for biosensing applications, through their enhanced ability to measure many particles with single particle accuracy.

Appendix A – Validation of the model against literature

A1 – Detection of a global, uniform magnetic field - [110]

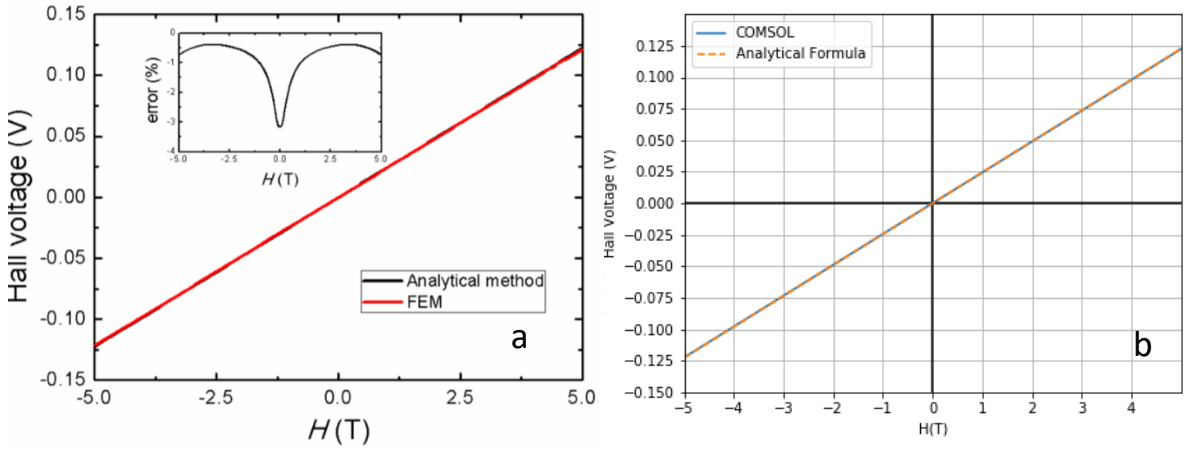

Figure 115: Hall voltage response of Hall cross sensor to a global, uniform applied field. (a) Reproduced from reference [110]*, J. Sun and J. Kosel, "Finite-Element Modelling and Analysis of Hall Effect and Extraordinary Magnetoresistance Effect," Finite Element Analysis - New Trends and Developments. IntechOpen, 2012, doi: 10.5772/47777 . (b) Our calculations.*

We estimate agreement to within 2%.

A2 – Detection of local, inhomogeneous magnetic field profiles

A2.1 – Magnetic dot field profile [111]

a

Figure redacted for copyright reasons

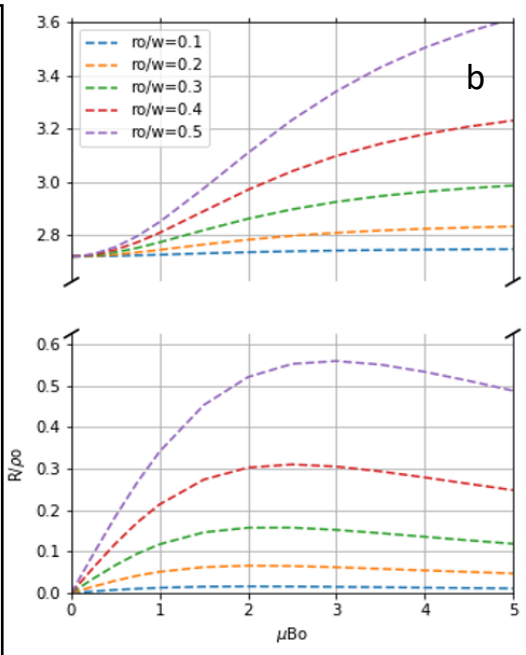

Figure 116: Hall voltage response, expressed as the Hall and Longitudinal resistances, of a 2DEG Hall cross in the diffusive regime, to the field profile of a magnetic dot, as a function of dot field strength. (a) Figure reprinted from reference [111]. (b) Our calculations.

We estimate agreement to within 4%.

A2.2 – Axially symmetric gaussian field profile [111]

a

Figure redacted for copyright reasons

b

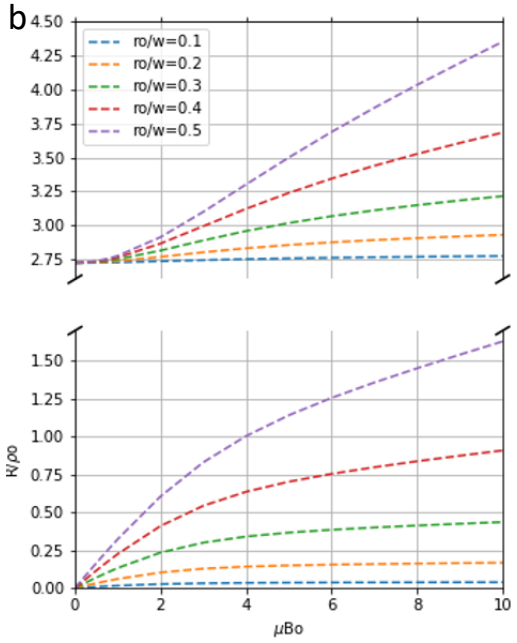

Figure 117: Hall voltage response, expressed as the Hall and longitudinal resistances, of a 2DEG Hall cross in the diffusive regime to a gaussian magnetic field profile as a function of field strength. (a) Figure reprinted from reference [111]. *(b) Our calculations.*

We estimate agreement to within 3%.

A2.3 – Magnetic dipole [111]

For best fit with the authors of reference [111], we use the volume of a sphere with radius of 1.315 mm, to translate magnetisation to moment.

Figure redacted for copyright reasons

Figure 118: Hall voltage response, expressed in terms of the Hall resistance, of a 2DEG Hall cross in the diffusive regime, to the field profile of a magnetic dipole as a function of distance between point dipole and sensor plane. In black: figure reprinted from reference [111]. *In colour: Our calculations.*

We estimate agreement to within 2%.

A2.3 – Single super-paramagnetic bead [85].

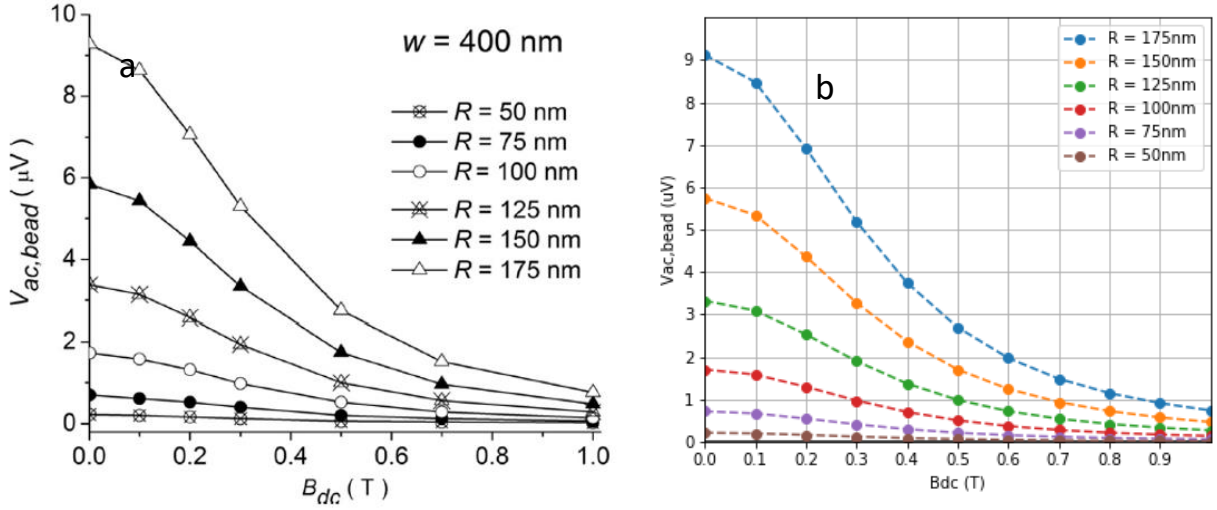

Figure 119: AC Hall voltage V_{ac} response of a Hall cross sensor to the presence of a superparamagnetic bead, as a function of the applied DC magnetising field B_{dc}. (a) Figure reprinted from reference [85], *Modelling and optimization of submicron Hall sensors for the detection of superparamagnetic beads, A. Manzin; V. Nabaei; O. Kazakova, Journal of Applied Physics 111(7):07E513, 2012, with the permission of AIP publishing. doi: 10.1063/1.3678322. (b) Our calculations.*

We estimate agreement to within 2%.

A2.4 – Array of super-paramagnetic beads [80]

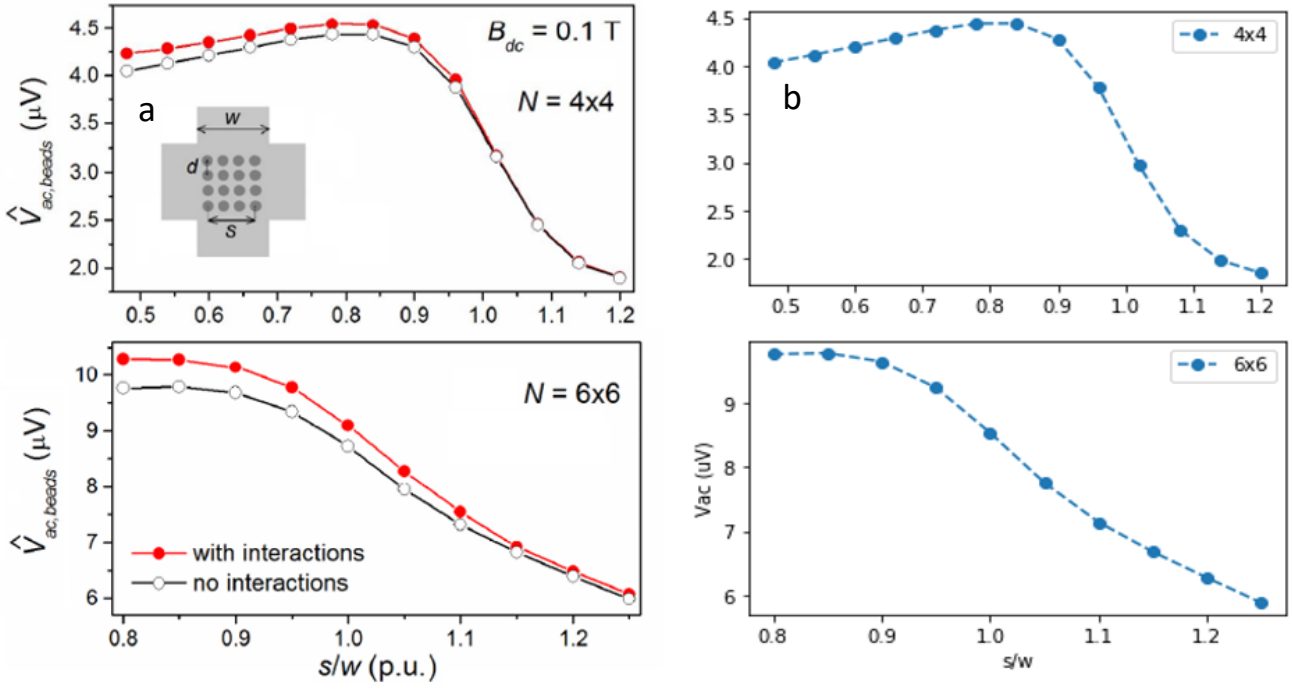

Figure 120: AC Hall votlage response, Vav, of a Hall cross sensor to a 4x4 and 6x6 array of superparamagnetic beads, as a function of the interbead spacing. (a) © [2018] IEEE, Figure reprinted with permission from reference [80], Alessandra Manzin , Vahid Nabaei, and Riccardo Ferrero, Quantification of Magnetic Nanobeads With Micrometer Hall Sensors, IEEE Sensors journal, Vol 18 (24), 2018. Doi: 10.1109/JSEN.2018.2874520 . (b) Our calculations, without inter-bead dipolar interactions.

We estimate agreement to within 4%.

Appendix B– Mesh Analysis

The mesh independence study is performed by calculating the V_{Hall} signal for our arrangement of 13 particles. The study is conducted as a function of the maximum cell size in the active area, the minimum cell size in the active area and the maximum cell size in the arms.

- Active area:
  - curvature = 0.1
  - growth rate = 1.1
- Arms:
  - minimum cell size = 0.01 µm
  - curvature = 0.1
  - growth rate = 1.1
- Contact pads:
  - maximum cell size = 1 µm
  - minimum cell size = 0.002 µm
  - curvature = 0.2
  - growth rate = 1.3

We consider mesh independence to have been reached as a function of a given mesh parameter when the results vary by less than 2% as a function of that parameter.

B1 – Continuous device

Magnetic disks at a 90 nm working distance.

B1.1 – Mesh independence vs maximum cell size in active area

- minimum cell size in the active area = 0.01 µm
- maximum cell size in the arms of 2.5 µm

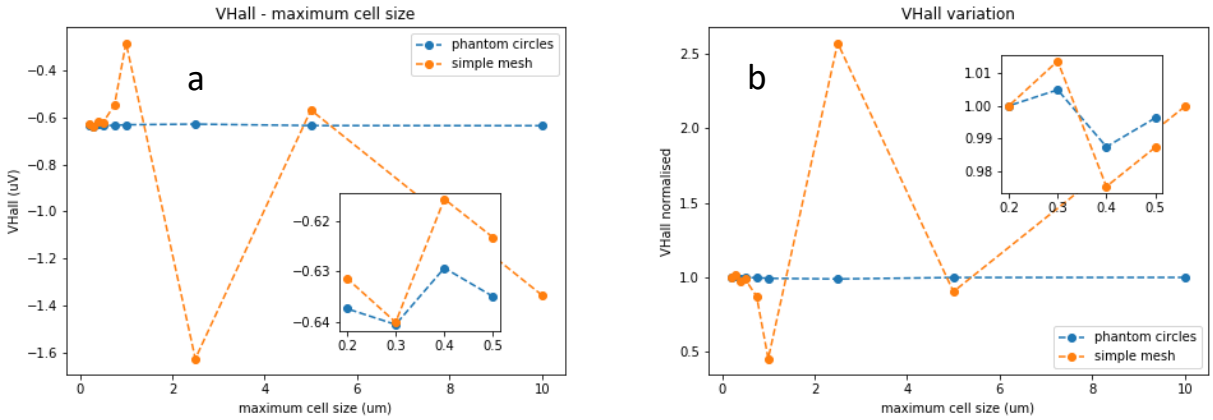

Figure 121: Mesh analysis results for the maximum cell size, for the simple mesh (orange curves) and the mesh calculated with phantom circles (blue curves). a) V_{Hall} results. b) Same V_{Hall} results normalised by the value at the smallest maximum cell size investigated with phantom circles mesh. Insets: zoom of the corresponding data at small maximum cell sizes.

B1.2 – Mesh independence vs minimum cell size in active area

- maximum cell size in the active area = 0.3 µm for the simple mesh and = 2.5 µm for the mesh with the phantom circles.
- maximum cell size in the arms = 2.5 µm.

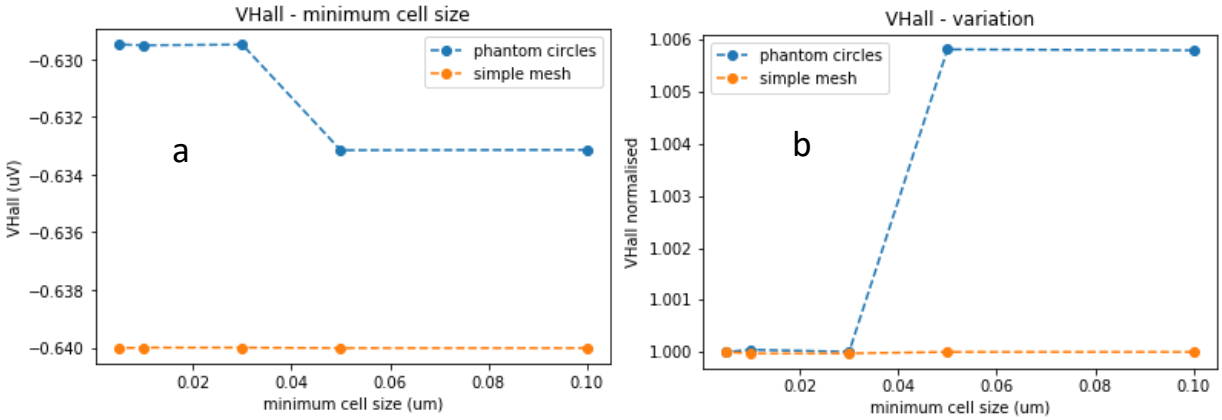

Figure 122: Mesh analysis results for the minimum cell size, for the simple mesh (orange curves) and the mesh calculated with phantom circles (blue curves). a) V_{Hall} results. b) Percentage difference between mesh types.

B1.3 – Mesh independence vs maximum cell size in the arms

- maximum cell size in the active area = 0.3 µm for the simple mesh and = 2.5 µm for the mesh with phantom circles.
- minimum cell size in the active area = 0.01 µm.

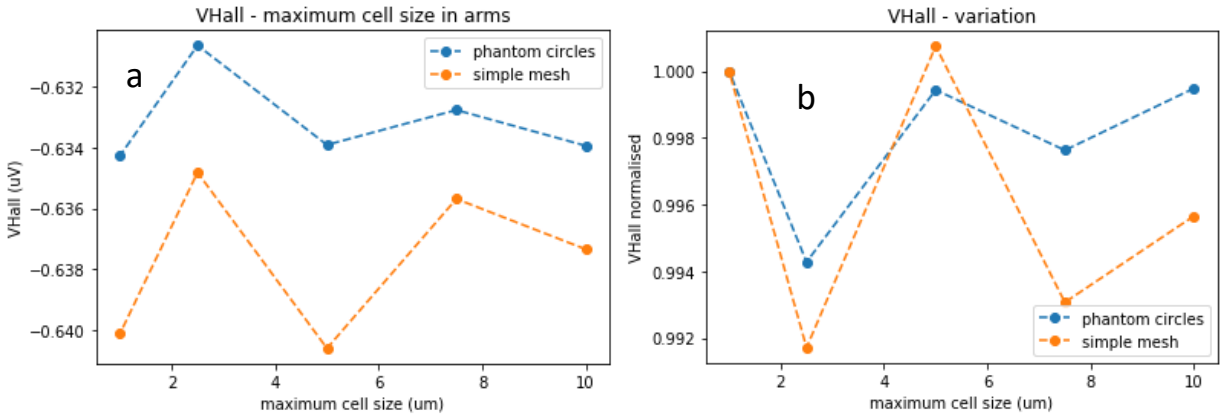

Figure 123: Mesh analysis results for the maximum cell size in the arms of the cross, for the simple mesh (orange curves) and the mesh calculated with phantom circles (blue curves). a) V_{Hall} results. b) Percentage difference between mesh types.

B2 – Perforated device

Particles embedded in the perforations (working distance of 0) and particles situated in the diagonal position between perforations at a working distance of 90 nm.

B2.1 – Particles embedded in the perforations.

B2.1.1 – Mesh independence vs maximum cell size in the active area

- minimum cell size in the active area = 0.01 µm.
- maximum cell size of in the arms = 2.5 µm.

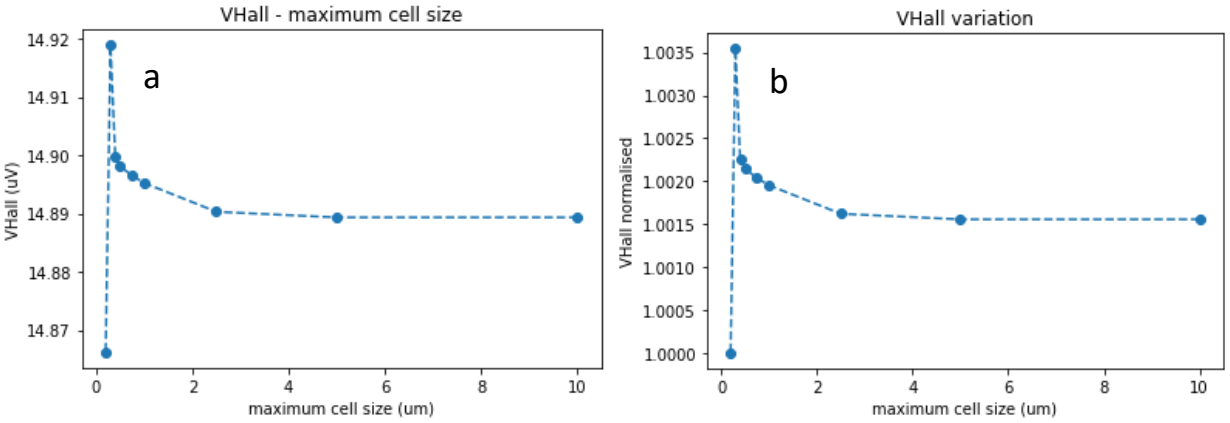

Figure 124: Mesh analysis results for the maximum cell size in the active area in the case of the perforated cross with particles embedded in the holes. a) V_{Hall} results. b) same V_{Hall} results normalised by the value at the smallest maximum cell size investigated.

B2.1.2 – Mesh independence vs minimum cell size in the active area

- maximum cell size in the active area = 2.5 µm.
- maximum cell size in the arms = 2.5 µm.

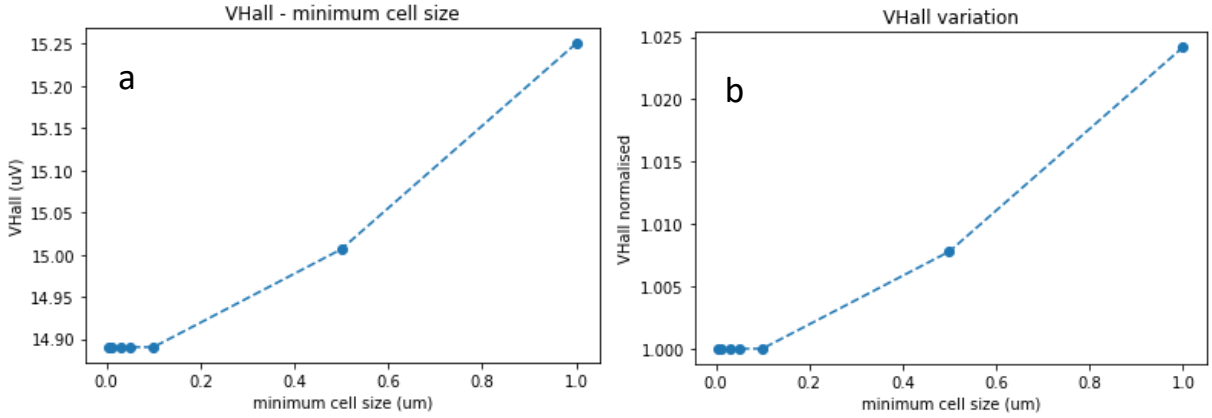

Figure 125: Mesh analysis results for the minimum cell size in the active area in the case of the perforated cross with particles embedded in the holes. a) V_{Hall} results. b) same V_{Hall} results normalised by the value at the smallest minimum cell size investigated.

B2.1.3 – Mesh independence vs maximum cell size in the arms

- maximum cell size in the active area = 2.5 µm.
- minimum cell size in the active area = 0.01 µm.

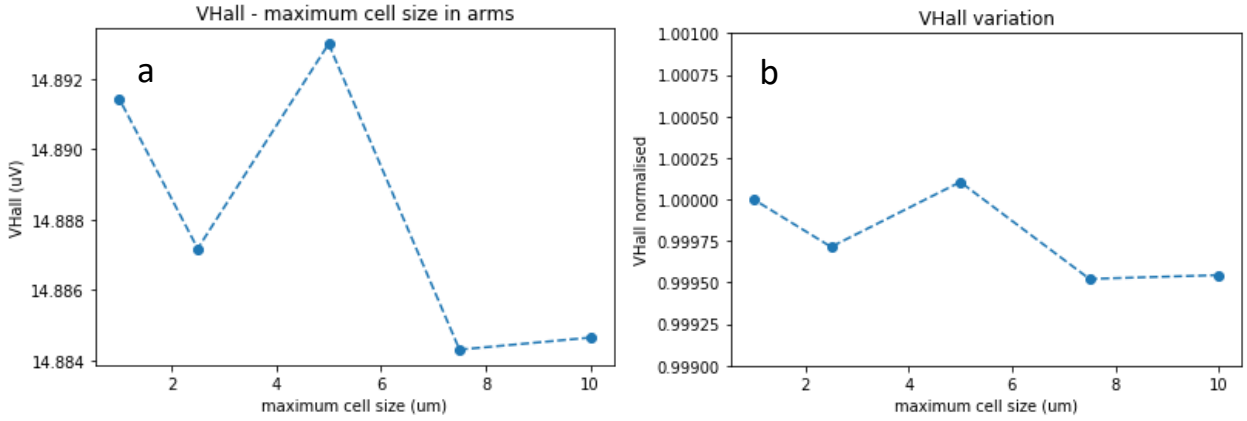

Figure 126: Mesh analysis results for the maximum cell size in the arms in the case of the perforated cross with particles embedded in the perforations. a) V_{Hall} results. b) same V_{Hall} results normalised by the value at the smallest maximum cell size in the arms investigated.

B2.2 – Particles at diagonal positions at 90 nm working distance

B2.2.1 – Mesh independence vs maximum cell size in the active area

- minimum cell size in active area = 0.01 µm.
- maximum cell size in the arms = 2.5 µm.

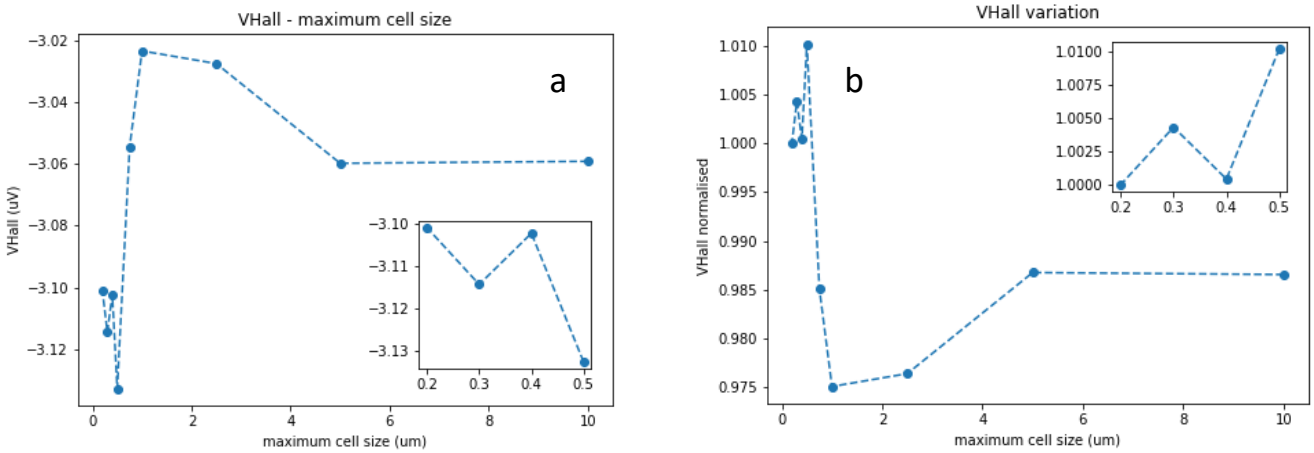

Figure 127: Mesh analysis results for the maximum cell size in the active area in the case of the perforated cross with particles at diagonal positions between the holes. a) V_{Hall} results. b) Same V_{Hall} results normalised by the value at the smallest maximum cell size in the active area investigated. Insets: zoom of the data at small maximum cell size.

B2.2.2 – Mesh independence vs minimum cell size in the active area

- maximum cell size in active area = 0.4 µm.
- maximum cell size in the arms = 2.5 µm.

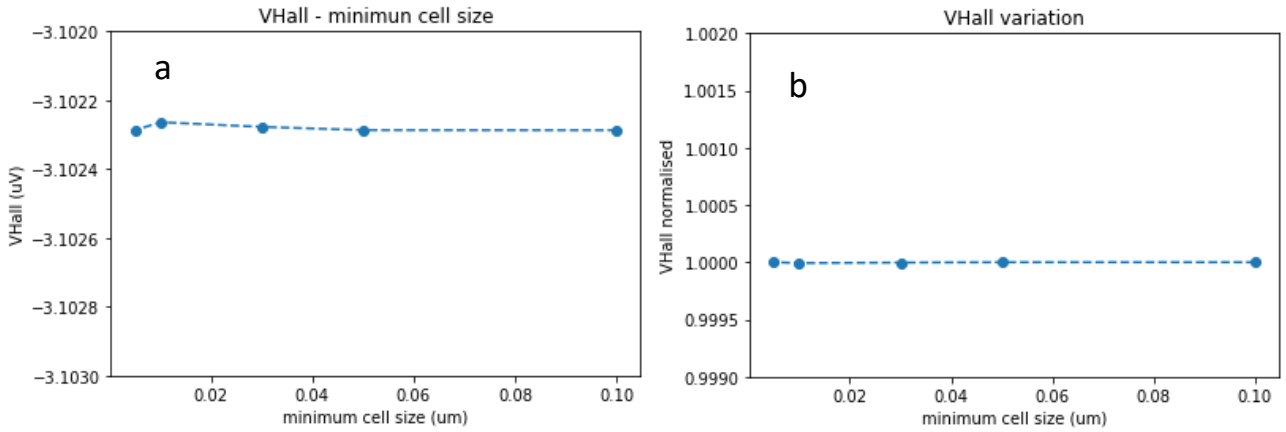

Figure 128: Mesh analysis results for the minimum cell size in the active area in the case of the perforated cross with particles at diagonal positions between the holes. a) V_{Hall} results. b) Same V_{Hall} results normalised by the value at the smallest minimum cell size in the active area investigated.

B2.2.3 – Mesh independence vs maximum cell size in the arms

- maximum cell size in active area = 0.4 µm.
- minimum cell size in active area = 0.01 µm.

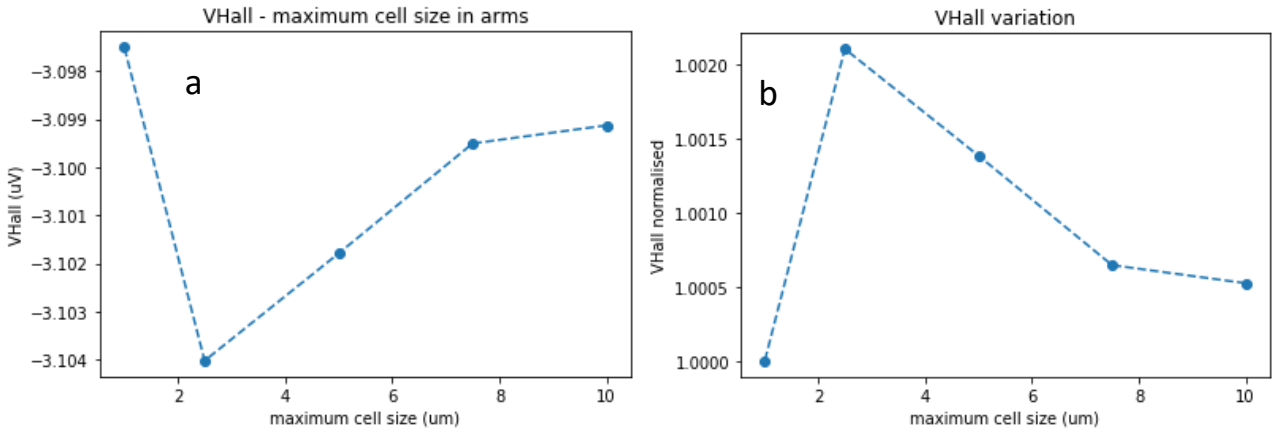

Figure 129: Mesh analysis results for the maximum cell size in the arms in the case of the perforated cross with particles at diagonal positions between the holes. a) V_{Hall} results. b) Same V_{Hall} results normalised by the value at the smallest maximum cell size in the arms investigated.

The mesh parameters at which the results attain mesh independence for each configuration are compiled in Table 18. These values represent the meshing parameters that will provide accurate results with the shortest possible computation times. Any mesh parameter which provides finer mesh resolution than that compiled here can be used and trusted to provide accurate results.

Device type	Mesh type	Max cell size (µm), active area	Min cell size (µm), active area	Max cell size (µm), arms
Continuous	simple	0.3	0.1	10
Continuous	phantom holes	10	0.1	10
Perforated, disks embedded	simple	10	0.5	10
Perforated, disks between perforations	simple	0.4	0.1	10

Table 18: Summary of mesh parameters for which mesh independence is reached.

Appendix C – Arm length study

The arm length study was performed in the case of 13 magnetic disks and in the case of a global uniform field of strength 0.01 T + all boundary conditions (indicated in the legend of the figures). W = 100 µm.

C1 – Continuous cross

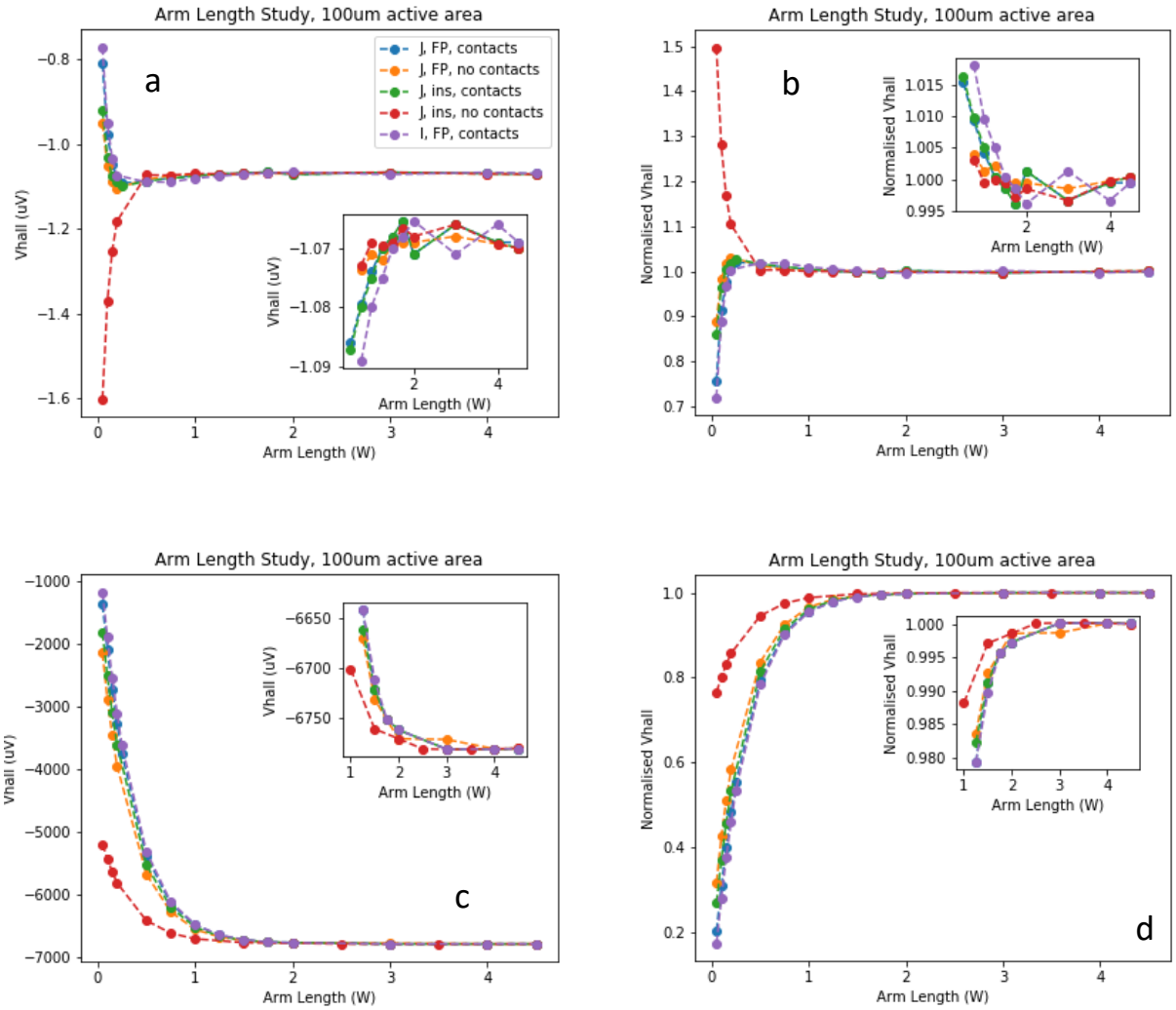

Figure 130: V_{Hall} as a function of arm length (in units of W) for different combinations of boundary conditions (floating point – FP, insulating – ins), current conditions (constant current density - J, constant current – I) and contact configurations (contacts, no contacts) for the continuous model device and (a), (b) a set of 13 magnetic disks. (a): raw Hall voltage. (b): same data normalised by the average of the Hall voltages at the highest arm length. The same is shown for a uniform field of 0.01T in (c) and (d). Insets: zoom of the data for the longest arm lengths investigated.

C2 – Perforated device

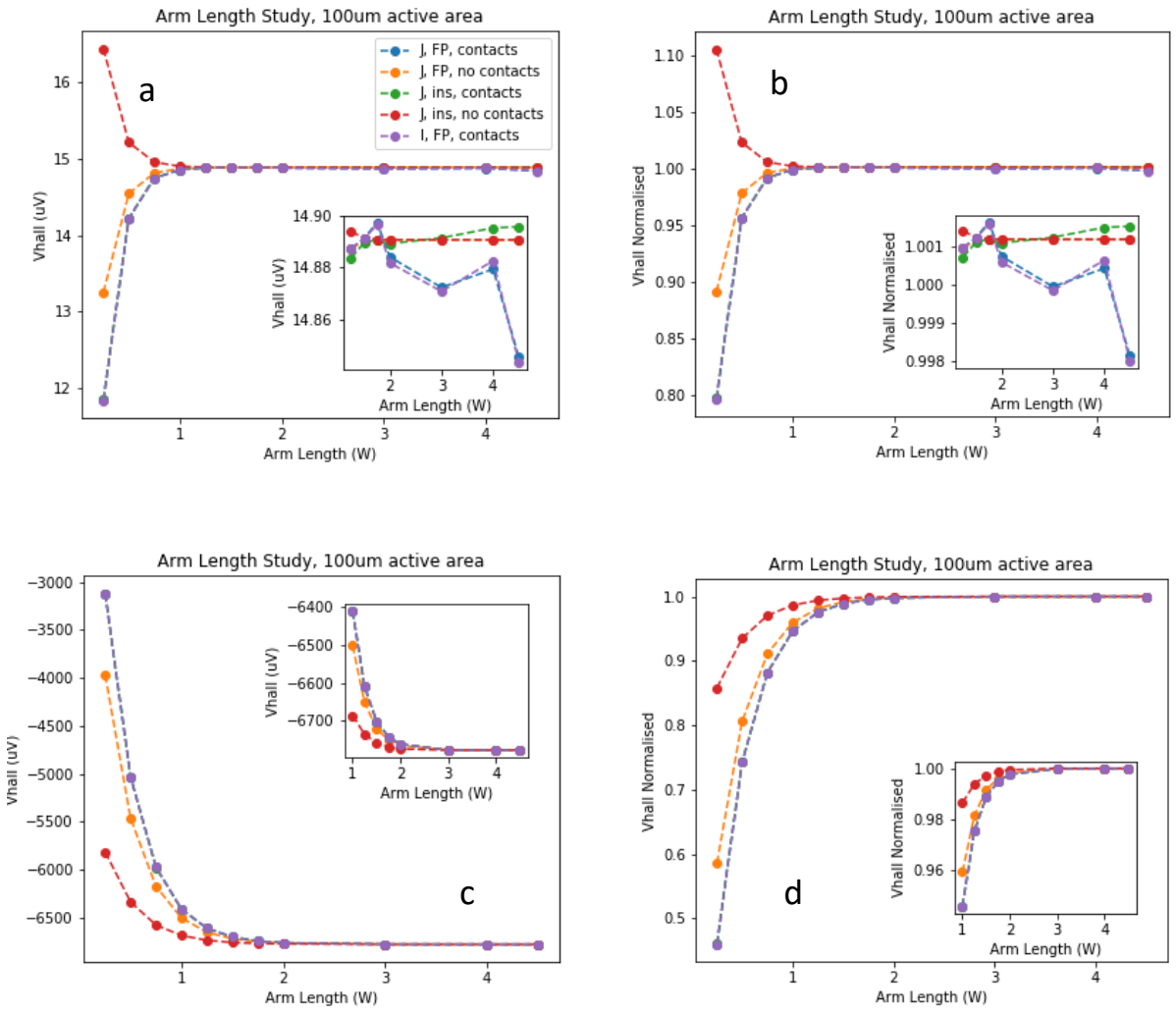

Figure 131: V_{Hall} as a function of arms length (in units of W) for different combinations of boundary conditions (floating point – FP, insulating – ins), current conditions (constant current density - J, constant current – I) and contact configurations (contacts, no contacts) for the perforated model device and (a), (b) a set of 13 magnetic disks. (a): raw Hall voltage. (b): same data normalised by the average of the Hall voltages at the highest arm length. The same is shown for a uniform field of 0.01T in (c) and (d). Insets: zoom of the data for the longest arm lengths investigated.

C3 – Summary of arm length study for 100 µm Hall cross

In Table 19, we compile the results for the minimum arm length at which the V_{Hall} results, calculated with all possible boundary condition combinations, converge to within 1%.

Device type	Applied field	Arm Length (W)
Continuous	Magnetic Disks	1.5
Continuous	Uniform 0.01T Field	1.5
Perforated	Magnetic Disks	1
Perforated	Uniform 0.01T Field	2

Table 19: Summary of minimum arm length for which arm length independence is reached.

C4 – Validity for various active area sizes

The arm length study was performed for a perforated cross with various active area (AA) widths in the case of an arrangement of 6 µm magnetic disks aligned with the perforations at 90 nm a working distance and in the case of a global uniform field of 0.01T. As the active area width is varied, the number of perforations that fit within also varies. We maintain a centre-to-centre distance between perforations of twice the perforation diameter (12 µm), and a boundary between the edge of the outermost perforation and the active area edge of one perforation diameter (6 µm). With these constraints in place, we fill each active area with as large an array of perforations as will fit.

- W = 75, 100, 125 µm: 13 disks.
- W = 50 µm: 9 disks.
- W = 25 µm: 1 disk.

Current density kept constant at 1e8 A/m^2 for all active area widths.

The Hall voltage results presented are normalised by the number of particles present, representing the average single particle signal.

C4.1 – Array of magnetic disks

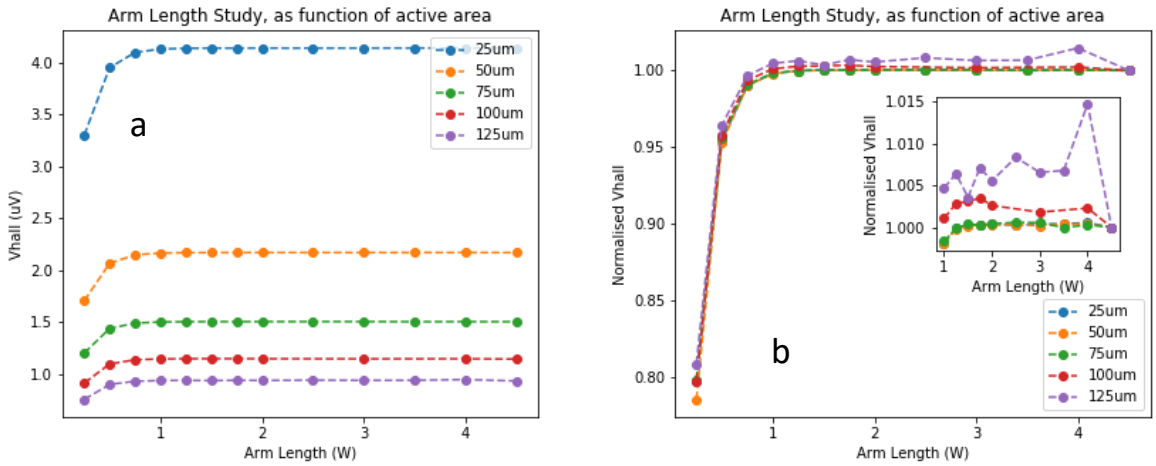

Figure 132: a) Average V_{Hall} per particle as a function of arm length for different active area widths and for as many 6 µm particles as can fit into the AA. b) Same data as a), normalised by the value at the longest arm length. Inset: zoom on the plateau.

C4.2 – Uniform field of 0.01 T

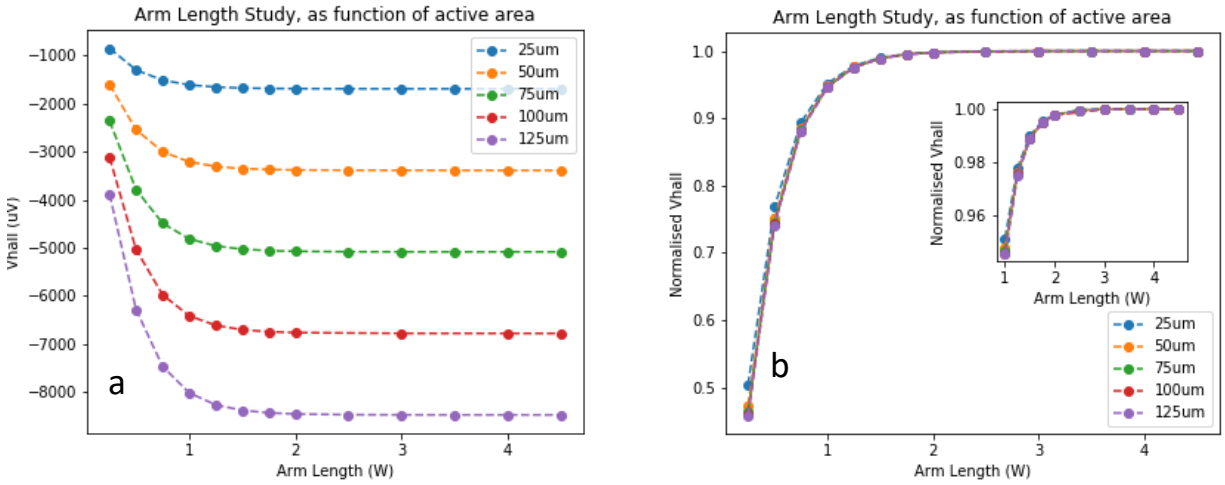

Figure 133: a) V_{Hall} as a function of arm length for different active area widths and for a globally applied magnetic field of 0.01 T. b) Same data as a), normalised by the value at the longest arm length. Inset: zoom on the plateau.

C5 – Validity for various perforation sizes

The arm length study was performed for a perforated cross with various perforation sizes in the case of an arrangement of 13 magnetic disks and in the case of a global uniform field of 0.01 T. As the perforation diameter is varied, the number of perforations that fit within the 100 µm x 100 µm active area also varies. We maintain a centre-to-centre distance between perforations of twice the perforation diameter, and a boundary between the edge of the outermost perforation and the active area edge of one perforation diameter. With these constraints in place, we fill each active area with as large an array of perforations as will fit.

C5.1 – Array of magnetic disks, 90 nm working distance

The particle size is varied to match the perforation size, with the saturation magnetisation, M_S, and working distance of 90 nm kept constant. The Hall voltage results presented are normalised by the number of particles present, representing the average single particle signal.

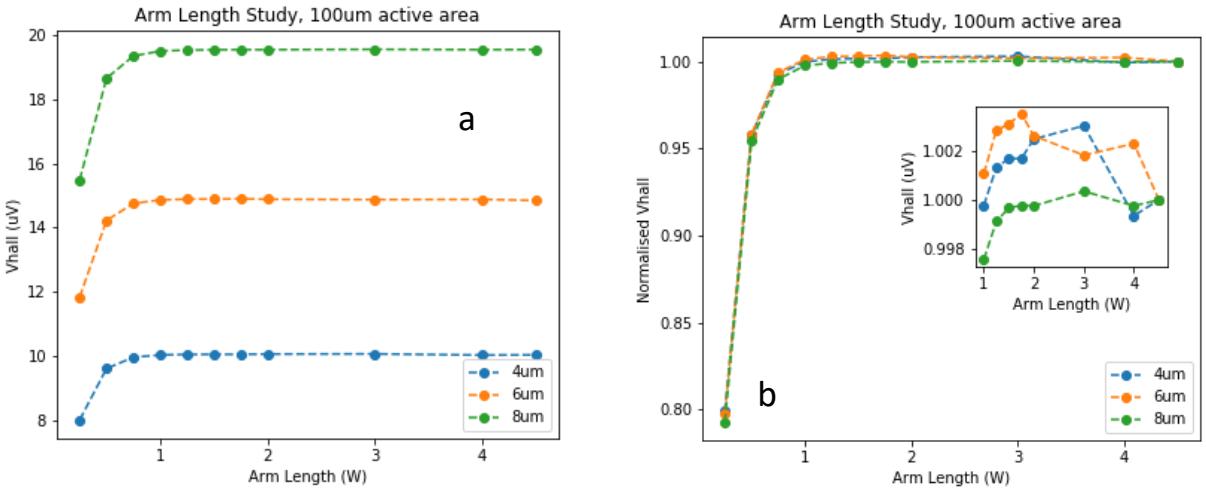

Figure 134: a) V_{Hall} of a 100 µm x 100 µm AA device as a function of arm length for different particle/hole diameters and for as many particles of the given diameter as can fit into the AA. b) Same data as a), normalised by the value at the longest arm length. Inset: zoom on the plateau.

C5.2 – Uniform field of 0.01T

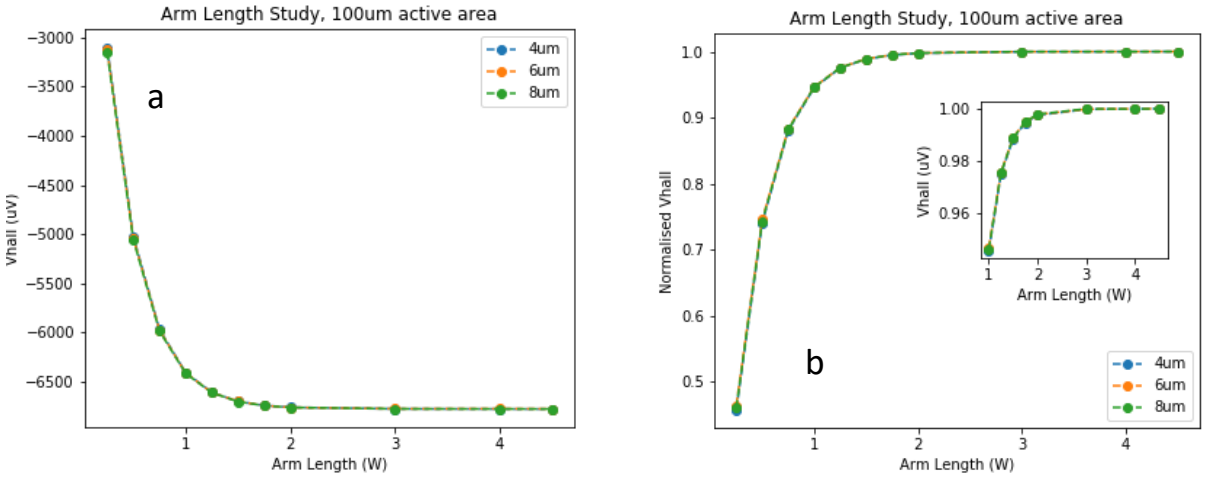

Figure 135: a) V_{Hall} as a function of arm length for different perforation diameters and for a globally applied magnetic field of 0.01 T. b) Same data as a), normalised by the value at the longest arm length. Inset: zoom on the plateau.

We have found that the arm lengths required for arm length independent results is not impacted by the size or arrangement of perforations within the active area, or by the AA width. Thus, the results compiled in table 2 can be applied to a device of any AA size, as well as perforation diameter.

Appendix D – Quantification of signal homogeneity

D1 – Response of continuous cross – (7x7) beads

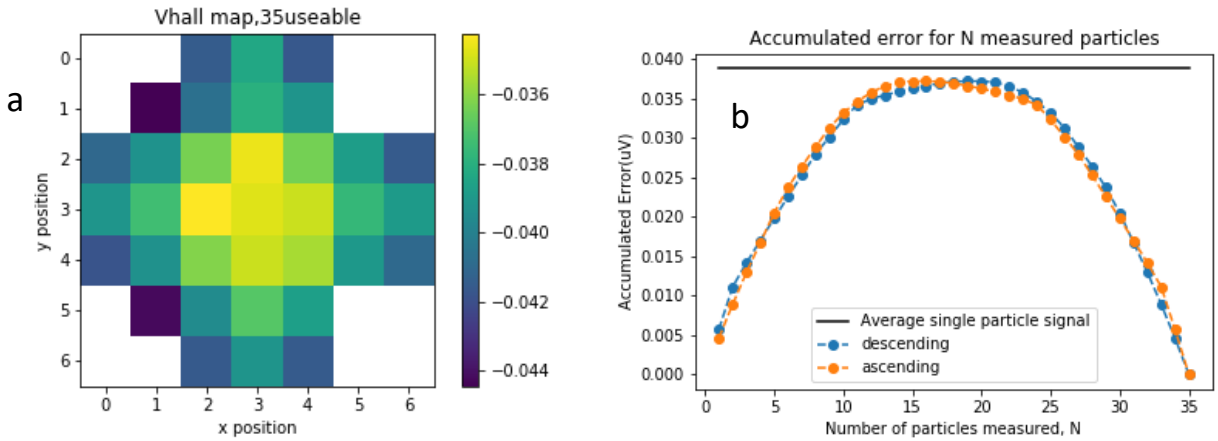

Figure 136 a) V_{Hall} map for magnetic beads on continuous Hall cross for the measurable positions only. Positions that are not measurable were left blank. b) Accumulated error versus N for the same set of measurable positions. The black horizontal line indicates the average single bead signal from the set.

D2 – Response of perforated cross - (7x7) perforations, (7x7) disks, embedded

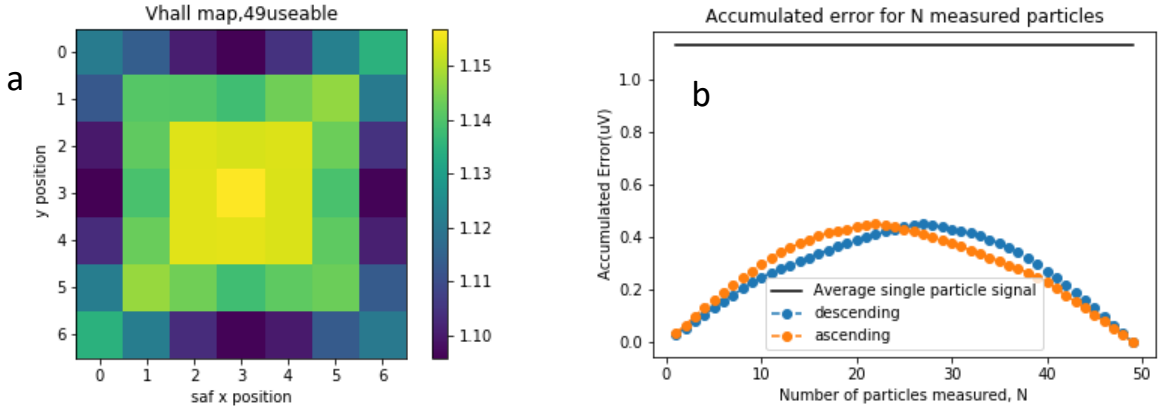

Figure 137: V_{Hall} map for magnetic disks embedded within perforations. b) Accumulated error versus N. The black horizontal line indicates the average single disk signal from the set.

D3 – Response of perforated cross - (7x7) perforations, (8x8) disks, diagonal position

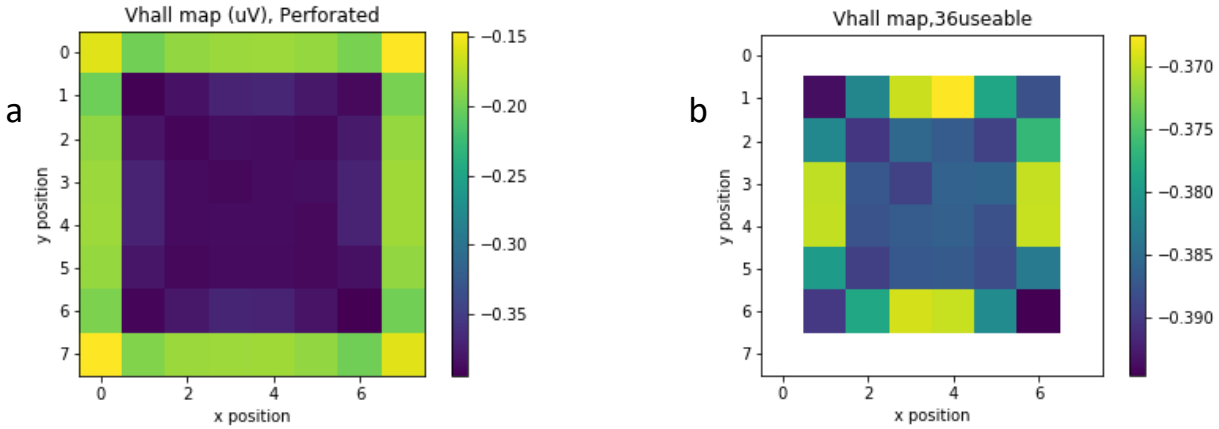

Figure 138: V_{Hall} map for magnetic disks at the diagonal postions between perforations at a working distance of 90 nm. (a) All 8x8 positions considered, and (b) only the measurable positions. Positions that are not measurable were left blank.

D4 – Response of perforated cross - (9x9) perforations, (8x8) disks, diagonal position

The perforations extend beyond the bounds of the active area and thus, as shown, cannot be added to the four corners without significantly altering the global geometry of the cross.

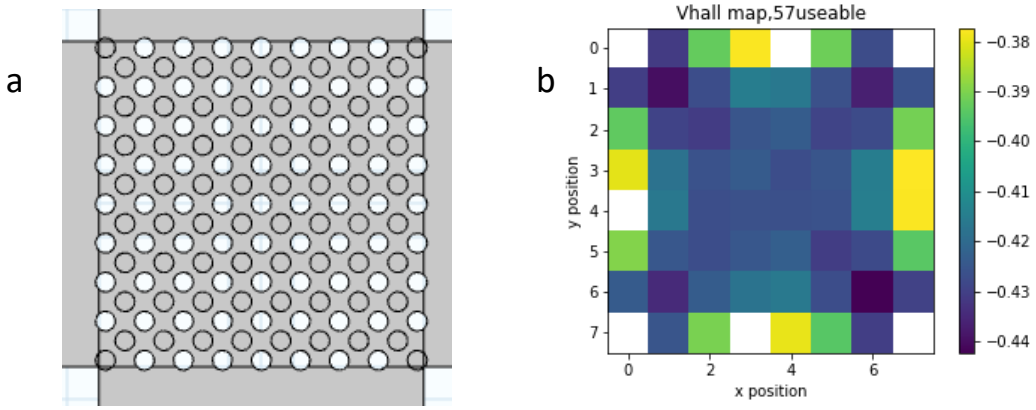

Figure 139: (a) Schematic showing the altered perforated cross geometry, including an additional ring of perforations, used in the calculation of the data shown in b. (b) V_{Hall} map for magnetic disks at the diagonal postions between perforations at a working distance of 90 nm, when an additional ring of perforations has been added to the cross.

D5 – Response of perforated cross – (7x7) perforations, (7x7) beads, aligned

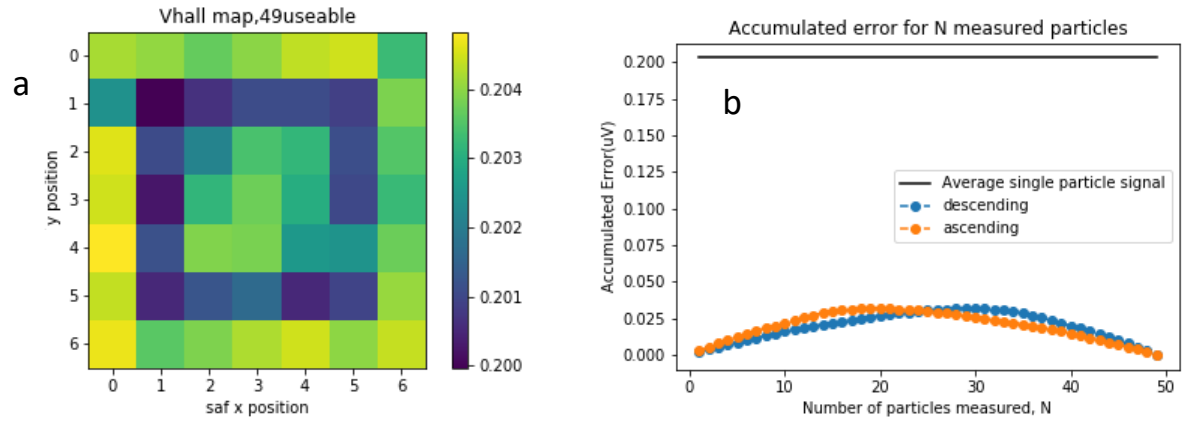

Figure 140: V_{Hall} map for magnetic beads aligned with perforations at a working distance of 90 nm. b) Accumulated error versus N. The black horizontal line indicates the average single bead signal from the set.

D6 – Response of perforated cross – (7x7) perforations, (7x7) beads, embedded

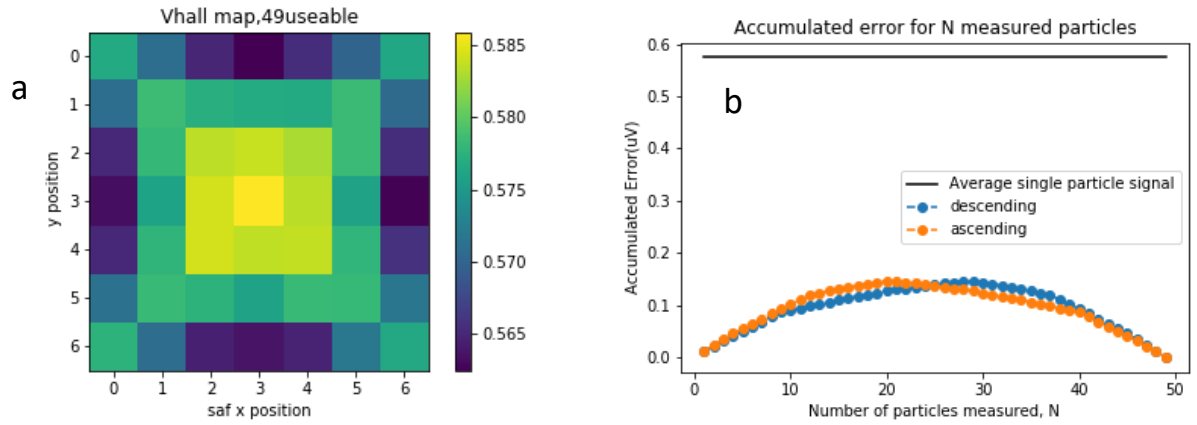

Figure 141: V_{Hall} map for magnetic beads embedded within perforations. b) Accumulated error versus N. The black horizontal line indicates the average single bead signal from the set.

D7 – Response of perforated cross – (7x7) perforations, (8x8) beads, diagonal position

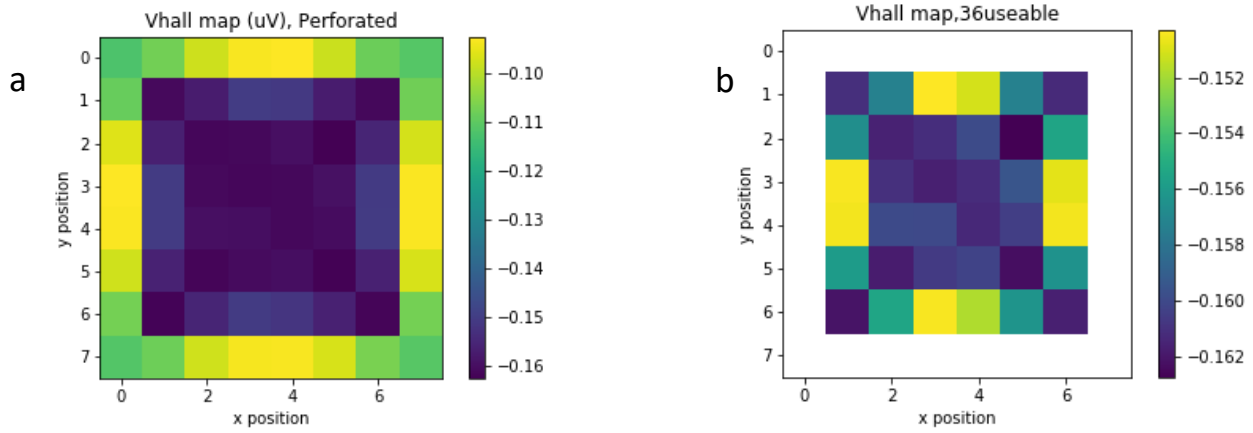

Figure 142: V_{Hall} map for magnetic beads, at the diagonal postions between perforations at a working distance of 90 nm. (a) shows all 8x8 positions considered, and (b) shows only the measurable positions. Positions that are not measurable were left blank.

D8 – Response of perforated cross, (9x9) perforations, (8x8) beads, diagonal position

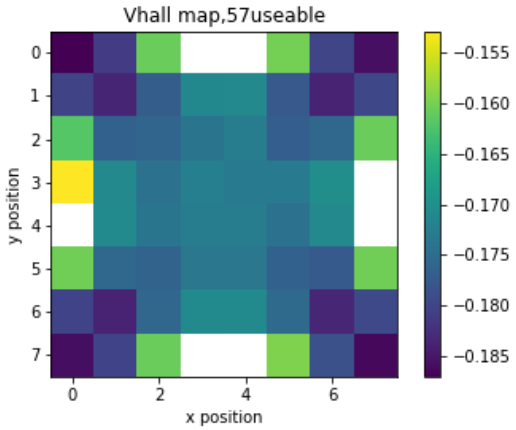

Figure 143: V_{Hall} map for magnetic beads at the diagonal postions between perforations at a working distance of 90 nm, when an additional ring of perforations has been added to the cross.

Appendix E – Justification for the use of symmetry

The Hall voltage maps produced at the model perforated Hall crosses in response to the presence of magnetic disks aligned with the perforations generally exhibit a 4-fold symmetry through the x and y axes when the disks are at a working distance of 90 nm and a 2-fold symmetry though the x-axis when the disks are embedded at the level of the 2DEG. Here we show that we can simulate only half the Hall voltage map and produce the rest by symmetry, thus reducing the computation time required to simulate Hall voltage response maps for magnetic disks in the aligned configuration.

E1 – Magnetic disks, aligned, 90 nm working distance

We demonstrate this by calculating Hall voltage map to magnetic disks in the aligned configuration at a working height of 90 nm for all available particle positions, as shown in Figure 144 (a). We then use the upper half of this map plus the row running through the centre of the array to generate the full response map by symmetry, as shown in figure (b). The percentage difference between maps is displayed in figure (c), showing a maximum of 0.15%.

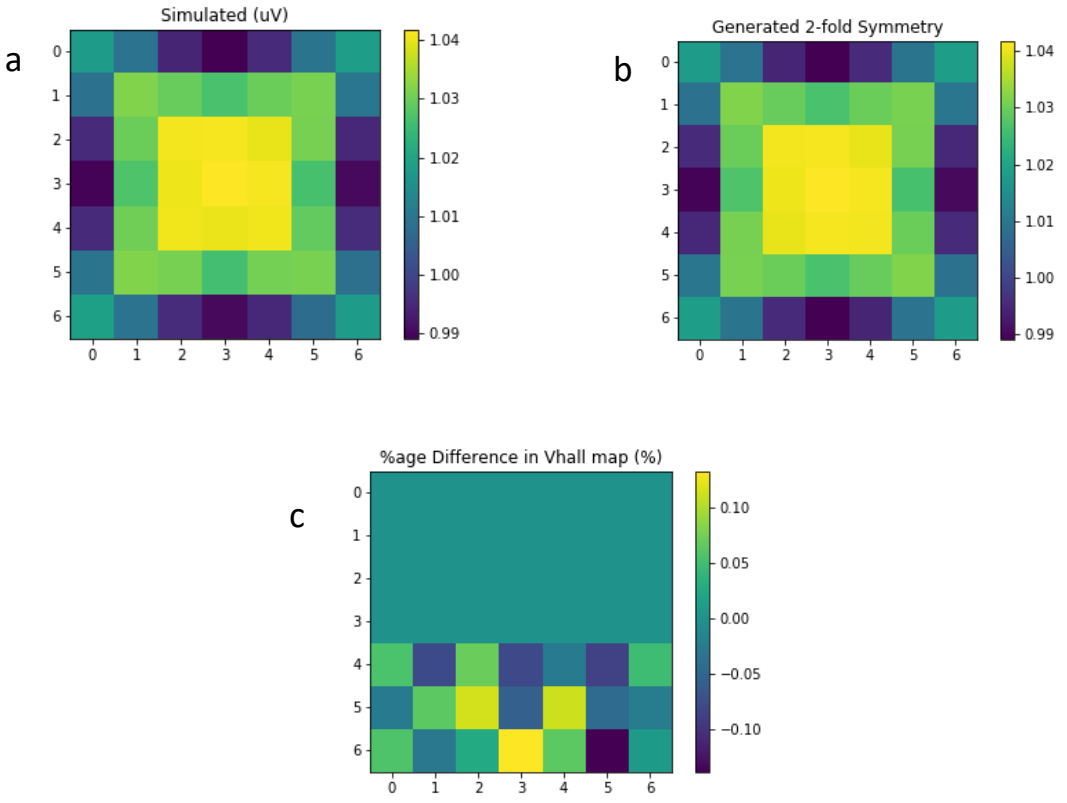

Figure 144: (a) Hall voltage response map for magnetic disks aligned with the perforations at a working distance of 90 nm, calculated by COMSOL. (b) The same response map, with the lower half generated by symmetry from the upper half. (c) The percentage difference between the maps shown in (a) and (b).

E2 - Magnetic disks, embedded

We demonstrate the same for the case of the particle embedded within the 2DEG. In Figure 145 (a) we show the fully simulated Hall voltage response map and in figure (b), the response map calculated by symmetry. As can be seen from figure (c), in this case the maximum percentage difference is 0.2%

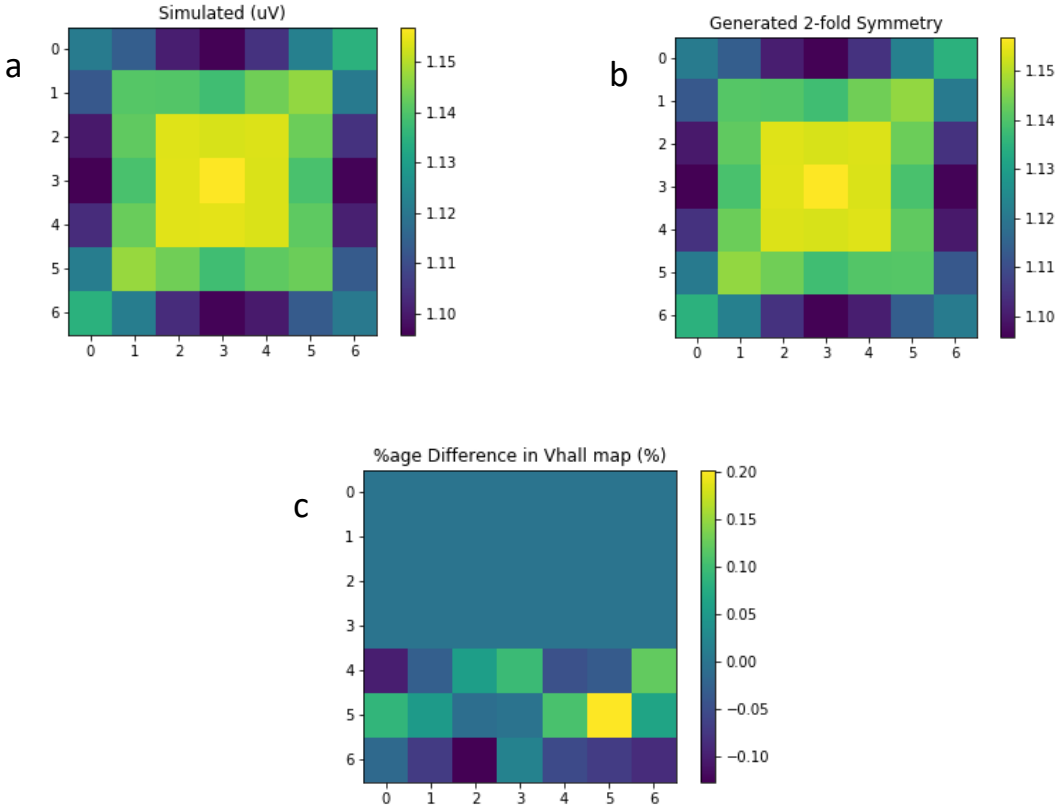

Figure 145: (a) Hall voltage response map for magnetic disks embedded within the perforations, calculated by COMSOL. (b) The same response map, with the lower half generated by symmetry from the upper half. (c) The percentage difference between the maps shown in (a) and (b)

We thus conclude that this symmetry can be employed to roughly half the number of data points to be computed, allowing us to generate the lower half of the hall voltage maps by symmetry.

References

[1] D. Egger and K. Bienz, “Protein (western) blotting,” *Mol Biotechnol*, vol. 1, no. 3, pp. 289–305, 1994, doi: 10.1007/BF02921696.

[2] S. Aydin, “A short history, principles, and types of ELISA, and our laboratory experience with peptide/protein analyses using ELISA,” *Peptides (N.Y.)*, vol. 72, pp. 4–15, 2015, doi: https://doi.org/10.1016/j.peptides.2015.04.012.

[3] D. A. Hall, J. Ptacek, and M. Snyder, “Protein Microarray Technology Types of protein microarrays.” Accessed: May 30, 2019. [Online]. Available: https://www.ncbi.nlm.nih.gov/pmc/articles/PMC1828913/pdf/nihms17379.pdf

[4] T. Brown, “Southern Blotting,” in *Current Protocols in Immunology*, Hoboken, NJ, USA: John Wiley & Sons, Inc., 2001, p. Unit 10.6A. doi: 10.1002/0471142735.im1006as06.

[5] R. Bumgarner, “Overview of DNA microarrays: types, applications, and their future.,” *Curr Protoc Mol Biol*, vol. Chapter 22, p. Unit 22.1., Jan. 2013, doi: 10.1002/0471142727.mb2201s101.

[6] S. A. , Dunbar and Michaela R. Hoffmeyer, “Microsphere-based multiplex immunoassays: development and applications using Luminex® xMAP® technology.,” in *The Immunoassay Handbook: Theory and applications of ligand binding, ELISA and related techniques*, 2013, p. Chpt 2.9.

[7] A. Adan, G. Alizada, Y. Kiraz, Y. Baran, and A. Nalbant, “Flow cytometry: basic principles and applications,” *Crit Rev Biotechnol*, vol. 37, no. 2, pp. 163–176, Feb. 2017, doi: 10.3109/07388551.2015.1128876.

[8] S. J. KARCHER and S. J. KARCHER, “POLYMERASE CHAIN REACTION,” *Mol Biol*, pp. 215–227, Jan. 1995, doi: 10.1016/B978-012397720-5.50040-2.

[9] N. L. Rosi and C. A. Mirkin, “Nanostructures in Biodiagnostics,” *Chem Rev*, vol. 105, no. 4, pp. 1547–1562, Apr. 2005, doi: 10.1021/cr030067f.

[10] S. Zhang, A. Garcia-D’Angeli, J. P. Brennan, and Q. Huo, “Predicting detection limits of enzyme-linked immunosorbent assay (ELISA) and bioanalytical techniques in general,” *Analyst*, vol. 139, no. 2, pp. 439–445, 2014, doi: 10.1039/C3AN01835K.

[11] Y. M. Shlyapnikov, E. A. Malakhova, A. Z. Vinarov, A. A. Zamyatnin, and E. A. Shlyapnikova, “Can new immunoassay techniques improve bladder cancer diagnostics With protein biomarkers?,” *Front Mol Biosci*, vol. 7, 2021, doi: 10.3389/fmolb.2020.620687.

[12] N. A. W. Bell and U. F. Keyser, “Digitally encoded DNA nanostructures for multiplexed, single-molecule protein sensing with nanopores,” *Nat Nanotechnol*, vol. 11, no. 7, pp. 645–651, 2016, doi: 10.1038/nnano.2016.50.

[13] M. Alvarez and L. M. Lechuga, “Microcantilever-based platforms as biosensing tools,” *Analyst*, vol. 135, pp. 827–836, 2010, doi: 10.1039/b908503n.

[14] F. Patolsky and C. M. Lieber, “Nanowire nanosensors,” *Materials Today*, vol. 8, no. 4, pp. 20–28, Apr. 2005, doi: 10.1016/S1369-7021(05)00791-1.

[15] R. J. Chen *et al.*, “Noncovalent functionalization of carbon nanotubes for highly specific electronic biosensors,” *PROCEEDINGS OF THE NATIONAL ACADEMY OF SCIENCES*, vol. 100, no. 9, 2003, Accessed: May 30, 2019. [Online]. Available: www.pnas.orgcgidoi10.1073pnas.0837064100

[16] M. Hu *et al.*, “Gold nanostructures: engineering their plasmonic properties for biomedical applications,” 2006, doi: 10.1039/b517615h.

[17] W. R. Algar, A. J. Tavares, and U. J. Krull, “Beyond labels: A review of the application of quantum dots as integrated components of assays, bioprobes, and biosensors utilizing optical transduction,” *Anal Chim Acta*, vol. 673, no. 1, pp. 1–25, Jul. 2010, doi: 10.1016/j.aca.2010.05.026.

[18] C. Rümenapp, B. Gleich, and A. Haase, “Magnetic Nanoparticles in Magnetic Resonance Imaging and Diagnostics,” *Pharm Res*, vol. 29, no. 5, pp. 1165–1179, May 2012, doi: 10.1007/s11095-012-0711-y.

[19] J. Dobson, “Magnetic nanoparticles for drug delivery,” *Drug Dev Res*, vol. 67, no. 1, pp. 55–60, Jan. 2006, doi: 10.1002/ddr.20067.

[20] S. Kossatz *et al.*, “Efficient treatment of breast cancer xenografts with multifunctionalized iron oxide nanoparticles combining magnetic hyperthermia and anti-cancer drug delivery,” *Breast Cancer Research*, vol. 17, no. 1, p. 66, Dec. 2015, doi: 10.1186/s13058-015-0576-1.

[21] H. P. Khng, D. Cunliffe, S. Davies, N. A. Turner, and E. N. Vulfson, “The synthesis of sub-micron magnetic particles and their use for preparative purification of proteins,” *Biotechnol Bioeng*, vol. 60, no. 4, pp. 419–424, Nov. 1998, doi: 10.1002/(SICI)1097-0290(19981120)60:4<419::AID-BIT3>3.0.CO;2-P.

[22] R. J. C. David R. Baselt, Gil U. Lee, Mohan Natesan, Steven W. Metzger, Paul E. Sheehan, “A Biosensor based in magnetoresistance technology,” *Biosens Bioelectron*, vol. 13, pp. 731–739, 1998.

[23] R. L. Edelstein *et al.*, “The BARC biosensor applied to the detection of biological warfare agents,” *Biosens Bioelectron*, vol. 14, no. 10–11, pp. 805–813, Jan. 2000, doi: 10.1016/S0956-5663(99)00054-8.

[24] M. M. Miller *et al.*, “A DNA array sensor utilizing magnetic microbeads and magnetoelectronic detection,” *J Magn Magn Mater*, vol. 225, no. 1–2, pp. 138–144, Jan. 2001, doi: 10.1016/S0304-8853(00)01242-7.

[25] J. C. Rife, M. M. Miller, P. E. Sheehan, C. R. Tamanaha, M. Tondra, and L. J. Whitman, “Design and performance of GMR sensors for the detection of magnetic microbeads in biosensors,” *Sens Actuators A Phys*, vol. 107, no. 3, pp. 209–218, 2003, doi: 10.1016/S0924-4247(03)00380-7.

[26] S. P. Mulvaney *et al.*, “Rapid, femtomolar bioassays in complex matrices combining microfluidics and magnetoelectronics,” *Biosens Bioelectron*, vol. 23, no. 2, pp. 191–200, Sep. 2007, doi: 10.1016/J.BIOS.2007.03.029.

[27] S. P. Mulvaney, K. M. Myers, P. E. Sheehan, and L. J. Whitman, “Attomolar protein detection in complex sample matrices with semi-homogeneous fluidic force discrimination assays,” *Biosens Bioelectron*, vol. 24, no. 5, pp. 1109–1115, Jan. 2009, doi: 10.1016/J.BIOS.2008.06.010.

[28] L. J. W. S.P. Mulvaney *, C.N. Ibe, C.R. Tamanaha, “Direct detection of genomic DNA with fluidic force discrimination assays,” *Anal Biochem*, vol. 392, no. 139–144, 2009, Accessed: May 19, 2019. [Online]. Available: https://pdf.sciencedirectassets.com/272363/1-s2.0-S0003269709X00163/1-s2.0-S0003269709003790/main.pdf?x-amz-security-token=AgoJb3JpZ2luX2VjEFEaCXVzLWVhc3QtMSJHMEUCIQDfnKZ6sK9S2SUQdR20snB4sbFboozFgZ04Q%2FjfagWeewIgdVip8CMIhMr56ZUSecE8wawPFc40Tw2PIzISm4YCPd

[29] C. R. Tamanaha, S. P. Mulvaney, and J. C. Rife, “Evolution of a magnetic-based biomolecular detection system,” in *2009 Annual International Conference of the IEEE Engineering in Medicine and Biology Society*, IEEE, Sep. 2009, pp. 5425–5427. doi: 10.1109/IEMBS.2009.5332482.

[30] D. L. Graham, H. Ferreira, J. Bernardo, P. P. Freitas, and J. M. S. Cabral, “Single magnetic microsphere placement and detection on-chip using current line designs with integrated spin valve sensors: Biotechnological applications,” *J Appl Phys*, vol. 91, p. 7786, 2002, doi: 10.1063/1.1451898.

[31] D. L. Graham, H. A. Ferreira, P. P. Freitas, and J. M. S. Cabral, “High sensitivity detection of molecular recognition using magnetically labelled biomolecules and magnetoresistive sensors,” *Biosens Bioelectron*, vol. 18, no. 4, pp. 483–488, Apr. 2003, doi: 10.1016/S0956-5663(02)00205-1.

[32] H. A. Ferreira, D. L. Graham, P. P. Freitas, and J. M. S. Cabral, “Biodetection using magnetically labeled biomolecules and arrays of spin valve sensors (invited),” *J Appl Phys*, vol. 93, p. 7281, 2003, doi: 10.1063/1.1544449.

[33] L. Lagae *et al.*, “On-chip manipulation and magnetization assessment of magnetic bead ensembles by integrated spin-valve sensors,” *J Appl Phys*, vol. 91, p. 7445, 2002, doi: 10.1063/1.1447288.

[34] H. A. Ferreira, N. Feliciano, D. L. Graham, L. A. Clarke, M. D. Amaral, and P. P. Freitas, “Rapid DNA hybridization based on ac field focusing of magnetically labeled target DNA,” *Appl Phys Lett*, vol. 87, no. 1, p. 13901, Jun. 2005, doi: 10.1063/1.1984090.

[35] D. L. Graham, H. A. Ferreira, N. Feliciano, P. P. Freitas, L. A. Clarke, and M. D. Amaral, “Magnetic field-assisted DNA hybridisation and simultaneous detection using micron-sized spin-valve sensors and magnetic nanoparticles,” *Sensors and Actuators B*, vol. 107, pp. 936–944, 2005, doi: 10.1016/j.snb.2004.12.071.

[36] J. Germano *et al.*, “A portable and autonomous magnetic detection platform for biosensing.,” *Sensors (Basel)*, vol. 9, no. 6, pp. 4119–37, 2009, doi: 10.3390/s90604119.

[37] V. C. Martins *et al.*, “Femtomolar limit of detection with a magnetoresistive biochip,” *Biosens Bioelectron*, vol. 24, no. 8, pp. 2690–2695, Apr. 2009, doi: 10.1016/J.BIOS.2009.01.040.

[38] V. C. Martins *et al.*, “Challenges and trends in the development of a magnetoresistive biochip portable platform,” *J Magn Magn Mater*, vol. 322, no. 9–12, pp. 1655–1663, May 2010, doi: 10.1016/J.JMMM.2009.02.141.

[39] E. Fernandes *et al.*, “A bacteriophage detection tool for viability assessment of Salmonella cells,” *Biosens Bioelectron*, vol. 52, pp. 239–246, Feb. 2014, doi: 10.1016/J.BIOS.2013.08.053.

[40] T. G. Barroso, R. C. Martins, E. Fernandes, S. Cardoso, J. Rivas, and P. P. Freitas, “Detection of BCG bacteria using a magnetoresistive biosensor: A step towards a fully electronic platform for tuberculosis point-of-care detection,” *Biosens Bioelectron*, vol. 100, pp. 259–265, Feb. 2018, doi: 10.1016/j.bios.2017.09.004.

[41] A. Fernandes *et al.*, “Lab-on-Chip Cytometry Based on Magnetoresistive Sensors for Bacteria Detection in Milk,” *Sensors*, vol. 14, no. 8, pp. 15496–15524, Aug. 2014, doi: 10.3390/s140815496.

[42] C. M. Duarte, C. Carneiro, S. Cardoso, P. P. Freitas, and R. Bexiga, “Semi-quantitative method for Staphylococci magnetic detection in raw milk,” *Journal of Dairy Research*, vol. 84, no. 1, pp. 80–88, Feb. 2017, doi: 10.1017/S0022029916000741.

[43] “Magnomics | Nanotech for Life.” https://www.magnomics.pt/ (accessed Jun. 24, 2019).

[44] S. X. Wang *et al.*, “Towards a magnetic microarray for sensitive diagnostics,” *J Magn Magn Mater*, vol. 293, pp. 731–736, 2005, doi: 10.1016/j.jmmm.2005.02.054.

[45] S.-J. Han *et al.*, “CMOS Integrated DNA Microarray Based on GMR Sensors,” in *2006 International Electron Devices Meeting*, IEEE, 2006, pp. 1–4. doi: 10.1109/IEDM.2006.346887.

[46] L. Xu *et al.*, “Giant magnetoresistive biochip for DNA detection and HPV genotyping,” *Biosens Bioelectron*, vol. 24, pp. 99–103, 2008, doi: 10.1016/j.bios.2008.03.030.

[47] R. S. Gaster *et al.*, “Matrix-insensitive protein assays push the limits of biosensors in medicine,” *Nat Med*, vol. 15, no. 11, pp. 1327–1332, Nov. 2009, doi: 10.1038/nm.2032.

[48] I. Fishbein and R. J. Levy, “The matrix neutralized,” *Nature*, vol. 461, no. 7266, pp. 890–891, Oct. 2009, doi: 10.1038/461890a.

[49] D. Kim *et al.*, “Nanosensor dosimetry of mouse blood proteins after exposure to ionizing radiation,” 2013, doi: 10.1038/srep02234.

[50] E. Ng, K. C. Nadeau, and S. X. Wang, “Giant magnetoresistive sensor array for sensitive and specific multiplexed food allergen detection,” 2016, doi: 10.1016/j.bios.2016.02.002.

[51] A. C. Mak *et al.*, “Sensitive giant magnetoresistive-based immunoassay for multiplex mycotoxin detection,” *Biosens Bioelectron*, vol. 25, no. 7, pp. 1635–1639, Mar. 2010, doi: 10.1016/J.BIOS.2009.11.028.

[52] R. S. Gaster, D. A. Hall, and S. X. Wang, “Autoassembly Protein Arrays for Analyzing Antibody Cross-Reactivity,” *Nano Lett*, vol. 11, pp. 2579–2583, 2011, doi: 10.1021/nl1026056.

[53] R. S. Gaster, D. A. Hall, and S. X. Wang, “nanoLAB: An ultraportable, handheld diagnostic laboratory for global health,” *Lab Chip*, vol. 11, no. 5, p. 950, Mar. 2011, doi: 10.1039/c0lc00534g.

[54] J. Choi, A. W. Gani, D. J. B. Bechstein, J.-R. Lee, P. J. Utz, and S. X. Wang, “Portable, one-step, and rapid GMR biosensor platform with smartphone interface,” *Biosens Bioelectron*, vol. 85, pp. 1–7, Nov. 2016, doi: 10.1016/j.bios.2016.04.046.

[55] E. Ng, C. Yao, T. O. Shultz, S. Ross-Howe, and S. X. Wang, “Magneto-nanosensor smartphone platform for the detection of HIV and leukocytosis at point-of-care,” *Nanomedicine*, vol. 16, pp. 10–19, Feb. 2019, doi: 10.1016/J.NANO.2018.11.007.

[56] N. N. Trivedi *et al.*, “Analytical validation of a novel multi-analyte plasma test for lung nodule characterization,” *Research Article Biomedical Research and Reviews Biomed Res Rev*, vol. 2, no. 3, pp. 1–10, 2018, doi: 10.15761/BRR.1000123.

[57] “Home - MagArray.” https://magarray.com/ (accessed Jun. 24, 2019).

[58] Reinder Coehoorn and Menno Willem Jose Prins, “SENSOR AND METHOD FOR MEASURING THE AREAL DENSITY OF MAGNETIC NANOPARTICLES ON A MICRO-ARRAY,” US 7,048,890 B2, May 23, 2006 Accessed: May 22, 2019. [Online]. Available: https://patentimages.storage.googleapis.com/4d/20/88/e0576b7dab5540/US7048890.pdf

[59] J. Schotter, P. B. Kamp, A. Becker, A. Pühler, G. Reiss, and H. Brückl, “Comparison of a prototype magnetoresistive biosensor to standard fluorescent DNA detection,” *Biosens Bioelectron*, vol. 19, pp. 1149–1156, 2004, doi: 10.1016/j.bios.2003.11.007.

[60] B. Srinivasan *et al.*, “A Detection System Based on Giant Magnetoresistive Sensors and High-Moment Magnetic Nanoparticles Demonstrates Zeptomole Sensitivity: Potential for Personalized Medicine,” *Angewandte Chemie International Edition*, vol. 48, no. 15, pp. 2764–2767, Mar. 2009, doi: 10.1002/anie.200806266.

[61] Y. R. Chemla *et al.*, “Ultrasensitive magnetic biosensor for homogeneous immunoassay,” *Proc Natl Acad Sci U S A*, vol. 97, no. 26, pp. 14268–72, Dec. 2000, doi: 10.1073/pnas.97.26.14268.

[62] X.-C. Sun, C. Lei, L. Guo, and Y. Zhou, “Sandwich immunoassay for the prostate specific antigen using a micro-fluxgate and magnetic bead labels”, doi: 10.1007/s00604-016-1889-1.

[63] L. Guo, S. Zhi, X. Sun, C. Lei, and Y. Zhou, “Ultrasensitive detection of bioanalytes based on signal amplification of coil-integrated giant magnetoimpedance biosystems,” *Sens Actuators B Chem*, vol. 247, pp. 1–10, Aug. 2017, doi: 10.1016/j.snb.2017.01.095.

[64] M. M. Miller, G. A. Prinz, S.-F. Cheng, and S. Bounnak, “Detection of a micron-sized magnetic sphere using a ring-shaped anisotropic magnetoresistance-based sensor: A model for a magnetoresistance-based biosensor,” *Appl. Phys. Lett*, vol. 81, p. 2211, 2002, doi: 10.1063/1.1507832.

[65] G. Boero, M. Demierre, P. A. Besse, and R. S. Popovic, “Micro-Hall devices: Performance, technologies and applications,” in *Sensors and Actuators, A: Physical*, Elsevier, Sep. 2003, pp. 314–320. doi: 10.1016/S0924-4247(03)00192-4.

[66] A. Sandhu and H. Handa, “Practical Hall sensors for biomedical instrumentation,” *IEEE Trans Magn*, vol. 41, no. 10, pp. 4123–4127, 2005, doi: 10.1109/TMAG.2005.855339.

[67] P.-A. Besse, G. Boero, M. Demierre, V. Pott, and R. Popovic, “Detection of a single magnetic microbead using a miniaturized silicon Hall sensor,” *Appl. Phys. Lett*, vol. 80, p. 4199, 2002, doi: 10.1063/1.1483909.

[68] G. Mihajlović *et al.*, “Detection of single magnetic bead for biological applications using an InAs quantum-well micro-Hall sensor,” *Appl Phys Lett*, vol. 87, no. 11, p. 112502, Sep. 2005, doi: 10.1063/1.2043238.

[69] G. Mihajlović, P. Xiong, S. Von Molnár, M. Field, and G. J. Sullivan, “InAs quantum well Hall devices for room-temperature detection of single magnetic biomolecular labels ARTICLES YOU MAY BE INTERESTED IN,” *J. Appl. Phys*, vol. 102, p. 34506, 2007, doi: 10.1063/1.2767385.

[70] L. Di Michele, C. Shelly, J. Gallop, and O. Kazakova, “Single particle detection: Phase control in submicron Hall sensors,” *J. Appl. Phys*, vol. 108, p. 103918, 2010, doi: 10.1063/1.3514097.

[71] L. Di Michele, C. Shelly, P. de Marco, P. See, D. Cox, and O. Kazakova, “Detection and susceptibility measurements of single Dynal bead,” *Hall sensors Journal of Applied Physics*, vol. 110, p. 103918, 2011, doi: 10.1063/1.3638124.

[72] O. Kazakova *et al.*, “Ultrasmall particle detection using a submicron Hall sensor”.

[73] A. Sandhu, K. Kurosawa, and M. Dede, “High Sensitivity InSb Ultra-Thin Film Micro-Hall Sensors for Bioscreening Applications Related content 50 nm Hall Sensors for Room Temperature Scanning Hall Probe Microscopy,” *Japanese Journal of Applied Physics To*, vol. 43, p. 868, 2004, doi: 10.1143/JJAP.43.L868.

[74] G. Mihajlović, K. Aledealat, P. Xiong, S. Von Molnár, M. Field, and G. J. Sullivan, “Magnetic characterization of a single superparamagnetic bead by phase-sensitive micro-Hall magnetometry,” *Appl. Phys. Lett*, vol. 91, p. 172518, 2007, doi: 10.1063/1.2802732.

[75] S. Gambini, K. Skucha, P. P. Liu, J. Kim, and R. Krigel, “A 10 kPixel CMOS Hall Sensor Array With Baseline Suppression and Parallel Readout for Immunoassays,” *IEEE J Solid-State Circuits*, vol. 48, no. 1, pp. 302–317, 2013, doi: 10.1109/JSSC.2012.2224531.

[76] S. K. D. Y. Liu PP, Megens M, Kim J, Izyumin II, Gambini S, and Boser B., “Magnetic Relaxation Detector for microbead labels,” *IEEE J Solid-State Circuits.*, vol. 47, pp. 1056-1064., 2012.

[77] D. Issadore, H. J. Chung, J. Chung, G. Budin, R. Weissleder, and H. Lee, “µHall Chip for Sensitive Detection of Bacteria”, doi: 10.1002/adhm.201200380.

[78] D. Issadore *et al.*, “Ultrasensitive Clinical Enumeration of Rare Cells ex Vivo Using a Micro-Hall Detector,” *Sci Transl Med*, vol. 4, no. 141, pp. 141ra92-141ra92, Jul. 2012, doi: 10.1126/scitranslmed.3003747.

[79] W. Lee *et al.*, “Magnetic bead counter using a micro-Hall sensor for biological applications,” *Appl. Phys. Lett*, vol. 94, p. 153903, 2009, doi: 10.1063/1.3122142.

[80] A. Manzin, V. Nabaei, and R. Ferrero, “Quantification of Magnetic Nanobeads With Micrometer Hall Sensors,” *IEEE Sens J*, vol. 18, no. 24, pp. 10058–10065, 2018, doi: 10.1109/JSEN.2018.2874520.

[81] Y. Kumagai, Y. Imai, M. Abe, S. Sakamoto, H. Handa, and A. Sandhu, “Sensitivity dependence of Hall biosensor arrays with the position of superparamagnetic beads on their active regions,” *J Appl Phys*, vol. 103, no. 7, p. 07A309, Feb. 2008, doi: 10.1063/1.2833306.

[82] S. Liu, H. Guillou, A. D. Kent, G. W. Stupian, and M. S. Leung, “Effect of probe geometry on the Hall response in an inhomogeneous magnetic field: A numerical study,” *J Appl Phys*, vol. 83, no. 11, pp. 6161–6165, Jun. 1998, doi: 10.1063/1.367485.

[83] H. Guillou, A. D. Kent, G. W. Stupian, and M. S. Leung, “Geometries for high spatial resolution Hall probes,” *J Appl Phys*, vol. 93, no. 5, pp. 2746–2751, Mar. 2003, doi: 10.1063/1.1543651.

[84] Y. G. Cornelissens and F. M. Peeters, “Response function of a Hall magnetosensor in the diffusive regime,” *J Appl Phys*, vol. 92, no. 4, pp. 2006–2012, Jul. 2002, doi: 10.1063/1.1487909.

[85] A. Manzin, V. Nabaei, and O. Kazakova, “Modelling and optimization of submicron Hall sensors for the detection of superparamagnetic beads,” *J Appl Phys*, vol. 111, no. 7, p. 07E513, Mar. 2012, doi: 10.1063/1.3678322.

[86] S. Rampini, P. Li, and G. U. Lee, “Micromagnet arrays enable precise manipulation of individual biological analyte–superparamagnetic bead complexes for separation and sensing,” *Lab Chip*, vol. 16, no. 19, pp. 3645–3663, 2016, doi: 10.1039/C6LC00707D.

[87] S. Rampini *et al.*, “Design of micromagnetic arrays for on-chip separation of superparamagnetic bead aggregates and detection of a model protein and double-stranded DNA analytes,” *Sci Rep*, vol. 11, no. 1, p. 5302, 2021, doi: 10.1038/s41598-021-84395-3.

[88] G. Vieira *et al.*, “Magnetic Wire Traps and Programmable Manipulation of Biological Cells,” *Phys Rev Lett*, vol. 103, no. 12, p. 128101, Sep. 2009, doi: 10.1103/PhysRevLett.103.128101.

[89] C. S. Lee, H. Lee, and R. M. Westervelt, “Microelectromagnets for the control of magnetic nanoparticles,” *Appl Phys Lett*, vol. 79, no. 20, pp. 3308–3310, Nov. 2001, doi: 10.1063/1.1419049.

[90] A. K. Visvkarma *et al.*, “Comparative study of Au and Ni/Au gated AlGaN/GaN high electron mobility transistors,” *AIP Adv*, vol. 9, no. 12, p. 125231, Dec. 2019, doi: 10.1063/1.5116356.

[91] D. M. Bruls *et al.*, “Rapid integrated biosensor for multiplexed immunoassays based on actuated magnetic nanoparticles,” *Lab Chip*, vol. 9, no. 24, pp. 3504–3510, 2009, doi: 10.1039/B913960E.

[92] O. Florescu *et al.*, “On-chip magnetic separation of superparamagnetic beads for integrated molecular analysis,” *J Appl Phys*, vol. 107, no. 5, p. 054702, Mar. 2010, doi: 10.1063/1.3272779.

[93] G. Fonnum, C. Johansson, A. Molteberg, S. Mørup, and E. Aksnes, “Characterisation of Dynabeads® by magnetization measurements and Mössbauer spectroscopy,” *J Magn Magn Mater*, vol. 293, no. 1, pp. 41–47, 2005, doi: https://doi.org/10.1016/j.jmmm.2005.01.041.

[94] K. Seleznyova, M. Strugatsky, and J. Kliava, “Modelling the magnetic dipole,” *Eur J Phys*, vol. 37, no. 2, p. 025203, 2016, doi: 10.1088/0143-0807/37/2/025203.

[95] T. Vemulkar, R. Mansell, D. C. M. C. Petit, R. P. Cowburn, and M. S. Lesniak, “Highly tunable perpendicularly magnetized synthetic antiferromagnets for biotechnology applications.,” *Appl Phys Lett*, vol. 107, no. 1, p. 012403, Jul. 2015, doi: 10.1063/1.4926336.

[96] E. N. Welbourne, T. Vemulkar, and R. P. Cowburn, “High-yield fabrication of perpendicularly magnetised synthetic antiferromagnetic nanodiscs,” *Nano Res*, vol. 14, no. 11, pp. 3873–3878, 2021, doi: 10.1007/s12274-021-3307-1.

[97] P. Bruno and C. Chappert, “Ruderman-Kittel theory of oscillatory interlayer exchange coupling,” *Phys Rev B*, vol. 46, no. 1, pp. 261–270, Jul. 1992, doi: 10.1103/PhysRevB.46.261.

[98] R. Lavrijsen,) A Ferná Ndez-Pacheco, D. Petit, R. Mansell, J. H. Lee, and R. P. Cowburn, “Tuning the interlayer exchange coupling between single perpendicularly magnetized CoFeB layers,” 2012, doi: 10.1063/1.3682103.

[99] M T Johnson, P J H Bloemen, F J A den Broeder, and J J de Vries, “Magnetic anisotropy in metallic multilayers,” *Reports on Progress in Physics*, vol. 59, no. 11, p. 1409, 1996, doi: 10.1088/0034-4885/59/11/002.

[100] O. Hellwig, A. Berger, J. B. Kortright, and E. E. Fullerton, “Domain structure and magnetization reversal of antiferromagnetically coupled perpendicular anisotropy films,” *J Magn Magn Mater*, vol. 319, no. 1, pp. 13–55, 2007, doi: https://doi.org/10.1016/j.jmmm.2007.04.035.

[101] S. Bandiera, R. C. Sousa, S. Auffret, B. Rodmacq, and B. Dieny, “Enhancement of perpendicular magnetic anisotropy thanks to Pt insertions in synthetic antiferromagnets,” *Appl Phys Lett*, vol. 101, no. 7, p. 072410, Aug. 2012, doi: 10.1063/1.4745924.

[102] T. Vemulkar,) E N Welbourne, R. Mansell, D. C. M. C. Petit, and R. P. Cowburn, “The mechanical response in a fluid of synthetic antiferromagnetic and ferrimagnetic microdiscs with perpendicular magnetic anisotropy”, doi: 10.1063/1.4974211.

[103] A. Caciagli, R. J. Baars, A. P. Philipse, and B. W. M. Kuipers, “Exact expression for the magnetic field of a finite cylinder with arbitrary uniform magnetization,” *J Magn Magn Mater*, vol. 456, pp. 423–432, 2018, doi: https://doi.org/10.1016/j.jmmm.2018.02.003.

[104] N. Derby and S. Olbert, “Cylindrical magnets and ideal solenoids,” *Am J Phys*, vol. 78, no. 3, pp. 229–235, Feb. 2010, doi: 10.1119/1.3256157.

[105] E. H. Hall, “On a New Action of the Magnet on Electric Currents,” *American Journal of Mathematics*, vol. 2, no. 3, pp. 287–292, 1879, doi: 10.2307/2369245.

[106] R.S. Popovic, *Hall Effect Devices*, 2nd ed. Institute of Physics Publishing, Bristol, UK, 2004.

[107] K. S. Novoselov *et al.*, “Submicron probes for Hall magnetometry over the extended temperature range from helium to room temperature,” *J Appl Phys*, vol. 93, no. 12, pp. 10053–10057, May 2003, doi: 10.1063/1.1576492.

[108] John H. Davies, *The Physics of Low Dimensional Semiconductors: An Introduction*. Cambridge University Press, 1998.

[109] A. Manzin, E. Simonetto, G. Amato, V. Panchal, and O. Kazakova, “Modeling of graphene Hall effect sensors for microbead detection,” *J Appl Phys*, vol. 117, no. 17, p. 17B732, Apr. 2015, doi: 10.1063/1.4917323.

[110] J. Sun and J. Kosel, “Finite-Element Modelling and Analysis of Hall Effect and Extraordinary Magnetoresistance Effect,” *Finite Element Analysis - New Trends and Developments*. IntechOpen, 2012. doi: 10.5772/47777.

[111] I. S. Ibrahim, V. A. Schweigert, and F. M. Peeters, “Diffusive transport in a Hall junction with a microinhomogeneous magnetic field,” *Phys Rev B*, vol. 57, no. 24, pp. 15416–15427, Jun. 1998, doi: 10.1103/PhysRevB.57.15416.

[112] S. J. Bending and A. Oral, “Hall effect in a highly inhomogeneous magnetic field distribution,” *J Appl Phys*, vol. 81, no. 8, pp. 3721–3725, Apr. 1997, doi: 10.1063/1.365494.

[113] F. M. Peeters and X. Q. Li, “Hall magnetometer in the ballistic regime,” *Appl Phys Lett*, vol. 72, no. 5, pp. 572–574, Feb. 1998, doi: 10.1063/1.120759.

[114] https://www.comsol.com/multiphysics, “COMSOL Multiphysics Cyclopedia,” *https://www.comsol.com/multiphysics*.

[115] D. W. Shaw, “Localized GaAs Etching with Acidic Hydrogen Peroxide Solutions,” *J Electrochem Soc*, vol. 128, no. 4, p. 874, 1981, doi: 10.1149/1.2127524.

[116] Z. Q. Qiu and S. D. Bader, “Surface magneto-optic Kerr effect,” *Review of Scientific Instruments*, vol. 71, no. 3, pp. 1243–1255, Mar. 2000, doi: 10.1063/1.1150496.

[117] A. Zieba and S. Foner, “Detection coil, sensitivity function, and sample geometry effects for vibrating sample magnetometers,” *Review of Scientific Instruments*, vol. 53, no. 9, pp. 1344–1354, Sep. 1982, doi: 10.1063/1.1137182.

[118] A. Niazi, P. Poddar, and A. K. Rastogi*, “A precision , low-cost vibrating sample magnetometer,” *Curr Sci*, vol. 79, no. 1, 2000.

[119] A W Pacyna, “General theory of the signal induced in a vibrating magnetometer,” *J Phys E*, vol. 15, no. 6, p. 663, 1982, doi: 10.1088/0022-3735/15/6/014.

[120] A. D. Kent, S. von Molnár, S. Gider, and D. D. Awschalom, “Properties and measurement of scanning tunneling microscope fabricated ferromagnetic particle arrays (invited),” *J Appl Phys*, vol. 76, no. 10, pp. 6656–6660, Nov. 1994, doi: 10.1063/1.358160.

[121] Y. Li, P. Xiong, S. von Molnár, S. Wirth, Y. Ohno, and H. Ohno, “Hall magnetometry on a single iron nanoparticle,” *Appl Phys Lett*, vol. 80, no. 24, pp. 4644–4646, Jun. 2002, doi: 10.1063/1.1487921.

[122] V. Nabaei, R. K. Rajkumar, A. Manzin, O. Kazakova, and A. Tzalenchuk, “Optimization of Hall bar response to localized magnetic and electric fields,” *J Appl Phys*, vol. 113, no. 6, p. 064504, Feb. 2013, doi: 10.1063/1.4790508.

[123] D. Weiss, P. Grambow, K. von Klitzing, A. Menschig, and G. Weimann, “Fabrication and characterization of deep mesa etched ‘“anti”’-dot superlattices in GaAs-AlGaAs heterostructures,” *Appl Phys Lett*, vol. 58, no. 25, pp. 2960–2962, Jun. 1991, doi: 10.1063/1.104708.

[124] C.-J. Lin *et al.*, “Magnetic and structural properties of Co/Pt multilayers,” *J Magn Magn Mater*, vol. 93, pp. 194–206, 1991, doi: https://doi.org/10.1016/0304-8853(91)90329-9.

[125] S. J. Greaves, P. J. Grundy, and R. J. Pollard, “Magnetic properties of cobalt layers and Co/Pt multilayers,” *J Magn Magn Mater*, vol. 121, no. 1, pp. 532–535, 1993, doi: https://doi.org/10.1016/0304-8853(93)91262-6.

[126] L. Cestarollo, K. Srinivasan, and A. El-Ghazaly, “Investigation of perpendicular magnetic anisotropy in Pt/Co20Fe60B20/Pt multi-layer structures,” *J Magn Magn Mater*, vol. 562, p. 169825, 2022, doi: https://doi.org/10.1016/j.jmmm.2022.169825.

[127] J. W. Knepper and F. Y. Yang, “Oscillatory interlayer coupling in Co/Pt multilayers with perpendicular anisotropy,” *Phys Rev B*, vol. 71, no. 22, p. 224403, Jun. 2005, doi: 10.1103/PhysRevB.71.224403.

[128] M. R. Stanton, “Self-assembly of ferromagnetic micro/nano-particles with perpendicular magnetic anisotropy (Doctoral thesis),” 2020. Accessed: Dec. 12, 2022. [Online]. Available: https://doi.org/10.17863/CAM.72291

[129] J. M. Shaw, H. T. Nembach, and T. J. Silva, “Roughness induced magnetic inhomogeneity in Co/Ni multilayers: Ferromagnetic resonance and switching properties in nanostructures,” *J Appl Phys*, vol. 108, no. 9, p. 093922, Nov. 2010, doi: 10.1063/1.3506688.

[130] T. Thomson, G. Hu, and B. D. Terris, “Intrinsic Distribution of Magnetic Anisotropy in Thin Films Probed by Patterned Nanostructures,” *Phys Rev Lett*, vol. 96, no. 25, p. 257204, Jun. 2006, doi: 10.1103/PhysRevLett.96.257204.

[131] J. M. Shaw *et al.*, “Reversal mechanisms in perpendicularly magnetized nanostructures,” *Phys Rev B*, vol. 78, no. 2, p. 24414, Jul. 2008, doi: 10.1103/PhysRevB.78.024414.

[132] H. van Houten, B. J. van Wees, M. G. J. Heijman, and J. P. André, “Submicron conducting channels defined by shallow mesa etch in GaAs-AlGaAs heterojunctions,” *Appl Phys Lett*, vol. 49, no. 26, pp. 1781–1783, Dec. 1986, doi: 10.1063/1.97243.

[133] G. L. Snider, I. -H. Tan, and E. L. Hu, “Electron states in mesa-etched one-dimensional quantum well wires,” *J Appl Phys*, vol. 68, no. 6, pp. 2849–2853, Sep. 1990, doi: 10.1063/1.346443.

[134] S. Wirth, S. von Molnár, M. Field, and D. D. Awschalom, “Magnetism of nanometer-scale iron particles arrays (invited),” *J Appl Phys*, vol. 85, no. 8, pp. 5249–5254, Apr. 1999, doi: 10.1063/1.369957.

[135] P. D. Ye, D. Weiss, K. von Klitzing, K. Eberl, and H. Nickel, “Fabrication and characterization of micromagnet arrays on top of GaAs/AlGaAs heterostructures,” *Appl Phys Lett*, vol. 67, no. 10, pp. 1441–1443, Sep. 1995, doi: 10.1063/1.114520.

[1] D. Egger and K. Bienz, “Protein (western) blotting,” *Mol Biotechnol*, vol. 1, no. 3, pp. 289–305, 1994, doi: 10.1007/BF02921696.

[2] S. Aydin, “A short history, principles, and types of ELISA, and our laboratory experience with peptide/protein analyses using ELISA,” *Peptides (N.Y.)*, vol. 72, pp. 4–15, 2015, doi: https://doi.org/10.1016/j.peptides.2015.04.012.

[3] D. A. Hall, J. Ptacek, and M. Snyder, “Protein Microarray Technology Types of protein microarrays.” Accessed: May 30, 2019. [Online]. Available: https://www.ncbi.nlm.nih.gov/pmc/articles/PMC1828913/pdf/nihms17379.pdf

[4] T. Brown, “Southern Blotting,” in *Current Protocols in Immunology*, Hoboken, NJ, USA: John Wiley & Sons, Inc., 2001, p. Unit 10.6A. doi: 10.1002/0471142735.im1006as06.

[5] R. Bumgarner, “Overview of DNA microarrays: types, applications, and their future.,” *Curr Protoc Mol Biol*, vol. Chapter 22, p. Unit 22.1., Jan. 2013, doi: 10.1002/0471142727.mb2201s101.

[6] S. A. , Dunbar and Michaela R. Hoffmeyer, “Microsphere-based multiplex immunoassays: development and applications using Luminex® xMAP® technology.,” in *The Immunoassay Handbook: Theory and applications of ligand binding, ELISA and related techniques*, 2013, p. Chpt 2.9.

[7] A. Adan, G. Alizada, Y. Kiraz, Y. Baran, and A. Nalbant, “Flow cytometry: basic principles and applications,” *Crit Rev Biotechnol*, vol. 37, no. 2, pp. 163–176, Feb. 2017, doi: 10.3109/07388551.2015.1128876.

[8] S. J. KARCHER and S. J. KARCHER, “POLYMERASE CHAIN REACTION,” *Mol Biol*, pp. 215–227, Jan. 1995, doi: 10.1016/B978-012397720-5.50040-2.

[9] N. L. Rosi and C. A. Mirkin, “Nanostructures in Biodiagnostics,” *Chem Rev*, vol. 105, no. 4, pp. 1547–1562, Apr. 2005, doi: 10.1021/cr030067f.

[10] S. Zhang, A. Garcia-D’Angeli, J. P. Brennan, and Q. Huo, “Predicting detection limits of enzyme-linked immunosorbent assay (ELISA) and bioanalytical techniques in general,” *Analyst*, vol. 139, no. 2, pp. 439–445, 2014, doi: 10.1039/C3AN01835K.

[11] Y. M. Shlyapnikov, E. A. Malakhova, A. Z. Vinarov, A. A. Zamyatnin, and E. A. Shlyapnikova, “Can new immunoassay techniques improve bladder cancer diagnostics With protein biomarkers?,” *Front Mol Biosci*, vol. 7, 2021, doi: 10.3389/fmolb.2020.620687.

[12] N. A. W. Bell and U. F. Keyser, “Digitally encoded DNA nanostructures for multiplexed, single-molecule protein sensing with nanopores,” *Nat Nanotechnol*, vol. 11, no. 7, pp. 645–651, 2016, doi: 10.1038/nnano.2016.50.

[13] M. Alvarez and L. M. Lechuga, “Microcantilever-based platforms as biosensing tools,” *Analyst*, vol. 135, pp. 827–836, 2010, doi: 10.1039/b908503n.

[14] F. Patolsky and C. M. Lieber, “Nanowire nanosensors,” *Materials Today*, vol. 8, no. 4, pp. 20–28, Apr. 2005, doi: 10.1016/S1369-7021(05)00791-1.

[15] R. J. Chen *et al.*, “Noncovalent functionalization of carbon nanotubes for highly specific electronic biosensors,” *PROCEEDINGS OF THE NATIONAL ACADEMY OF SCIENCES*, vol. 100, no. 9, 2003, Accessed: May 30, 2019. [Online]. Available: www.pnas.orgcgidoi10.1073pnas.0837064100

[16] M. Hu *et al.*, “Gold nanostructures: engineering their plasmonic properties for biomedical applications,” 2006, doi: 10.1039/b517615h.

[17] W. R. Algar, A. J. Tavares, and U. J. Krull, “Beyond labels: A review of the application of quantum dots as integrated components of assays, bioprobes, and biosensors utilizing optical transduction,” *Anal Chim Acta*, vol. 673, no. 1, pp. 1–25, Jul. 2010, doi: 10.1016/j.aca.2010.05.026.

[18] C. Rümenapp, B. Gleich, and A. Haase, “Magnetic Nanoparticles in Magnetic Resonance Imaging and Diagnostics,” *Pharm Res*, vol. 29, no. 5, pp. 1165–1179, May 2012, doi: 10.1007/s11095-012-0711-y.

[19] J. Dobson, “Magnetic nanoparticles for drug delivery,” *Drug Dev Res*, vol. 67, no. 1, pp. 55–60, Jan. 2006, doi: 10.1002/ddr.20067.

[20] S. Kossatz *et al.*, “Efficient treatment of breast cancer xenografts with multifunctionalized iron oxide nanoparticles combining magnetic hyperthermia and anti-cancer drug delivery,” *Breast Cancer Research*, vol. 17, no. 1, p. 66, Dec. 2015, doi: 10.1186/s13058-015-0576-1.

[21] H. P. Khng, D. Cunliffe, S. Davies, N. A. Turner, and E. N. Vulfson, “The synthesis of sub-micron magnetic particles and their use for preparative purification of proteins,” *Biotechnol Bioeng*, vol. 60, no. 4, pp. 419–424, Nov. 1998, doi: 10.1002/(SICI)1097-0290(19981120)60:4<419::AID-BIT3>3.0.CO;2-P.

[22] R. J. C. David R. Baselt, Gil U. Lee, Mohan Natesan, Steven W. Metzger, Paul E. Sheehan, “A Biosensor based in magnetoresistance technology,” *Biosens Bioelectron*, vol. 13, pp. 731–739, 1998.

[23] R. L. Edelstein *et al.*, “The BARC biosensor applied to the detection of biological warfare agents,” *Biosens Bioelectron*, vol. 14, no. 10–11, pp. 805–813, Jan. 2000, doi: 10.1016/S0956-5663(99)00054-8.

[24] M. M. Miller *et al.*, “A DNA array sensor utilizing magnetic microbeads and magnetoelectronic detection,” *J Magn Magn Mater*, vol. 225, no. 1–2, pp. 138–144, Jan. 2001, doi: 10.1016/S0304-8853(00)01242-7.

[25] J. C. Rife, M. M. Miller, P. E. Sheehan, C. R. Tamanaha, M. Tondra, and L. J. Whitman, “Design and performance of GMR sensors for the detection of magnetic microbeads in biosensors,” *Sens Actuators A Phys*, vol. 107, no. 3, pp. 209–218, 2003, doi: 10.1016/S0924-4247(03)00380-7.

[26] S. P. Mulvaney *et al.*, “Rapid, femtomolar bioassays in complex matrices combining microfluidics and magnetoelectronics,” *Biosens Bioelectron*, vol. 23, no. 2, pp. 191–200, Sep. 2007, doi: 10.1016/J.BIOS.2007.03.029.

[27] S. P. Mulvaney, K. M. Myers, P. E. Sheehan, and L. J. Whitman, “Attomolar protein detection in complex sample matrices with semi-homogeneous fluidic force discrimination assays,” *Biosens Bioelectron*, vol. 24, no. 5, pp. 1109–1115, Jan. 2009, doi: 10.1016/J.BIOS.2008.06.010.

[28] L. J. W. S.P. Mulvaney *, C.N. Ibe, C.R. Tamanaha, “Direct detection of genomic DNA with fluidic force discrimination assays,” *Anal Biochem*, vol. 392, no. 139–144, 2009, Accessed: May 19, 2019. [Online]. Available: https://pdf.sciencedirectassets.com/272363/1-s2.0-S0003269709X00163/1-s2.0-S0003269709003790/main.pdf?x-amz-security-token=AgoJb3JpZ2luX2VjEFEaCXVzLWVhc3QtMSJHMEUCIQDfnKZ6sK9S2SUQdR20snB4sbFboozFgZ04Q%2FjfagWeewIgdVip8CMIhMr56ZUSecE8wawPFc40Tw2PIzISm4YCPd

[29] C. R. Tamanaha, S. P. Mulvaney, and J. C. Rife, “Evolution of a magnetic-based biomolecular detection system,” in *2009 Annual International Conference of the IEEE Engineering in Medicine and Biology Society*, IEEE, Sep. 2009, pp. 5425–5427. doi: 10.1109/IEMBS.2009.5332482.

[30] D. L. Graham, H. Ferreira, J. Bernardo, P. P. Freitas, and J. M. S. Cabral, “Single magnetic microsphere placement and detection on-chip using current line designs with integrated spin valve sensors: Biotechnological applications,” *J Appl Phys*, vol. 91, p. 7786, 2002, doi: 10.1063/1.1451898.

[31] D. L. Graham, H. A. Ferreira, P. P. Freitas, and J. M. S. Cabral, “High sensitivity detection of molecular recognition using magnetically labelled biomolecules and magnetoresistive sensors,” *Biosens Bioelectron*, vol. 18, no. 4, pp. 483–488, Apr. 2003, doi: 10.1016/S0956-5663(02)00205-1.

[32] H. A. Ferreira, D. L. Graham, P. P. Freitas, and J. M. S. Cabral, “Biodetection using magnetically labeled biomolecules and arrays of spin valve sensors (invited),” *J Appl Phys*, vol. 93, p. 7281, 2003, doi: 10.1063/1.1544449.

[33] L. Lagae *et al.*, “On-chip manipulation and magnetization assessment of magnetic bead ensembles by integrated spin-valve sensors,” *J Appl Phys*, vol. 91, p. 7445, 2002, doi: 10.1063/1.1447288.

[34] H. A. Ferreira, N. Feliciano, D. L. Graham, L. A. Clarke, M. D. Amaral, and P. P. Freitas, “Rapid DNA hybridization based on ac field focusing of magnetically labeled target DNA,” *Appl Phys Lett*, vol. 87, no. 1, p. 13901, Jun. 2005, doi: 10.1063/1.1984090.

[35] D. L. Graham, H. A. Ferreira, N. Feliciano, P. P. Freitas, L. A. Clarke, and M. D. Amaral, “Magnetic field-assisted DNA hybridisation and simultaneous detection using micron-sized spin-valve sensors and magnetic nanoparticles,” *Sensors and Actuators B*, vol. 107, pp. 936–944, 2005, doi: 10.1016/j.snb.2004.12.071.

[36] J. Germano *et al.*, “A portable and autonomous magnetic detection platform for biosensing.,” *Sensors (Basel)*, vol. 9, no. 6, pp. 4119–37, 2009, doi: 10.3390/s90604119.

[37] V. C. Martins *et al.*, “Femtomolar limit of detection with a magnetoresistive biochip,” *Biosens Bioelectron*, vol. 24, no. 8, pp. 2690–2695, Apr. 2009, doi: 10.1016/J.BIOS.2009.01.040.

[38] V. C. Martins *et al.*, “Challenges and trends in the development of a magnetoresistive biochip portable platform,” *J Magn Magn Mater*, vol. 322, no. 9–12, pp. 1655–1663, May 2010, doi: 10.1016/J.JMMM.2009.02.141.

[39] E. Fernandes *et al.*, “A bacteriophage detection tool for viability assessment of Salmonella cells,” *Biosens Bioelectron*, vol. 52, pp. 239–246, Feb. 2014, doi: 10.1016/J.BIOS.2013.08.053.

[40] T. G. Barroso, R. C. Martins, E. Fernandes, S. Cardoso, J. Rivas, and P. P. Freitas, “Detection of BCG bacteria using a magnetoresistive biosensor: A step towards a fully electronic platform for tuberculosis point-of-care detection,” *Biosens Bioelectron*, vol. 100, pp. 259–265, Feb. 2018, doi: 10.1016/j.bios.2017.09.004.

[41] A. Fernandes *et al.*, “Lab-on-Chip Cytometry Based on Magnetoresistive Sensors for Bacteria Detection in Milk,” *Sensors*, vol. 14, no. 8, pp. 15496–15524, Aug. 2014, doi: 10.3390/s140815496.

[42] C. M. Duarte, C. Carneiro, S. Cardoso, P. P. Freitas, and R. Bexiga, “Semi-quantitative method for Staphylococci magnetic detection in raw milk,” *Journal of Dairy Research*, vol. 84, no. 1, pp. 80–88, Feb. 2017, doi: 10.1017/S0022029916000741.

[43] “Magnomics | Nanotech for Life.” https://www.magnomics.pt/ (accessed Jun. 24, 2019).

[44] S. X. Wang *et al.*, “Towards a magnetic microarray for sensitive diagnostics,” *J Magn Magn Mater*, vol. 293, pp. 731–736, 2005, doi: 10.1016/j.jmmm.2005.02.054.

[45] S.-J. Han *et al.*, “CMOS Integrated DNA Microarray Based on GMR Sensors,” in *2006 International Electron Devices Meeting*, IEEE, 2006, pp. 1–4. doi: 10.1109/IEDM.2006.346887.

[46] L. Xu *et al.*, “Giant magnetoresistive biochip for DNA detection and HPV genotyping,” *Biosens Bioelectron*, vol. 24, pp. 99–103, 2008, doi: 10.1016/j.bios.2008.03.030.

[47] R. S. Gaster *et al.*, “Matrix-insensitive protein assays push the limits of biosensors in medicine,” *Nat Med*, vol. 15, no. 11, pp. 1327–1332, Nov. 2009, doi: 10.1038/nm.2032.

[48] I. Fishbein and R. J. Levy, “The matrix neutralized,” *Nature*, vol. 461, no. 7266, pp. 890–891, Oct. 2009, doi: 10.1038/461890a.

[49] D. Kim *et al.*, “Nanosensor dosimetry of mouse blood proteins after exposure to ionizing radiation,” 2013, doi: 10.1038/srep02234.

[50] E. Ng, K. C. Nadeau, and S. X. Wang, “Giant magnetoresistive sensor array for sensitive and specific multiplexed food allergen detection,” 2016, doi: 10.1016/j.bios.2016.02.002.

[51] A. C. Mak *et al.*, “Sensitive giant magnetoresistive-based immunoassay for multiplex mycotoxin detection,” *Biosens Bioelectron*, vol. 25, no. 7, pp. 1635–1639, Mar. 2010, doi: 10.1016/J.BIOS.2009.11.028.

[52] R. S. Gaster, D. A. Hall, and S. X. Wang, “Autoassembly Protein Arrays for Analyzing Antibody Cross-Reactivity,” *Nano Lett*, vol. 11, pp. 2579–2583, 2011, doi: 10.1021/nl1026056.

[53] R. S. Gaster, D. A. Hall, and S. X. Wang, “nanoLAB: An ultraportable, handheld diagnostic laboratory for global health,” *Lab Chip*, vol. 11, no. 5, p. 950, Mar. 2011, doi: 10.1039/c0lc00534g.

[54] J. Choi, A. W. Gani, D. J. B. Bechstein, J.-R. Lee, P. J. Utz, and S. X. Wang, “Portable, one-step, and rapid GMR biosensor platform with smartphone interface,” *Biosens Bioelectron*, vol. 85, pp. 1–7, Nov. 2016, doi: 10.1016/j.bios.2016.04.046.

[55] E. Ng, C. Yao, T. O. Shultz, S. Ross-Howe, and S. X. Wang, “Magneto-nanosensor smartphone platform for the detection of HIV and leukocytosis at point-of-care,” *Nanomedicine*, vol. 16, pp. 10–19, Feb. 2019, doi: 10.1016/J.NANO.2018.11.007.

[56] N. N. Trivedi *et al.*, “Analytical validation of a novel multi-analyte plasma test for lung nodule characterization,” *Research Article Biomedical Research and Reviews Biomed Res Rev*, vol. 2, no. 3, pp. 1–10, 2018, doi: 10.15761/BRR.1000123.

[57] “Home - MagArray.” https://magarray.com/ (accessed Jun. 24, 2019).

[58] Reinder Coehoorn and Menno Willem Jose Prins, “SENSOR AND METHOD FOR MEASURING THE AREAL DENSITY OF MAGNETIC NANOPARTICLES ON A MICRO-ARRAY,” US 7,048,890 B2, May 23, 2006 Accessed: May 22, 2019. [Online]. Available: https://patentimages.storage.googleapis.com/4d/20/88/e0576b7dab5540/US7048890.pdf

[59] J. Schotter, P. B. Kamp, A. Becker, A. Pühler, G. Reiss, and H. Brückl, “Comparison of a prototype magnetoresistive biosensor to standard fluorescent DNA detection,” *Biosens Bioelectron*, vol. 19, pp. 1149–1156, 2004, doi: 10.1016/j.bios.2003.11.007.

[60] B. Srinivasan *et al.*, “A Detection System Based on Giant Magnetoresistive Sensors and High-Moment Magnetic Nanoparticles Demonstrates Zeptomole Sensitivity: Potential for Personalized Medicine,” *Angewandte Chemie International Edition*, vol. 48, no. 15, pp. 2764–2767, Mar. 2009, doi: 10.1002/anie.200806266.

[61] Y. R. Chemla *et al.*, “Ultrasensitive magnetic biosensor for homogeneous immunoassay,” *Proc Natl Acad Sci U S A*, vol. 97, no. 26, pp. 14268–72, Dec. 2000, doi: 10.1073/pnas.97.26.14268.

[62] X.-C. Sun, C. Lei, L. Guo, and Y. Zhou, “Sandwich immunoassay for the prostate specific antigen using a micro-fluxgate and magnetic bead labels”, doi: 10.1007/s00604-016-1889-1.

[63] L. Guo, S. Zhi, X. Sun, C. Lei, and Y. Zhou, “Ultrasensitive detection of bioanalytes based on signal amplification of coil-integrated giant magnetoimpedance biosystems,” *Sens Actuators B Chem*, vol. 247, pp. 1–10, Aug. 2017, doi: 10.1016/j.snb.2017.01.095.

[64] M. M. Miller, G. A. Prinz, S.-F. Cheng, and S. Bounnak, “Detection of a micron-sized magnetic sphere using a ring-shaped anisotropic magnetoresistance-based sensor: A model for a magnetoresistance-based biosensor,” *Appl. Phys. Lett*, vol. 81, p. 2211, 2002, doi: 10.1063/1.1507832.

[65] G. Boero, M. Demierre, P. A. Besse, and R. S. Popovic, “Micro-Hall devices: Performance, technologies and applications,” in *Sensors and Actuators, A: Physical*, Elsevier, Sep. 2003, pp. 314–320. doi: 10.1016/S0924-4247(03)00192-4.

[66] A. Sandhu and H. Handa, “Practical Hall sensors for biomedical instrumentation,” *IEEE Trans Magn*, vol. 41, no. 10, pp. 4123–4127, 2005, doi: 10.1109/TMAG.2005.855339.

[67] P.-A. Besse, G. Boero, M. Demierre, V. Pott, and R. Popovic, “Detection of a single magnetic microbead using a miniaturized silicon Hall sensor,” *Appl. Phys. Lett*, vol. 80, p. 4199, 2002, doi: 10.1063/1.1483909.

[68] G. Mihajlović *et al.*, “Detection of single magnetic bead for biological applications using an InAs quantum-well micro-Hall sensor,” *Appl Phys Lett*, vol. 87, no. 11, p. 112502, Sep. 2005, doi: 10.1063/1.2043238.

[69] G. Mihajlović, P. Xiong, S. Von Molnár, M. Field, and G. J. Sullivan, “InAs quantum well Hall devices for room-temperature detection of single magnetic biomolecular labels ARTICLES YOU MAY BE INTERESTED IN,” *J. Appl. Phys*, vol. 102, p. 34506, 2007, doi: 10.1063/1.2767385.

[70] L. Di Michele, C. Shelly, J. Gallop, and O. Kazakova, “Single particle detection: Phase control in submicron Hall sensors,” *J. Appl. Phys*, vol. 108, p. 103918, 2010, doi: 10.1063/1.3514097.

[71] L. Di Michele, C. Shelly, P. de Marco, P. See, D. Cox, and O. Kazakova, “Detection and susceptibility measurements of single Dynal bead,” *Hall sensors Journal of Applied Physics*, vol. 110, p. 103918, 2011, doi: 10.1063/1.3638124.

[72] O. Kazakova *et al.*, “Ultrasmall particle detection using a submicron Hall sensor”.

[73] A. Sandhu, K. Kurosawa, and M. Dede, “High Sensitivity InSb Ultra-Thin Film Micro-Hall Sensors for Bioscreening Applications Related content 50 nm Hall Sensors for Room Temperature Scanning Hall Probe Microscopy,” *Japanese Journal of Applied Physics To*, vol. 43, p. 868, 2004, doi: 10.1143/JJAP.43.L868.

[74] G. Mihajlović, K. Aledealat, P. Xiong, S. Von Molnár, M. Field, and G. J. Sullivan, “Magnetic characterization of a single superparamagnetic bead by phase-sensitive micro-Hall magnetometry,” *Appl. Phys. Lett*, vol. 91, p. 172518, 2007, doi: 10.1063/1.2802732.

[75] S. Gambini, K. Skucha, P. P. Liu, J. Kim, and R. Krigel, “A 10 kPixel CMOS Hall Sensor Array With Baseline Suppression and Parallel Readout for Immunoassays,” *IEEE J Solid-State Circuits*, vol. 48, no. 1, pp. 302–317, 2013, doi: 10.1109/JSSC.2012.2224531.

[76] S. K. D. Y. Liu PP, Megens M, Kim J, Izyumin II, Gambini S, and Boser B., “Magnetic Relaxation Detector for microbead labels,” *IEEE J Solid-State Circuits.*, vol. 47, pp. 1056-1064., 2012.

[77] D. Issadore, H. J. Chung, J. Chung, G. Budin, R. Weissleder, and H. Lee, “µHall Chip for Sensitive Detection of Bacteria”, doi: 10.1002/adhm.201200380.

[78] D. Issadore *et al.*, “Ultrasensitive Clinical Enumeration of Rare Cells ex Vivo Using a Micro-Hall Detector,” *Sci Transl Med*, vol. 4, no. 141, pp. 141ra92-141ra92, Jul. 2012, doi: 10.1126/scitranslmed.3003747.

[79] W. Lee *et al.*, “Magnetic bead counter using a micro-Hall sensor for biological applications,” *Appl. Phys. Lett*, vol. 94, p. 153903, 2009, doi: 10.1063/1.3122142.

[80] A. Manzin, V. Nabaei, and R. Ferrero, “Quantification of Magnetic Nanobeads With Micrometer Hall Sensors,” *IEEE Sens J*, vol. 18, no. 24, pp. 10058–10065, 2018, doi: 10.1109/JSEN.2018.2874520.

[81] Y. Kumagai, Y. Imai, M. Abe, S. Sakamoto, H. Handa, and A. Sandhu, “Sensitivity dependence of Hall biosensor arrays with the position of superparamagnetic beads on their active regions,” *J Appl Phys*, vol. 103, no. 7, p. 07A309, Feb. 2008, doi: 10.1063/1.2833306.

[82] S. Liu, H. Guillou, A. D. Kent, G. W. Stupian, and M. S. Leung, “Effect of probe geometry on the Hall response in an inhomogeneous magnetic field: A numerical study,” *J Appl Phys*, vol. 83, no. 11, pp. 6161–6165, Jun. 1998, doi: 10.1063/1.367485.

[83] H. Guillou, A. D. Kent, G. W. Stupian, and M. S. Leung, “Geometries for high spatial resolution Hall probes,” *J Appl Phys*, vol. 93, no. 5, pp. 2746–2751, Mar. 2003, doi: 10.1063/1.1543651.

[84] Y. G. Cornelissens and F. M. Peeters, “Response function of a Hall magnetosensor in the diffusive regime,” *J Appl Phys*, vol. 92, no. 4, pp. 2006–2012, Jul. 2002, doi: 10.1063/1.1487909.

[85] A. Manzin, V. Nabaei, and O. Kazakova, “Modelling and optimization of submicron Hall sensors for the detection of superparamagnetic beads,” *J Appl Phys*, vol. 111, no. 7, p. 07E513, Mar. 2012, doi: 10.1063/1.3678322.

[86] S. Rampini, P. Li, and G. U. Lee, “Micromagnet arrays enable precise manipulation of individual biological analyte–superparamagnetic bead complexes for separation and sensing,” *Lab Chip*, vol. 16, no. 19, pp. 3645–3663, 2016, doi: 10.1039/C6LC00707D.

[87] S. Rampini *et al.*, “Design of micromagnetic arrays for on-chip separation of superparamagnetic bead aggregates and detection of a model protein and double-stranded DNA analytes,” *Sci Rep*, vol. 11, no. 1, p. 5302, 2021, doi: 10.1038/s41598-021-84395-3.

[88] G. Vieira *et al.*, “Magnetic Wire Traps and Programmable Manipulation of Biological Cells,” *Phys Rev Lett*, vol. 103, no. 12, p. 128101, Sep. 2009, doi: 10.1103/PhysRevLett.103.128101.

[89] C. S. Lee, H. Lee, and R. M. Westervelt, “Microelectromagnets for the control of magnetic nanoparticles,” *Appl Phys Lett*, vol. 79, no. 20, pp. 3308–3310, Nov. 2001, doi: 10.1063/1.1419049.

[90] A. K. Visvkarma *et al.*, “Comparative study of Au and Ni/Au gated AlGaN/GaN high electron mobility transistors,” *AIP Adv*, vol. 9, no. 12, p. 125231, Dec. 2019, doi: 10.1063/1.5116356.

[91] D. M. Bruls *et al.*, “Rapid integrated biosensor for multiplexed immunoassays based on actuated magnetic nanoparticles,” *Lab Chip*, vol. 9, no. 24, pp. 3504–3510, 2009, doi: 10.1039/B913960E.

[92] O. Florescu *et al.*, “On-chip magnetic separation of superparamagnetic beads for integrated molecular analysis,” *J Appl Phys*, vol. 107, no. 5, p. 054702, Mar. 2010, doi: 10.1063/1.3272779.

[93] G. Fonnum, C. Johansson, A. Molteberg, S. Mørup, and E. Aksnes, “Characterisation of Dynabeads® by magnetization measurements and Mössbauer spectroscopy,” *J Magn Magn Mater*, vol. 293, no. 1, pp. 41–47, 2005, doi: https://doi.org/10.1016/j.jmmm.2005.01.041.

[94] K. Seleznyova, M. Strugatsky, and J. Kliava, “Modelling the magnetic dipole,” *Eur J Phys*, vol. 37, no. 2, p. 025203, 2016, doi: 10.1088/0143-0807/37/2/025203.

[95] T. Vemulkar, R. Mansell, D. C. M. C. Petit, R. P. Cowburn, and M. S. Lesniak, “Highly tunable perpendicularly magnetized synthetic antiferromagnets for biotechnology applications.,” *Appl Phys Lett*, vol. 107, no. 1, p. 012403, Jul. 2015, doi: 10.1063/1.4926336.

[96] E. N. Welbourne, T. Vemulkar, and R. P. Cowburn, “High-yield fabrication of perpendicularly magnetised synthetic antiferromagnetic nanodiscs,” *Nano Res*, vol. 14, no. 11, pp. 3873–3878, 2021, doi: 10.1007/s12274-021-3307-1.

[97] P. Bruno and C. Chappert, “Ruderman-Kittel theory of oscillatory interlayer exchange coupling,” *Phys Rev B*, vol. 46, no. 1, pp. 261–270, Jul. 1992, doi: 10.1103/PhysRevB.46.261.

[98] R. Lavrijsen,) A Ferná Ndez-Pacheco, D. Petit, R. Mansell, J. H. Lee, and R. P. Cowburn, “Tuning the interlayer exchange coupling between single perpendicularly magnetized CoFeB layers,” 2012, doi: 10.1063/1.3682103.

[99] M T Johnson, P J H Bloemen, F J A den Broeder, and J J de Vries, “Magnetic anisotropy in metallic multilayers,” *Reports on Progress in Physics*, vol. 59, no. 11, p. 1409, 1996, doi: 10.1088/0034-4885/59/11/002.

[100] O. Hellwig, A. Berger, J. B. Kortright, and E. E. Fullerton, “Domain structure and magnetization reversal of antiferromagnetically coupled perpendicular anisotropy films,” *J Magn Magn Mater*, vol. 319, no. 1, pp. 13–55, 2007, doi: https://doi.org/10.1016/j.jmmm.2007.04.035.

[101] S. Bandiera, R. C. Sousa, S. Auffret, B. Rodmacq, and B. Dieny, “Enhancement of perpendicular magnetic anisotropy thanks to Pt insertions in synthetic antiferromagnets,” *Appl Phys Lett*, vol. 101, no. 7, p. 072410, Aug. 2012, doi: 10.1063/1.4745924.

[102] T. Vemulkar,) E N Welbourne, R. Mansell, D. C. M. C. Petit, and R. P. Cowburn, “The mechanical response in a fluid of synthetic antiferromagnetic and ferrimagnetic microdiscs with perpendicular magnetic anisotropy”, doi: 10.1063/1.4974211.

[103] A. Caciagli, R. J. Baars, A. P. Philipse, and B. W. M. Kuipers, “Exact expression for the magnetic field of a finite cylinder with arbitrary uniform magnetization,” *J Magn Magn Mater*, vol. 456, pp. 423–432, 2018, doi: https://doi.org/10.1016/j.jmmm.2018.02.003.

[104] N. Derby and S. Olbert, “Cylindrical magnets and ideal solenoids,” *Am J Phys*, vol. 78, no. 3, pp. 229–235, Feb. 2010, doi: 10.1119/1.3256157.

[105] E. H. Hall, “On a New Action of the Magnet on Electric Currents,” *American Journal of Mathematics*, vol. 2, no. 3, pp. 287–292, 1879, doi: 10.2307/2369245.

[106] R.S. Popovic, *Hall Effect Devices*, 2nd ed. Institute of Physics Publishing, Bristol, UK, 2004.

[107] K. S. Novoselov *et al.*, “Submicron probes for Hall magnetometry over the extended temperature range from helium to room temperature,” *J Appl Phys*, vol. 93, no. 12, pp. 10053–10057, May 2003, doi: 10.1063/1.1576492.

[108] John H. Davies, *The Physics of Low Dimensional Semiconductors: An Introduction*. Cambridge University Press, 1998.

[109] A. Manzin, E. Simonetto, G. Amato, V. Panchal, and O. Kazakova, “Modeling of graphene Hall effect sensors for microbead detection,” *J Appl Phys*, vol. 117, no. 17, p. 17B732, Apr. 2015, doi: 10.1063/1.4917323.

[110] J. Sun and J. Kosel, “Finite-Element Modelling and Analysis of Hall Effect and Extraordinary Magnetoresistance Effect,” *Finite Element Analysis - New Trends and Developments*. IntechOpen, 2012. doi: 10.5772/47777.

[111] I. S. Ibrahim, V. A. Schweigert, and F. M. Peeters, “Diffusive transport in a Hall junction with a microinhomogeneous magnetic field,” *Phys Rev B*, vol. 57, no. 24, pp. 15416–15427, Jun. 1998, doi: 10.1103/PhysRevB.57.15416.

[112] S. J. Bending and A. Oral, “Hall effect in a highly inhomogeneous magnetic field distribution,” *J Appl Phys*, vol. 81, no. 8, pp. 3721–3725, Apr. 1997, doi: 10.1063/1.365494.

[113] F. M. Peeters and X. Q. Li, “Hall magnetometer in the ballistic regime,” *Appl Phys Lett*, vol. 72, no. 5, pp. 572–574, Feb. 1998, doi: 10.1063/1.120759.

[114] https://www.comsol.com/multiphysics, “COMSOL Multiphysics Cyclopedia,” *https://www.comsol.com/multiphysics*.

[115] D. W. Shaw, “Localized GaAs Etching with Acidic Hydrogen Peroxide Solutions,” *J Electrochem Soc*, vol. 128, no. 4, p. 874, 1981, doi: 10.1149/1.2127524.

[116] Z. Q. Qiu and S. D. Bader, “Surface magneto-optic Kerr effect,” *Review of Scientific Instruments*, vol. 71, no. 3, pp. 1243–1255, Mar. 2000, doi: 10.1063/1.1150496.

[117] A. Zieba and S. Foner, “Detection coil, sensitivity function, and sample geometry effects for vibrating sample magnetometers,” *Review of Scientific Instruments*, vol. 53, no. 9, pp. 1344–1354, Sep. 1982, doi: 10.1063/1.1137182.

[118] A. Niazi, P. Poddar, and A. K. Rastogi*, “A precision , low-cost vibrating sample magnetometer,” *Curr Sci*, vol. 79, no. 1, 2000.

[119] A W Pacyna, “General theory of the signal induced in a vibrating magnetometer,” *J Phys E*, vol. 15, no. 6, p. 663, 1982, doi: 10.1088/0022-3735/15/6/014.

[120] A. D. Kent, S. von Molnár, S. Gider, and D. D. Awschalom, “Properties and measurement of scanning tunneling microscope fabricated ferromagnetic particle arrays (invited),” *J Appl Phys*, vol. 76, no. 10, pp. 6656–6660, Nov. 1994, doi: 10.1063/1.358160.

[121] Y. Li, P. Xiong, S. von Molnár, S. Wirth, Y. Ohno, and H. Ohno, “Hall magnetometry on a single iron nanoparticle,” *Appl Phys Lett*, vol. 80, no. 24, pp. 4644–4646, Jun. 2002, doi: 10.1063/1.1487921.

[122] V. Nabaei, R. K. Rajkumar, A. Manzin, O. Kazakova, and A. Tzalenchuk, “Optimization of Hall bar response to localized magnetic and electric fields,” *J Appl Phys*, vol. 113, no. 6, p. 064504, Feb. 2013, doi: 10.1063/1.4790508.

[123] D. Weiss, P. Grambow, K. von Klitzing, A. Menschig, and G. Weimann, “Fabrication and characterization of deep mesa etched ‘“anti”’-dot superlattices in GaAs-AlGaAs heterostructures,” *Appl Phys Lett*, vol. 58, no. 25, pp. 2960–2962, Jun. 1991, doi: 10.1063/1.104708.

[124] C.-J. Lin *et al.*, “Magnetic and structural properties of Co/Pt multilayers,” *J Magn Magn Mater*, vol. 93, pp. 194–206, 1991, doi: https://doi.org/10.1016/0304-8853(91)90329-9.

[125] S. J. Greaves, P. J. Grundy, and R. J. Pollard, “Magnetic properties of cobalt layers and Co/Pt multilayers,” *J Magn Magn Mater*, vol. 121, no. 1, pp. 532–535, 1993, doi: https://doi.org/10.1016/0304-8853(93)91262-6.

[126] L. Cestarollo, K. Srinivasan, and A. El-Ghazaly, “Investigation of perpendicular magnetic anisotropy in Pt/Co20Fe60B20/Pt multi-layer structures,” *J Magn Magn Mater*, vol. 562, p. 169825, 2022, doi: https://doi.org/10.1016/j.jmmm.2022.169825.

[127] J. W. Knepper and F. Y. Yang, “Oscillatory interlayer coupling in Co/Pt multilayers with perpendicular anisotropy,” *Phys Rev B*, vol. 71, no. 22, p. 224403, Jun. 2005, doi: 10.1103/PhysRevB.71.224403.

[128] M. R. Stanton, “Self-assembly of ferromagnetic micro/nano-particles with perpendicular magnetic anisotropy (Doctoral thesis),” 2020. Accessed: Dec. 12, 2022. [Online]. Available: https://doi.org/10.17863/CAM.72291

[129] J. M. Shaw, H. T. Nembach, and T. J. Silva, “Roughness induced magnetic inhomogeneity in Co/Ni multilayers: Ferromagnetic resonance and switching properties in nanostructures,” *J Appl Phys*, vol. 108, no. 9, p. 093922, Nov. 2010, doi: 10.1063/1.3506688.

[130] T. Thomson, G. Hu, and B. D. Terris, “Intrinsic Distribution of Magnetic Anisotropy in Thin Films Probed by Patterned Nanostructures,” *Phys Rev Lett*, vol. 96, no. 25, p. 257204, Jun. 2006, doi: 10.1103/PhysRevLett.96.257204.

[131] J. M. Shaw *et al.*, “Reversal mechanisms in perpendicularly magnetized nanostructures,” *Phys Rev B*, vol. 78, no. 2, p. 24414, Jul. 2008, doi: 10.1103/PhysRevB.78.024414.

[132] H. van Houten, B. J. van Wees, M. G. J. Heijman, and J. P. André, “Submicron conducting channels defined by shallow mesa etch in GaAs-AlGaAs heterojunctions,” *Appl Phys Lett*, vol. 49, no. 26, pp. 1781–1783, Dec. 1986, doi: 10.1063/1.97243.

[133] G. L. Snider, I. -H. Tan, and E. L. Hu, “Electron states in mesa-etched one-dimensional quantum well wires,” *J Appl Phys*, vol. 68, no. 6, pp. 2849–2853, Sep. 1990, doi: 10.1063/1.346443.

[134] S. Wirth, S. von Molnár, M. Field, and D. D. Awschalom, “Magnetism of nanometer-scale iron particles arrays (invited),” *J Appl Phys*, vol. 85, no. 8, pp. 5249–5254, Apr. 1999, doi: 10.1063/1.369957.

[135] P. D. Ye, D. Weiss, K. von Klitzing, K. Eberl, and H. Nickel, “Fabrication and characterization of micromagnet arrays on top of GaAs/AlGaAs heterostructures,” *Appl Phys Lett*, vol. 67, no. 10, pp. 1441–1443, Sep. 1995, doi: 10.1063/1.114520.